Low-pressure, radicals assisted CVD synthesis of SWCNTs for thepotential implementation in-situ and real-time analysis technique (ETEM)

Thi Thanh Loan Truong

▶ **To cite this version:**

Thi Thanh Loan Truong. Low-pressure, radicals assisted CVD synthesis of SWCNTs for thepotential implementation in-situ and real-time analysis technique (ETEM). Materials Science [cond-mat.mtrl-sci]. Institut Polytechnique de Paris, 2023. English. NNT : 2023IPPAX058 . tel-04496045

HAL Id: tel-04496045
https://theses.hal.science/tel-04496045

Submitted on 8 Mar 2024

HAL is a multi-disciplinary open access archive for the deposit and dissemination of scientific research documents, whether they are published or not. The documents may come from teaching and research institutions in France or abroad, or from public or private research centers.

L'archive ouverte pluridisciplinaire **HAL**, est destinée au dépôt et à la diffusion de documents scientifiques de niveau recherche, publiés ou non, émanant des établissements d'enseignement et de recherche français ou étrangers, des laboratoires publics ou privés.

INSTITUT POLYTECHNIQUE DE PARIS

NNT : 2023IPPAX058

Thèse de doctorat

Low – pressure, radical assisted chemical vapor deposition (CVD) synthesis of SWCNTs for potential implementation in-situ and real-time analysis technique (ETEM – NanoMax)

Thèse de doctorat de l'Institut Polytechnique de Paris

préparée à Ecole polytechnique

Ecole doctorale n°626 Ecole doctorale de l'Institut Polytechnique de Paris (EDIPP)
Spécialité de doctorat: Physique des particules

Thèse présentée et soutenue à Palaiseau, le 19 Septembre, 2023, par

Thi Thanh Loan TRUONG

Composition du Jury :

Tiberiu MINEA Professeur Université Paris-Saclay, directeur du LPGP Laboratoire de Physique des Gaz et des Plasmas LPGP - UMR 8578 CNRS/Université Paris-Saclay	Rapporteur
Cuong PHAM-HUU DR CNRS at Institut de chimie et procédés pour l'énergie, l'environnement et la santé (ICPEES), UMR 7515 CNRS et l'Université de Strasbourg	Rapporteur
Ovidiu ERSEN Professeur à l'Université de Strasbourg – CNRS, Institut de Physique et Chimie de Matériaux de Strasbourg (IPCMS)	Examinateur Président du jury
Salomé FOREL Maître de conférence, Université Claude Bernard Lyon 1 LMI-UMR 5615 CNRS / UCBL Domaine Scientifique de la Doua Université Claude Bernard Lyon 1	Examinateur
Costel-Sorin COJOCARU Directeur de Recherche CNRS, Ecole Polytechnique LPICM-UMR 7647 CNRS	Directeur de thèse
Lenuta Ileana FLOREA Ingénieur de Recherche – CNRS, UCA, CRHEA	Encadrante

Acknowledgments/ Remerciement

The research work presented in this manuscript was carried out at the Laboratory of Physics of Interfaces and Thin Films (LPICM). I extend my sincere gratitude to Mr. Costel-Sorin COJOCARU and Mrs. Ileana FLOREA for graciously welcoming me to the LPICM and agreeing to chair my thesis. Their invaluable guidance, the freedom to explore the subject, patience, and encouragement have been instrumental in the success of this work.

I would like to express my deep appreciation to Prof. Tiberiu MINEA and Prof. Cuong PHAM-HUU for agreeing to serve as the rapporteurs for this thesis. Additionally, I am grateful to Prof. Ovidiu ERSEN and Salomé FOREL for their time and expertise in reviewing this work.

Every result presented in this manuscript is a product of collaborative efforts and the dedication of numerous individuals. I would like to acknowledge and highlight the collaborations that have significantly contributed to this research. Special thanks to Costel Cojocaru for welcoming me into the "Eco-aware and Efficient Nano-Materials, Nano-Devices and Engineering (NanoMADE-3E Initiative)" group at the LPICM, where I had the privilege to learn about carbon nanotube synthesis with Mihai-Robert Zamfir and carbon nanotube characterization with Ileana Florea and Mariam Ezzedine, who also provided TEM images. My stays at the NanoMADE-3E group were enlightening, and I made significant progress in my research through fruitful exchanges with the entire team. I extend my gratitude to Michel, Fatme, and others from the NanoMade-3E group.

The successful completion of this project owes much to the expertise and generous assistance of Alex and Razvigor from the LPICM, who patiently answered my questions and shared their knowledge. The positive atmosphere and camaraderie at the LPICM are owed to its wonderful members. I am thankful to all, with a special mention to Hindia for her availability and invaluable assistance in overcoming

challenges. A heartfelt thanks to Ghewa Akiki for your support during my laboratory-life.

As this thesis marks the culmination of my studies, I want to express my gratitude to my steadfast friends who have been with me throughout this journey: Ha Tran, Hoang Ngo, Thao Mai, Anh Nguyen, Yen Pham, Thuy Nguyen, and others.

Finally, my deepest thanks go to my family—my parents(TRUONG Sy Linh, TRAN Thi Thanh), my brothers (TRUONG Sy Toan, TRUONG Tuan Anh)—for their unwavering encouragement during this adventure. To my husband, Van Toan Pham, I am grateful for your daily support, which has played a significant role in the completion of this thesis.

Le travail de recherche présenté dans ce manuscrit a été réalisé au Laboratoire de Physique des Interfaces et des Couches Minces (LPICM). J'exprime ma sincère gratitude à M. Costel-Sorin COJOCARU et Mme. Ileana FLOREA pour m'avoir chaleureusement accueilli au LPICM et avoir accepté de présider ma thèse. Leurs conseils précieux, la liberté d'explorer le sujet, la patience et l'encouragement ont été cruciaux pour le succès de ce travail.

Je tiens à exprimer ma profonde reconnaissance au Prof. Tiberiu MINEA et au Prof. Cuong PHAM-HUU pour avoir accepté d'être les rapporteurs de cette thèse. De plus, je suis reconnaissante au Prof. Ovidiu ERSEN et à Salomé FOREL pour avoir consacré leur temps et leur expertise à la révision de ce travail.

Chaque résultat présenté dans ce manuscrit est le fruit d'efforts collaboratifs et du dévouement de nombreuses personnes. J'aimerais reconnaître et souligner les collaborations qui ont contribué de manière significative à cette recherche. Un merci particulier à Costel Cojocaru de m'avoir accueilli dans le groupe "Initiative Eco-responsable et Efficace des Nano-Matériaux, Nano-Dispositifs et Ingénierie (NanoMADE-3E)" du LPICM, où j'ai eu le privilège d'apprendre la synthèse des

nanotubes de carbone avec Mihai-Robert Zamfir et la caractérisation des nanotubes de carbone avec Ileana Florea et Mariam Ezzedine, qui ont également fourni des images TEM. Mes séjours au sein du groupe NanoMADE-3E ont été enrichissants, et j'ai réalisé des progrès significatifs dans mes recherches grâce à des échanges fructueux avec toute l'équipe. J'étends ma gratitude à Michel, Fatme et aux autres membres du groupe NanoMade-3E.

La réussite de ce projet est largement due à l'expertise et à l'assistance généreuse d'Alex et Razvigor du LPICM, qui ont répondu patiemment à mes questions et partagé leurs connaissances. L'atmosphère positive et la camaraderie au LPICM sont dues à ses membres merveilleux. Je suis reconnaissant envers tous, avec une mention spéciale à Hindia pour sa disponibilité et son assistance inestimable pour surmonter les défis. Un grand merci à Ghewa Akiki pour son soutien pendant ma vie de laboratoire.

Cette thèse marque la fin de mes études, et je tiens à exprimer ma gratitude envers mes amis fidèles qui m'ont accompagné tout au long de ce parcours : Ha Tran, Hoang Ngo, Thao Mai, Anh Nguyen, Yen Pham, Thuy Nguyen, et d'autres.

Enfin, mes remerciements les plus sincères vont à ma famille, mes parents (TRUONG Sy Linh, TRAN Thi Thanh), mes frères (TRUONG Sy Toan, TRUONG Tuan Anh), pour leur encouragement indéfectible tout au long de cette aventure. À mon mari, Van Toan PHAM, je suis reconnaissante pour votre soutien quotidien, qui a joué un rôle significatif dans la réalisation de cette thèse.

CONTENTS

INTRODUCTION

In 1959, Richard P.Feynman sparked a frezy in the field of physics with his seminar titled "There's Plenty of Room at the Bottom", which focused on exploring and observing the infinitesimally small[1]. Feynman introduced the beginnings of what is now known as nanoscience and nanotechnology, using the example of cellular activity on a nanometric scale in biological systems. This involves manipulating matter at a billionth-of-a-meter scale, which can create new materials and processes. To properly appreciate the potential of the new discipline, it is necessary to understand that the matter is governed entirely by quantum effects, which literally modify its physical properties at the nanometric scale. As a result, reducing the size of a material can reveal previously undiscovered physical and chemical properties at a microscopic or macroscopic scale. Nanotechnology has already been implemented in various industrial markets, resulting in achievements such as the increase in the computer speed, the development of genetically active drugs, and the creation of high-performance miniaturized sensors.

In this context, since 1980s, carbon nanostructures have been a significant component of nanophysics and nanotechnology. Their family regroups all the diversity of the geometrically constrained nano-objects. For instance, fullerenes, discovered in 1985 [2] and awarded the Nobel Prize in Chemistry in 1996 to by Curl, Smalley and Kroto, are allotropes of carbon confined in all direction (0D), existing at the interface between molecules and solids in relation to their number of atoms and their structure. As a result, their study is both a matter of physics and chemistry. Similarly, carbon nanotube, first observed in 1991 by S.Iijima in Japan[3], are one-dimensional (1D) due to their tubular shape with a nanometric diameter and a micrometric or millimetric length. Graphene, which was isolated in 2004[4], has same sp^2 hybridization of carbon atoms as fullerenes and carbon nanotubes, but is structured in two dimensions. For their contribution to graphene research, Geim and Novoselov were awarded the Nobel Prize in Physics in [5]. In recent years, other 0D carbon nanostructures have been

developed; such graphene quantum dot [6], which have the same structure as graphene, but are confined in both directions of the plane.

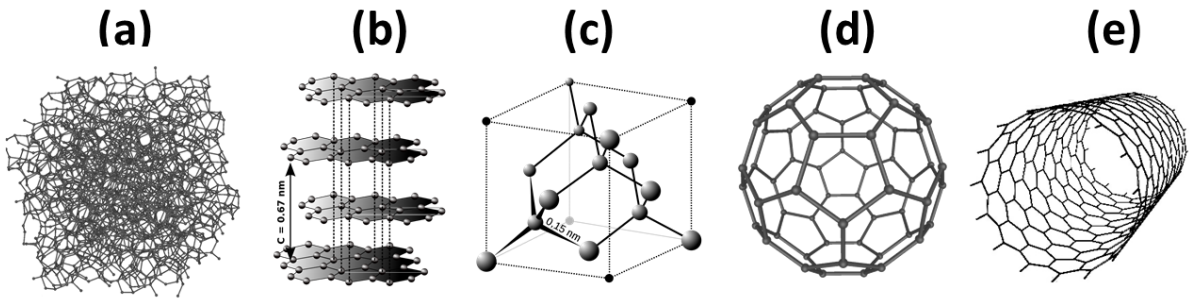

Figure 0.1. Structure of allotropic forms of carbon: (a) amorphous, (b) graphite, (c) diamond, (d) fullerene, (e) carbon nanotube[7]

Carbon nanotubes, as an allotrope of carbon, offer two particularly exciting perspectives: the incredible versatility of their properties in term of structure and dimension make them unique and original objects for fundamental studies and the exploration of nanoworld[8]–[10], while their outstanding physical properties such as mechanical strength, electrical conductivity, thermal conductivity, and optical properties give numerous prospects for industrial application [8]–[13]. Despite their promising prospects, several challenges remain, especially in controlling the manufacturing process to realize their full technological potential. Although mass production methods have been developed in recent years, there are still uncertainties in the understanding of the growth mechanisms[14], [15]. To full harness the potential of carbon nanotubes, significant process is necessary in understanding the factors controlling the synthesis yield, the sample purity, the crystalline quality, the length and chirality of carbon nanotubes.

The main focus of this manuscript is the investigation of the single-walled carbon nanotube (SWCNTs) growth using low-pressure chemical vapor deposition (LPCVD) and various characterization techniques, both ex-situ and in-situ. Chemical vapor deposition (CVD), and more particularly low-pressure CVD from methane, CH_4, is one of the potential ways to fabricate these single-wall carbon nanotubes. Carbon nanotubes have already been fabricated in recent years at LPICM with different types

of reactors on silicon oxide substrates, SiO_2. The main objective of this work has been to develop and parametrize a macroscopic CVD synthesis path compatible with the potential coupling with the in-situ and real-time experiments inside NanoMAX equipement an modified environmental transmission electron microscope (ETEM).

In the framework of thesis, the first chapter aims to provide a literature review on carbon nanotube, with a particular focus on single-walled carbon nanotubes (SWCNTs) and their structure and properties. Chapter 2 will delve into the main synthesis process of SWCNTs, with a detailed explanation of the chemical vapor deposition (CVD) principle and its unique characteristics. Furthermore, the different chemical mechanisms occurring in the gas phases and on the surface of catalysts, as well as the kinetic laws associated with the growth of CNTs from methane, will be discussed. The chapter will also include a review of existing literature on the influence of key operating parameters on the density and diameter of SWCNTs.

Chapter 3 will describe the technique used for the fabrication and characterization of SWCNTs. This includes a detailed description of the catalyst preparation by molecular beam evaporation (MBE) and the homemade hot-filament CVD method. The principles of Raman spectroscopy, scanning electron microscopy (SEM), and transmission electron microscopy (TEM) will be discussed in the context of SWCNT characterization. The chapter will also introduce the concept of the in-situ SWCNT synthesis through ETEM. All the experimental results obtained in the framework of our study will be presented in the subsequent chapters.

The fourth chapter focuses on the investigation of the crystalline quality, density, and diameter of as-grown SWCNTs when using the Mo-Fe binary metallic catalyst. A qualitative and quantitative comparison will be made with the Fe catalyst, which the most commonly used catalyst for SWCNT growth.

The fifth and sixth chapters are focused in presenting the results of the study on the reproducibility and the uniformity SWCNTs growth concerning process pressure and temperature. We will then describe the influence of the growth pressure and

temperature on the density and the diameter of SWCNTs. Finally, a diagram summarizing the experimental observations and the proposed interpretations will be discussed.

The work presented in these chapters sets the path for a reproducible synthesis of SWCNTs at low-pressure HFCVD, which could be used as a prototype for studying the synthesis conditions of SWCNTs in the in-situ Environmental TEM – NanoMax. The seventh chapter focuses on the nucleation and growth of SWCNTs in case of in-situ experiments in ETEM-NanoMax. We will describe their evolution in function of the different growth parameters and then propose an interpretation to explain the observed results.

This manuscript will end with a summary and the perspectives opened by this work.

1. Carbon nanotubes: Structure and properties

Defect-free single-walled carbon nanotubes (SWCNTs) are carbon atoms arranged in a cylindrical structure with a diameter in nanometer scale ranging from 0.4 to 5 nm and an unconstrained length. The structure of SWCNTs is similar to a graphene sheet rolled up on itself. This discovery of SWCNTs was firstly reported by Bethune et al [16], Ijima and Ichihashi[17] in 1993. Although the rolling of graphene sheet is not representative of the growth process, the concept of rolled graphene is used to account for the fundamental structure and properties of SWCNTs. In this chapter, we will provide a brief overview of the SWCNTs structure, followed by a review of the various properties of SWCNTs based on previous research.

1.1. Structure of SWCNT

The carbon atoms in the graphene structure are arranged in an in-plane hexagonal configuration due to their sp^2 hybridization. This structure may be considered as a hexagonal Bravais lattice whose unit is composed of two atoms separated by an inter atomic distance $a_{C\text{-}C} = 1.42\text{Å}$ and can be described through two direction vectors $\vec{a}_1$ and $\vec{a}_2$, which are represented in basic orthonormal vectors ($\vec{e}_x$ and $\vec{e}_y$):

$$\vec{a}_1=\left(\frac{\sqrt{3}}{2b}\ \vec{e}_x\ ;\ \frac{1}{2b}\vec{e}_y\right) \quad ; \quad \vec{a}_1=\left(\frac{\sqrt{3}}{2b}\ \vec{e}_x\ ;\ -\frac{1}{2b}\vec{e}_y\right) \ with\ b=\sqrt{3}\ a_{C\text{-}C} \qquad (1.1)$$

When the graphene is rolled up in a particular direction (Figure 1.1) [9], [10], [18], it might be interpreted in the following way: (i) the circumference of a nanotube is defined as starting at a point A and terminating at a point B, which is crystallographically equal to A, (ii) the graphene sheet is generated by unwinding this nanotube, and (iii) the circle AB becomes a straight line connecting two crystallographically equivalent positions of the graphene sheet. The vector AB, also defined as the chiral vector $\vec{C}_h$, is a linear combination of the two unit vectors $\vec{a}_1$, $\vec{a}_2$ of the Bravais lattice of graphene

sheet through the relative integers m and n, which are also known as the Hamada indices or chiral indices, named after the person who first introduced them in 1992 [19].

$$\vec{C}_h = n\vec{a}_1 + m\vec{a}_2 \ (0 \leq |n| \leq m) \qquad (1.2)$$

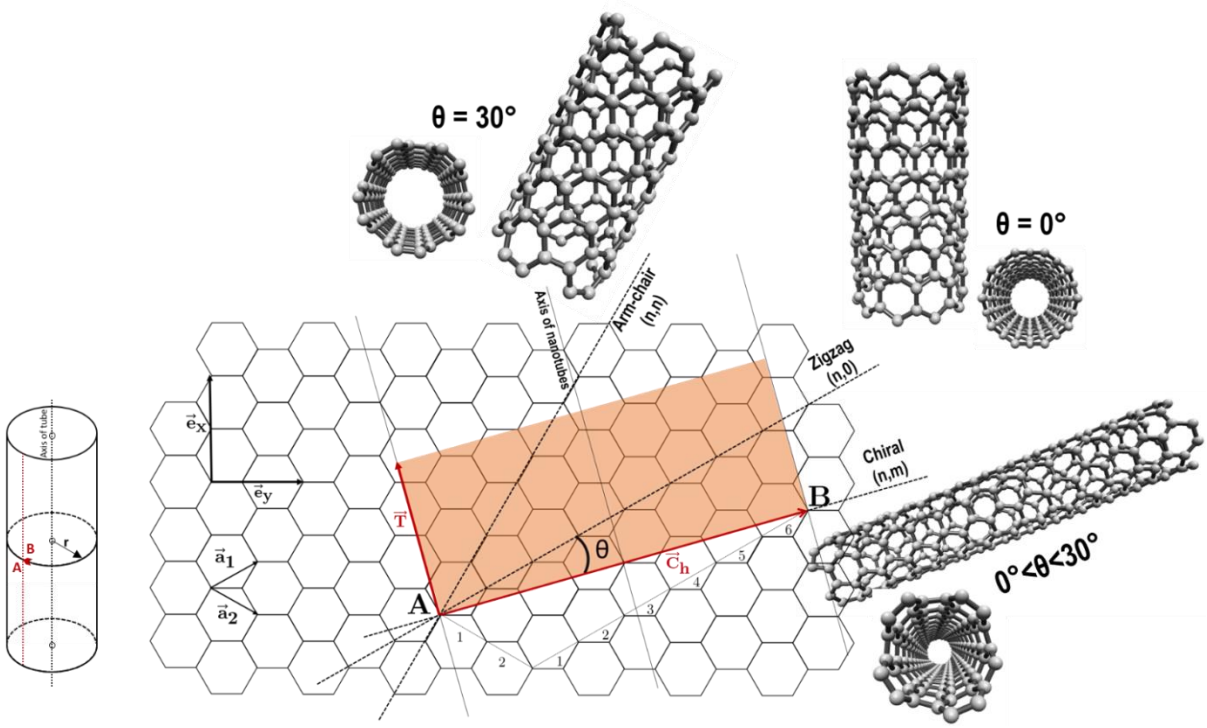

Figure 1.1. Schematic representation of the relationships between the radius (r), chiral angle (ϑ), and chiral vector ($\vec{C}_h$) for a single-walled carbon nanotube. We roll up the sheet so that point A coincides with point B, thus forming a nanotube whose 3 types of chirality are indicated on Figure [9], [15]

The pair of integers (n,m) uniquely defines the helicity of nanotube and identifies structural characteristic of a given nanotube, such as its diameter (d_t), the translation vector $\vec{T}$ (smallest vector belonging to the graphene lattice and orthogonal to $\vec{C}_h$), and the chiral angle (θ) [10] between the vector $\vec{C}_h$ and the unit vector $\vec{a}_1$:

$$d = \frac{\vec{C}_h}{\pi} = \frac{\sqrt{3}\times a_{C\text{-}C}}{\pi} \times \sqrt{n^2+mn+m^2} \qquad (1.3)$$

$$\vec{T} = t_1\vec{a}_1 + t_2\vec{a}_2 = -\frac{n+2m}{P}\vec{a}_1 + \frac{2n+m}{P}\vec{a}_2 \qquad (1.4)$$

$$\theta = \arctan\frac{\sqrt{3}\times m}{2n+m} \qquad (1.5)$$

where $a_{C\text{-}C}$ is the distance between two neighboring carbon atoms ($a_{C\text{-}C} = 1.42\text{Å}$ for graphene) and P is greatest common divisor of (n+2m) and (2n+m).

Indeed, it is feasible to distinguish various families of SWCNTs based on the values of these indices. While most tubes are statistically chiral, defined by the non-superimposition of their image by mirror symmetry, some of tubes have particular symmetries since they are wound along symmetrical axes of the graphene. These are referred to as armchair tubes when the two chiral indices are equal (m=n or $\theta = 30°$) while $m = 0$ *or* $\theta = 0°$, the SWCNT displays a zig-zag type. Both these types of tubes are achiral and exhibit a planar mirror symmetry with respect to the nanotube axis.

- Description in the reciprocal space

The chiral vector ($\vec{C}_h$) and the translation vector ($\vec{T}$) introduced previously delineate the elementary mesh of a SWCNT in real space. The first Brillouin zone in the reciprocal space is therefore described by the vectors ($\vec{K_1}$, $\vec{K_2}$) that satisfy the relations:

$$\vec{C_h} \times \vec{K_1} = 2\pi \; ; \; \vec{T} \times \vec{K_1} = 0 \; ; \; \vec{C_h} \times \vec{K_2} = 0 \; ; \; \vec{T} \times \vec{K_2} = 2\pi \qquad (1.6)$$

We obtain vectors $\vec{K_1}$ parallel to $\vec{C}_h$, directed perpendicular to the tube axis, and $\vec{K_2}$ parallel to $\vec{T}$, directed along the tube axis, such that:

$$\vec{K_1} = \frac{1}{N}\left[t_2\vec{b_1} - t_1\vec{b_2}\right] \; ; \; \vec{K_2} = \frac{1}{N}\left[-m\vec{b_1} + n\vec{b_2}\right] \qquad (1.7)$$

Where $\vec{b_1}$ and $\vec{b_2}$ are primitive vectors in the first Brillouin zone of graphene as shown in Figure 1.2 and N is number of hexagons in an elementary cell of a SWCNT, which is expressed as: $N = \frac{|\vec{C_h} \Lambda \vec{T}|}{|\vec{a_1} \Lambda \vec{a_2}|} = \frac{2(n^2+nm+m^2)}{P}$.

We can define any vector $\vec{k}$ of the reciprocal space decomposed according to: $\vec{k} = k_\perp \frac{\vec{K_1}}{|\vec{K_1}|} + k_{/\!/} \frac{\vec{K_2}}{|\vec{K_2}|}$ (Figure 1.2). Assuming an infinite medium in the direction of the nanotube axis, $k_{//}$ varies continuously, over $\left[-\pi/|\vec{T}|, \pi/|\vec{T}|\right]$ in the first Brillouin zone. On the other hand, depending on the circumference, the chiral vector $\vec{C}_h$ in real space

refers to an identical position. The corresponding periodic boundary condition implies the relation $\vec{k} \times \overrightarrow{C_h} = 2\mu\pi$ that is:

$$k_{\perp} = \mu \left| \overrightarrow{K_1} \right| \; ; \; \mu = 0, 1, ..., N-1 \qquad (1.8)$$

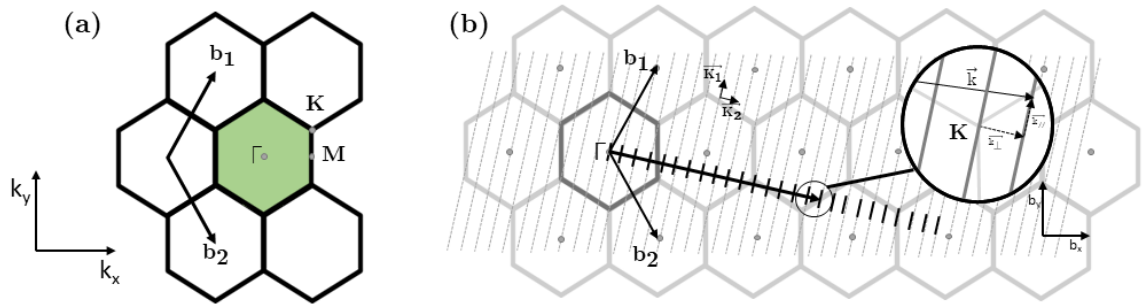

Figure 1.2 Reciprocal space of graphene defined by the vectors ($\overrightarrow{b_1}$, $\overrightarrow{b_2}$). (a) the first Brillouin zone, (b)Quantization along the circumference of the nanotube results in a restriction of this space for carbon nanotubes. The reciprocal space of a (5, 2) nanotube is shown in dashed lines, with the first Brillouin zone in solid lines. [20]

1.2. Electronic and Optical properties

From the beginning of research on SWCNTs, theorists expected unusual electronic properties due to their dual membership in the macroscopic world (by their length) and the quantum world (by their diameter). In the same way as for their crystalline structure, the analogy between the nanotube and graphene makes it possible to deduce the electronic properties of nanotubes from those of graphene, which may be obtained by using the tight-binding (TB) approach for the carbon π electrons [21]–[23]. In the case of a graphene layer, each carbon atom has four electrons in its valence band. The 2s orbital and two in-plane $2p_x$ and $2p_y$ hybridize to form σ bond at 120° and define the plane of the graphene sheet. The out-plane $2p_z$ orbitals, which form π bonds, are delocalized on the lattice, and dominate the electronic properties of graphene. With the simple assumptions (restriction of the interatomic interaction to the first

neighbors and neglecting the overlap integral between two nearest p_z orbitals), the dispersion relation could be expressed as[22]:

$$E(k_x k_y) = \pm \gamma_0 \sqrt{1+4\cos\frac{\sqrt{3}k_x a}{2}\cos\frac{k_y a}{2}+4\cos^2\frac{k_y a}{2}} \qquad (1.9)$$

where k_x and k_y are the basis vectors of the reciprocal space, γ_0 is the value of the transfer integral between two neighboring carbon atoms and the sign ± represents respectively the energies of the conduction (anti-bonding) band and valence (bonding) band [24]. The energy dispersion of graphene, which is derived from equation 1.4, is represented in Figure 1.3. The K and K' points of the first Brillouin zone, which are located at Fermi level, are points of electronic singularities where the conduction band and valence band are joined, which gives graphene its properties of zero gap semiconductor.

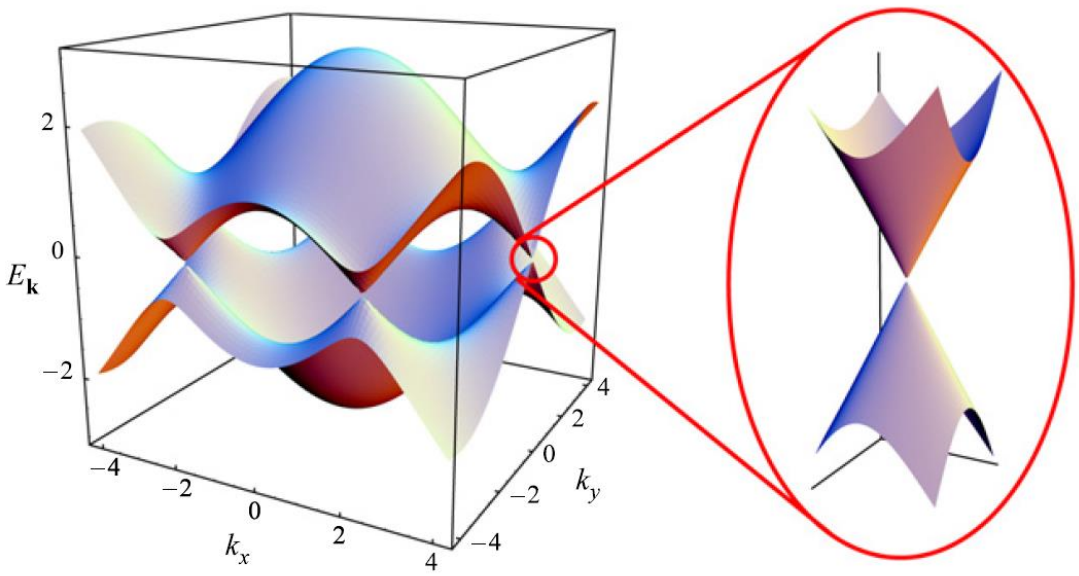

Figure 1.3. Three-dimensional representation of graphene dispersion. The vertical axis gives the energy, and the horizontal axis is the reciprocal lattice of graphene. The coordinates(k_x,k_y) are rotated by an angle π/3. In the vicinity of the K points, the dispersion is isotropic and linear [23], [25]

In the case of carbon nanotubes, the similar dispersion relation can be maintained to a first approximation by exclusively taking into account the restriction of the accessible $\overrightarrow{k_x}$ vector in the reciprocal space due to the quantization along the circumference of

the tube [22]. The nanotube dispersion is given by the zone folding approximation of the graphene dispersion [22], [26]: $E_{k\mu}=E_{2D}(k\frac{K_2}{|K_2|}+\mu K_1)$ with μ = 0, 1, 2, ..., $N-1$; $-\pi/T<k<\pi/T$.

The vectors K_1 and K_2 are expressed through the reciprocal lattice vectors b_1 and b_2 of the graphene sheet as

$$K_1=\frac{-t_2b_1+t_1b_2}{N}\ ;\ K_2=\frac{mb_1-nb_2}{N} \qquad (1.10)$$

These results in a profound variation in the electronic properties of nanotubes depending on their winding geometry. Indeed, for a (n,m) nanotube, if the (n-m) is a multiple of 3 or $\vec{k}_K \times \vec{C}_h = 2\pi$ ($\vec{k}_K$ describes a wave vector of six K points in the first Brillouin of graphene lattice), the $\vec{k}_K$ vector intersects the K point of the BZ (Figure 1.4a and Figure 1.4b), which thus exhibits metallic properties. In the group of metallic CNTs, *armchair* carbon tubes (n, n) show always metallic property with zero bandgap. Based on the experimental results, some CNTs are regarded as metallic at room temperature when they have a tiny small gap whose energy is inversely proportional to R^2, where R is radius of tube[27]. On the other hand, CNT is a semiconductor with a large gap when $\vec{k}_K$ vector does not intersect the K point (Figure 1.4c) or $(n - m)/3$ is non-integer.

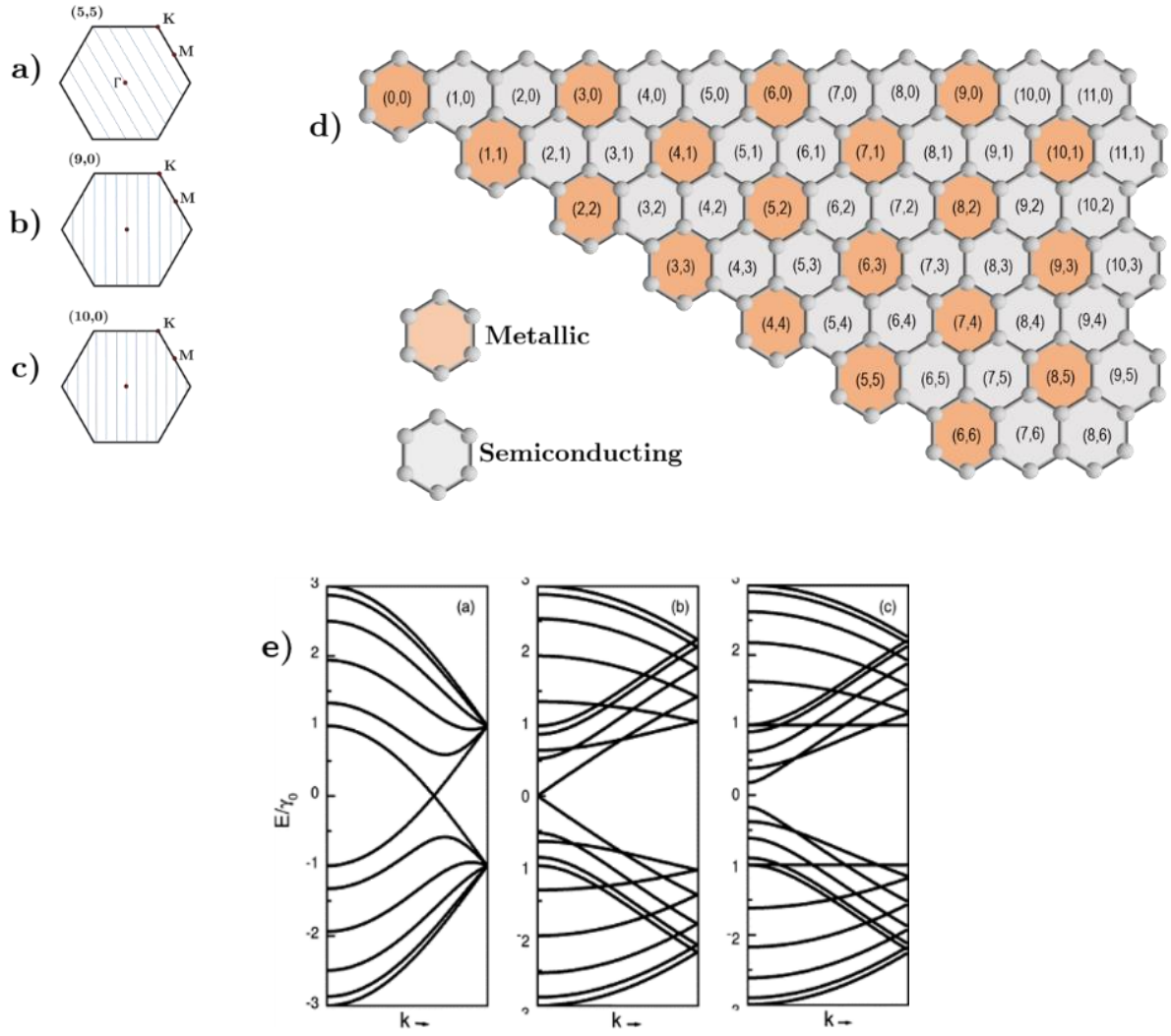

Figure 1.4. First Brillouin zone of carbon nanotubes with the different K-lines: (a) (5,5) metallic, (b) (9,0) metallic, and (c) (10,0) semiconductor. (d) Mapping of chiral indices of carbon nanotubes. Depending on the difference in indices, a carbon nanotube can be either metallic or semiconductor. (e) Electronic band structure of CNTs [9]

The band structure of SWCNTs corresponds to the intersection of the surface of scattering energy of graphene and the parallel vector k of the length $\frac{2\pi}{\|C_h\|}$ [22]. The energy dispersion relations are used to calculate the density of state (DOS), *n(E),* which represents the number of states available to be occupied for a given interval dE. Figure 1.5 illustrates the DOS of metallic (5,5), metallic (9,0), and semiconducting (10,0) tubes. The Fermi level crossover for armchair tubes, which are invariably metallic, is at $k= \pm\frac{2\pi}{3a_0}$. The level crossing of zig-zag tubes, on the other hand, lies in

the center of the Brillouin zone (k=0), and they may be metallic or semiconducting. Near the Fermi level placed at E = 0, the DOS of a semiconducting tube is zero (Figure 1.5c) while non-zero for the metallic tube (Figure 1.5a and Figure 1.5b). In both cases, the peaks are symmetrically distributed with respect to E=0. These different peaks are known as Van Hove singularities (VHS), characteristic of DOS of a one-dimensional system, which is proportional to $\frac{d_k}{d_E}$ [28], [29]. Indeed, this ratio tends towards infinity at the point of high symmetry *Γ,* which is the center of the Brillouin zone. Because these statistics relate to infinite, ideal, and isolated tubes, certain geometric parameters, such as the arrangement of nanotubes in bundles, are likely to change the electronic structure. It has been shown, for example, that the energy of VHS depends not only on the diameter but also on the chirality when the nanotubes are structured in bundles [30]–[33].

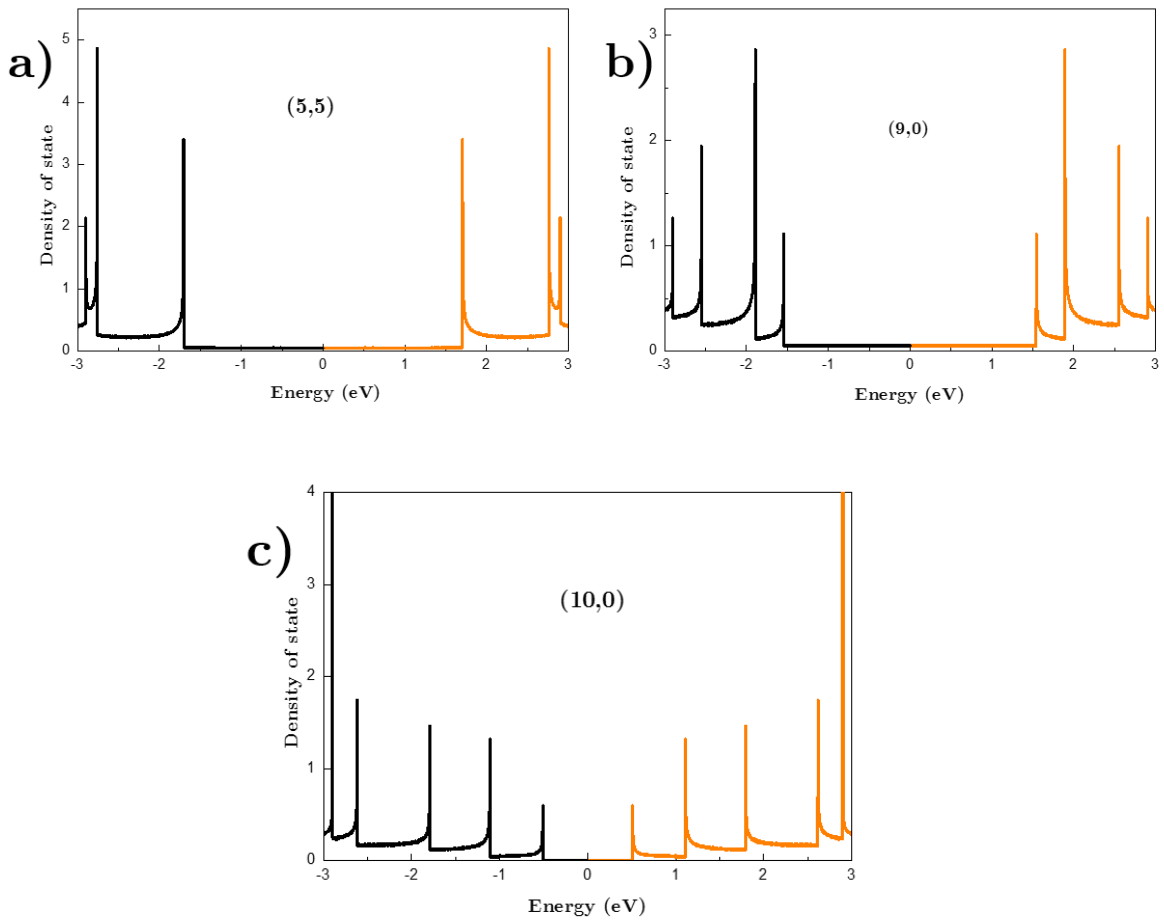

Figure 1.5 Density of state for carbon nanotubes (a) metallic (5,5), (b) metallic (9,0) and (c) semiconductor (10,0). We consider the model of π electron and a Fermi level at 0eV [34]

For an isolated nanotube, the optical properties are directly related to the electronic properties described above and in particular to the density of state. The transitions for absorption and photoluminescence in carbon nanotubes are possible to be determined due to the Fermi's golden rule[35]. The transitions occur between the singularities (i) symmetric with respect to the Fermi level, with the energy E_{ii} denoted as[36]:

$$E_{ii}^{metallic} = \frac{6a_{C\text{-}C} \times \gamma_0}{d_t} \quad (1.11)$$

$$E_{ii}^{semiconducting} = \frac{2a_{C\text{-}C} \times \gamma_0}{d_t} \quad (1.12)$$

Where $a_{C\text{-}C}$ is the carbon-carbon distance ($a_{C\text{-}C}$=1.42Å) and γ_0 is transfer integral corresponding to the interaction energy between two adjacent C, estimated $2.8eV \pm 0.1e$, and d_t is the diameter of the SWCNT. It is worth noting that the transition energy of a metal tube is three times greater than that of a semiconducting tube for a given diameter. For a semiconducting SWCNT, the possible transitions are E_{ii}^{sc}, $2E_{ii}^{sc}$, $4E_{ii}^{sc}$, $5E_{ii}^{sc}$, $7E_{ii}^{sc}$, etc .. and for a metallic tube, E_{ii}^{M}, $2E_{ii}^{M}$, etc...

1.3. Mechanical properties: Strength and Elasticity of SWCNTs

Each carbon atom in SWCNTs, like in graphene, is tightly connected with three neighboring atoms through the sp^2 covalent bond, in which the C-C covalent bond of graphene is one of the strongest in nature, thus the mechanical properties of SWCNTs are expected to match those of the strongest current materials. Early theoretical studies predict the Young's modulus value for SWCNTs of the order of 1TPa[37], [38]. This prediction is in good agreement with the values reported in the experimentally results [39]. The mechanical properties of CNTs are also different from other graphitic species due to their hollow structure. A plastic extension of 280% at 2000°C has also been reported for the synthesized SWCNTs by Huang et al [40]. Since the density of SWCNT is up to 3 or 4 times lighter than steel, and its tensile strength (T_{SWCNT} = 13-53GPa) is approximately 139 times that of steel (T_{steel} = 0.38-1.55GPa)[41]–[43],

SWCNTs could become excellent reinforcement fillers for materials such as rubber and polymers to enhance their strength, wear-resistance, and friction.

1.4. Thermal properties

The thermal conduction of a material results from the exchange of phonons, which are generated by lattice vibrations and the displacement of electrons in a material. In 1999, Hone et al. [44], [45] found that the thermal conductivity of a bundle of nanotubes could vary between 1800 and 6000 $Wm^{-1}K^{-1}$ at room temperature. The theoretical thermal conductivity of a defect-free, isolated SWCNTs in the longitudinal direction at the room temperature was evaluated at 6600 $Wm^{-1}K^{-1}$[46], but this value decreases to 2980 $Wm^{-1}K^{-1}$ [47], when the defects in the SWCNTs are considered. Similar measurements on individual and isolated nanotubes show that the conductivity of SWCNTs at the room temperature for a diameter of 1.7nm is 3500 $Wm^{-1}K^{-1}$ [48]. These values are greater than those of the best-known thermal conductors, such as diamond for example (around 1000 $Wm^{-1}K^{-1}$[49]). Such results could lead to the development of composites with improved thermal conduction or to microscopic temperature measurement and control systems, but the shaping of these materials is still insufficiently controlled. The short length of the nanotubes, the poor quality of their junctions, and the porosity of the material continue to affect the thermal conductivity values obtained on aligned SWCNTs [50].

1.5. Chemical properties

Initially, it was believed that carbon nanotubes were chemically inert due to their exposed surface consisting solely of graphene plane, which is known to have low reactivity. However, oxidation tests revealed that the ends of the tubes were more reactive than the sides and could be selectively opened [51]. The additional curvature and the presence of pentagonal defects are responsible for this heightened reactivity, particularly at the ends. Simple oxidation with nitric acid or hydrogen peroxide in acidic medium generates carboxyl functions that can be used as sites for grafting of new function[52], [53]. Alternatively, nanotubes can be functionalized non-covalently

using molecules of the pyrene family, which possess several fused aromatic rings and can stably adsorb onto the nanotube wall [54], [55]. This milder process has the advantage of causing less modification to the structure and properties of the nanotubes. By grafting chemical or biological functions onto the nanotubes, it is possible to better control their solubility, their reactivity and develop specific nano detectors [56], [57]. Finally, carbon nanotubes have an additional characteristic: the empty, straight, and one-dimensional channel in their center. Due to the high stability of nanotubes, this inner cavity constitutes a unique environment to study chemical reactivity, offering in addition a great potential for stabilization and spatial confinement within a controllable pore size.

2. Carbon nanotube: Synthesis methods

Since the discovery of carbon nanotubes, synthesized initially by the arc-discharge method [58], several techniques for CNTs production have been developed based on a combination of three essential ingredients: a carbon source, nanoparticle catalyst and energy input. The synthesis processes for CNTs can be broadly divided into two categories depending on their operating temperature: the high temperature processes that include the arc-electric discharge and the laser ablation, and the low temperature processes, generally chemical vapor deposition (CVD) technique and its derivatives. In the following paragraph, a short descriptive overview of each of these processes will be developed, with a particular focus on the hot filament assisted chemical vapor deposition (HFCVD) and low-pressure chemical vapor deposition (LPCVD) used in our study to synthesize SWCNTs.

2.1. High-temperature processes

This type of synthesis process is based on the sublimation of a solid carbon source which occurs from onset of 3200°C in vacuum or an inert atmosphere. The arc-electric discharge and the laser ablation methods are two well-known representatives of this group. The process consists of sublimating the carbon atoms from graphite and then allowing their rapid condensation in the presence of a catalyst under a strong temperature gradient. The various methods using this principle are distinguished from one another by the graphite sublimation process.

2.1.1. Arc-electric discharge

The arc-electric charge was the first approach utilized to synthesize CNTs, invented by Kroto et al. in 1985 [2]. Although this approach was simple to access and quite popular during the incipient period of CNTs studies, the cost of manufacture was found to be prohibitively high. This method is based on the sublimation of a graphite electrode using a strong electric current arc discharge. The parameters generally used to achieved the growth of CNTs are as follow: an inert gas (He or Ar) pressure between

100-300mbar, a reaction temperature of the order of 2000 to 3000°C at the discharge level, and an applied DC current of 100A for a voltage of 20V [59], [60]. A typical schematic diagram is shown in Figure 2.1 [61]. The process of arc-electric discharge for synthesizing CNTs involves ionization of gas between the two electrodes, turning it into a conductor. An arc is then created which causes the graphite at the anode electrode to evaporate. The anode is moved closer to the cathode during the process to compensate for the deterioration of the cathode and to maintain the inter-electrode distance. The resulting product settles on the cooler reactor walls. It is possible to favor the growth of various types of CNTs by changing the parameters. For example, using pure graphite electrodes primarily leads to the growth of MWCNTs and a significant amount of by-products (amorphous carbon, fullerenes, graphite carbon, etc). However, using a graphite anode with a metal core, typically an alloy containing Co, Ni, or Fe, can favor the growth of SWCNTs.

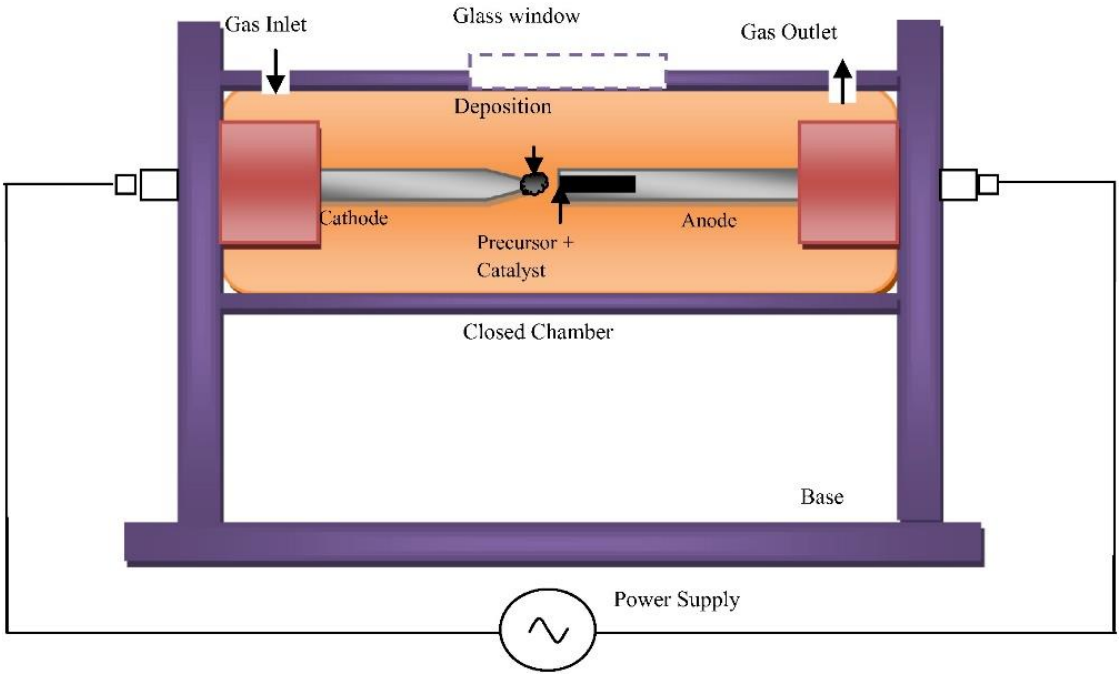

Figure 2.1. Schematic cross-sectional view of carbon arc fullerene generator[61]

In general, while the arc-electric discharge is a straightforward method to synthesize CNTs, it has a major drawback due to the low purity of the resulting products. Additional purification steps such as filtration, chemical treatments and/or

centrifugation are often necessary. Furthermore, due to the discontinuous and unstable nature of the arcing process, scaling up this method for mass production of CNTs is challenging. Several studies have shown that impurities and carbon nanoparticles are typically present with CNTs owing to the inhomogeneity of carbon vapor density and temperature [60]–[63]. To address this issue with traditional arc-electric discharge method, researchers have developed improved systems to increase efficiency. For instance, Lee et al. designed a plasma rotating arc-discharge system that induces vorticity to enhance the evaporation of carbon atoms in a vertical direction relative to the anode electrode [64]. This rotation leads to a more uniform discharge and produces a stable plasma, resulting in increased plasma volume and temperature. The CNTs synthesis yield using this method was 60% at a rotational speed of 5000 rpm and a temperature of 1025°C, with a possible yield of up to 90% at higher rotation speeds and temperature (1150°C)([65]-page 124).

2.1.2. Laser ablation

In 1995, Dr.Smalley's research group reported the use of pulsed Nd:YAG laser ablation to synthesize CNTs from a catalyst-enriched carbon target [66]. This process involves focusing a pulsed laser beam on the target, which is placed inside a furnace (Figure 2.2), consisting of a quartz tube surrounded by heating filament. The synthesis takes place at high temperature of around 1200°C, under an inert atmosphere of Helium (He) or Argon (Ar) at a pressure of about 500Torr. The target, composed of carbon and a metal such as Cobalt (Co), Nickel (Ni), or Iron (Fe), is ablated by the laser and vaporized. The metal catalyst on the target facilitates the nucleation of CNTs, which grow during the transport and condense on a cooled collector. The intensity and type of laser used in the ablation process, along with the temperature and the pressure within the furnace, are critical factors affecting the quality and purity of the final product. The development of this synthesis technique was done using a Nd:YAG laser, but other types of lasers have also been used successfully. For example, Braidy et al. [67] reported the synthesis of SWCNTs using a KrF laser. While this technique can selectively produce single-walled CNTs with high purity (>70%)[68], the product is

typically mixed with residues of the metal catalyst and requires chemical purification. However, the installation and the production costs as well as the production speed are major obstacles to large-scale industrial use of this method. As in the case of the electric discharge synthesis, the raw product of the synthesis is in the form of a powder or roughly rubbery agglomerate formed by tangles of CNTs.

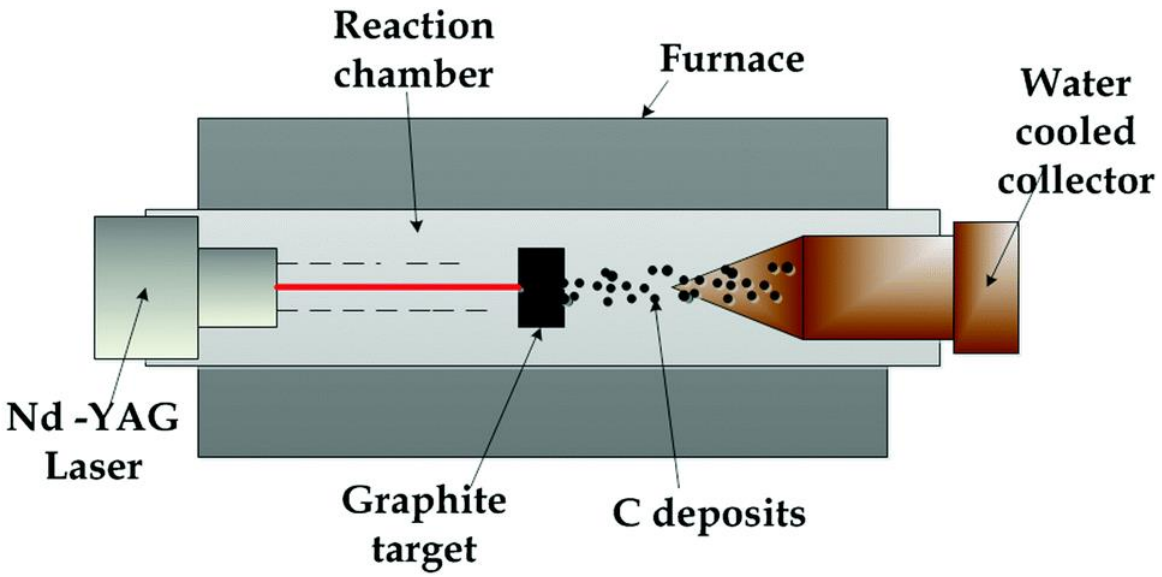

Figure 2.2. Diagram of a pulsed laser ablation synthesis reactor [12]

Compared to the electric arc method, the laser ablation method has the advantage of producing a product with higher purity, exceeding 90%. However, this method is still not economically viable as the production yield is low, the laser source requires high power, and the graphite targets need to be of high purity, all of which contribute to high production cost.

2.2. Medium temperature processes – Chemical vapor deposition (CVD)

The medium-temperature (600-1200K) route encompasses all techniques derived from the chemical vapor deposition (CVD). The formation of carbon filaments by the catalytic decomposition of hydrocarbon gas on the metal surface has been known for several years [69]–[71]. This technique has been adapted to synthesize carbon nanotubes in a furnace and has become a widely used technique for the CNTs synthesis[72]. Figure 2.3 shows the schematic of CVD and the steps necessary for the

synthesis of CNTs. The growth of the nanotubes is initiated by injecting gaseous hydrocarbons that are thermally decomposed at the precise place where the catalyst (mainly Ni[73], Fe[74], Co[74]) is deposited. Due to the use of the catalysts, it is sometimes referred to as the catalyst assisted CVD (CCVD) method. The CVD allows to grow the SWCNTs at various growth pressures from several bar [75], [76] to 10mbar [77]–[79]. The hydrocarbon gas is then flowed from minutes to hours over the catalyst at temperatures ranging from 500°C to 1100°C, where most hydrocarbon dissociate into carbon and hydrogen. Carbon released on the metal nanoparticles diffuses into them, and when the carbon content reaches the saturation value, the nucleation, and the subsequent growth of CNTs begins. Acetylene (C_2H_2)[80], methane (CH_4)[81] and ethane (C_2H_6) [82] are the most widespread hydrocarbon gases used in the CNTs synthesis diluted in a carrier gas (generally H_2 or Ar). This process allows the synthesis of CNTs on a multitude of different substrate such as quart, silicon and silicon oxide, metals such as steel, copper, nickel, carbon fibers. The simplicity of CVD process makes this technique very interesting for the synthesis of CNTs on substrates[83]–[90].

The growth of CNTs by the CVD technique can occur in entanglement form or in vertical/horizontal alignment. It is possible to switch from an entangled growth to aligned growth by controlling the density of CNTs, which must be large enough for the nanotubes to "hold" each other through Van Der Waals interaction (see for example [91]). This condition can be achieved specifically by manipulating the catalyst nanoparticle layer on the substrate, as demonstrated by Chiu et al [92] and An et al [93]. However, the conventional CVD requires high temperature for hydrocarbon gas decomposition, which may pose a challenge for heat-sensitive substrates. Therefore, it should be note that an alternative approach is the hot filament assisted chemical vapor deposition (HFCVD), in which the gas decomposition occurs at an extremely high temperature locally under the filament heating, while keeping the substrate temperature low.

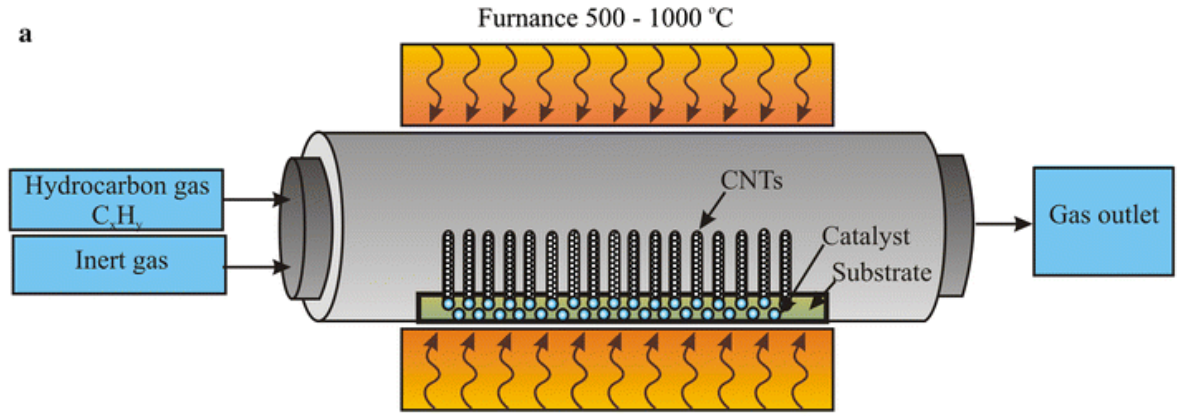

Figure 2.3. Schematic of typical Chemical vapor deposition (CVD)[94]

- Hot filament assisted chemical vapor deposition (HFCVD)

The hot filament assisted CVD method is commonly used in diamond synthesis[95]. This method utilizes metallic filaments that possess a catalytic ability to break down hydrogen molecules into atomic hydrogen at elevated temperature, typically around 2000°C. These activated atomic hydrogen particles are effective in enhancing the growth of diamonds by creating chemisorption sites for carbon species, as well as facilitating the preferential etching of graphite or amorphous carbon[96].

The HFCVD methods have been adapted for synthesis of carbon nanotube (CNTs) to enhance their quality. The filaments are usually made of refractory transition metals, and the most common in HFCVD are tungsten[97]–[99] filament, but there are also reported use of tantalum[100], rhenium[101], [102], or molybdenum filaments. Tungsten filaments, in particular, have been found to be highly catalytic and efficient in dissociating methane and hydrogen molecules into radicals, as reported by Choi et al in 2007 [103] They also indicated the dependence of tungsten filaments temperature on the growth rate of CNTs, with a significantly increase in growth rate observed when the temperature was reduced to 1900°C, particularly at high ratios of methane to hydrogen. Hong et al. [104], [105] obtained a height of 1.24mm for a VACNT forest on a 3x3cm^2 substrate by utilizing four tungsten filaments that were positioned parallel to the top of sample.

The HFCVD approach offers the advantage of dissociating gases such as methane and hydrogen, at much higher temperature than the substrate temperature. This allows for the growth of CNTs at lower substrate temperature than in conventional CVD. The metallic filaments used in this method heat the gas phase to around 2000°C, while the substrate is heated to approximately 600°C, as reported by Xu et al[106]. The gas is thermally decomposed when it collides with the resistively heated filament and then flows towards the substrate. The high amount of atomic hydrogen produced facilitates the formation of catalytic nanoparticles, while also preventing the deposition of amorphous carbon[107]. However, the metallic filaments can also become carburized due to the presence of carbonaceous species[105], [108], [109], which weakens or make them brittle; and alters their resistivity. Therefore, the applied current to the filament needs to be adjusted regularly to maintain a constant temperature of the filaments and substrate. For example, Haubner et al in 2008 [100] installed a power regulator the compensates for the loss of filament temperature due to the deposition of amorphous carbon on the filaments.

2.3. Growth Mechanism of carbon nanotubes (CNTs)

The growth of carbon nanotubes is a complicated process that has not yet been fully mastered. Nowadays, there is a lack of understanding regarding the main physical mechanisms that determine the structure, growth kinetic, and final length of carbon nanotubes under standard synthesis conditions. Over the years, numerous hypotheses on growth mechanisms have been proposed, resulting in accentuating the divergence of theory on nanotube growth in the scientific community. It is particularly challenging to establish a model that can define the primary steps involved in carbon nanotube synthesis and apply it across different processes and reactors. Therefore, it is crucial to identify and elucidate any factors that may impact the growth of carbon nanotubes.

This section will review the main mechanisms proposed to explain the growth of a nanotube. Various factors that are known to play an important role in this process,

including the catalyst, carbon precursors and the surrounding environment will be also discussed.

2.3.1. Nucleation and growth of the CNTs on the metallic catalyst

Since the 1970s, after the discovery of carbon fibers and later the nanotubes, many models of growth mechanisms have been proposed. The new generation of characterization techniques, such as the transmission electron microscope, has allowed the elaboration of new theories, confirming or contradicting the previous models. The main models of nanotube nucleation and growth are detailed below in order to understand the different theories on this subject. Adapting from the vapor-liquid-solid (VLS) model of silicon filaments proposed by Wagner and Ellis[110], the VLS model of the carbon filaments was first reported by Baker et al [111]–[113]. The mechanism of growth by this model can be described in three distinct steps: (i) the carbon precursors are absorbed and dissociated into carbon atoms on the surface of hot metallic catalytic particles; (ii) these carbon atoms are subsequently dissolved into the nanoparticle, resulting in the a liquid carbon-metal solution; (iii) The carbon then diffuses through the liquid nanoparticles until reaching the saturation which causes carbon to precipitate in the form of a cylindrical sp^2 carbon network. The CNTs will continue to grow as long as carbon is provided via an effective continuous decomposition of the carbon precursor at the catalytic surface. When too much carbon is absorbed on the surface of the catalyst nanoparticles, the CNTs do not have time to form and an amorphous carbon crust forms on the surface of the substrate, which stops the reactions[114].

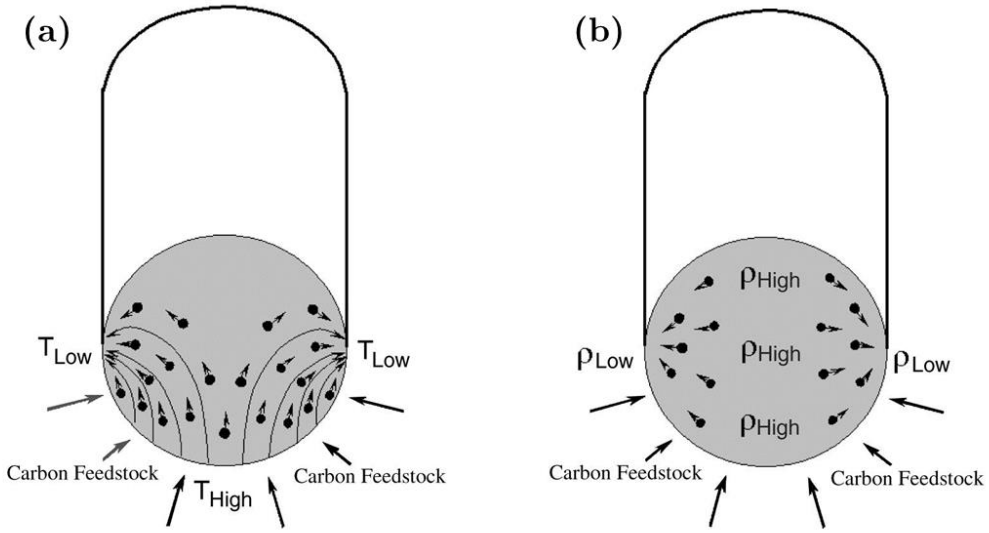

Figure 2.4 Schematics of a hypothetical gradient in temperature (a) or in carbon concentration (b) in the metallic nanoparticles to explain the localized precipitation of a carbon nanotube on the particles [115]

To explain the diffusion of carbon in the nanoparticles, Baker postulates the existence of temperature gradient in the particles[112], which would allow an exothermic decomposition of the gaseous species on hottest zone of the particle and the endothermic precipitation of carbon on the coldest zone of the particle as shown in Figure 2.4a. The theory of the temperature gradient was quickly replaced by that of the carbon concentration gradient (Figure 2.4b), which is proposed by Ducati et al in 2004 [116], and then confirmed by thermodynamic calculations [117]. This new theory is also consistent for the small size nanoparticle within the VLS model [115], [118]. Indeed, there are some problems with the carbon diffusion in the VLS model. Since the dissociation of many hydrocarbons on a metal surface is exothermic, Baker's explanation may remain valid, but these assumptions are invalid to explain the observed growth of CNTs when the precursor dissociation is endothermic, which is the case for alkanes [119], [120]

The diffusion of carbon only in volume in the nanoparticles has not always been verified. Oberlin et al proposed in the 70's that the growth by diffusion of carbon taking place on the surface or subsurface rather than in the volume of the nanoparticles [69], which was then reported by Yang et al in 1989 [121]. They assumed that the

particles existed in a solid state. In 2007, Hofmann and Robertson[122], through coupling CNTs growth results obtained under HRETEM with XPS and EELS analysis, reported that the Fe and Ni nanoparticles remained in a metallic and active state during the CNT growth phase. These results serve as the foundation for building the vapor-solid-solid (VSS) model. This growth hypothesis is supported by the fact that successful growths were also performed on non-metallic particles with rather low carbon solubility. These non-metallic particles are not favorable for carbon diffusion in volume and therefore nanotube growth is rather promoted by surface carbon diffusion[123]. Rinaldi et al proposed that carbon diffusion can also be subsurface, i.e. in the first atomic layer on the surface of nanoparticles, and this type diffusion does not require high temperature[124].

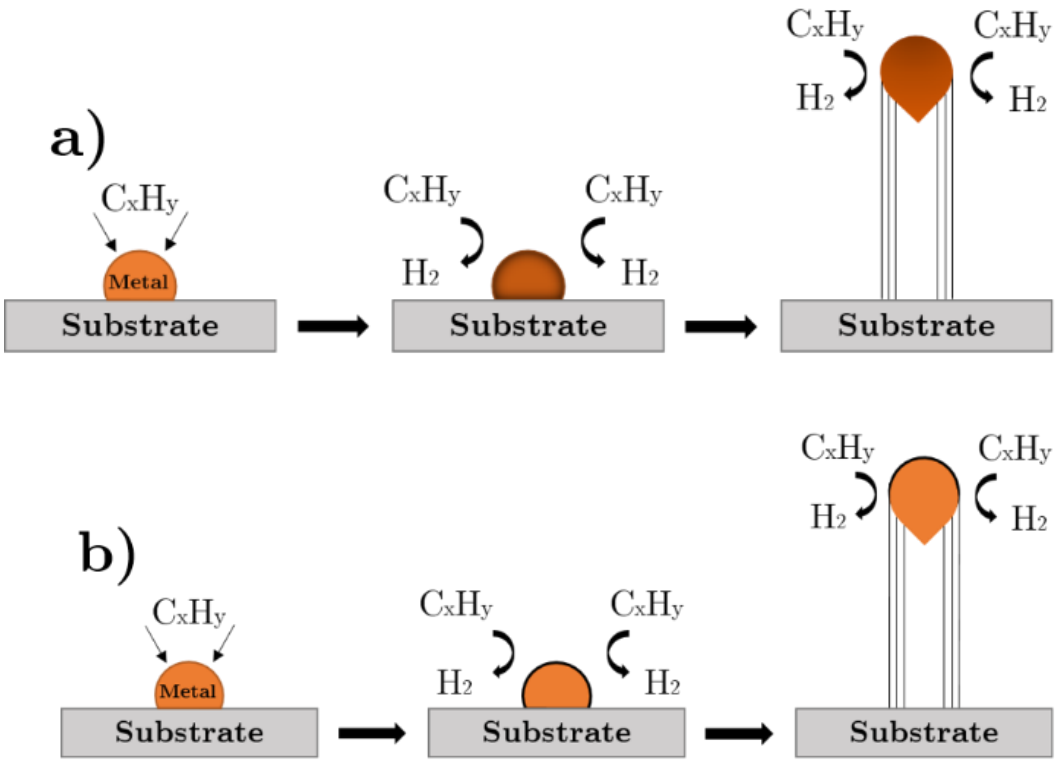

Figure 2.5. Growth mechanism for CNTs based on the state of metal catalyst and the diffusion way of carbon a) VLS, b) VSS (these images were reproduced from ref [125]*)*

2.3.2. Physical and chemical states of the catalyst

The size, phase and catalytic activity distribution of the catalytic nanoparticle population complicates the understanding of the growth mechanisms. Since the growth of carbon nanotubes, many authors have asked the question of the physical and chemical state of the catalyst before and during growth in order to understand the growth mechanisms. Today, the in-situ observation of the catalyst by HR-TEM (in addition to other characterization methods) has allowed establishing more precise theories on the state of the nanoparticle. However, the observations can be contradictory from one process to another, which still generates controversy on this subject.

2.3.2.1. Physical state of catalyst

A material retains the same physical and chemical properties at the macroscopic scale as at the microscopic scale. From a hundred nanometers, when the size of the particle decreases, the physical properties evolve. This evolution is caused by the increase in the ratio of the number of atoms on the surface compared to the number of atoms in the volume of particle. Indeed, when the size of the nanoparticle decreases, its carbon solubility increases while its melting temperature decreases. The melting point of a nanoparticle can be modified by:

❖ Incorporating carbon into a metal having a eutectic in its metal-carbon phase diagram: The melting temperature may decrease by a few degrees [126]. Wirth, Hoffman and Robertson calculated that the melting point of 1-2 nm iron particles can be reduced [127]. Ding et al. confirmed a lower melting temperature of an iron/carbon compound than pure iron via a series of simulations (Figure 2.6) [128].

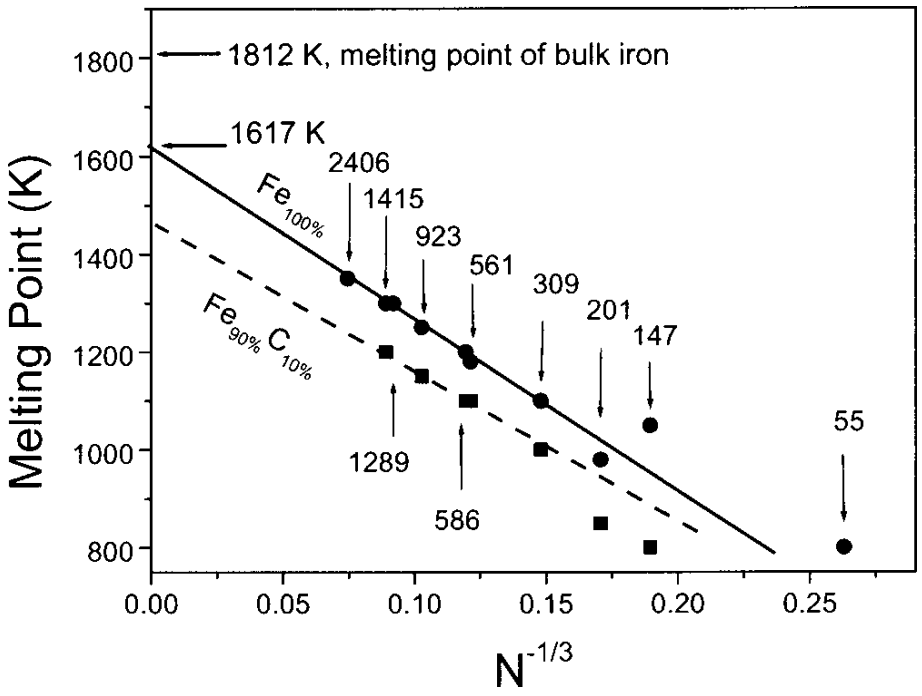

Figure 2.6 Comparison of the melting temperature evolution in pure iron nanoparticles and Fe/C compound nanoparticles as a function of their size N, by Ding et al in 2004[128]

❖ Decrease the size of the particle to less than a hundred nanometers: the melting temperature decreases slightly and then drastically when it exceeds the threshold of ten nanometers (Figure 2.7 [129])

Recently, the physical state of the nanoparticle during growth is still unclear. The nanoparticle can be liquid or solid [130]. Observed by TEM, the deformation of the particle visible in the nanotube has caused this controversy over the state of the nanoparticle. Nevertheless, in situ TEM images showed that nanoparticles remained crystalline during nanotube growth [122], [131], [132].

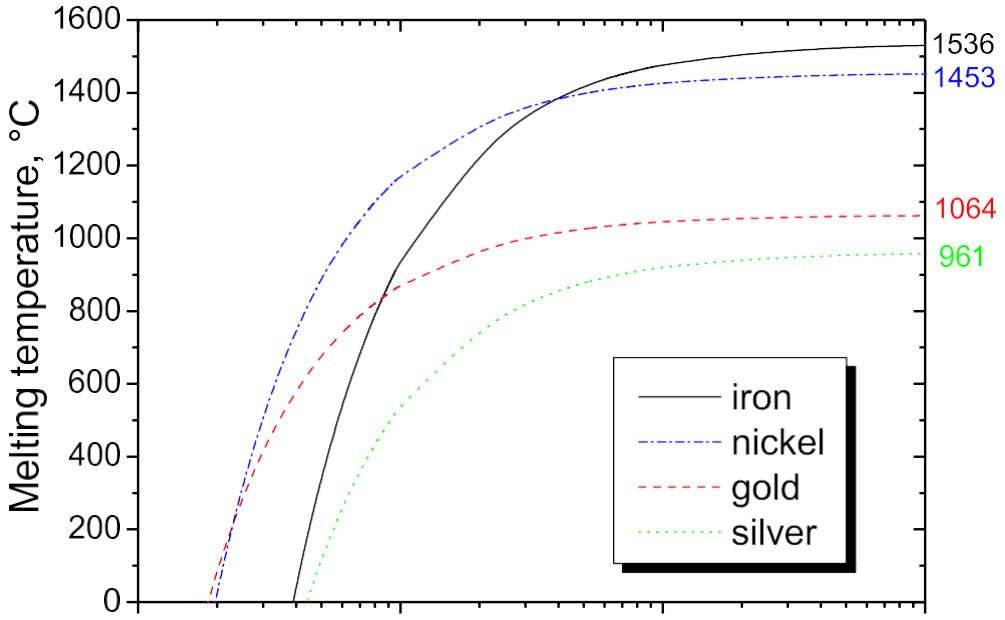

Figure 2.7 Evolution of the melting temperature of Fe, nickel, gold and silver as a function of their nanometric diameter[129]

2.3.2.2. Chemical state of catalyst

The role of the chemical state of the catalyst is still under discussion, especially the carburization or oxidation of the metal before or during nanotubes growth. There are several contradictory theories on the carburization of the metal. For example, for the growth on iron (Fe) nanoparticles, the formation of Fe_3C (iron carbide) leads to the end of lifetime of the catalyst[133]. Yoshida and his team showed in 2008 on in-situ HR-TEM images that the nanoparticle was in the form of Fe_3C in the solid state[130]. Esconjauregui et al.[134] and other authors [135], [136] have also shown the presence of a carbide intermediate phase in nickel (Ni). In a contrasting observation, Hofmann and his team [127] found that nickel (Ni) and iron (Fe) nanoparticles are metallic during carbon nanotube growth via the analysis of XPS data. In 2004, de Los Arcos [137] observed that iron was metallic on some supports, such as TiN, but was oxidized (FeO) when it was on alumina.

Nevertheless, it is possible that the nanoparticle is not only or fully metallic or a carbide. The presence of Fe_3C could indeed be just partial in the nanoparticle [138]. The nanoparticle may be a carbide only on the surface or on the extrusion area of the

nanotube and stay metallic in the core. The carbide formation may also be present just prior to the growth [139] and become metallic during the nanotube growth. It is also possible that the nanoparticle becomes carbide-forming during growth and then metallic again as soon as the growth is complete. On the other hand, Wirth et al. [140] note that there may be a mixture of phases (alpha - σ or gamma - γ) in the iron nanoparticles. Iron σ could generate an iron carbide while the iron γ remained metallic during the growth.

2.3.3. Growth through tip or base-growth mode

On the other hand, during the growth, there is a competition between the adsorption of carbon on the surface of catalyst nanoparticles and the recombination of C radicals with H atoms. Due to the adhesion strength of the catalyst particles on the substrate, there are two possible growth modes of CNTs growth, which are tip-growth and base–growth, respectively, as shown in Figure 2.8. Following the absorption of carbon on the surface of the catalyst nanoparticles, two scenarios can occur that depend on the position of nucleation site relative to the nanoparticle.

❖ In the tip-growth mode (Figure 2.8a), the interaction strength between the catalyst and the substrate is weak and the dewetting angle is large, the nucleation occurs at the interface between the nanoparticle and the substrate. The carbon found preferentially at the interface of nanoparticle and substrate creates a concentration gradient that will determine the direction of the absorbed carbon diffusion, the catalyst particles are then pushed off the substrate surface and transferred to the top of CNTs.

❖ In the case of base–growth mode (Figure 2.8b), due to the strong catalyst-substrate interaction strength, the catalyst particles still adhere to the substrate, carbon precipitates and form into a hemispherical dome on top of the catalyst nanoparticle, which then continues to grow as a cylinder to form CNTs[114].

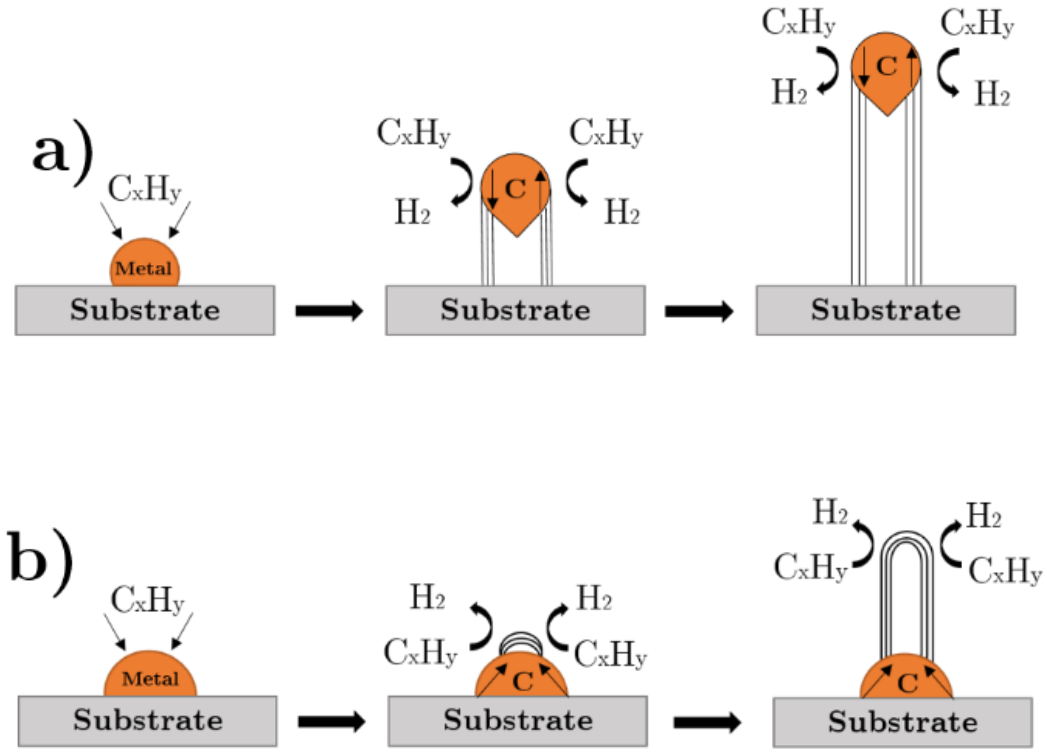

Figure 2.8. (a) Tip-mode and (b) Base-mode of the carbon nanotube growth (these images were reproduced from ref [125])

The time-resolved in-situ high-resolution transition electron microscopes (HR-TEM) have been employed to study not only the growth mechanism but also the structure properties of CNTs [122], [141]–[143]. For example, Yoshida et al. [130] used the environmental HRTEM to study the base-growth mode of SWCNTs from the acetylene decomposition on the Fe nanoparticles on SiO_2 substrate at 600°C. Figure 2.9a presents the sequence of HRTEM images of the consecutive growth stages extracted from a continuous video. Several research groups have also documented SWCNT's base–growth mechanism [122], [144]–[146]. Figure 2.9b, extracted from studies by He et al. in 2019[147], records the growth of SWCNTs by the tip–growth mode of CNTs with CO as the carbon feedstock on a MgO support and Co catalyst at 700°C.

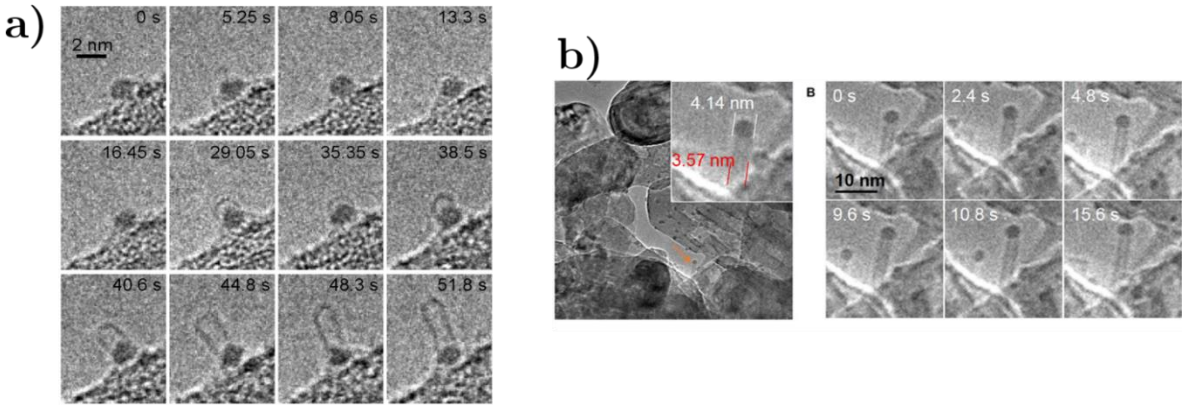

Figure 2.9. In-situ HRTEM images of: (a) base-growth mode of SWCNT synthesized from Fe catalyst [130], (b) tip-growth mode of SWCNT with Co catalyst [148]

In addition to the above two growth models, studies in recent years have investigated a correlation between the size of the nanoparticles and the diameter of the SWCNTs based on statistical analyses from TEM data, thereby proving basis to demonstrate the existence of two other growth models: the tangential and the perpendicular growth models [149], [150]. The carbon wall of the CNTs grows in a direction perpendicular to the surface of the catalyst nanoparticles in the perpendicular growth model. As a result, the diameter of the nanotube is smaller or different than that of the nanoparticle. In the tangential growth model, on the other hand, the carbon wall grows in a direction tangential to the nanoparticle surface, resulting in nanotubes with a diameter near to that of the nanoparticle. These two growth models are shown to be dependent not only on the nanoparticle diameter but also on the synthesis time [151]. With a short synthesis time (40 seconds to 2 minutes), CNTs grow in a tangential growth mode mainly; in contrast, the perpendicular growth model predominates with a lengthy synthesis time (10 min to 30 min).

2.4. Key factors in the growth of carbon nanotubes

The growth of carbon nanotube (CNTs) generally takes place within a narrow window of conditions including several parameters such as pressure (total and partial), temperature (gas and substrate) and gas flow/dilution that vary depending on the catalyst, the gaseous precursor, and the substrate. These parameters influence the activity of the catalyst, the density and length of the nanotube in addition to the

structure of the nanotube. The choice of a catalyst/substrate couple and the gaseous precursor must be adapted for the growth of carbon nanotubes. This section presents the main catalysts and precursors that are efficient for the growth of carbon nanotube and discusses the theories on the origin of this efficiency.

2.4.1. The reactive gas phases.

The choice of the carbonaceous precursor in the growth of a nanotube is based on different criteria, such as its thermal stability and its hydrogen and oxygen supply. The carbonaceous precursors for the synthesis of SWCNTs can be unsaturated hydrocarbons (acetylene or ethylene) [80], [90], [133], [152], saturated hydrocarbons (methane)[81], [153], oxygenated compounds (ethanol, carbon monoxide) [154]–[156], or aromatic compounds (xylene, toluene, benzene) [157]–[159]. Most carbonaceous precursors used for nanotube growth decompose exothermically, except methane. The majority of existing studies are based on CVD experiments using acetylene as a carbon precursor and point to that an increase in growth temperature leads to the increase in the diameter of SWCNTs [160]. The reactivity of the carbon precursor, or its thermal stability, can be represented by its Gibbs free energy (free enthalpy) as a function of temperature in the Ellingham approximation [161] (Figure 2.10). In the context of CNTs growth, the Gibbs free energy (ΔG) change for the reaction determines whether the process is energetically favorable: if the ΔG is negative, the reaction is thermodynamically favorable; In other words, the formation of CNTs from precursor molecules is spontaneous under the given condition. Most carbonaceous precursors used for nanotube growth decompose exothermically, except methane. Methane is thermodynamically stable up to rather high temperatures and its pyrolysis begins at temperatures above 1000 °C [162]. However, as compared to acetylene, the use of methane as a carbon precursor leads to different growth dynamics. For example, when CH_4 dissociates during the reaction, it produces more H_2 than C_2H_2 dissociation[163]. H_2 is thought to help minimize catalyst poisoning and cleans the surface of the sample during the growth of CNTs [164].

The gas phase can be supplemented by other gaseous species such as H_2 [106], [162], [165], H_2O [166], [167], NH_3 [168], N_2 [90], [169], and even CO_2 [170], [171] in order to improve the growth of the single walled nanotubes and/or the lifetime of the catalyst. Hata et al. [166] showed the beneficial effects of adding a few ppm of water to the gas phase on the catalyst lifetime. Amama et al. [172] assumed that hydroxyl groups from water intercalate between the catalytic nanoparticles reducing the Ostwald ripening and thus increasing their lifetime. The carbonaceous precursor can also be combined with an oxygen growth stimulator, such as water or ethanol, to increase the efficiency of the carbon nanotube growth [173]. The role of the oxygenated stimulator is to activate the catalyst by cleaning the amorphous carbon layer that covers it. On the other hand, Chen's team studied the effect of methane supplementation on growth. They showed that a small amount of methane added to acetylene could prevent the increase of iron particle size, increase the duration of growth [174], and improve acetylene-activated growth.

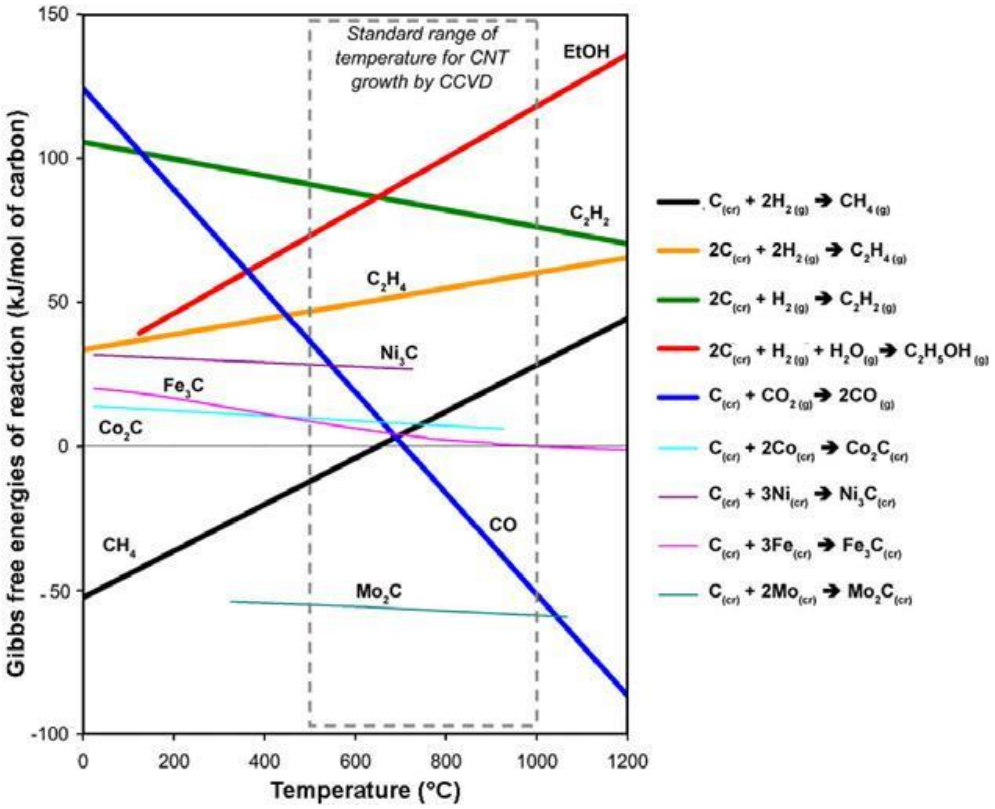

Figure 2.10 Gibbs free energies of reaction per mole of carbon for the formation of carbon and metal carbides (at atmospheric pressure) [126]

2.4.2. Catalyst

Generally, the role of a catalyst is to facilitate a chemical reaction by creating an intermediate state of lower energy. This decrease in energy required for the reaction depends strongly on the strength of the catalyst-reactants bond [175]. In the case of CNTs synthesis by CVD, the catalyst will accelerate the decomposition of the carbonaceous precursor[175]. Iron [74], [176]–[179], nickel [176]–[179], and cobalt[16], [74], [176], [177], [179], [180]are widely used to catalyze the synthesis of carbon nanotubes. As for the gaseous precursors, Esconjauregui et al. [134] performed calculations on the variation of the free enthalpy of reaction of acetylene on different metals (nickel, cobalt, iron, tungsten and molybdenum) with temperature. They found that the highest variations in free enthalpy were for nickel, cobalt and iron (Figure 2.11). Catalytic activity is strongly dependent on the electronic structure of the metal. Metals with few vacant d orbitals, such as Ni, Co, and Fe, are the best catalysts for the nucleation and growth of carbon nanotubes. Their ability to catalyze the decomposition of gaseous carbonaceous precursors, their ability to form carbides and the possibility for carbon atoms to diffuse in volume or on the surface have been known for a long time, especially in the context of carbon fiber growth [113], [181]. In the case of carbon nanotubes, a great deal of work has reported the growth of MWNTs or SWNTs from these three metals. Hongo et al [182] reported a growth of SWCNTs from the Fe catalyst in the growth temperature range of 650-800°C. Lee et al [183] controlled the CNTs growth with CH_4 source gas and H_2 carrier gas via the oxidation of Ni catalyst in specific positions. Besides, other species have also enabled the growth of SWCNTs: (i) Takagi et al. [184] demonstrated the SWNTs synthesis with catalytic gold particles with diameter smaller than 5 nm, (ii) Zhou et al.[185] studied the growth of SWNT with copper (Cu) particles under certain conditions, and (iii) Takagi et al. [186] and Yuan et al. [187] went even farther by successfully growing SWNT with a whole range of new catalysts such as Fe, Co, Ni, Cu, Pt, Pd, Mn, Mo, Cr, Sn, Au, Mg and Al by catalytic-CVD.

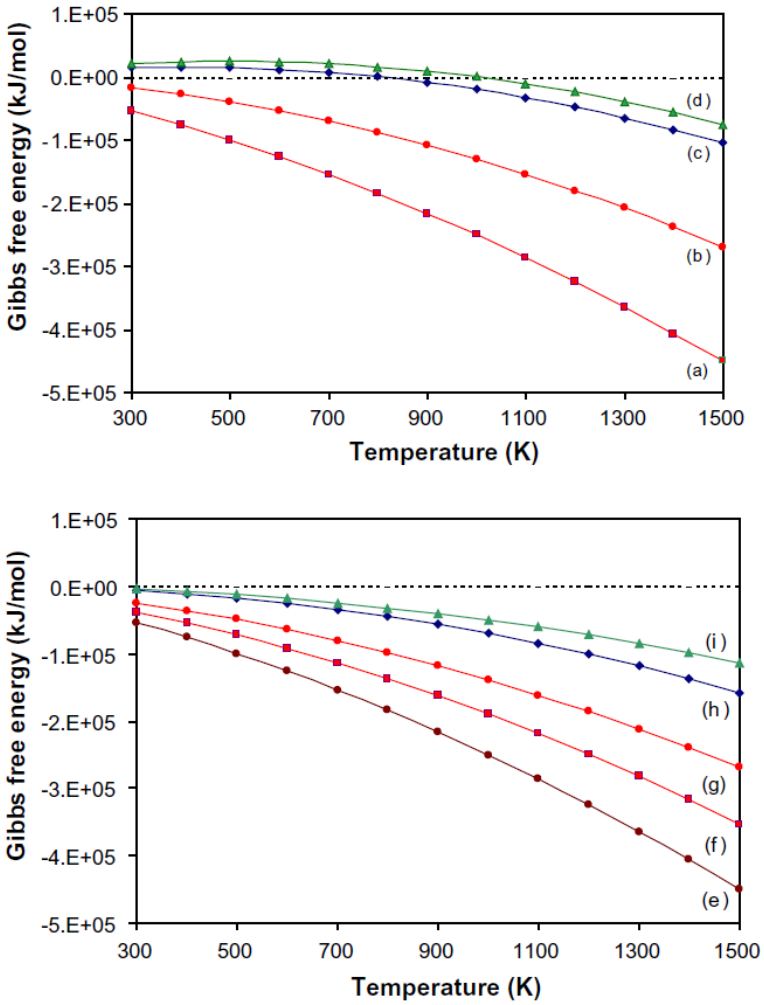

Figure 2.11 Calculation of the free enthalpy variation (Gibbs energy) for the reactions between nickel and (a) C_2H_2, (b) C_2H_4, (c) CH_4, and (d) CO. Estimation of the free enthalpy of reaction between C_2H_2 and (e) Ni, (f) Co, (g) Fe, (h) W, and (i) Mo[134]

In the process of the catalyst development for the selective CNTs synthesis via CVD, there is a trend of the preparation of bimetallic catalysts by adding a second metal as a co-catalyst which is not found to be active alone but which, when combined, improves the overall catalytic performance of the catalyst. Molybdenum [188] is by far the most used in the case of SWCNTs synthesis, but we have noted catalysts containing tungsten[189], tin [190], platinum[191], palladium[191] or chromium[191]. The contribution of molybdenum as a co-catalyst for the growth of CNTs, especially SWCNTs, has been recognized for a long time. The best known example is surely the CoMoCat catalyst of the Resasco team [188], [192], which has led to the filing of a patent [193] exploited today by SouthWest Nanotechnology. It is a catalyst composed

of cobalt and molybdenum deposited on different supports. This catalyst is very active for the production of SWCNTs from the disproportionation of carbon monoxide. This selective synthesis presents a good yield thanks to the combined effect of two metals: they likely form a mixed oxide that resists reduction and allows to stabilize and keep dispersed the Co^{2+} species that generates the active species. As soon as the carbonaceous species is injected at high temperature of the process, the mixed oxide reacts to logically give a molybdenum carbide and release the active species to directly initiate the growth. The advantage of this stabilization by formation of a mixed oxide is the elimination of any coalescence, very likely at this temperature without stabilization, which allows to give the active species in a suitable form and size as soon as the carbon species is introduced. The presence of excess cobalt oxide (Co_3O_4) is ultimately a source of by-products (multiwall nanotubes, encapsulated particles, nanofibers) because these particles are not stabilized and are likely to coalesce during the process.

2.4.3. Nanoparticles/substrate interactions

In order to improve the growth conditions, the effect of the catalyst on growth has been studied many times. As seen in section 2.3.2.2, the chemical state of the catalyst can vary from one growth to another. The catalyst can undergo different treatments before growth which subsequently influences its catalytic activity. The nature of the substrate can also have an impact on the growth efficiency. It is for these reasons that the choice of a pretreatment and the type of substrate are important factors to take into account in order to optimize the growth of SWCNTs.

2.4.3.1 Catalyst pretreatment

The catalyst can undergo a pretreatment step under oxygen (calcination) and/or under hydrogen before the start of nanotubes growth. Pretreatment under oxygen is intended to eliminate carbonaceous contaminants and to reduce the Ostwald ripening phenomenon. Catalysts like nickel, cobalt or iron type oxidize easily under air, causing a change in morphology. The Ellingham diagram makes it possible to evaluate

the predisposition of an element to oxidation. For example, we can read in the Ellingham diagram (Figure 2.12) that FeO is more difficult to reduce than NiO or CoO. The oxides and hydroxides of iron, nickel and cobalt can be reduced under hydrogen [194], ammonia [195] or under methane at high temperature [196].

Thermal pretreatment of the catalyst under the reducing gas - hydrogen just before growth changes the morphology and catalytic activity of the metal film [197]. The parameters of the hydrogen pretreatment should be optimized to improve the growth efficiency. Adjusting the time and temperature of the pretreatment can indeed control the diameter of the tubes [194], [198] and then the density of CNTs [107], [194]. A hydrogen plasma can also have an influence on the metal catalyst film, both on the size of the nanoparticles and their size distribution [199], [200]. Kim et al. [107] used atomic hydrogen exposure for the catalyst pretreatment process. They showed that by decreasing the pretreatment temperature, the tube diameter could also be reduced. However, hydrogen treatment may not always have the desired effect. Excess hydrogen can degrade the catalytic activity by sintering the nanoparticles and changing the interaction between the nanoparticles and the oxide layer[201], [202]. Hydrogen in a small amount can provide better dewetting and increase of the contact angle between the nanoparticle and the substrate.

2.4.3.2. Support layer

The particular interaction between the metal catalyst and its support plays an essential role in the synthesis of nanotubes. It influences the morphology, the dispersion, and the electronic properties of the active phase and consequently the growth process of the nanotubes. The three most common supports are silica (SiO_2)[203], alumina (Al_2O_3) [88], [204], [205] and magnesia (MgO) [206]. Other supports have also been reported: (i) zeolites (Y, MCM-41, ZSM-5, ...) [207], [208] for their confinement effect, (ii) titanium oxide (TiO_2) [209] for semiconductor properties, (iii) water-soluble supports such as calcium carbonate ($CaCO_3$) [210], [211] for their purification which is much easier to implement after synthesis, (iv) the carbon in the form of nanofibers or

nanotubes [212] or graphite [213], or (v) more exotic supports such as perovskites [214] or zirconia [209]. Experimental studies comparing several substrates for the same metal catalyst and the same preparation method [210], [215], [216] provide extremely diverse and divergent results with regard to the choice of an optimal substrate. This variability arises due to significant differences in electronic interactions, particularly charge transfer, and metal-support affinities that can vary widely from one metal to another. The nature of the metal-support interaction is pivotal in this context, and it primarily occurs through a process of charge transfer between the metal catalyst and the support material. This charge transfer is not a singular phenomenon but can result from different types of reactions[210]: oxidation/reduction, acid/base (Lewis), donor/acceptor. The surface functions of the support, including their density, nature, and properties, play a critical role in regulating the quality of the metal-support interaction. These surface functions act as active sites for the charge transfer process and significantly influence the catalytic properties of the system. The diversity in the nature of metal-support interactions ultimately impacts the electronic structure and dispersion of the active catalytic phase.

This intricate interplay between the metal and support is especially crucial in the context of nanotube growth mechanisms. The metal-support interaction, by influencing the electronic structure and dispersion of the active phase, essentially dictates the preferred mechanism for nanotube growth. Consequently, understanding and controlling the quality of the metal-support interaction are pivotal factors in tailoring and optimizing the catalytic properties for various applications. The choice of substrate, in conjunction with the specific metal catalyst and preparation method, becomes a critical consideration in achieving desired and reproducible catalytic.

outcomes

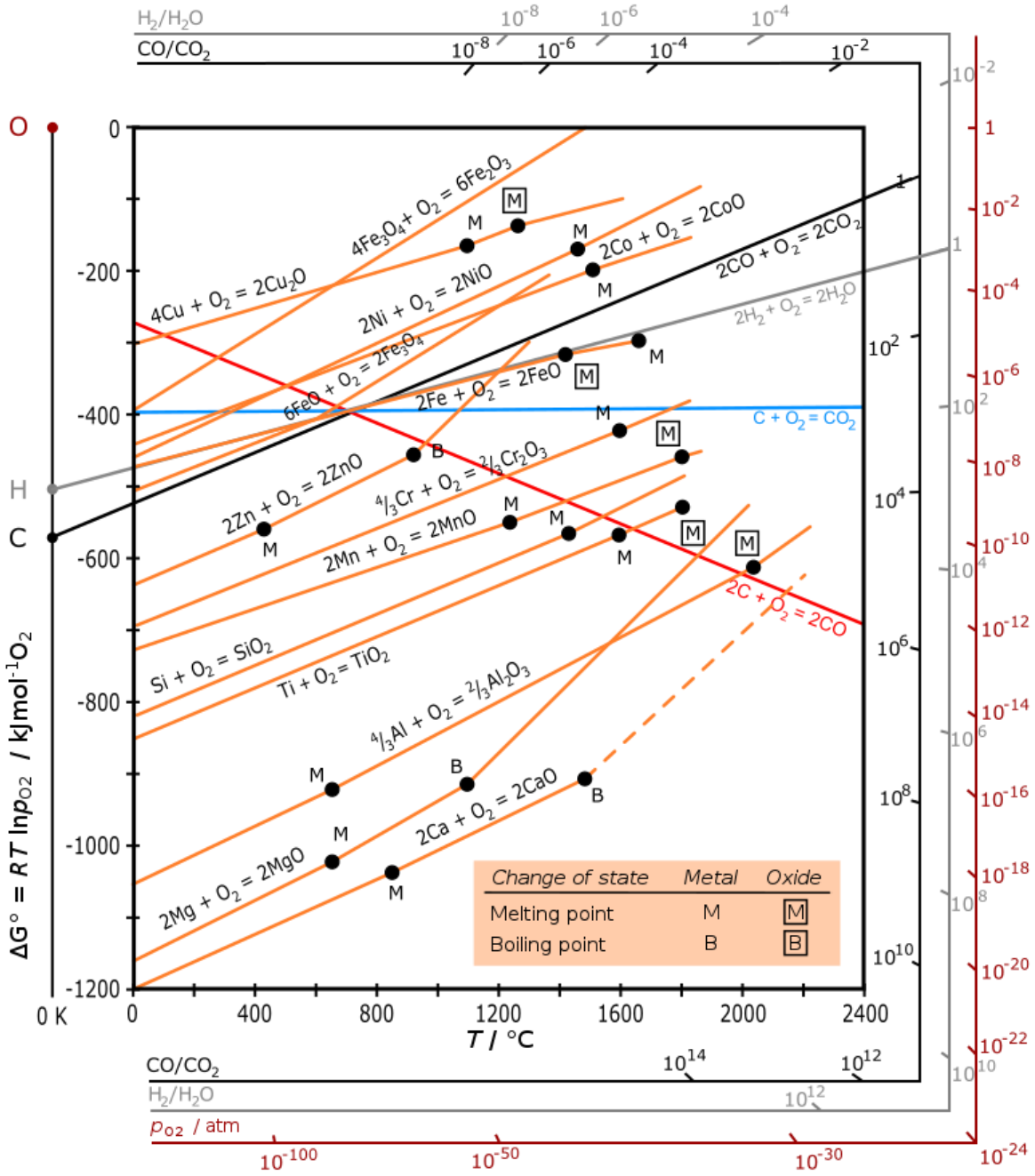

Figure 2.12 Ellingham diagram of oxides [217]

3. Experimental methods

The aim of this chapter is to describe the different techniques used in the framework of this thesis work. It is divided into three main parts: the synthesis methods, the characterization methods, and the in-situ experimental method with ETEM. The first part details the catalyst preparation via molecular beam evaporation (MBE) and the SWCNTs synthesis using the new HFCVD approach developed in our team, with a main focus on the experimental protocols used to synthesize SWCNTs at low-pressure. In order to obtain reproducible results, we performed series of SWCNTs' growth in our home-made HFCVD system followed by the optimization of different parameters that highlighted the necessity to achieve a well-controlled and systematic method of fabrication and calibration of the SWCNTs. In the second part of this chapter, we will present the different techniques used for the quantification of the CNTs' structural properties (Raman spectroscopy, Transmission electron microscopy), CNTs densities (Scanning electron microscopy) and will explain the method needed to infer on the chemical state of catalytic nanoparticles, for example X-ray photoelectron spectroscopy (XPS). The rest of the chapter is dedicated to the in-situ growth of SWCNTs using the CVD-assisted environmental TEM.

3.1. Synthesis of SWCNTs

Our SWCNTs synthesis process distinguishes the catalyst preparation step from the SWCNTs growth step. The catalyst preparation steps consist of depositing a film of catalyst on a substrate and subjecting it to pretreatment process before the carbon nanotubes growth.

3.1.1. Catalyst thin film preparation

The catalyst film deposition methods can be referenced into two categories: the dry methods, which includes physical vapor deposition (PVD), and wet methods. The most popular PVD techniques for catalyst deposition are sputtering [218], [219], vacuum evaporation [106], [196] and related electron beam PVD also known as e-beam

evaporation [220], [221] . Regarding the wet methods, the sol-gel [222] and impregnation [223], [224] methods are the best known for the growth of SWCNTs. In our study, the catalyst and buffer layers are deposited by physical vapor deposition (PVD) method, namely the molecular beam evaporation (MBE). This method allows the evaporation of metal with high melting temperatures by transferring a large amount of energy into the source materials[225]. The photo and schematic diagram of our MBE are presented in Figure 3.1. An inlet lock, where the sample was put in or taken out, is connected with the main chamber through a gate valve (Figure 3.1b), which serves as a barrier between the inlet lock and the main chamber. When the valve is closed, it isolates the inlet lock from the main chamber, preventing any potential disturbance to the ultra-high vacuum (UHV) conditions within the main chamber. In our study, Si wafers covered with a 200nm thick thermal oxide (SiO_2) were used as a substrate. This substrate was first cleaned using an ultrasonic bath of acetone for 30minutes and then divided into several 0.5cm^2 specimen before loading in the evaporator. There are 4 available metals in our system: cobalt (Co), iron (Fe), molybdenum (Mo) and nickel (Ni). Additionally, we also have two oxide sources: alumina (Al_2O_3), and oxides silicon dioxide (SiO_2). An electron emitted from the hot tungsten filament bombard not only the crucible, but also the region surrounded and partially ionize the evaporated vapor stream. The partially ionized vapor beam was measured as a flux current, acting like a local partial pressure gauge, which allows us to determine the time of evaporation by using the equation:

$$t_{(min)} = \frac{T(nm) \times C(\mu A nm^{-1} min^{-1})}{F\ (\mu A)},$$

where T is desired thickness of thin-film, C is constant of evaporation, F is flux current. The constant requires preliminary calibration and is various for each material, for example $C_{Al_2O_3}$=1.2 $\mu A nm^{-1} min^{-1}$, C_{Fe} = 0.22 $\mu A nm^{-1} min^{-1}$ and C_{Mo} = 0.35 $\mu A nm^{-1} min^{-1}$. In our study, a thin layer of Alumina (Al_2O_3) was first deposited under ultra-high vacuum (10^{-9}mbar). This alumina layer is known as a catalyst supporter, which acts as a barrier layer between the catalyst and the substrate to not

only prevent the diffusion of catalyst nanoparticles (NPs) into the substrate but also to reduce the hydrocarbon contamination [226], restrict the NPs mobility [205] and to stabilize the oxidation state of NPs [227]. Following this step, a catalyst layer was evaporated on top of the alumina layer at room temperature in the same set-up experiment.

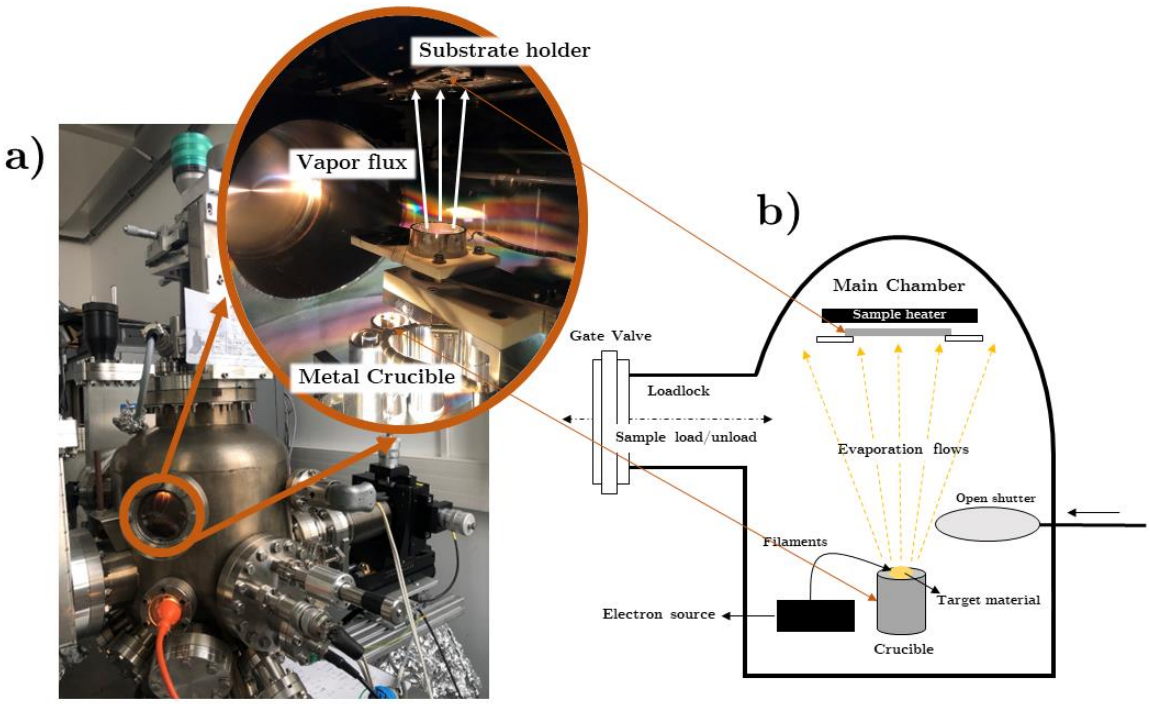

Figure 3.1. Home-made Molecular Beam Evaporation (MBE) (a) photo and(b) schematic diagram

3.1.2. Chemical vapor deposition (CVD) set-up

A versatile platform named Facility for Elaboration of Nanomaterials with in-situ and real-time analysis at X (FENIX) was designed to perform carbon nanotube growth in a hot filament assisted CVD reactor and to in situ analyze the sample surface by XPS (X-ray photoelectron), AES (Auger electron) and ELS (energy loss) spectroscopy. This configuration makes it possible to study the nucleation and growth of carbon nanotubes on the same substrate by successive deposition and analysis. The set-up consists of three chambers placed under ultra-high vacuum (ultimate vacuums of 10^{-8}, 10^{-8} and $<10^{-9}$mbar in the synthesis chamber, the transfer chamber, and the analysis chamber, respectively) and isolated between them by valves. The transfer of a substrate from one chamber to the other is done with a transfer rod. From two gas

cylinders, one of which contains high purity hydrogen and the other containing pure methane, the composition and the flow rate of the gas mixture are controlled and regulated by a debimetric mixer.

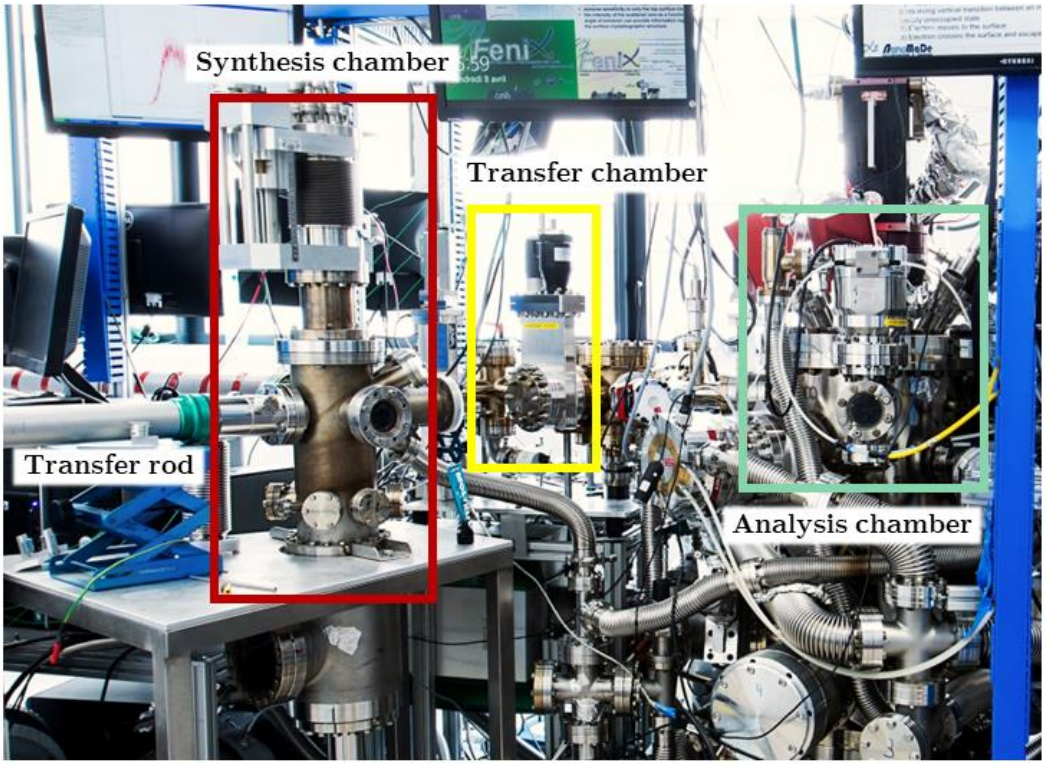

Figure 3.2 Facility for Elaboration of Nanomaterials with in-situ and real-time analysis at X (photo by École polytechnique - J.Barande) [228]

In the synthesis chamber, the HFCVD allows us to grow the carbon nanotube in the large temperature (500°C – 1200°C) and pressure (from UHV to few hundreds of mbar) ranges. The reactor chamber fitted with a 6 Ta-filaments assembly confined within the gas inlet, a heated substrate holder, and pumping ports. The chamber is initially evacuated with a turbo molecular pump which helps us reach ultra-high vacuum (at least 10^{-8} mbar of base pressure), which help to minimize the wall contamination particularly for experiments performed at low pressure conditions. Then, the reactor is filled with chosen specific gas flow (in sccm) of hydrogen, and the valve of the turbopump is slowly closed until the chamber reaches the desired growth pressure. The IR heated substrate temperature was measured with a thermocouple mounted within the heated block directly under the substrate. In parallel, the filaments

can be powered in order to increase the temperature locally and allow the independent decomposition of gases into the reactive species. In our experiments, H_2 is significant for the growth SWCNTs. It not only helps to shape the catalyst during pretreatment, but it also dewetting the catalyst layers to form metal clusters and assists in the elimination the excess of carbon arriving to the surface of catalyst during the growth [197]. In the case of using the radical gas, it could help to form the catalytic NPs with smaller sizes, restrict the cluster migration and contribute to a lower synthesis temperature [229]. After the pretreatment time, the mixture of gas (hydrogen and methane) is introduced to initiate and sustain the growth of CNTs for 30 minutes. The growth pressure is continuously adjusted to maintain the set value. The synthesis of CNTs can be sharply terminated as soon as the valve is fully opened so that the reactor returns to high vacuum environment (within seconds). Subsequently the gas valves are totally closed and the power supply for the filament and substrate heating turned off.

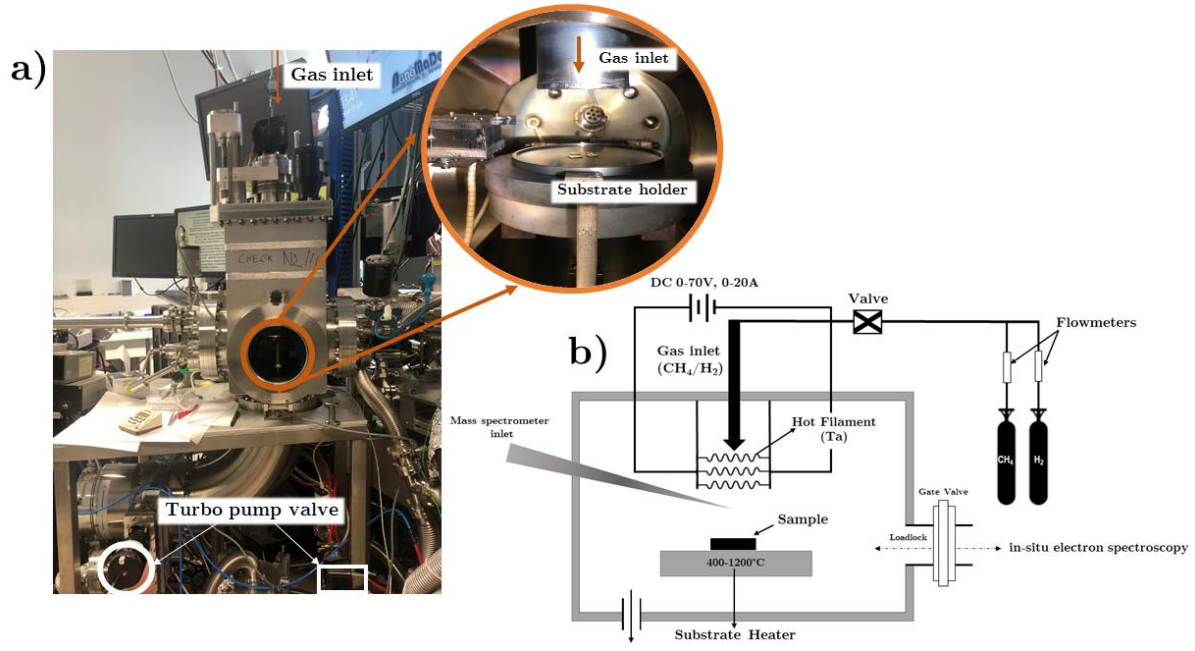

Figure 3.3. (a) The HFCVD reactor in FENIX, (b) Schematization of our HFCVD reactor

3.2. Characterization techniques

There are many available techniques to characterize the structural and morphological characteristics of SWCNTs [230]. Among these, available in the laboratory are Scanning electron microscopy (SEM) and Raman spectroscopy which

were performed to get first overview of the quality and structural characteristic of our samples. Furthermore, Transmission electron microscopy (TEM) allowed us to access structural and morphological characteristics (growth mode, diameter, length) of the SWCNTs after growth. In-situ experiments using two different techniques, XPS and ETEM were also carried out to study the chemical state, nucleation of the catalyst and the growth mechanism of SWCNTs.

3.2.1. Raman Spectroscopy

Raman spectroscopy is a non-destructive characterization technique providing information on the structure of a material by observing vibrational modes. When a beam of the monochromatic laser beam produced by a continuous laser is focused on the surface of the sample, the scattered photons are reflected in all directions. If their energy is the same as that of the incident photons, this phenomenon is described as elastic scattering or Rayleigh scattering. If the photons are re-emitted at a different frequency compared to that of the incident photon, the process is known as inelastic scattering or Raman effect. In Raman effect, the incident photons exchange energy with the matter with the creation (process "Stokes"), or annihilation (process "anti-Stokes" of an excitation. The anti-Stokes process involves the scattering of incident photons and the generation of new photons with different energies, a result of the interaction with vibrational or rotational modes of the sample. The energy of these excitations is then analyzed by a chromatic detector, corresponding to the Raman shift. The depth of Raman interaction with matter depends on various factors: wavelength of incident light, sample preparation and properties, and instrument configuration. A Raman spectrum presents the Raman intensity scattered as a function of the frequency difference between incident photon and scattered photon: if we consider the Stokes lines, this difference is positive and zero in the case of Rayleigh scattering. In practice, this frequency difference is converted into a wavenumber $\bar{\nu}$ defined by the following relation: $\bar{\nu} = \frac{1}{\lambda} = \frac{\nu}{c}$ where $\bar{\nu}$ is wavenumber (in cm^{-1}), λ is the wavelength of radiation (in cm), ν is the frequency of radiation (in Hz), and c is the speed of light in a vacuum.

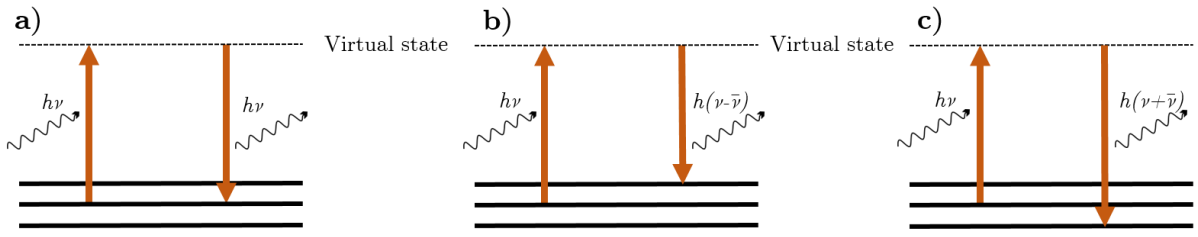

Figure 3.4. Interaction between a photon and a molecule characterized by vibrational energy levels: (a) Rayleigh process, (b) Stokes process, (c) Anti-stokes process[20]

The use of Raman spectroscopy for the analysis of carbon materials appears as one of the most powerful, non-invasive method for the characterization of SWCNTs [226], [227]. Generally, at different wavelengths of laser-excited, the Raman spectrum of SWCNTs has two principal regions: a low-frequency region with radial breathing mode (RBM) peaks and a high-frequency region consisting of D and G peaks [20] (Figure 3.5a).

Radial Breathing Mode (RBM): The RBM region is mainly used to study the diameter of single-walled carbon nanotubes. It provides information on the electronic structure of the tube (peak intensity) and allows assigning the chirality (n, m) of the tube[20], [233]. It corresponds to the in-phase vibration of the carbon atoms in the radial direction as if the tube is breathing. This mode, which is characteristic of SWCNT, exhibits a maximum range of 100 cm^{-1} to 350 cm^{-1} for tubes with diameters from 0.7 nm to 2 nm. RBMs are not observed in MWCNTs due to their layered structure; MWCNTs consist of many concentric cylinders with oscillation modes at different frequencies, which can interfere with each other leading to the quenching of RBM. This mode is an excellent way to identify if a sample contains SWCNTs and to calculate their diameter by following the relationship[20], [231], [233], [234]:

$$\omega_{RBM} = \frac{A}{d_t} + B \qquad (3.1)$$

Where d is the diameter of the tube, A and B are constants that are determined experimentally. The constants A and B are highly dependent on different environmental effects: Van der Waals interactions, adsorption of molecules to surfaces,

interactions with the substrate, tube bunding. For bundles of SWCNTs with an average diameter of 1.5 nm, the diameter can estimated using values A = 234 $cm^{-1}nm$ and B = 10 [234], [235]. For SWCNTs–HiPco scattered in SDS surfactant, the relationship between diameter and wavenumber of Raman shift is determined through A = 223.5 $cm^{-1}nm$ and B = 12.5 [236]. For single-walled carbon nanotubes isolated and deposited on a substrate of oxidized silicon, values of A = 248 $cm^{-1}nm$ and B = 0 were found [233], [234] and furthermore we will only use this approximation. Nevertherless, it is important to highlight the constraint associated with using Raman spectroscopy for characterizing the diameter of SWCNTs: Challenge in indistinguishability of diameter (The Raman spectroscopy encounters difficulties in the distinguishing between tubes with similar diameters, especially when dealing with SWCNTs that have a narrow diameter distribution)

G mode: The most intense characteristic band for graphitic materials is the G band, which lies in the frequency range 1500 to 1600cm^{-1} (Figure 3.5a). The G peak comes from the phonons with E2g symmetry near the Γ point and is associated with a first-order single-phonon Raman process [237]. The excited electron scatters inelastically staying in the same electronic band of the Dirac cone and emitting a phonon. Unlike the G band of graphite (similar to that of a MWCNT) represented by a single Lorentzian peak at 1582cm^{-1}, the G band of an SWCNT comprises several peaks[231]. Its characteristic shape results from the superposition of several lines corresponding to different tangential vibration modes of carbon atoms. In general, the G band is composed of two peaks, which have the most vigorous intensity. The first peak is called G^+ peak, located at 1590cm^{-1} and corresponding to the displacement of atoms along the axis of the tube. The second component (G^- peak) is located at 1570cm^{-1} and corresponds to the vibrational modes of the atom along the circumferential direction of CNTs. The shape of the G–band makes it possible to distinguish the metallic or semiconductor nature of the SWCNT: Lorentzian for a semiconductor tube and Breit – Wigner type (Fano widening) for a metallic tube [32], [238]. The frequency

at the component G^- is linked to the diameter of the nanotube, to its metallic or semiconductor property, but it is independent of the chirality angle[239].

D (Disorder) mode: The D band in the Raman spectrum of the SWCNTs appears in the range from 1250 - 1450 cm^{-1}, depending on E_{laser}[240]. It is associated with the out-of-plane vibrations generated by the presence of defects inside the SWCNTs such as twisted tubes, impurities in the lattice, or the existence of amorphous carbon[231], [240]. Several calculations of Saito et al [241] indicates that no D band intensity occurred in the study of defect-free SWCNTs. However, in the experimental observations, the SWCNTs always contain various types of defects, resulting in the presence of D-band. For example, Duesberg et al [242] concluded that the D band signal comes from bending, defects or finite size effects when analyzing the separated and purified SWCNTs on a glass substrate. These SWCNTs were guaranteed to be free of amorphous carbon after purification. Another study of Pimenta et al [243] indicates that the D-band frequency of isolated SWCNTs grown by CVD is linearly dependent on the diameter of SWCNTs. Moreover, the intensity ratio between G band and D band (I_G/I_D) is often used to estimate the amount of defects in a sample of nanotubes [244]–[246]. The smaller this ratio, the greater the structural disorder of the carbon material considered[241], [247], [248]. Another interpretation of Raman spectra is generally accepted: the degree of crystallinity decreases when the G band becomes more expansive and the D band more intense [249].

The nano-Raman spectrometer used in all our experiments is a HORIBA Jobin Yvon, LabRam HR 800 set-up installed at LPICM. Three different lasers (633nm, 532nm and 473nm) were used as excitation wavelengths. For all the experiments, and for each laser, several mappings were carried out by using x100 objective and scanning 50µm by 50µm surface with a step of 5µm to obtain the overview evaluation of diameter and chirality of the SWCNTs. The diameters of SWCNTs were calculated from the frequency of RBM peak through Eq 3.1, and then were compared with the Kataura diagram[250] to determine the chirality (n,m) (Figure 3.5b), thereby estimating their electronic property (metal or semiconducting tube). Reportedly, the transition energy

between a pair of singularities depends on the diameter of the tubes[32]. It is presented in the Kataura diagram which is used as a basis for the interpretation of the Raman scattering spectra of carbon nanotubes (Figure 3.5b). This diagram shows the transition energy (E_{ii}) as a function of the CNTs diameter. Depending on the laser excitation wavelength, a given diameter, either semiconducting tubes or metallic tubes may enter in resonance. For example, for a tube diameter of 1.5nm, if the laser excites at 1.96eV, the metallic tubes are in resonance and can be observed, whereas the semiconducting tubes are observed if the energy of the excitation laser is 2.33eV.

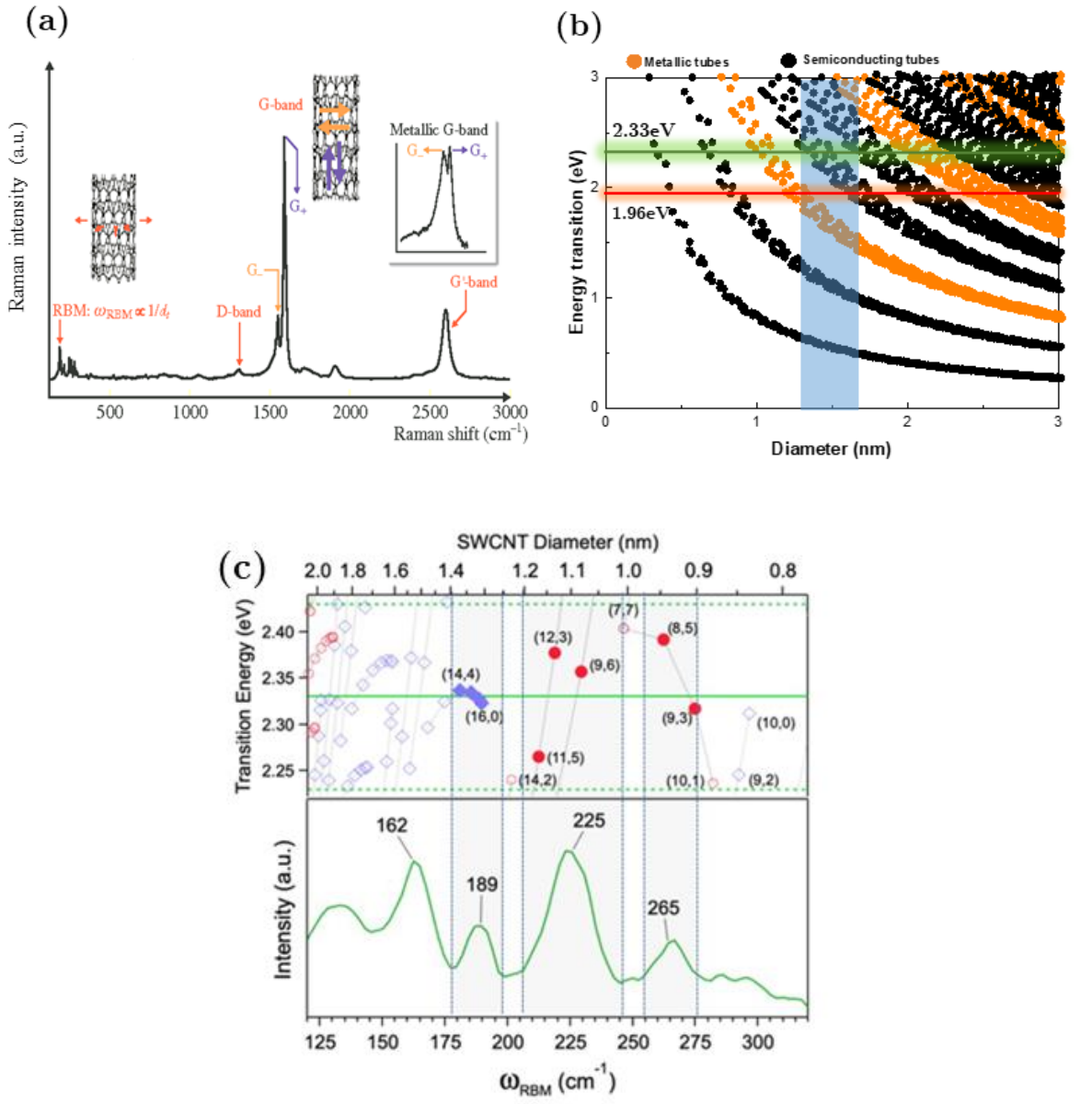

Figure 3.5 (a) Typical Raman spectrum for an incident wavelength of 785nm for SWCNTs [251], (b) Kataura diagram based on the ETB calculation, from the equation, γ_0=2.9 eV and a_{cc} = 0.144nm. The black circles correspond to semiconducting SWCNTs and the orange ones to metallic SWCNTs. Each excitation energy of Raman lasers used in this thesis was plotted (red: 633nm/1.96eV, green: 532nm/2.33eV)[250]. (c) Bottom: RBM of a carbon nanotubes sample for a laser excitation wavelength of 532 nm (2.33 eV). Top: portion of a Kataura diagram which corresponds the laser energy used to realize the Raman spectrum, and on the abscissa the range of frequencies where the RBM are observed. Note that the abscissa of this Kataura diagram has been converted into frequency by using an RBM law of the type $\omega = 235.9/d_t+5.5$[252].

3.2.2. Scanning Electron Microscopy (SEM)

Scanning electron microscopy (SEM) allows the observation of the morphology and topology of objects' surface from macroscopic scale down to nanoscale. The major difference as compared to optical microscopy is the replacement of the light source with electrons whose wavelength is equivalent to the size of atoms[253]. It is based on the detection of secondary electrons emerging from the surface under the impact of monokinetic primary electron beam that scans the surface of a sample where the electron-matter interactions occur in a zone called the interaction bulb (as it could be detected by a sensor that controls the brightness of a cathode-ray oscilloscope whose scanning is synchronized with that of the electron beam). The electron-matter interaction gives rise to various types of radiation: emission of low energy secondary electrons (<50 eV), electron backscattering of the incident beam, X-ray emission in competition with that of Auger electrons, transmitted electrons, and UV-visible photon emission. Typically, the SEM image of the object is obtained from the first two types of radiation: secondary electrons and/or backscattered electrons. The detection of these two types of electrons can be separated since their energies and trajectories are different. Thus, the position and the type of the detectors favors one or the other type of electron. Secondary electrons are resulted from the inelastic interaction of the primary electron beam and the sample. Due to their low energy, we can collect the electrons emitted from the sample surface with a depth of only a few nanometers, thus creating a two-dimensional image of the sample surface [254], [255]. Backscattered electrons are incident electron beams that bounce back when interacting with the sample surface through successive elastic collisions. The energy of these electrons depends on the

number of collisions they have suffered [255], [256]. It will always be greater than the energy of the secondary electrons. Thus, scattering is highly dependent on the chemical composition of the sample surface, so the backscattered electron image is helpful for chemical composition contrast analysis. In addition, the backscattered electrons can be used to record backscattered electron diffraction images, helping to analyze the crystal structure[253].

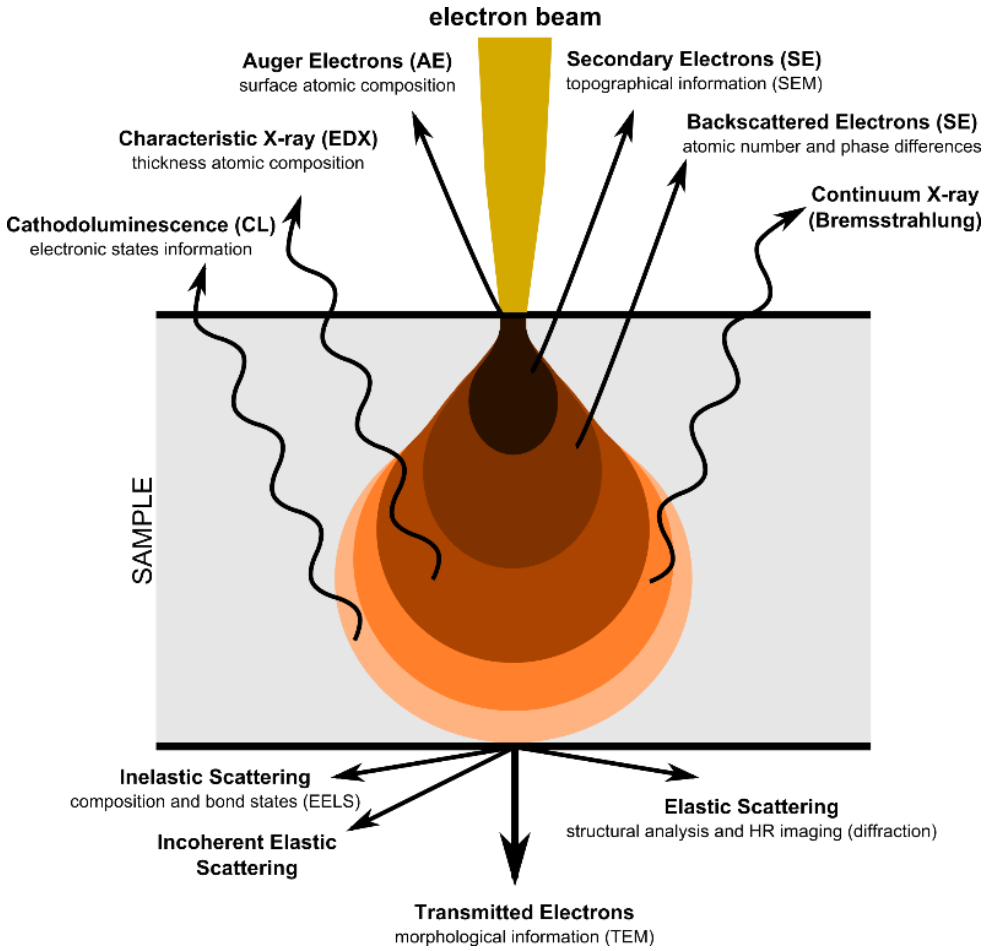

Figure 3.6 Schematic view of electron-matter interaction adapted from SEM [257]

All the samples are characterized using a Hitachi S4800 FEG scanning electron microscope (SEM) (Figure 3.7) at LPICM of Ecole Polytechnique. This instrument is able to work at equivalent resolution even with a low acceleration voltage. This sometime allows reducing the sample charging effects and improving the image quality without a real need of the surface metallization. Two types of detectors are available

on our equipment and were used for the acquisition of all images: (i) the secondary electron detector allows obtaining information on the morphology of sample, and (ii) a backscattered electron detector allows observing the chemical contrast of the sample. Although the SEM is easy to operate, there are a few constraints specifically related to our sample preparation, which is poorly electrically conductive and prone to the effects of accumulation of charges. Thus, all samples were placed on carbon-based tape to have the best possible charge transfer while the acceleration voltage is fixed at 1kV (or 0.5kV), and the beam current at 10µA.

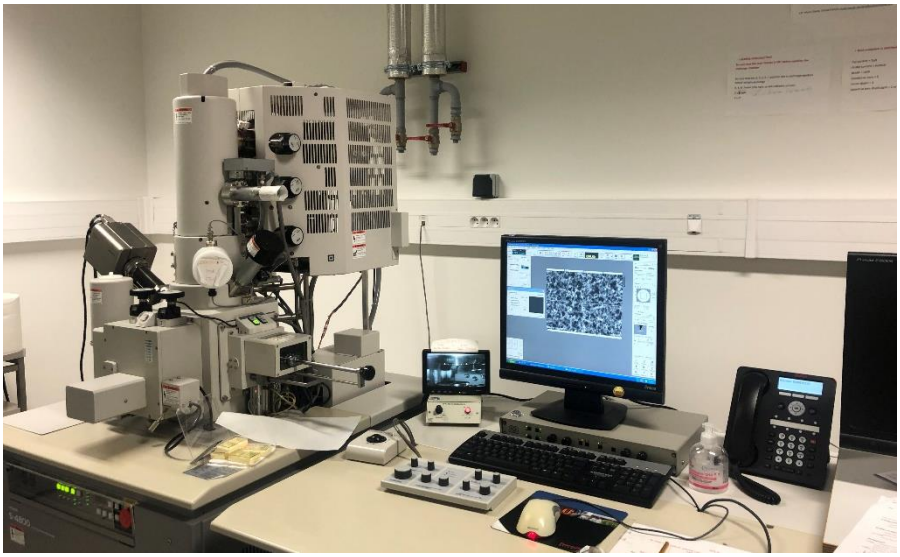

Figure 3.7 Photograph of Hitachi S4800 FESEM equipment available at LPICM.

3.2.3. Transmission Electron Microscopy (TEM)

Another important characterization technique used to access morphological and structural characteristics of the synthetized carbon nanotubes are transmission electron microscopy (TEM) based techniques. Similar to light microscopy the electron microscope operating principle is generally the same: A beam of particle waves is observed after passing through and interacting with the studied object. The essential differences arise from: 1) the nature of the incident beam: electron for the TEM and photons for the light microscopes, 2) the resulting technology: electromagnetic lenses instead of traditional optical lenses, a high vacuum necessary because of the strong interaction between electrons and thin samples, and 3) a thin sample with a thickness

close to ten nanometers. Considering the generator of electron beam, there are two typical types of guns: thermionic guns and filed emission guns. In the thermionic gun, a metal filament is heated close to its melting point to extract electrons (2400°C for tungsten and 1500°C for lanthanum hexaboride single (LaB6) crystal). At the same time, a very high voltage (up to 200kV in the JEOL 2100) is applied between the filament and the anode, so that the electrons are emitted from the cloud surrounding the filament and crossed the Wehnelt, which functions as an electrostatic lens, and converge in a "cross-over", to finally be accelerated to the anode. A field emission gun (FEG) produces electrons when a efficiently high electric potential is applied between the source and the anode. These electrons, which are extracted by field emission at a lower temperature around 700°C under the effect of an acceleration voltage of a few kV by tunneling effect from a tungsten tip, will then be accelerated from a second anode. The combination of these two anodes acts as an electrostatic lens to create the "cross-over". The tungsten tip must remain free of any contamination and oxidation, which is why this type of gun must be under ultra-high vacuum (10^{-9} Pa). This is the case of the cold field emission gun where the tip is operational at ambient temperature. The good condition of the tip can be maintained under a lower vacuum (10^{-6} Pa) by heating it at high temperature. This is the case of the hot field emission gun also called "Schottky" (for example, tungsten is only heated to temperature of 1800°C). The emission of FEGs is much brighter (more electrons extracted) but also much more coherent (electrons more spatially close). The use of accelerated electrons in an electron microscope causes these charged particles to have a wavelength of about 0.02Å, less than the interatomic distance (about 1Å). When these electrons pass through the sample, they are scattered by the constituent atoms of the sample. It is therefore important to know the nature of this diffusion process well in order to be able to interpret the images obtained.

When the electrons of the incident beam interact with the sample, different signals result as shown in Figure 3.8. The two types of interaction when the electrons pass through the sample are elastic and inelastic. Elastic scattering results from the

Coulombic interaction of electrons with the nucleus of the sample atoms. The electron being much lighter than the nucleus, the energy transfer is negligible. We can therefore consider, because of these interactions, that the electrons will be scattered at a wide angle with the same energy as the incident electron. Besides, inelastic scattering results from the Coulombic interaction of electrons with the electrons of the sample atoms. This interaction leads to a loss of energy of the incident electrons. This type of interaction is used in particular in the chemical analysis of samples.

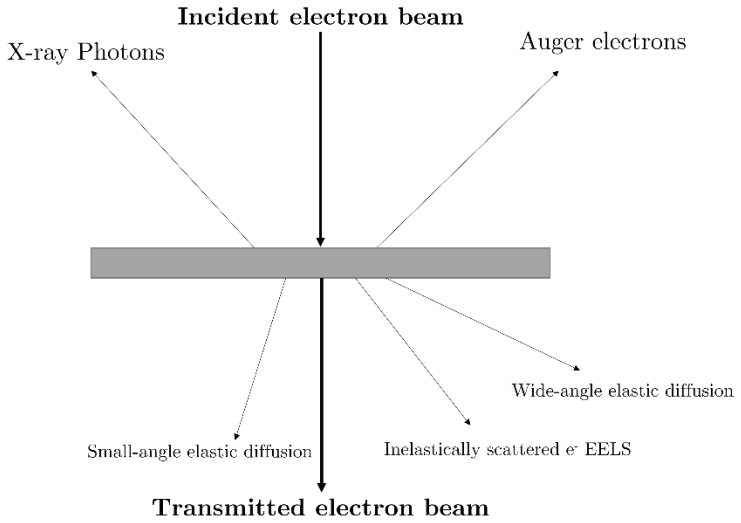

Figure 3.8. Nature of the signals resulting from the electron-matter interaction.

The ex-situ post-synthesis characterization of SWCNTs were conducted within the CIMEX platform using mainly 2 different transmission electron microscopes: a Jeol 2010F microscope operating at 300kV and a ThermoFischer Titan Themis X-FEG operating at 80 and 300kV equipped with an EDX detector. The Jeol microscopy operates Schottky FEG at 300keV. The FEI Titan Themis 300 could operate at 80 and 300keV.

3.2.4. X-ray photoelectron spectroscopy

The chemical composition of the topmost surface was investigated with X-ray Photoelectron Spectroscopy (XPS) technique, which is a non-destructive surface characterization technique based on the use of the photoelectric effect discovered by H. Hertz in 1887 [258], then explained by A. Einstein in 1905 [259]. The current XPS

technology was developed in the 1950s by K. Siegbahn [260] for which he was awarded the Nobel Prize in Physics in 1981[261]. The XPS measurement is based on the study of the kinetic energy distribution of photoelectrons ejected from a sample under the impact of X-rays of known energy hν[262]. The variation of the binding energy of the photoelectrons as a function of the chemical state of the atoms from which they originate is the main interest of this technique: $E_B = E_{phot(x\text{-}rays)} - E_K - \phi$ where E_{phot} is the energy of the incident photons by the X-ray source, E_B is the binding energy of the core level under the consideration, E_K is the kinetic energy of the photoelectron and ϕ is the work function. Indeed, this metrology allows to determine the electronic structure and the chemical state of the atoms present in the sample, but also to quantify the elements present in the different layers, to measure the thickness of the nanometric layers on the surface, and even to perform chemical profile reconstructions when the instrument allows access to the angular information[263]. This characterization technique is mainly adapted to the surface study of the sample since the average free path of the emitted photoelectrons in the material is very low (i.e. of the order of 5 nanometer). Thus, the depth of analysis does not exceed 10nm [264], a considerably smaller range compared to depth capabilities of SEM and Raman Spectroscopy, which typically operate in the range of few micrometers.

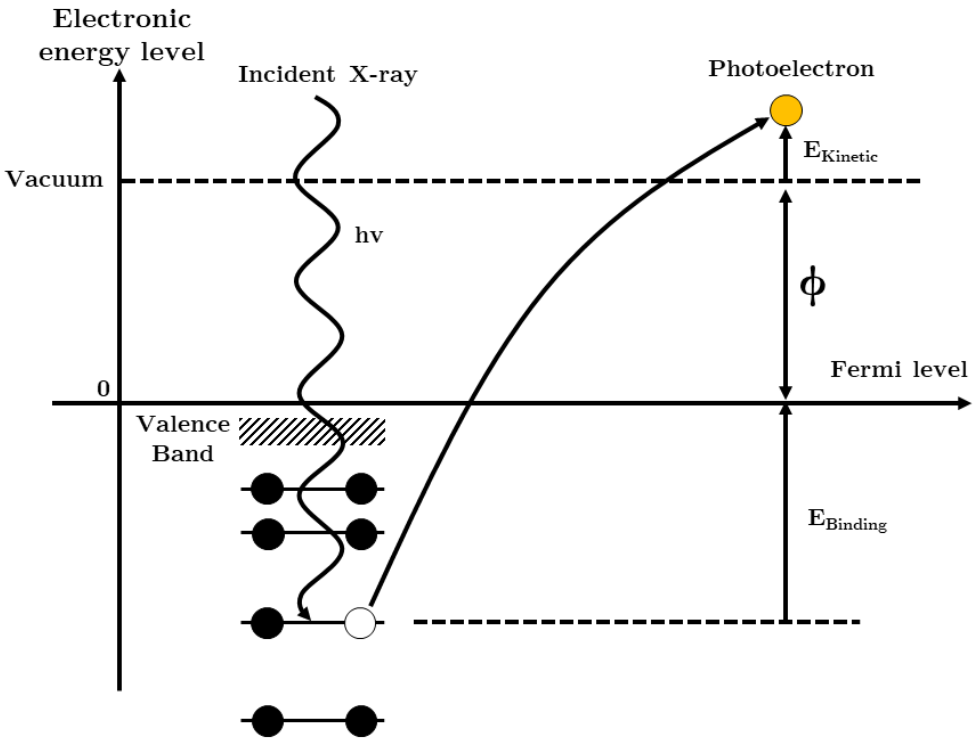

Figure 3.9 Conservation of the total energy during a photoelectronic phenomenon [265]

The XPS system used in this thesis is a part of FENIX platform, with AlKα radiation at 1486.6 eV. A pass energy of 90eV was used to measure the survey spectra in the range of 0eV to 1100eV of binding energy. However, there are some interested regions were recorded with a pass energy of 12eV to obtain the high-resolution spectra at step-scan of 0.1eV for Fe 2p, C 1s, O1s, Si 2p and Al 2p regions. The observed XPS peaks were decomposed and fitted using the Thermo Fisher Avantage XPS software [266] accounting in a smart background and Gaussian-Lorentizian functions. To compensate for charge-shifts correction to the calibration in binding energy was conducted using the C 1s as a reference at 284.5 eV.

3.3. In-situ synthesis and characterization by ETEM – NANOMAX

For the in-situ real time TEM experiments we used the NanoMAX electron microscope, a modified environmental transmission electron microscope (Titan ETEM 60-300ST) available within the CIMEX platform. It is a prototype microscope designed in collaboration with Thermofischer Scientific which has been developed in the framework of TEMPOS Equipex by two main parteners LPICM and C2N (Center of

Nanoscience and Nanotechnologies). The microscope is equipped with a Cs image corrector, an UltraScan 2kx2k CCD camera and a direct electron K2 camera. The particularity of the microscope relies on the presence of two external ports which give access to the objective chamber to provide matter to the sample. The base pressure in the object chamber without the cells mounted is 10^{-7} mbar, value which is not affected when the CVD cells are installed.

During the above processes, the kinetics of the catalyst nanoparticles and the CNTs were observed and recorded using a Gatan US1000 camera with an exposure time of 0.25s. The HDvideo plugging in Digital Micrograph was used to record the videos using a 4fps speed. The structural and morphological characterizations were performed during or after the growth. The detection of reactants and products was performed using a (Quadrupole Mass Spectrometer) QMS 220 PrismaPlus from Pfeiffer with a range of 1–100 amu.

3.3.1. Gas Sources for carbon nanotubes growth

The distinctiveness of NanoMax microscope originates from the matter sources (gas, radicals, vapors) that could be plugged within the microscope column to generate different desired nanostructures growth environments. The sources are installed via two primary ports on the side of TEM column in order to minimize the migration distance of precursors inside the TEM. There are currently four basic types of matter sources which could be plugged within the NanoMAX column compatible with two synthesis techniques: the Molecular Beam Epitaxy (MBE) and Chemical Vapor Deposition (CVD). For our experiments the CVD cells are fitted via the two ports and connected to an external differential pumping system. Inside the microscope, the CVD cells are designed so that their collimators are directed towards the sample holder reaching 3mm distance far from the growth area (Figure 3.10). Outside the microscope each cell is connected to a gas distribution board. With the CVD cells two scenarios can be realized. We can send gas molecules or radicals of different environments such as H_2, CH_4. Each CVD source is designed in such manner that it accommodates a tungsten filament that can be heated at high temperatures (2500K-3000K) allowing

thus 99% dissociation of hydrocarbons gases and molecular hydrogen leading to the production of radicals/activated species before reaching the substrate. This design is similar to the HFCVD system given in section 3.1.2. The cell can work at different growth temperatures and different pressure ranging from high vacuum to a few mbars in the microscope.

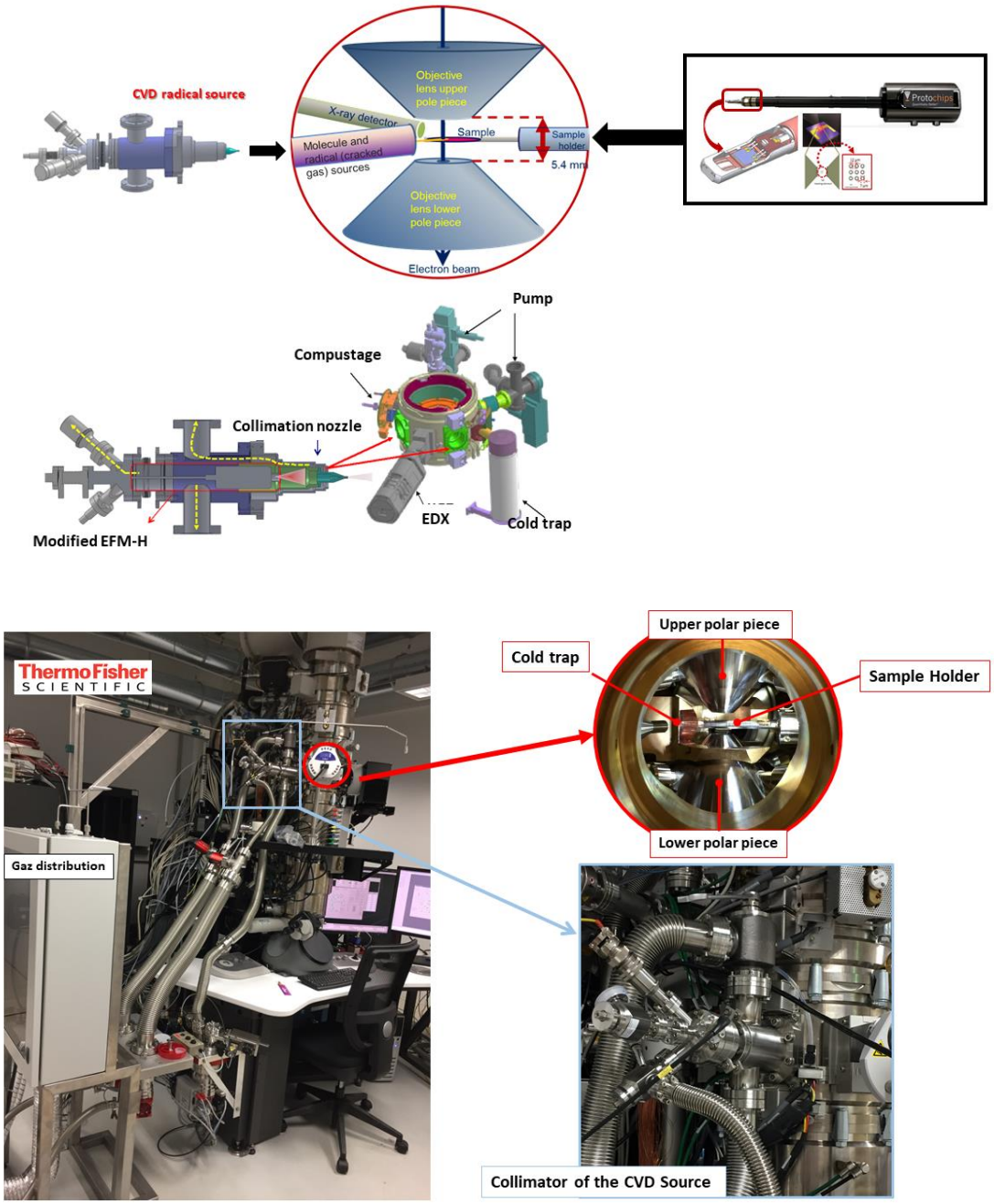

Figure 3.10 (a) Model, and (b) Photography of the radical-assisted CVD modified HR-ETEM (NANOMAX)

3.3.2. Preparation of samples

A heated sample holder is required to observe and study chemical reactions, phase transitions as well as the nucleation and growth process in real time and at atomic scale. Various holders have been developed for imaging and analytical measurement under applied heat, stress, electrical biasing, magnetic field and optical excitation. All in-situ observations were done using the Protochips Fusion Select [267] sample holder that has been slightly modified in order to be compatible with the CVD cells collimators. This holder is designed with the electrical connectors compatible with power supplies that are highly sensitive to the heat and biasing (Figure 3.11). Special supports called E-chips compatible with this sample holder, were used during all our experiments. For all the experiments we used SiC (silicon carbide) heating membranes with different coatings provided with the sample holder. The sample could be heated up to 1200°C when connecting to the source meter via the contact in the holder. The heating is done by the Joule effect and temperature is controlled and measured via the Clarity system software. The temperature is controlled by the sample holder and all the indicated temperatures are based on the company provided calibrations. A schematic representation of the modified microscope and sample holder are shown in Figure 3.10.

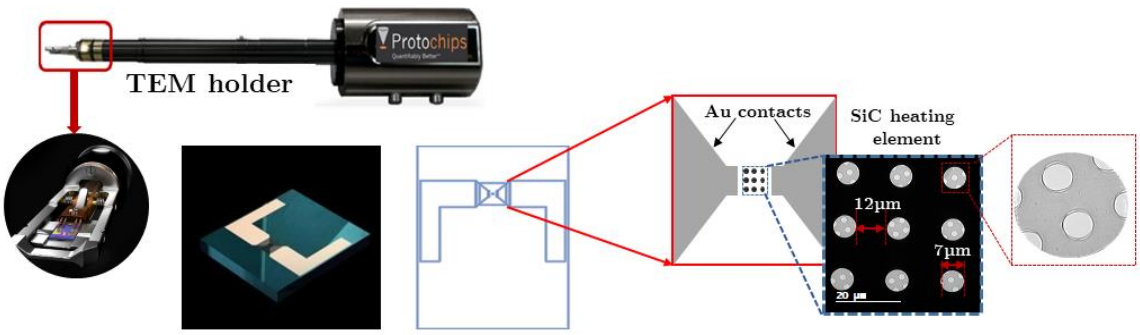

Figure 3.11 Illustration of substrate holder and substrates used for all TEM in-situ growth experiments.

RESULTS AND DISCUSSION

The previous chapters provided a comprehensive overview of current knowledge of CNTs, with a particular focus on the hot filament-assisted chemical vapor deposition (HFCVD) technique. In the chapter 2, section 2.4, we discussed how various parameters of CVD growth can significantly impact the structure of the resulting CNTs, and thus potentially offer a means of controlling the growth of single-walled carbon nanotubes (SWCNTs). In the following chapter, we will focus on the effect of several key parameters, including temperature, pressure, catalyst nature, on SWCNT synthesis, which we carried out in our custom-modified ultrahigh vacuum (UHV) (section 3.1.2). We will also present our in-situ experiments in ETEM-NanoMax to validate the compatibility between two platforms: LPCVD – FENIX and RaCVD@ETEM – NanoMax, and present several promising results

4. Growth of SWCNT using PVD catalyst layer in vertical CVD reactor

This chapter examines the impacts of support/catalyst system on the formation of nanoparticles as well as the characteristics of single-walled carbon nanotubes (SWCNTs) growth via hot filament-assisted chemical vapor deposition (HFCVD) in platform FENIX. The objective is to investigate the growth processes of SWCNTs under various parameters to produce high-quality, high-quantity, and maximum-height vertically aligned SWCNTs. In this framework, we conducted systematic studies on different support layers with monometallic Fe catalyst and various thicknesses of bimetallic Fe-Mo catalyst to analyze their effects on SWCNT synthesis. We used Raman spectroscopy, transmission electron microscopy (TEM), and scanning electron microscopy (SEM) to investigate the properties of the as-grown SWCNTs from different samples with respect to their quantity, structural quality, and morphology.

4.1. Study the structure and properties of SWCNTs grown with monometallic Fe catalyst supported on Al_2O_3/Si substrate.

In this part of the manuscript we investigated the influence of the alumina layer (Al_2O_3), which is widely recognized for its barrier properties in the growth of carbon nanotubes [88], [205], [268]. Indeed, Al_2O_3 is known for its excellent combination of physical and chemical properties, such as thermal stability, chemical inertness, good electrical insulation, low density and permeability, high strength and toughness[269]. To evaluate the influence of a deposited Al_2O_3 support layer on the nanoparticle's formation, and then the properties of the as-grown SWCNTs, a set of samples were prepared, possessing a various thickness of the Al_2O_3 interface layer (0, 3nm, and 5nm) between the Si/SiO_2 substrate and the 0.5nm layer of Fe catalyst. The preparation of the support/catalyst system was performed using the molecular beam evaporation (as described in chapter 3) and the growth of SWCNT was subsequently conducted in the HFCVD-FENIX reactor. The three different samples were named as A1(0nm Al_2O_3/0.5 nmFe), A2(3nm Al_2O_3/0.5 nmFe), and A3(5nm Al_2O_3/0.5 nmFe), respectively. The

growth parameters of the HFCVD-FENIX were set up as summarized in Table 4.1. The as-grown SWCNTs were then analyzed by Raman spectroscopy, SEM and TEM.

Table 4.1 The parameters of growth SWCNTs via HFCVD-FENIX

Growth temperature	800°C
Growth pressure	2mbar
Filament power	900W
Pretreatment	5 minutes with 30sccmH_2
SWCNTs growth	30 minutes with 20sccmCH_4/10sccmH_2

The growth of SWCNTs can be confirmed by the presence of RBM peaks (100-300cm^{-1}), D(~1330cm^{-1}), and G(~1590cm^{-1}) peaks in all three sample A1, A2 and A3 as shown in the Raman spectra of Figure 4.1.

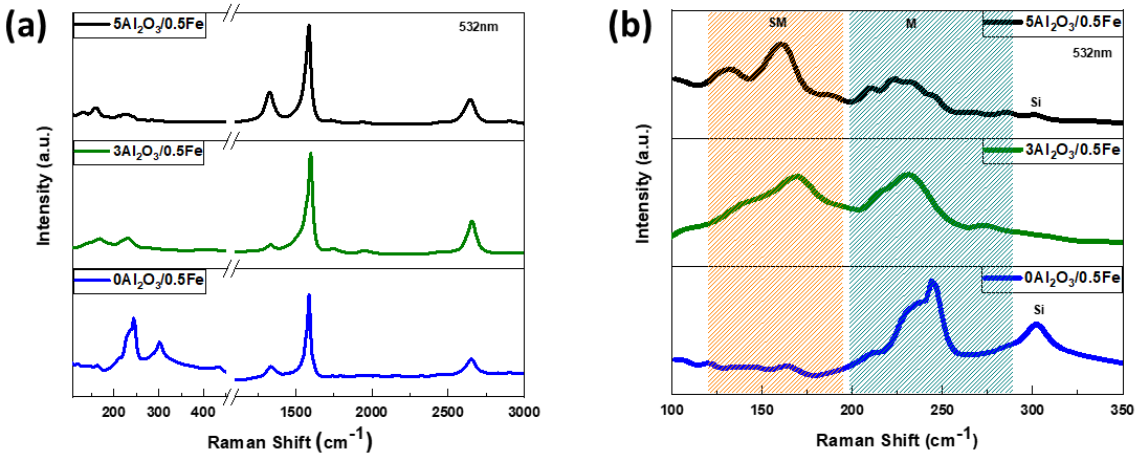

Figure 4.1 The average Raman spectra of 100 points mapping spectra recorded under the 532nm of excitation laser: (a) the whole spectra of A1, A2 and A3 samples which includes the RBM region and high frequency region (D, G, and 2D peaks), (b) focusing on the RBM region. The peak at 300cm^{-1} corresponds to Si peak.

In Figure 4.2a, the top-view SEM image shows that the as-grown SWCNTs on the sample A1 were grown randomly in-plan. During the pretreatment step (see chapter 3), the reducing gas - H_2 will play a role in two different phenomena. Firstly, it causes the deposited thin layer of Fe catalyst to crack and form small islands which are more energetically stable[270]–[272] under the certain temperature. This formation

follows the Volmer-Weber mode on the Si/SiO_2 substrate, as the catalyst atoms prefer to bond to each other instead of the substrate[273]. As a results, the exposure to H_2 gas will reduce the oxidation of the catalyst, and leads to the formation of the particles with a smaller diameter than those obtained during vacuum heating, as reported by Cantoro et al[274]. These small islands, typically 2-4nm in size, are more favorable for the formation of SWCNTs. However, during the 30-minute growth, the catalyst particles eventually diffuse, ripen and agglomerate to form larger catalyst islands [194]. This results in the formation of MWCNTs or other carbon nanostructures[275]. Moreover, the formation of larger catalytic island could lead to a decrease in surface density of the catalyst nanoparticles and an increase in the distance between nanoparticles, and thus induce the growth of the random network SWCNTs with low density[276], [277]. Furthermore, the presence of hydrogen could prolong the lifetime of the catalyst nanoparticles [106], [278] during the carbon nanotubes synthesis by limiting the absorption of C on their surface[279], [280].

The areal density of as-grown SWCNTs increases significantly when Al_2O_3 is used as a barrier layer, as depicted in Figure 4.2b and Figure 4.2c. It is also observed that the resulting carbon nanotubes tend to grow as vertically aligned carpets with different heights as measured from the cross-sectional SEM images (Figure 4.3): 600nm and 900nm of height for the sample A2 and A3, respectively. These observations support the hypothesis that the size of the as-formed catalyst nanoparticles strongly depends on not only on the initial thickness of the deposited catalyst layer[180], [281], [282] and the annealing temperature[279], [280], [283], [284], but also on the Ostwald ripening[285]–[289] and the sub-diffusion of the catalyst atom into the support layer[290] (as proposed in Figure 4.4). In the particular case of Al_2O_3 as a support layer, its surface morphology contributes to reducing the Ostwald ripening and restricting the size of nanoparticles [290]. Moreover, the smaller average Fe nanoparticle size and narrower size distribution that could be achieved via a dominant sub-diffusion of iron nanoparticle into the support layer under the activated H_2 environment treatment [290], are essential prerequisites for growth of VACNTs. These

results are in the good agreement with the investigation of Sakurai et al [290], which demonstrated that a disordered Al-Si-O mixed oxide formed during the annealing process with the presence of H_2 as a reducing gas, helps to promote the iron diffusion. Furthermore, since the metallic Fe has a higher surface energy than the iron oxide [291], the reduced iron atoms could readily react with the Al_2O_3 support and diffuse into Al_2O_3 layer. The proposed underlaying mechanism is summarized in Figure 4.4[178].

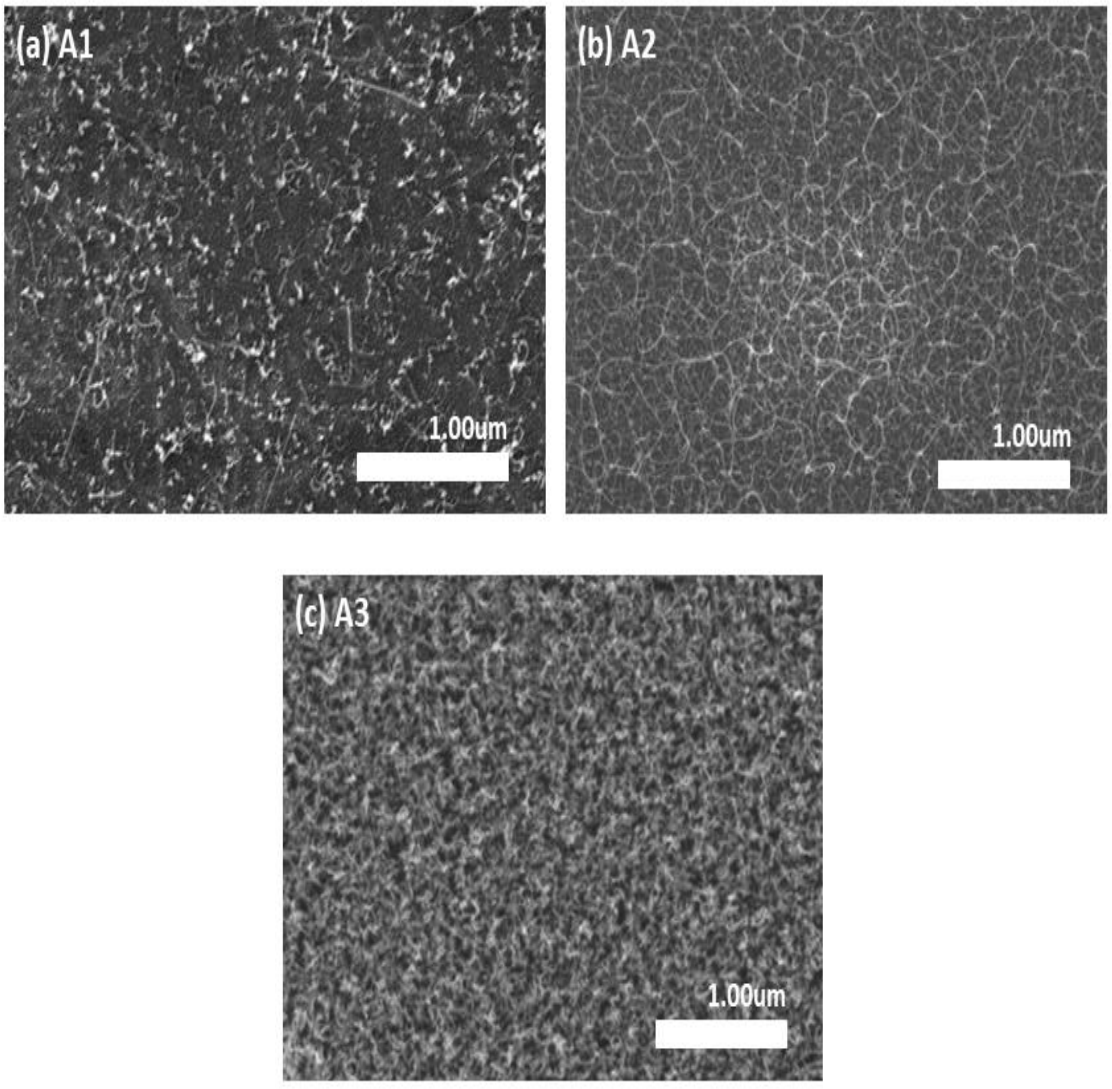

Figure 4.2 : Top view SEM of as-grown SWCNTs on three different samples: (a) A1 – 0nmAl_2O_3/0.5nmFe, (b) A2 – 3nmAl_2O_3/0.5nmFe, and (c) A3 – 5nmAl_2O_3/0.5nmFe

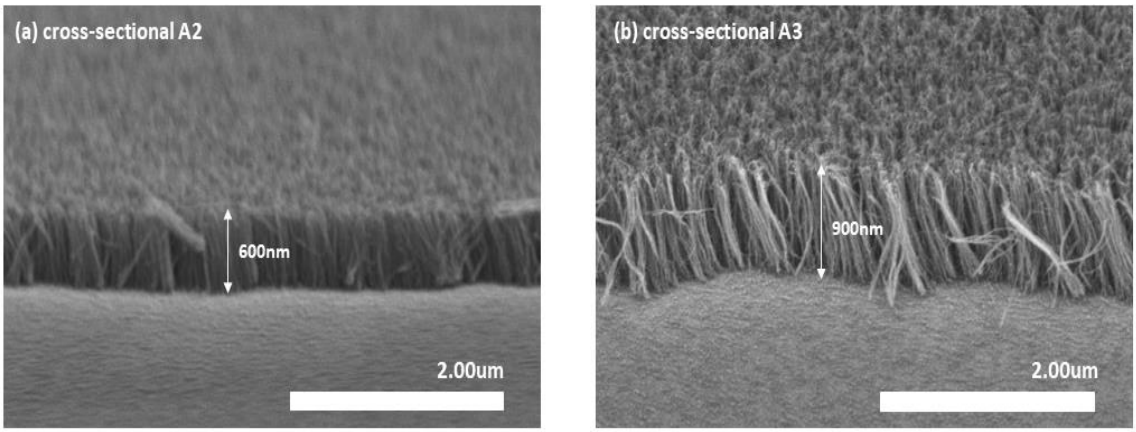

Figure 4.3 Cross section SEM images of as-gown SWCNTs on monolayer Fe catalyst supported by Al_2O_3: (a) A2 – 3nmAl_2O_3/0.5nmFe, and (c) A3 – 5nmAl_2O_3/0.5nmFe

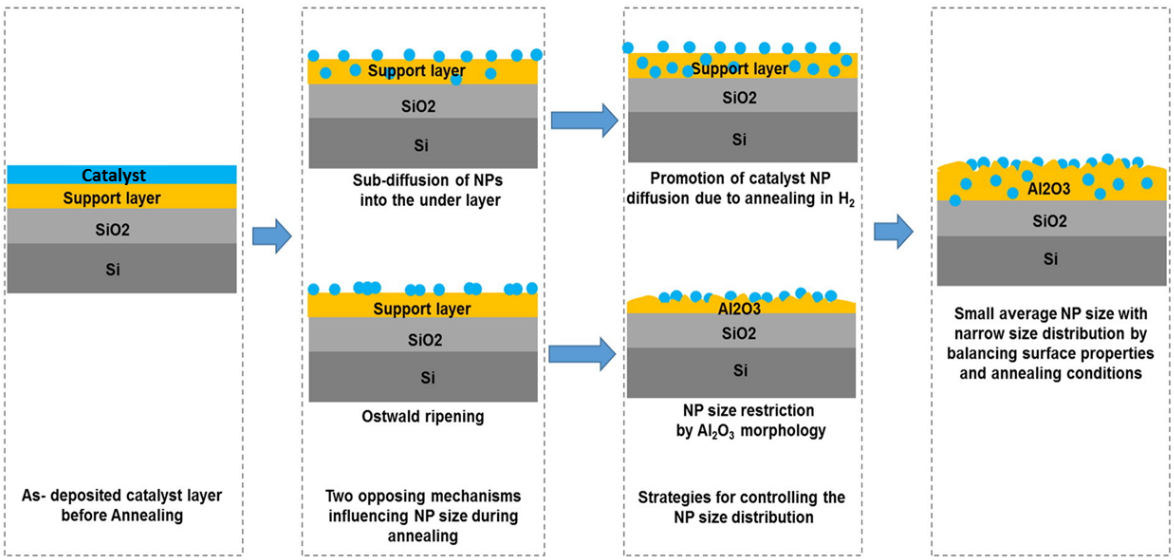

Figure 4.4 The mechanism of catalyst nanoparticle formation on Al_2O_3 support layer under H_2 gas treatment[178]

As previously stated, compared to SiO_2, the use of Al_2O_3 as a support layer can lead to a reduction in the nanoparticle size and an increase in the areal nanoparticles density, thus resulting in a decrease of the distance between the active catalyst nanoparticles [74], [292], especially when using a 0.5nm thick Fe catalyst layer. As a consequence, the SWCNTs growth is promoted as vertically aligned due to the Van der Waals interaction[293], [294]. On the other hand, the chosen thickness of Al_2O_3 layer is observed to also influence the height of the vertically aligned SWCNTs forest. This observation is consistent with the study of Zhang et al. [295], which showed an increase in the height of array VACNTs as the thickness of Al_2O_3 layer increased from

5nm to 50nm with a step of 5nm while using fixed Fe layer thickness at 1nm. The differences in the catalyst nanoparticles formation and the CNTs growth on SiO_2 /Si and $Si/SiO_2/Al_2O_3$ system are schematically summarized in Figure 4.5.

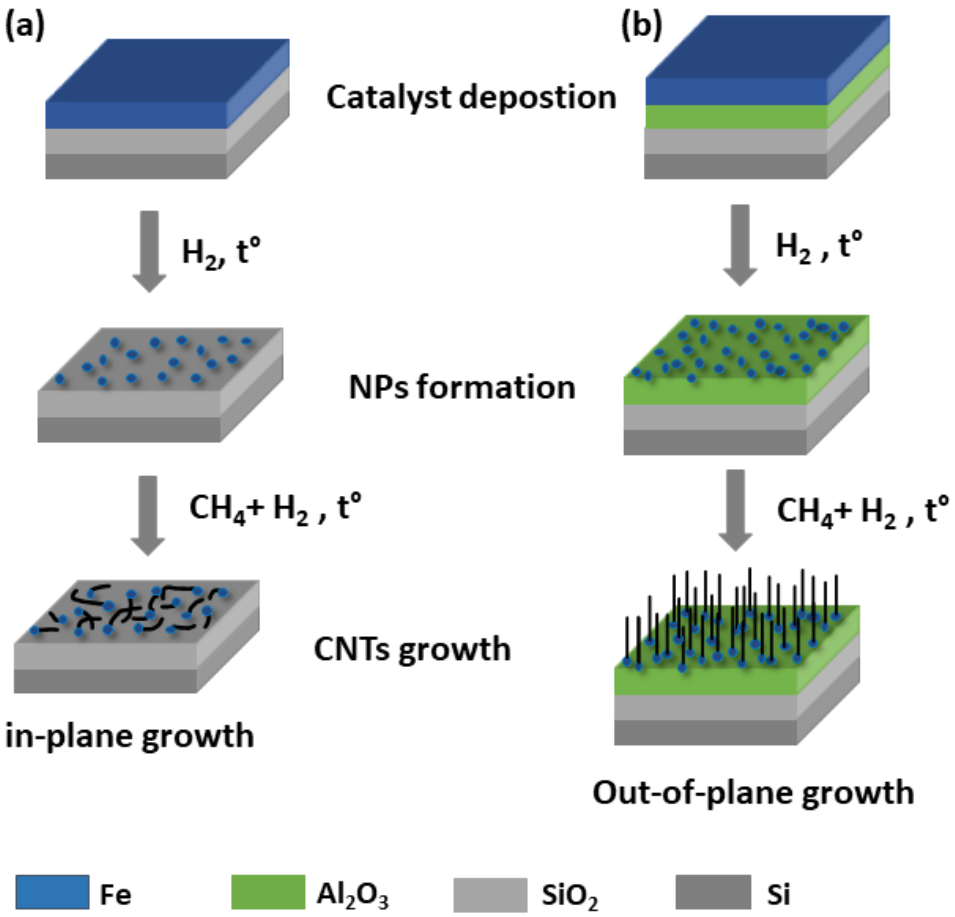

Figure 4.5. Schematic of NP formation and SWCNTs growth on: (a) monometallic Fe on SiO_2/Si substrate, (b) monometallic Fe supported by Al_2O_3 on SiO_2/Si substrate.

4.2. Study of co-catalyst Mo on the Fe-Mo catalyst system supported on Al_2O_3 for the SWCNT growth.

The Fe-Mo/Al_2O_3 system has been widely recognized for its effectiveness in the synthesis of SWCNTs [89], [169], [296]–[299]. Although, the role of this cocatalyst is still under debate, it has consistently demonstrated high productivity [81],[306]. Several explanations have been proposed to explain this success. Firstly, the molybdenum could act as a pre-catalyst facilitating the rapid decomposition of carbon source [306]. Additionally, it would also seem that molybdenum can accelerate the carbon diffusion within the particle through a synergistic effect between nickel and molybdenum[301]. In the case of Fe-Mo/Al_2O_3 system prepared by the fluidized bed CVD [298], the authors have observed a mechanism similar to that of the CoMoCat catalyst. This involves a $FeMoO_4$ mixed oxide that can resist reductive heat treatment and prevent the coalescence phenomena until the introduction of the carbonaceous reagent, which causes the release of the active species and the almost instantaneous carbide formation reaction. In a paper by Liu et al [80], Fe-Mo/MgO catalysts were prepared through alumina impregnation with iron nitrate solution and aqueous solution of Mo in water, then used to synthesize carbon nanotubes by catalytic-CVD from acetylene (C_2H_2). The authors noted a positive effect of Mo as a co-catalyst which achieves high yield of high-quality synthesized SWCNTs. This chapter is particularly interesting as it focuses on the role of molybdenum and highlights the finding that an optimal Mo content in the catalyst leads to the formation of an Fe-Mo alloys that slows the growth rate at the beginning of the reaction but improves stability of the catalytic system over time.

4.2.1. Condition of synthesis

The initial aim of the study was to investigate how the adding of Mo as a co-catalyst with Fe affects the growth of SWCNTs. The first step involved preparing samples using different thickness of Mo and 0.5nm of Fe as catalysts, using a molecular beam evaporator (MBE) under reduced pressure (10^{-7}mbar) at room temperature (as described in Chapter 3). The Si/SiO_2 substrate was cleaned and then a 5nm barrier

layer of Al_2O_3 was deposited using MBE. Thin films of Mo/Fe bilayers with varying thicknesses were then deposited onto the Al_2O_3 layer (as summarized in Table 4.2). After metal deposition, the sample was quickly transfer to the HFCVD system to carry out CNT synthesis. The grow process involved using a temperature of 800°C, a pressure of 5mbar, and a gas flow of 30sccm H_2 for 5minutes for pretreatment, followed by a gas flow of 10sccm H_2/20sccm CH_4 for 30-minute of the growth.

Table 4.2 The different thickness of Mo layer and the corresponding samples

Sample	Thickness of Al_2O_3 (nm)	Thickness of Mo (nm)	Thickness of Fe (nm)
CVD1	5	0	0.5
CVD2	5	0.3	0.5
CVD3	5	0.5	0.5
CVD4	5	0.7	0.5
CVD5	5	1.0	0.5

4.2.2. Morphology – SEM observation

In Figure 4.6, the top-view SEM micrographs obtained from CVD1 to CVD5 samples are presented as a function of the amount of Mo added. We can note successful growth of CNTs for all thicknesses of Mo evaluated in our experiments. The top-view images show a large amount of entangled CNTs that appear uniformly dispersed across the substrate area, making it difficult to identify the length of the CNTs and their tube ends. A related work by Pint et al [284] demonstrated a high-density CNTs growth when using Mo as co-catalyst in Fe-Mo system. The apparent areal coverage of CNTs was estimated by an image processing program called ImageJ [302], [303]. The results are 88% for CVD1, 79% for CVD2, 77% for CVD3, 80% for CVD4, and 85% for CVD5, respectively, which indicate that density of CNTs grown from bimetallic Mo-Fe is lower than that obtained from only Fe catalyst. However, the determination of the correct threshold using ImageJ encounters difficulty because of

the imperfection of image focus and contrast, resulting in a fuzzy area surrounding each CNT. When multiple CNTs overlap, the fuzzy areas of the different tubes are superimposed, causing bright regions where no CNT actually exists. As a consequence, the areal coverage results are only estimates and have significantly high errors.

The cross-sectional SEM analysis of CVD1, CVD2 and CVD3 samples reveals the activation of vertically aligned carbon nanotubes (VACNTs) growth. The height of the VACNTs forest of sample CVD1 is approximately 0.5µm, as shown in Figure 4.7a. The CVD2 sample yielded better vertical orientation, density, and height of VACNTs compared CVD1. However, the height of VACNTs is reduced to 0.3µm when the thickness of Mo achieved 0.5nm. In contrast, spaghetti-like CNTs were formed on the surface of CVD4 and CVD5 sample, corresponding to the Mo thickness of 0.7 and 1.0nm, respectively, and the VACNTs growth mode was not activated.

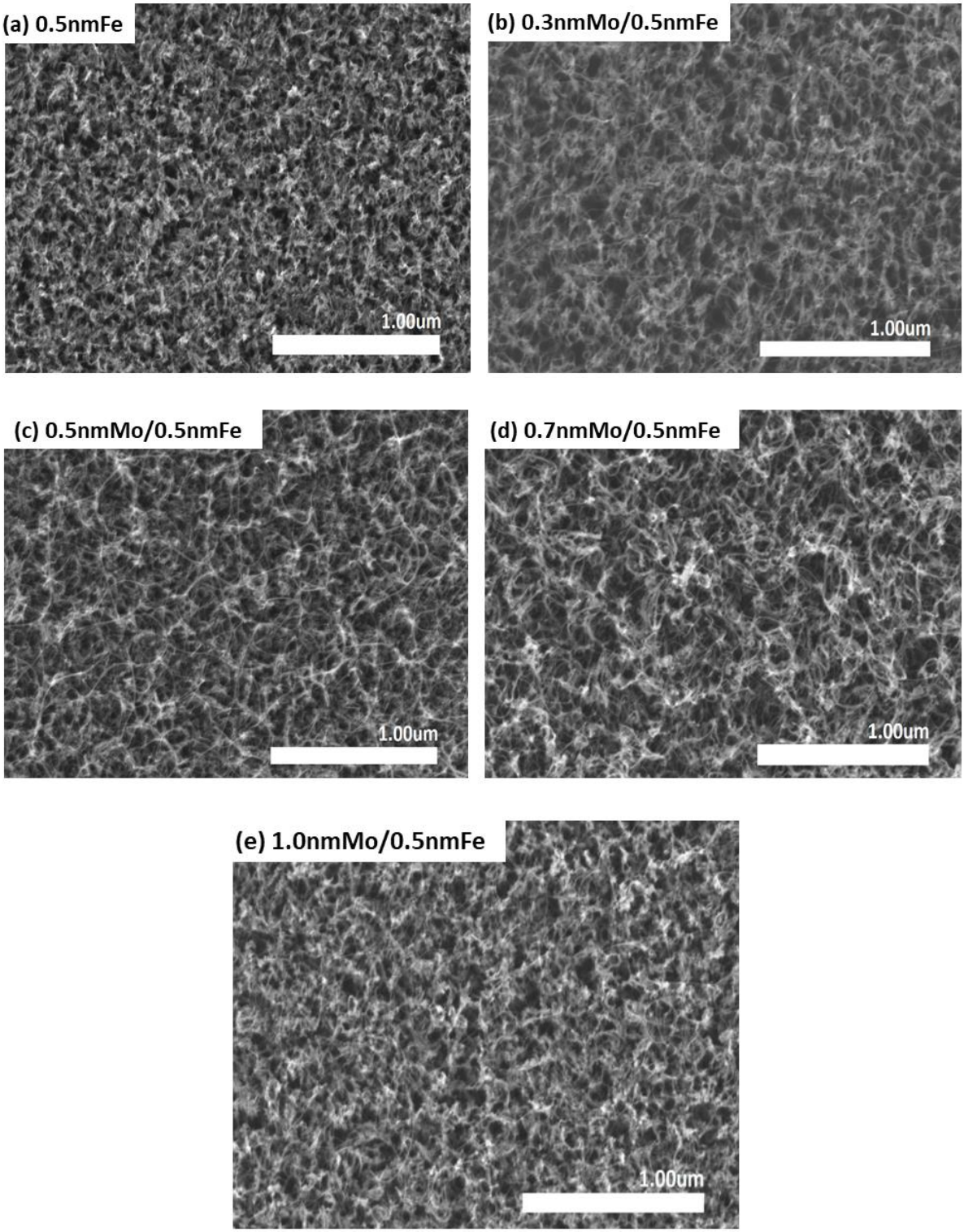

Figure 4.6 Top-view SEM image of HFCVD nanotubes synthesized by different thicknesses of Molybdenum and 0.5nm of Fe: (a)CVD1(0.5nmFe), (b)CVD2(0.3nmMo/0.5nmFe), (c)CVD3(0.5nmMo/0.5nmFe), (d)CVD4(0.7nmMo/0.5nmFe), (e)CVD5(1.0nmMo/0.5nmFe). Experimental conditions: T=800 °C, P=5mbar, $t_{synthesis}$ = 30 min with 20sccmCH_4/10sccmH_2

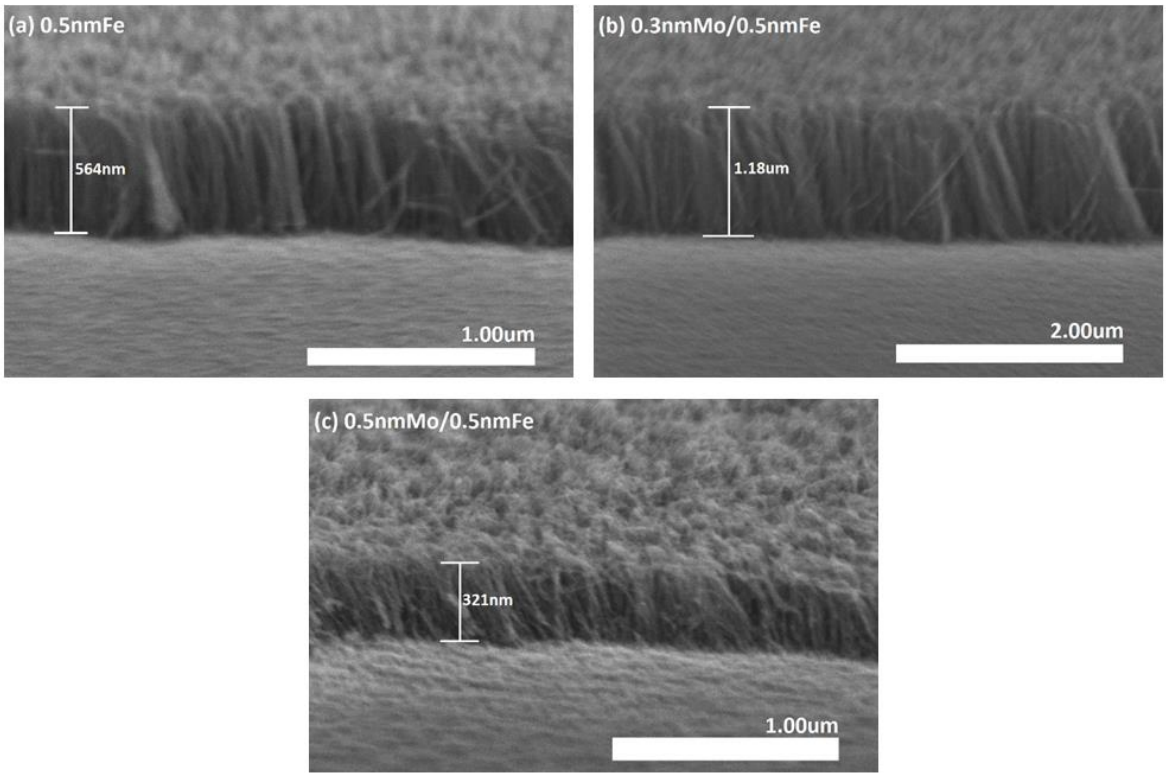

Figure 4.7 Cross-sectional SEM image of HFCVD nanotubes synthesized by: (a) CVD1(0.5nmFe), (b) CVD2(0.3nmMo/0.5nmFe), (c) CVD3(0.5nmMo/0.5nmFe).

4.2.3. Study of the as-grown SWCNTs via Raman spectroscopy

In order to understand the structure of the as-grown CNTs, Raman spectroscopy was performed using three excitation wavelengths of 473, 532 and 633nm. The abundance of single-walled carbon nanotubes (SWCNTs) is confirmed by the distinct peaks in the low-frequency radial breathing mode (RBM) region (100 to 300cm^{-1}) as observed in Figure 4.9a. In the high-frequency region, D band peaks at approximate 1321cm^{-1} and G band peaks at 1594cm^{-1} are also observed in all samples, however there is a variation in the intensity ratio of the G to D band which is an indicator of SWCNTs quality. Figure 4.8a illustrates the comparison between Raman spectra of several samples with 473nm wavelength excitation laser. In general, the shape of the D and G band did not considerably change when varying the thickness of the Mo layer. The G peaks appears separated into two components: G^- and G^+, indicating that the SWCNTs were successfully synthesized. We also plotted the G/D ratio from the Raman spectrum when varying the amount of Mo to study the relationship between

the crystalline quality and the amount of Mo. Whereas the value of G/D ratio of the same sample changes when the excitation wavelength increased from 473 nm to 532 and 633 nm due to different Raman scattering cross section of the D-band mode for each laser wavelength[304], this ratio tended to vary similarly between samples at all three wavelengths. As shown in the Figure 4.8b, the G/D ratio is higher when adding Mo and reached maxima (9 with 473nm laser, 7.3 with 532nm laser, and 5.3 with 633nm laser for CVD2 sample), which indicates the improvement of SWCNTs quality. However, the quality of SWCNTs started to degrade from 0.5nm added Mo, as suggested by the decrease of the ratio when increasing the amount of Mo.

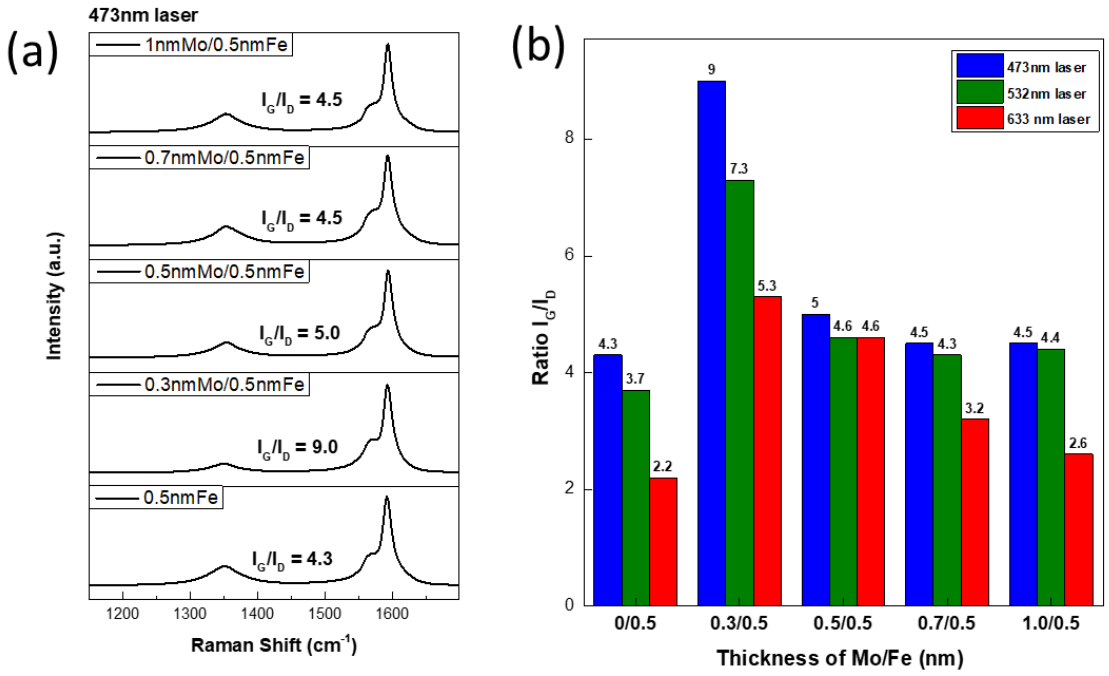

Figure 4.8 (a) Example of D and G band of different samples as an averaged spectra using Origin software from the mapping using 473nm laser excitation. (b) The intensity ratio between G and D peaks for different laser excitation.

Figure 4.9a provides an example of RBM peak identification for the CVD1 sample at different excitation laser wavelengths. Typically, the RBM peak positions were recorded through 100 steps of mapping. Furthermore, we estimated the SWCNTs diameter using the relation with the RBM peak wavenumber in the Raman spectrum (refer to Chapter 3). These calculated diameters were then compared with the Kautara's plot to determine their assignment. For the pure 0.5nm Fe sample (CVD1),

the diameters distribution is bimodal, with two main regions: 1.0 – 1.5nm (70.8%) and around 1.8nm (18%). The CVD2 sample contains a larger amount of small diameter SWCNTs (<1.0nm), while overall the diameter of SWCNTs appears to be more evenly distributed from 0.7 to 2.5nm. In contrast to the other samples, this sample exhibits a notable increase in the quantity of small-diameter single-walled carbon nanotubes (SWCNTs), constituting the most abundant at 39.6% of the total detected SWCNTs. Other abundant populations are 19% for 1.0 – 1.4nm, 15% for 1.8 – 2.0nm and 14% for 2.2 – 2.4nm, respectively. The amount of small diameter CNTs decreases gradually when the Mo thickness increases, and SWCNTs with large diameter (>2.4nm) start to be observed in larger proportion. Notably, the distribution of sample (d), (e) and (f) can be fitted with a Gaussian function. Most of the synthesized SWCNTs have diameters in the range of 1.0 to 1.5nm (CVD3 - 69.7%, CVD4 - 72.5%, CVD5 - 81%) and the mean diameter is 1.30±0.27nm, 1.37±0.14nm, 1.30±0.07nm for the CVD3, CVD4 and CVD5 sample, respectively. Based on these results, we hypothesize that with a sufficient amount of Mo added as a co-catalyst with Fe, it can contribute to the reduction of the nanoparticles size of the main catalyst, resulting in the formation of small diameter SWCNTs. However, it gradually loses its effectiveness when the amount of Mo exceeds a threshold.

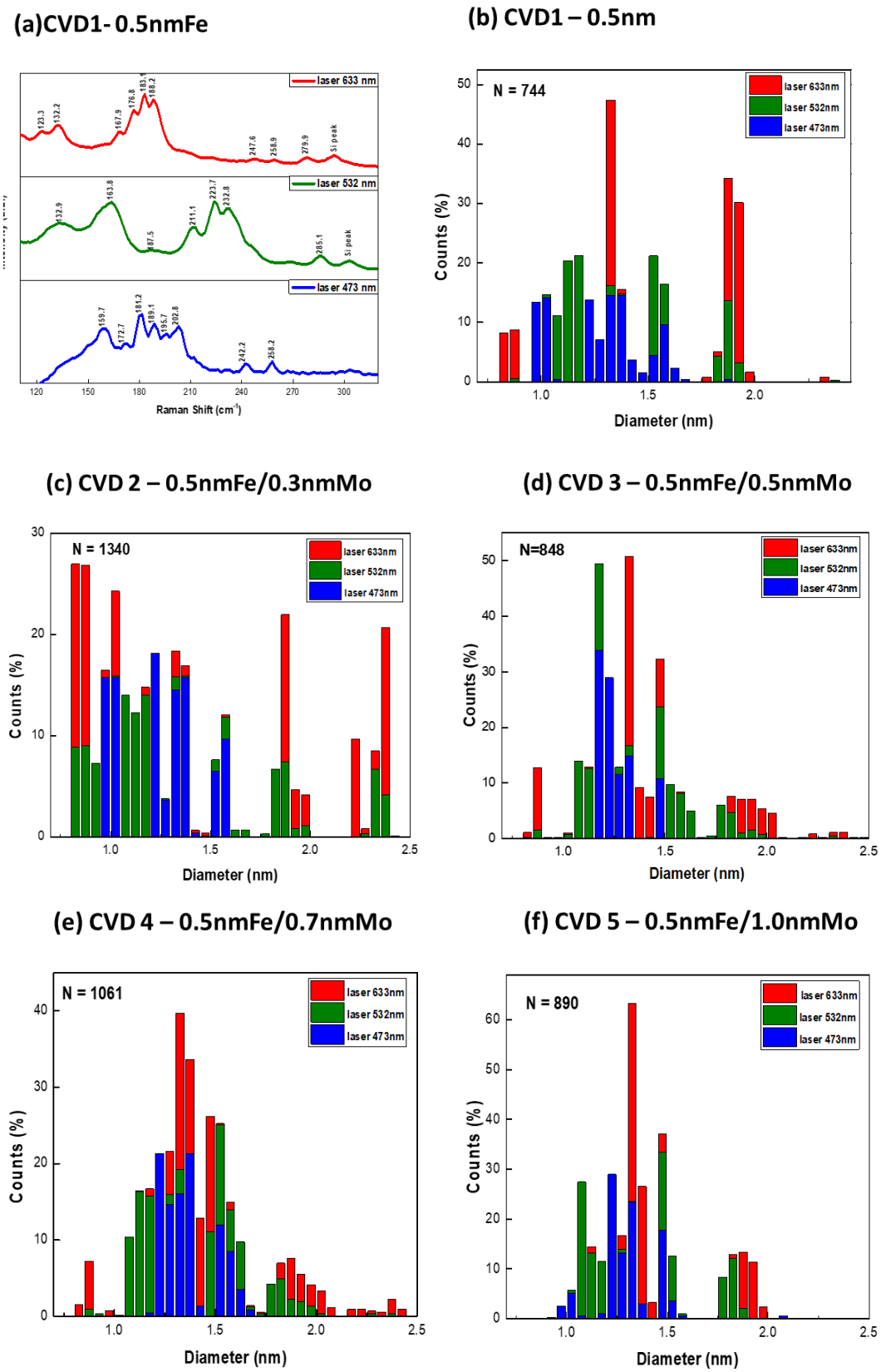

Figure 4.9. (a) An example of RBM region recorded with CVD1 under the excitation of 473nm, 532nm and 633nm wavelengths laser. (b) - (e) The diameter distribution of different samples: CVD1, CVD2, CVD3, CVD4 and CVD5, respectively.

4.2.4. Catalyst state before and after growth

To better understand the catalyst behavior before, during and after the growth, we conducted in-situ X-ray photoelectron spectroscopy (XPS) analyses. These measurements allowed us to identify the presence of Fe and Mo in the sample and monitor any changes in their states. Figure 4.10 shows the results of XPS analyses for the CVD2 sample (0.3nmMo and 0.5nm Fe catalyst). The spectra are relative to a charge reference of adventitious carbon with a core level binding energy of 285eV. Prior to the synthesis, the Mo spectrum exhibits two different peaks: 231.4eV for $3d_{3/2}$ and 228.4eV for $3d_{5/2}$ (Figure 4.10a). A consistent splitting of Mo peaks of 3.2eV is observed, which is in agreement with the known value of 3.13eV[263]. These values correspond best to MoO_2[263], [305], which suggests that the thin layer of Mo oxidized after the deposition due to air exposure prior to insertion into the HFCVD reactor. After the pretreatment with H_2, the peaks centered at 231.5eV and 228.4eV are assigned to Mo^{4+} $3d_{3/2}$, and Mo^{4+} $3d_{5/2}$. We also observed the peak at 226.5eV (47.3% atomic), which could correspond for the $3d_{5/2}$ of Mo metal [306], [307]. This could suggest that during the pretreatment, a part of oxidized Mo was reduced under the H_2 environment to form the metallic state of Mo. After the growth, the core level XPS spectra of Mo-3d (Figure 4.10c) appears with attenuated intensity and split into $3d_{3/2}$ (231.6eV) and $3d_{5/2}$ (228.5eV) peaks. The peak fitting shows two chemical states of Mo, including Mo^0 and Mo^{4+}. The dominant Mo^{4+} peaks and the smaller peak of Mo^0 could be attributed to the molybdenum carbide due to the coexistence of Mo_2C and Mo-Mo bonds in molybdenum carbide[308], [309].

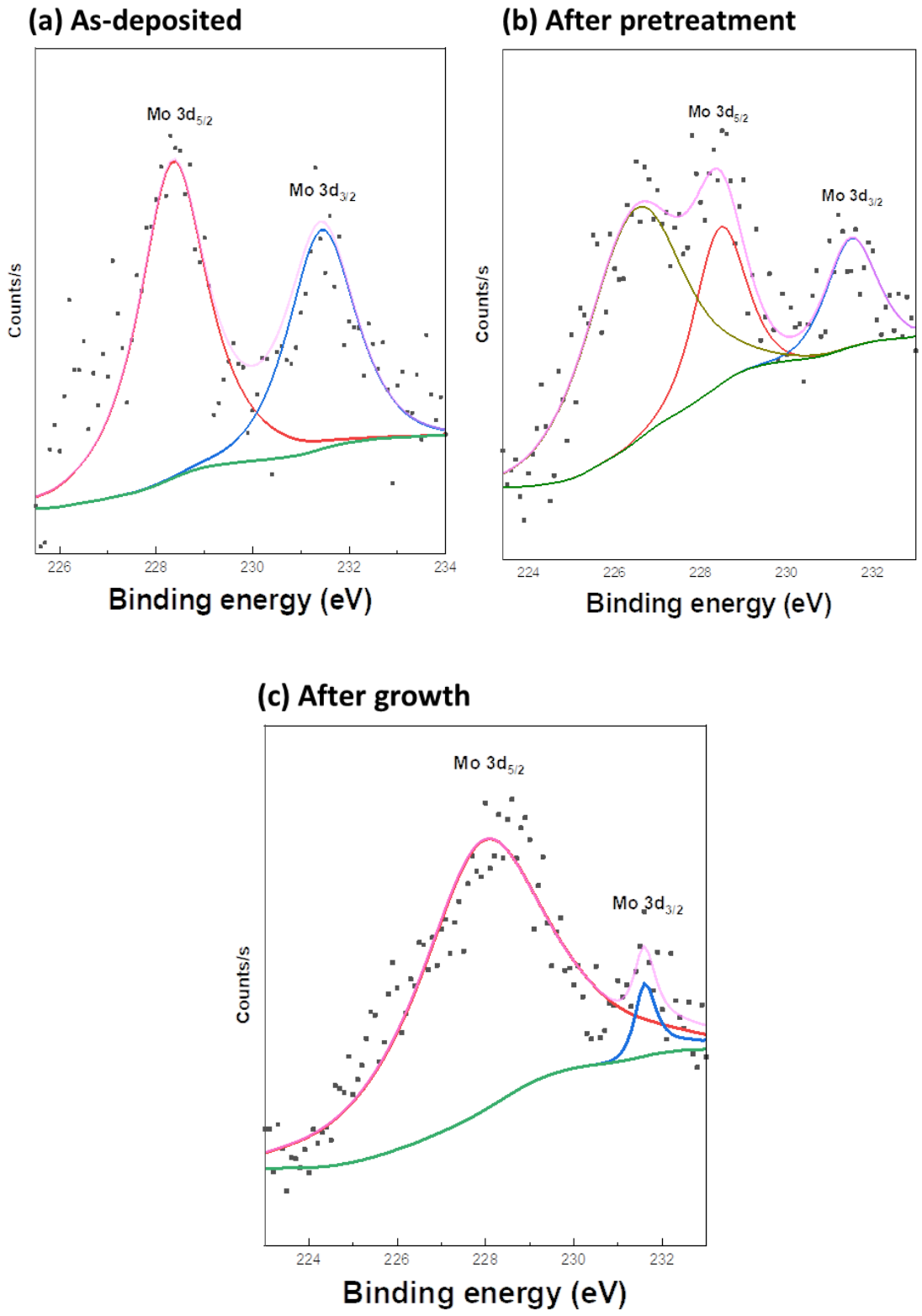

Figure 4.10 XPS spectra of 0.3nm Mo layer in bimetallic catalyst MoFe at three different process: (a) before the pretreatment, (b) after 5 minutes of pretreatment and (c) after 30 minutes of CNTs synthesis

In the X-ray photoelectron spectroscopy (XPS) spectrum of the as-deposited iron layer, two distinct peaks are observed in the 2p region at 710.7eV and 723.8eV (Figure 4.11a). These peaks correspond respectively to the $2p_{3/2}$ and $2p_{1/2}$ orbitals of iron. The chemical compositions FeO (Fe(II)), Fe_2O_3 (Fe(III)) or Fe_3O_4 (mixed oxide of Fe(II) and Fe(III))[310] may account for these values. Additionally, two other peaks at 715.6eV and 729.4eV are distinguishable. The presence of these peaks indicates the presence of either Fe(II) or Fe(III). However, they disappear in the mixed oxide[310]. The position of these "satellite" peaks provides information on the oxidation state of the iron. If the energy difference between the Fe $2p_{3/2}$ peak and its satellite is between 4.3eV and 5.6eV, the oxidation state of the iron is II. Conversely, if this difference is about 8eV, the degree of oxidation of iron is III[311], [312]. In our spectrum, the energy difference between the Fe $2p_{3/2}$ peak and its satellite is 4.9eV. Based on this observation, we conclude that the nanoparticles present on our sample mainly consist of ferrous oxide thin film (FeO).

Following a 5-minute pretreatment under the hydrogen environment, the Fe2p core level displays only two primary peaks due to the spin-orbit coupling $Fe2p_{3/2}$ and $Fe2p_{1/2}$, which are located at 707.6eV and 720.4eV, respectively (Figure 4.11b). These peaks are associated with the metallic state, confirming that the iron oxide thin film was reduced to form metallic Fe nanoparticles, which serve as the nuclei for the growth of carbon nanotubes (CNTs). Notably, the shape and position of these two peaks remain essentially unchanged after the CNTs synthesis, indicating that the iron nanoparticles still maintain their metallic state. However, it should be noted that the peak at 707.6eV is close to the position of Fe_3C peak at 708.1eV, which corresponds to the formation of the carbide state of Fe [313]. TEM analysis further reconfirms the existence of other carbide states in addition to Fe_3C, which may correspond to a less carbon-rich Fe carbide. The formation of the Fe carbide could have occurred either during or after the CNTs synthesis in the presence of a carbonaceous gas flow. This underscores the possibility of carbide formation as a mechanism of catalyst poisoning and eventual catalyst deactivation in this system.

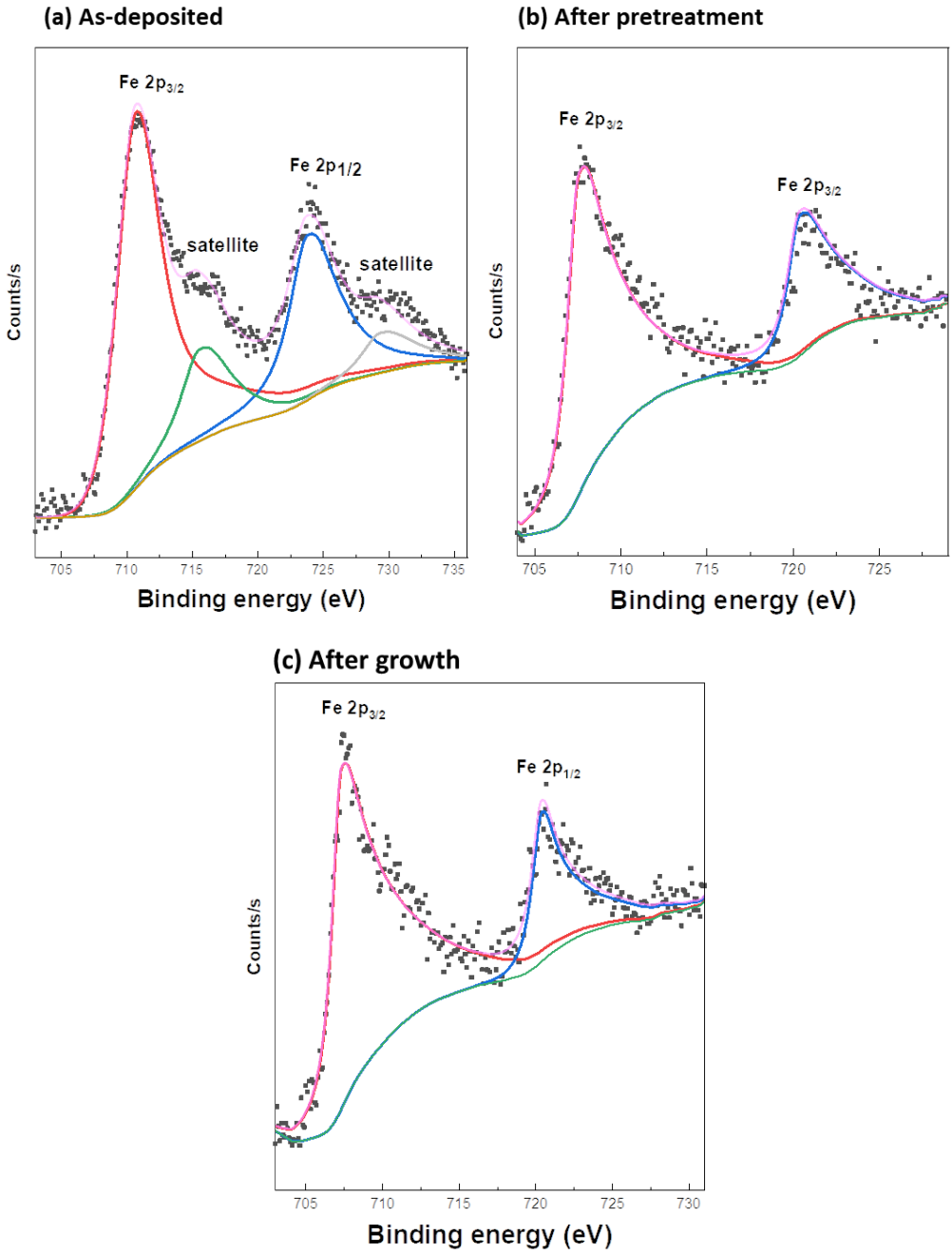

Figure 4.11 XPS spectra of 0.5nm Fe layer in bimetallic catalyst MoFe at three different process: (a) before the pretreatment, (b) after 5 minutes of pretreatment and (c) after 30 minutes of CNTs synthesis

4.2.5. Ex-situ TEM characterization of SWCNTs

It is important to consider that the structural integrity of carbon nanotubes (CNTs) may be compromised during the sample preparation procedures of the ex-situ characterization. The techniques such as transferring CNTs from conventional substrates (Si/SiO_2 wafer) to TEM grids using the ultrasonic bath or scratching the

support and recovering a small amount of CNTs on the TEM grids may cause modification or disintegration of the CNTs structure. Verissimo et al [314] observed the significant damage to MWCNTs after transferring them using an ultrasonic bath in isopropyl alcohol. To address this issue, a promising solution is to grow the CNTs directly on the TEM grids [315], [316]. For example, Gu et al [317] reported the synthesis of SWCNTs on 20nm thick silicon nitrides substrate while using the methane as a carbon precursor in the chemical vapor deposition. More recent work on the growth of CNTs on Si_3N_4 substrates was cited by Nerushev et al [318].

Figure 4.12 shows several TEM images recorded on a carbon-coated copper grid to which the CNTs were transferred from the Si/SiO_2 substrate using the scratching method. Although this method confirms the formation of SWCNTs and determines their diameter, it still contains several limitations, such as: (i) the clustering of CNTs into high-density clouds (Figure 4.12a), (ii) non-exactly indicative of the length and changes in the morphology of CNTs due to the damage, (iii) the uncertainty of position of catalyst nanoparticles relative to the CNTs, making it difficult to conclude the growth.

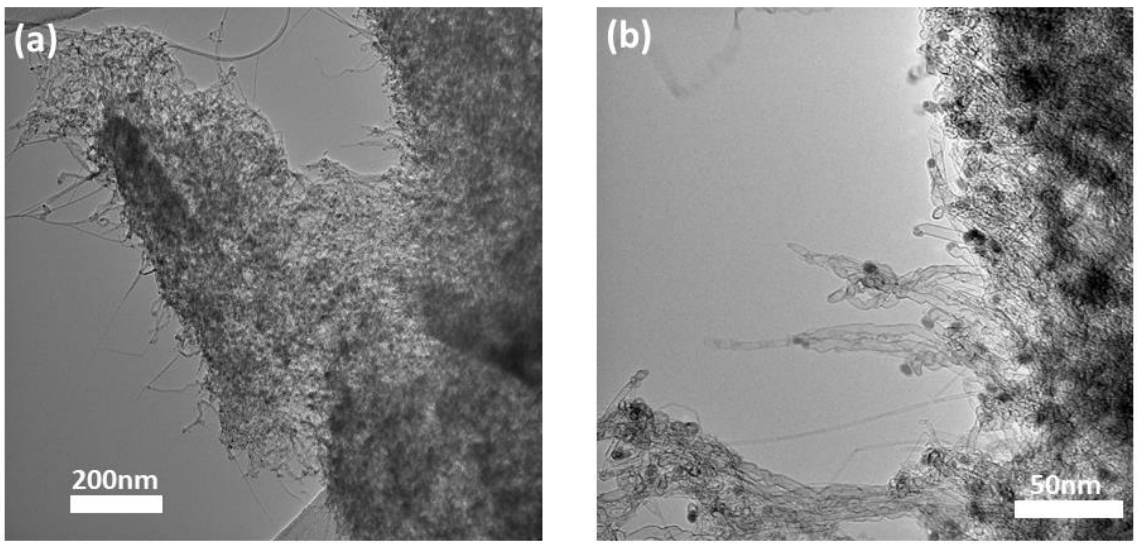

Figure 4.12 TEM observation on TEM grids. The CNT transfer was carried out by cracking method.

To overcome these limitations, we choose to perform a parallel experiment, which includes the strict identical catalyst preparation and CNTs synthesis via HFCVD, with

the same set-up but carried out directly on the TEM-grid (300 mesh) coated with Au. After synthesis, TEM images were recorded using the FEI Titan Themis200 TEM microscope at LPICM. The diameter of approximately 100 CNTs was estimated in order to plot the distribution histogram and then fitted by Gaussian function to identify the average diameter. A series of TEM images of the sample grown from 0.5nm Fe catalyst (TEM1) is shown in Figure 4.13. Several long SWCNTs with a length of hundreds of nm are observed from the low-magnification TEM image (Figure 4.13a). The diameters of the SWCNTs range from 0.6 to 2.4nm, with 69% of the distribution in the 0.9 to 1.4nm range. A Gaussian fitting yields an average diameter of 1.18±0.27nm (Figure 4.13f). The dark spots visible in the TEM grid membrane (Figure 4.13b) can be attributed to the Fe catalyst remaining in the sample after the synthesis, with a size distribution ranging from 3nm to 10nm, which is much large than that of the observed SWCNTs diameter. Although several ends of tube can be observed as in Figure 4.13e, it is difficult to identify the associated catalyst nanoparticles either at the tips or inside the CNTs, which tends to suggest the base-growth mode. However, precise observation of nanoparticle position in the TEM grid membrane is challenging, hindering the assignment of growth mode. Most of the observed SWCNTs exhibited significant number of defects (i.e., amorphous carbon, bending) on the CNTs walls.

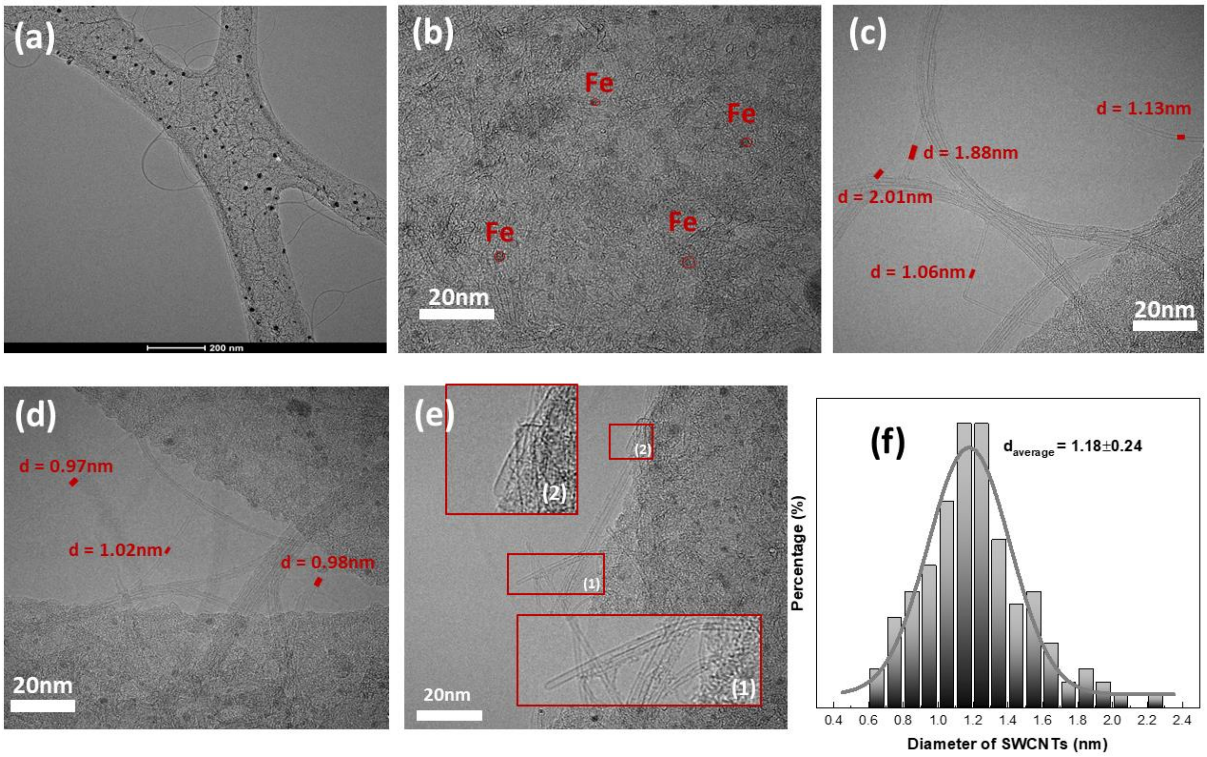

Figure 4.13 TEM images of SWCNTs synthesized using 0.5nm iron: (a) low-magnification image, (b) the Fe catalyst nanoparticles remain in the membrane of the gird, (c -d) the estimated diameter of SWCNTs from high-magnification images, and (e) the histogram of SWCNTs diameter, which was fitting by Gaussian function to determine the mean diameter of SWCNTs

To further investigate by TEM the synthesized carbon nanotubes, we analyzed the sample called TEM2, containing 0.3nm Mo and 0.5nm Fe). Figure 4.14 gives an overall view of catalyst nanoparticles after the synthesis, with the sizes ranging from 2nm to 10nm. A high-resolution TEM image and its fast Fourier transform (FFT) indicates that most of the nanoparticles remaining on the surface correspond to different structures of iron carbide (such as Fe_5C_2, Fe_7C_3 and Fe_3C), which is consistent with the XPS observation. The formation of iron carbide has also reported by Sharma et al. [319] when synthesizing the SWCNTs. Similarly, Hofmann et al also observed Fe_3C during growth by in-situ XPS [127]. Although the contribution of the Fe_3C was small compared to that of Fe, they concluded only that there is a layer of carbide on the subsurface, and the rest of the particle is metallic, indicating surface or subsurface diffusion of the carbon atoms during growth.

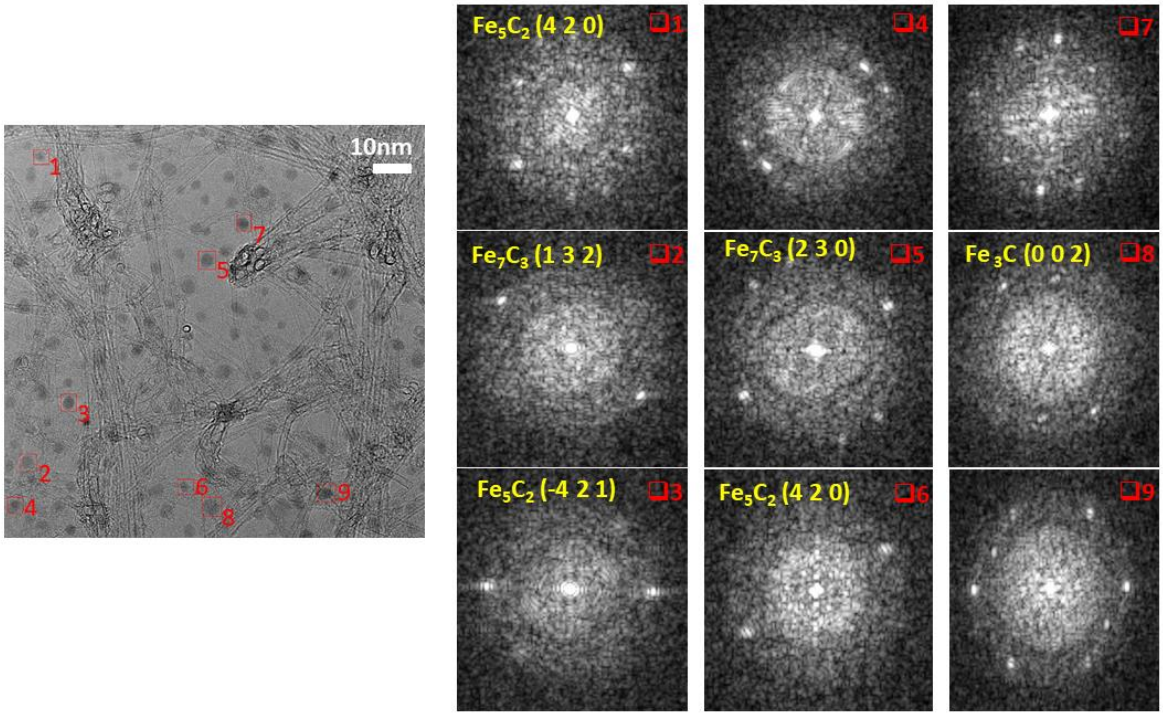

Figure 4.14 TEM micrograph of nanoparticles remaining in the membrane of TEM grid and its FFT images.

Low-magnification TEM image (Figure 4.15b) revealed that several long CNTs are observed in the sample TEM2, similar to the observations in the sample TEM1. However, they appear relatively clean with few amorphous carbons adhering to the wall. An investigation of the dependence of the as-grown CNTs on the diameter of nanoparticles can be made using Figure 4.15a. We remind here that while the nanoparticles with the diameter of ≤5nm are expected to act as nuclei for the SWCNTs formation, the MWCNTs synthesis requires larger catalyst diameter (≥6nm). A narrow diameter distribution with an average diameter of 1.02±0.28 nm from the Gaussian fitting was determined through 100 observed SWCNTs in the sample TEM2 (Figure 4.15f). This average diameter suggests a reduction in diameter of the as-grown SWCNTs using 0.3nm thick of Mo as a co-catalyst. Similar observations were also reported by S.K. Youn and H.G.Park[320], who found that adding 0.2nm of Mo to a 0.4nm Fe catalyst layer can reduce the size of nanoparticles, thus leading to the formation of much smaller diameter nanotubes.

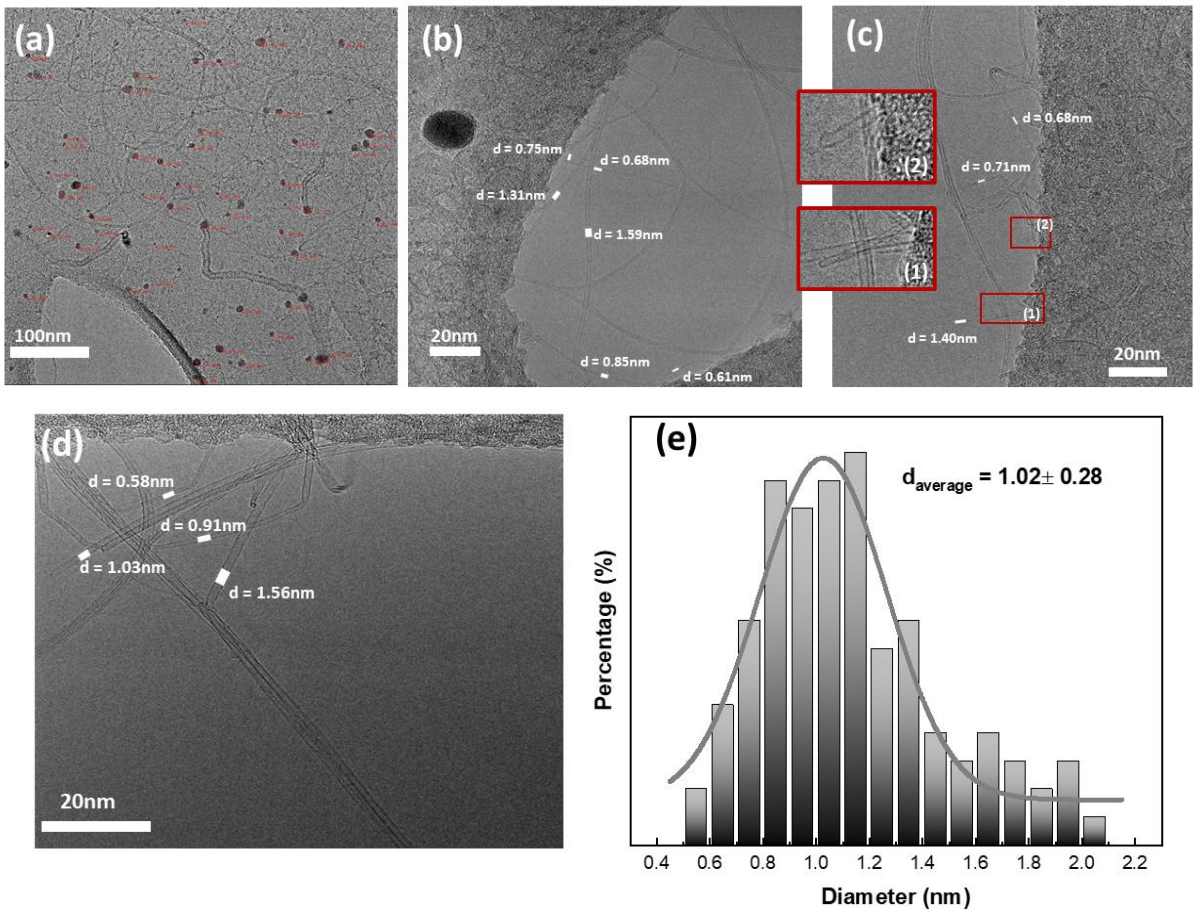

Figure 4.15 TEM images of SWCNTs synthesized using 0.3nm Mo and 0.5nm iron as the catalysts: (a) the catalyst nanoparticles remain in the membrane of the gird, (b -d) the estimated diameter of SWCNTs from high-magnification images, and (e) the distribution of diameter, in which the average diameter was determined by the fitting through Gaussian function.

The formation of nanoparticles in the binary catalyst Mo-Fe is a complex process influence by several factors, including the amount of Fe and Mo, the aggregation of the metal and the surface diffusion during the pretreatment under a hydrogen atmosphere. During the thermal pretreatment process, Fe tends to form the nanoparticles, which act as nucleation seeds for the SWCNTs growth[296]. The Mo itself is not an effective catalyst for SWCNT growth under the conventional conditions [297], [321], but it could convert to Mo carbide (Mo_2C) during the CVD process[178], [296], [299], [321]–[323]. When interacting with Fe, it can thus be expected that Mo stabilizes the Fe and limits the Ostwald ripening of the Fe nanoparticles, resulting in smaller NPs with a narrower size distribution[297], thus translating into the formation of smaller diameter CNTs.

Although, the role of Mo as a co-catalyst is still controversial, one explanation would be that it allows a dilution of the active phase by creating mixed phases which would release the active metal during the process of initiation and growth of the nanotubes [324] or it would seem that the formation of mixed oxides allows the dispersion of the active phase to be increased and maintained for longer. These mixed oxides are typically resistant to reductive heat treatment, preventing coalescence phenomena until the introduction of a carbonaceous reagent which causes the release of the active species and the almost instantaneous carbide formation reaction[188]. However, our study observes considerable variance in the resulting CNTs when using different thicknesses of the Mo co-catalyst. With a sufficient quantity of Mo (0.3nm), the agglomeration/migration of Fe nanoparticles was inhibited, thereby lowering the size of Fe nanoparticle, preventing the formation of large Fe clusters, and subsequently reducing the diameter of the SWCNTs. Furthermore, in this sample, the catalyst NPs appear to form uniformly and densely distribute on the surface of the sample, leading to the activation of VACNTs growth condition with high quality and length. However, the effectiveness Mo co-catalyst decreases as its thickness is increased, particularly in terms of the density and the related alignment characteristics of CNTs. While more experiments are required to full understand the Fe-Mo bimetallic catalyst, this study helps further to improve the preparation and design of catalysts for the synthesis of CNTs.

5. Study of the SWCNTs synthesis at different growth pressure

In recent years, there have been significant efforts toward the industrialization of single-walled carbon nanotubes (SWCNTs). However, several restrictions still exist in their synthesis, including the ability to produce SWCNTs with the desired diameter and chirality for specific applications [230], [325], [326]. In light of this challenge, it is essential to improve our understanding of the growth mechanisms of SWCNTs and develop highly selective chemical vapor deposition (CVD) synthesis methods. While many studies have examined the influence of the catalysts [74], [176], [177], [327], [328] or the temperature [115], [195], [196], [280], [329], there is limited literature on the influence of the growth pressure, particularly in the low-pressure range (less than mbar), on SWCNTs synthesis. Unlike the diamond, which forms at very high pressure, the CVD synthesis of SWCNTs is generally carried out under atmospheric pressure [330], [331], which could cause the non-uniformity of as-synthesized SWCNTs [332]. Therefore, a low-pressure type chemical vapor deposition (LP-CVD) synthesis method that guarantees uniformity could be desirable [333]. Despite this advantage, almost no attempt has been reported to synthesize SWCNTs by LPCVD. Kasumov and co-workers have obtained a good number of nanotubes synthesized at 5mbar with acetylene [334]. A very dense forest of vertically aligned single-walled carbon nanotubes was synthesized under the pressure of 27mbar with an iron catalyst [77]. The influence of pressure on the number and the quality of nanotubes is also studied by Akinari Kozawa et al [335]. The optimal ethanol pressure to obtain the highest yield of SWCNTs was $1x10^{-2}$ Pa at 600°C when using Pd as a catalyst. The group of Shiokawa confirmed the successful synthesis of SWCNTs at 0.001mbar [336]. Consequently, the present study in the following paragraphs follows the logic of a phenomenological understanding and control of SWCNTs growth at different growth pressure in the HFCVD reactor under different conditions of gas flow. It aims at carrying out a systematic study by varying certain parameters of process in order to apprehend the potentialities of this approach, especially in the range of low-pressure. The optimization

of SWCNTs growth and obtaining a satisfactory homogeneity and quality of SWCNTs on Si/SiO_2 substrates guided the first steps of this study.

5.1. High gas flow regime – fixed CH_4:H_2 = 10:20 sccm

Prior to undertaking a rigorous experimental study of the effect of pressure on carbon nanotubes growth, it was imperative that we develop a stable and highly reproducible fabrication process of the CNTs. Due to that, other parameters (growth temperature, gas flow, and catalyst) were set based on the optimized parameters derived from our other HFCVD studies [78], [198] for the SWCNT synthesis.

5.1.1. Experimental growth conditions

The oxidized silicon substrates for this study were coated with 5nmAl_2O_3 and 1nm Fe layers using the molecular beam evaporation (Section 3.1.1). The main parameters of the CVD process set for this study were: the hot filament power of 900W, substrate temperature of 800°C, the pretreatment time of 2 minutes under 30sscm H_2, a gas mixture of 67%H_2, and 33%CH_4 with a total flow rate of 30sscm, the growth time of 30 minutes. In order to discern the effect of the CVD growth pressure, the growths were performed at 7 pressures of 0.02, 0.05, 0.2, 0.5, 1, 2, and 5mbar. We will discuss the obtained observations aiming to identify the influence of various growth pressures.

5.1.2. The CNTs morphology

The top-view SEM images of CNTs grown at 0.02, 0.05, 0.2, 0.5, 1, 2, and 5mbar under a total gas flow of 30sccm are shown in Figure 5.1. Although the SEM technique allows us to confirm the formation of CNTs in all the samples, however, the quality of the images is not clear enough to determine the type of CNTs (either SWCNTs or MWCNTs) because of the practical limit of conventional SEM. The apparent as-observed areal density of the nanotubes seems to increase considerably when the pressure increased up to 0.5mbar and to vary significantly less from the pressure of 1mbar and more. A significant proportion of the nanotubes appear to be assembled in bundles. For the samples synthesized at low pressure (<= 0.2mbar), the observations

seem consistent with the incipient stages of the growth CNTs: initial seeds of CNTs and short CNTs on the catalyst are detected. The residence time of the gas is linearly dependent on the growth pressure according to the equation: $\tau = \frac{V_t TP}{QTP^0}$, where τ is the gas residence time; V_t is the volume of the furnace chamber; Q is the total flux of both precursor gas and carrier gas; T and P are the temperature and pressure, respectively[337]–[339]. Due to that, when we reduced the growth pressure, the residence time of methane decreases, resulting in the decrease in carbon feeding of catalyst, thereby expectedly forming sparser CNTs nuclei and shorter CNTs. Furthermore, as pressure increases, so appears to do the length of the carbon nanotube.

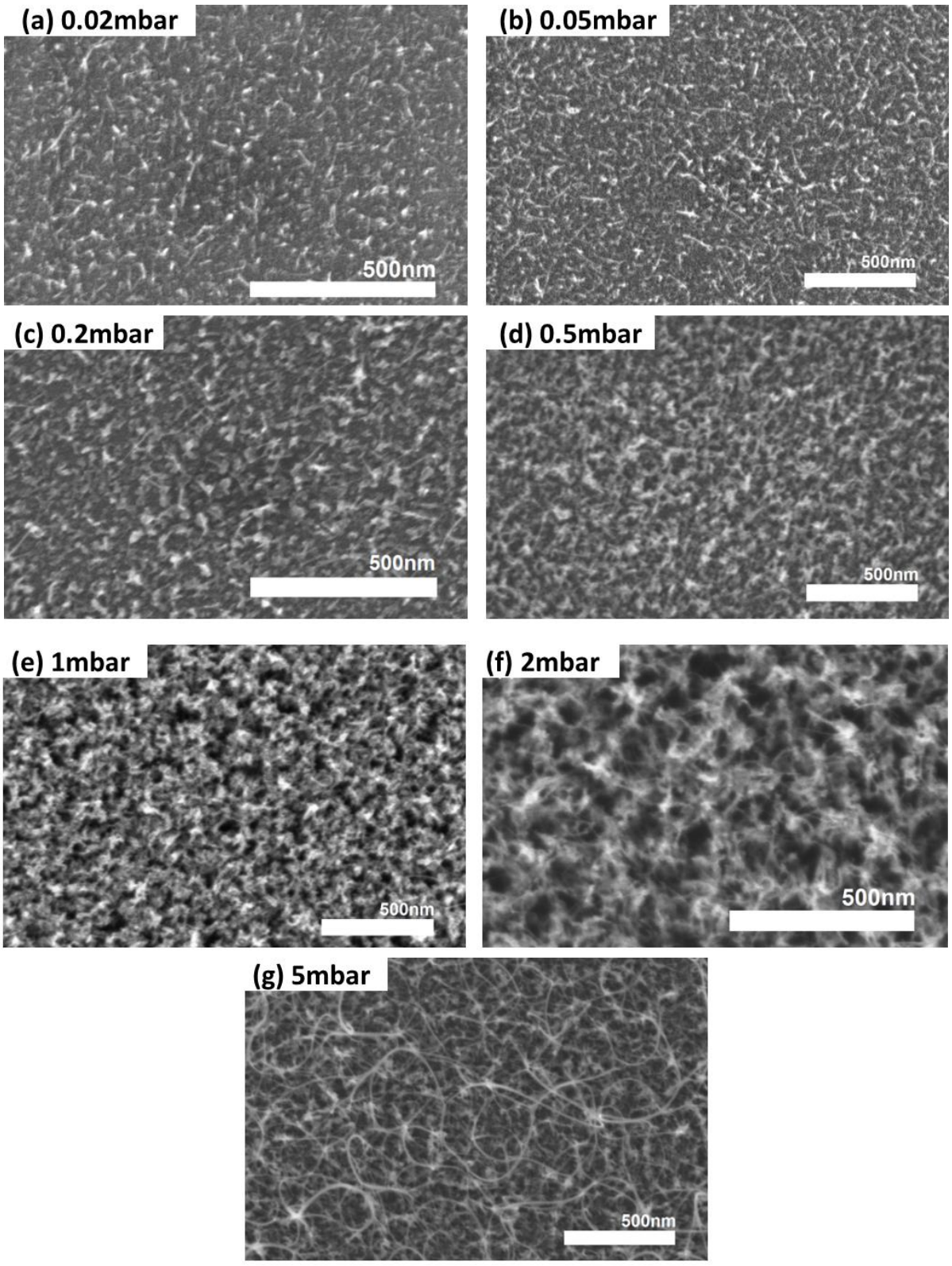

Figure 5.1 SEM images of grown samples synthesized under different growth pressure: (a)0.02mbar, (b)0.05mbar, (c)0.2mbar, (d)0.5mbar, (e)1mbar, (f)2mbar and (g)5mbar, respectively

A series of cross-sectional SEM were performed to evaluate the alignment of the as-grown CNTs and to estimate the thickness of the obtained CNTs forest. Below the

growth pressure of 1mbar, there is no observation of vertically aligned CNTs, the CNTs were observed in the randomly spaghetti-like growth mode. From the growth pressure higher than 1mbar, the cross-sectional SEM images confirm the formation of vertically aligned CNTs with different thicknesses, depending on the growth pressures. The height of VACNTs is around 200nm corresponding to growth pressure of 1mbar (Figure 5.2a), and then it increases up to 400nm at 2mbar (Figure 5.2b) and around 900nm at 5mbar (Figure 5.2c) respectively. It is to be noted that the 215nm layer in Figure 5.2a corresponds to the SiO_2 layer of the substrate. In general, the observed length of CNTs gets longer following a quasilinear dependence with increasing growth pressure.

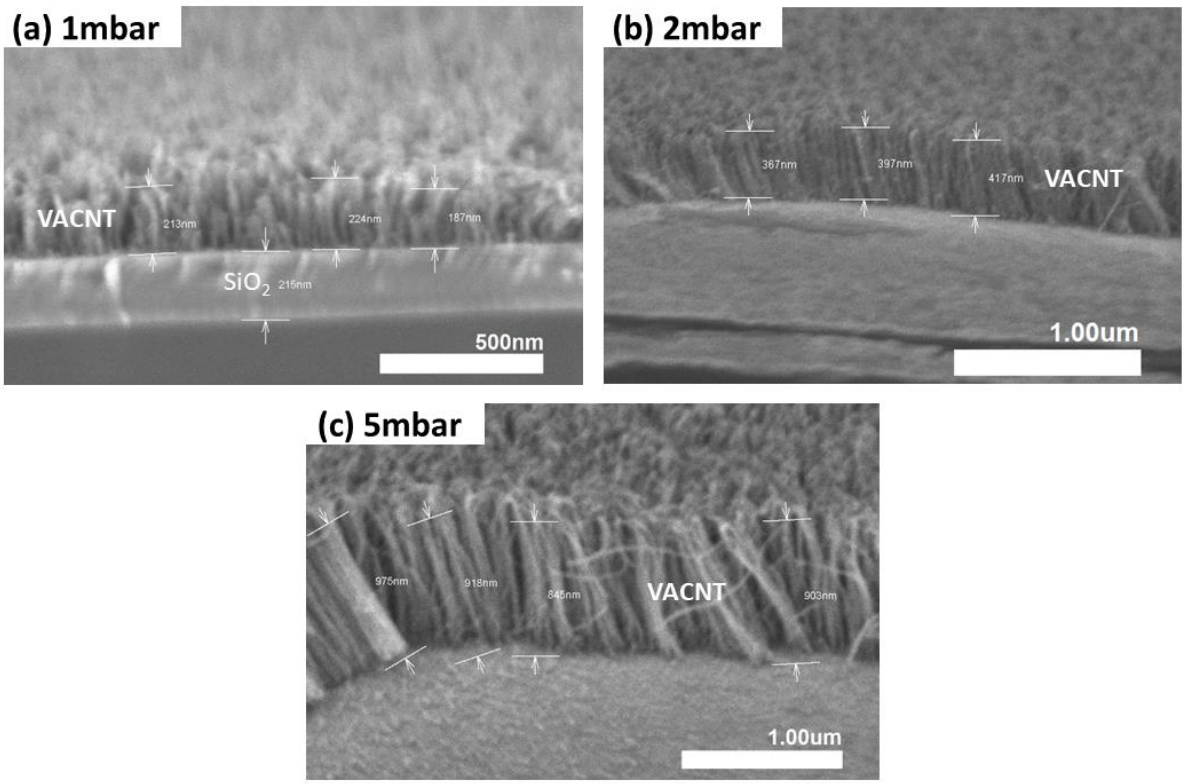

Figure 5.2 SEM Cross-sectional image of the sample grown at different growth pressure: (a)1mbar, (b)2mbar, and (c)5mbar, indicating the vertically aligned carbon nanotubes.

5.1.3. Analysis of Raman spectra

In order to evidence the presence of SWCNTs and the influence of growth pressure on the SWCNTs synthesis process, we have conducted the characterization of the as-grown SWCNTs through Raman spectroscopy measurements. For each sample in this study, we have performed Raman mapping (50µmx50µm with a step of 5 µm)

for two excitation wavelength lasers (532 and 633nm) in a random position over the wafer surface. An average spectrum of 100 spectra from the mappings was analysed using Origin software. Then a qualitative analysis of different carbonaceous phases present in the sample is performed. Finally, the understanding and interpretation of the main observations are given.

- Diameter of SWCNTs

Figure 5.3 presents the detected peaks in the RBM region under the 532nm and 633nm excitation wavelength lasers, recorded from an average spectrum of the mapping. These peaks group located from 100cm^{-1} to 300cm^{-1} corroborate the presence of SWCNTs in all samples. For the sample grown at 0.02mbar, there are 4 peaks (136.6, 163.6, 234.5, and 242.1cm^{-1}) and 2 peaks (175.4 and 190.7 cm^{-1}) obtained when using excitation laser at 532nm and 633nm, respectively. From the relationship $d_t = \frac{248}{\omega_{RBM}}$ [231] relating the diameter d_t of the tube to the RBM frequency and comparing with the Kataura plot [250], we can derive two resonant Raman semiconductor tubes [32] with the diameter d = 1.81nm, d = 1.51nm, and four metallic tubes with the diameter d = 1.06nm, d = 1.02nm, d = 1.30nm and d = 1.41nm. Similarly, we could determine the diameters of the SWCNTs and their electronic properties of the remaining samples through the observed RBM peaks (Table 5.1). The appearance of several RBM peaks at lower wavenumber suggests the formation of large diameter SWCNTs with an increase in growth pressure. Experimentally, the RBM band is resonant in nature and its intensity can be affected not only by the chiral angle of the CNTs, but also by its length, the position of the laser spot, and also eventual tube-tube, tube-substrates interactions [234], [340]. As a general observation, for the sample obtained at higher growth pressure, the width of RBM peaks tends to broaden significantly, which might

be related to the formation of bundles of SWCNTs containing several tubes of comparable diameter, which increases the number of carbons in laser spots [20], [165].

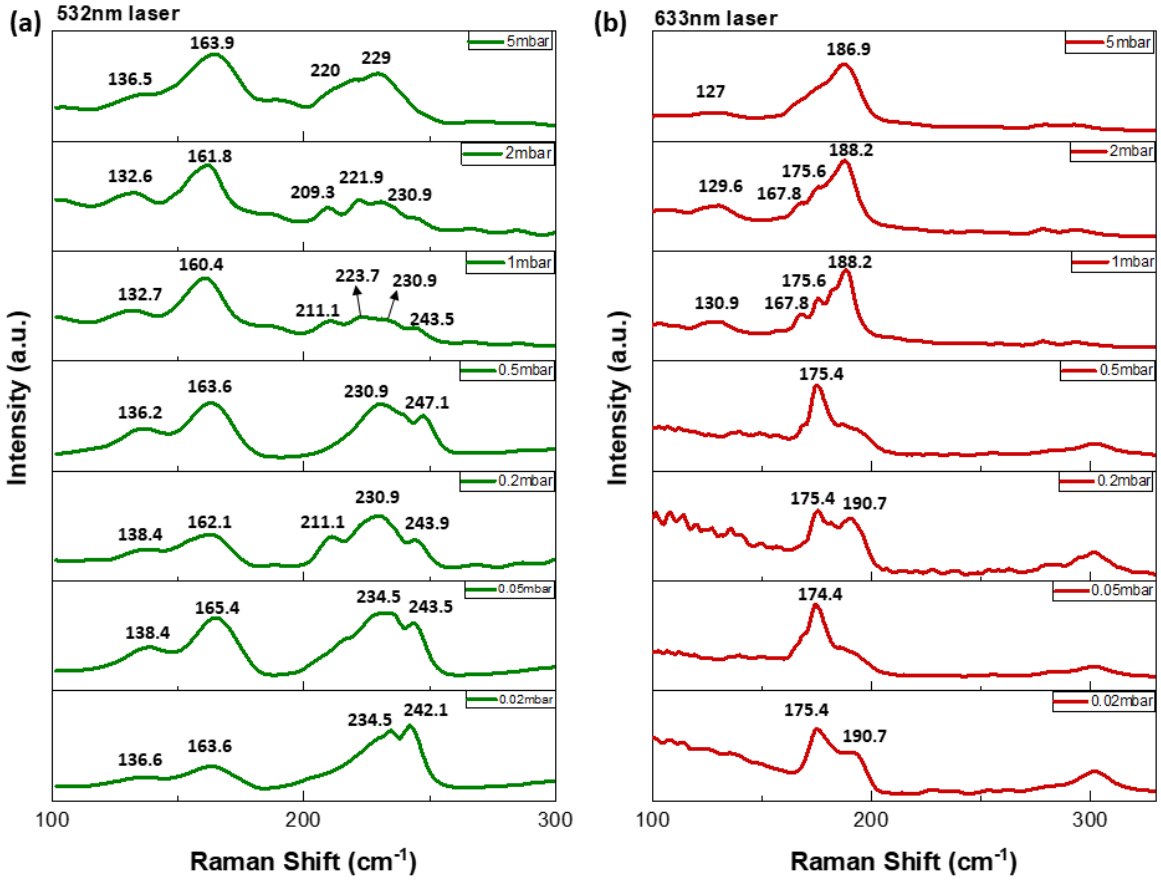

Figure 5.3 An average Raman spectrum of RBM region from 100 points mapping for the samples synthesized at different growth pressure are recorded under the excitation wavelength lasers of: (a) 532nm and (b) 633nm. The peak at 300cm^{-1} is related to Si/SiO_2 substrate.

Table 5.1: Calculated diameter of SWCNTs from the RBM peaks via the relationship $d_t = \frac{248}{\omega_{RBM}}$ *[341]*

Growth pressure	Semiconducting tube diameter	Metallic tube diameter
0.02mbar	Green laser: 1.52nm, 1.82nm Red laser:	Green laser: 1.02nm, 1.06nm Red laser: 1.30nm, 1.41nm
0.05mbar	Green laser: 1.50nm, 1.79nm Red laser:	Green laser: 1.02nm, 1.06nm Red laser: 1.42nm
0.2mbar	Green laser: 1.53nm, 1.79nm Red laser:	Green laser: 1.02nm, 1.07nm, 1.17nm Red laser: 1.30nm, 1.41nm
0.5mbar	Green laser: 1.52nm, 1.82nm Red laser:	Green laser: 1.00nm, 1.07nm Red laser: 1.41nm
1mbar	Green laser: 1.55nm, 1.87nm Red laser: 1.48nm, 1.89nm	Green laser: 1.02nm, 1.07nm, 1.11nm, 1.17nm Red laser: 1.32nm, 1.41nm
2mbar	Green laser: 1.53nm, 1.87nm Red laser: 1.48nm, 1.91nm	Green laser: 1.07nm, 1.12nm, 1.18nm Red laser: 1.31nm, 1.41nm
5mbar	Green laser: 1.51nm, 1.84nm Red laser: 1.95nm	Green laser: 1.08nm, 1.13nm Red laser: 1.33nm

- Qualitative analysis of SWCNTs

The carbon structure of CNTs analyzed by Raman spectroscopy can also be inferred from the different peaks in the high-frequency region (Figure 5.4). The D band, which relates to the defects in the sp^2 carbon structures, is located at around 1350cm^{-1}, while the G band at 1589cm^{-1} corresponds to the carbon sp2 bond vibration in the direction parallel to the nanotube surface[20]. A frequently used approach to infer the quality of the as-grown CNTs is to use the I_G/I_D ratio where I_G and I_D are intensities of the G and D band, respectively[231]. As we can observe from Figure 5.4, the shape

of the G^- peak, the position of D and G bands, and the I_G/I_D ratio have similar trends: (i) an increase of when the pressure ranges from 0.02mbar to 0.5mbar, (ii) a drastically drop down if pressure is in between 0.5mbar and 1mbar; and (iii) an increase when pressure increases from 1mbar to 5mbar, which could be related to the alignment of as-grown SWCNTs mentioned in SEM images. Considering the samples prepared at a pressure range between 0.02mbar and 0.5mbar, there is an observation of a narrow G^+ (FWHM = 28cm^{-1}) peak at around 1590cm^{-1} and a lower intensity G^- peak located at 1567cm^{-1} which appear like a shoulder to the assigned G^+ peak under excitation of 532nm laser. We also noticed a linear downshift of the D position (from 1336cm^{-1} to 1331cm^{-1} and from 1314cm^{-1} to 1312cm^{-1} with 532nm and 633nm excited wavelength lasers, respectively), G band position (from 1590cm^{-1} to 1586cm^{-1} and from 1594cm^{-1} to 1590cm^{-1} with 532nm and 633nm excited wavelength lasers, respectively), and I_G/I_D ratio (from 10.67 to 6.99 and from 6.12 to 3.29 with 532nm and 633nm excited wavelength lasers, respectively) with the decrease of growth pressure. We can recall here that consistent with SEM observations, in this range of growth pressure, the as-grown CNTs are short and located randomly on the substrate, which may promote the detection of the signal from the vibrations along circumferential direction (G^- peak). For the growth pressure of 1mbar, along with the formation of VACNTs, we observed the drop in I_G/I_D ratio from 10.67 at 0.5mbar to 2.9 at 1mbar and 3.65 at 2mbar, the G^- peak tends to merge with G^+ peak to form a broaden G peak (FWHM = 60cm^{-1}) under the excitation of 532nm wavelength laser. There is a similar observation when the sample was rechecked with the 633nm wavelength laser: I_G/I_D ratio drops from 6.12 at 0.5mbar to 2.39 at 1mbar and then increases up to 3.1 at 2mbar. We can hypothesize that a change in the morphology of synthesized-SWCNTs (VACNTs or spaghetti-like CNTs) could significantly impact the I_G/I_D ratio. Moreover, the formation of amorphous carbon due to a superabundance of the gas species [284], [342] at high growth pressure could be a factor that decreases the value of I_G/I_D ratio. The appearance of G^- a peak at the growth pressure of 5mbar could be due to the formation

of a long-filamentous structure on the surface of VACNTs forest, which was observed in Figure 5.1g.

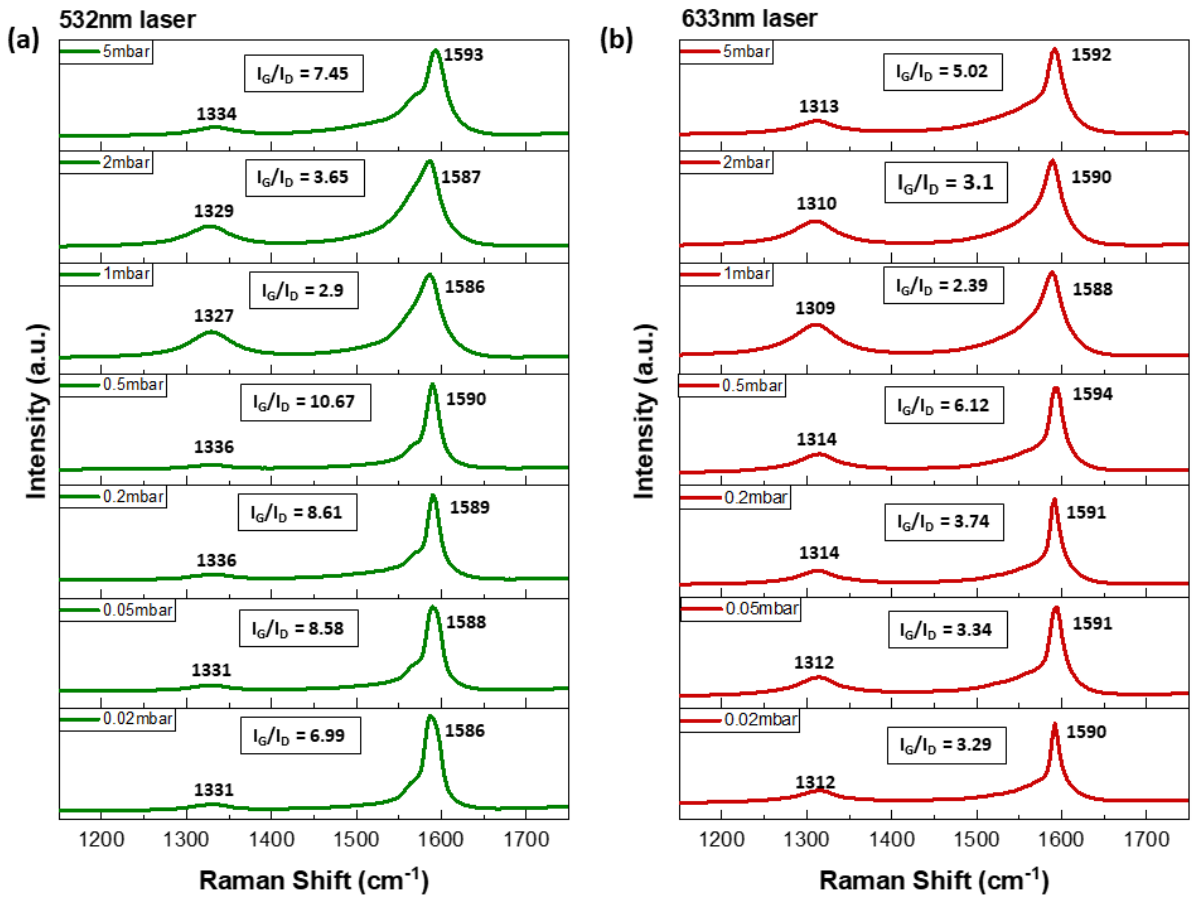

Figure 5.4 An average Raman spectrum in high-frequency region from 100 points mapping of SWCNTs synthesized at various growth pressure. The excited wavelength lasers are 532nm and 633nm corresponding to Figure a and Figure b, respectively.

5.2. Low gas flow regime - fixed CH_4:H_2 = 5:2.5sccm

Different from typical CVD systems (and other HFCVD available at LPICM), the HFCVD-FENIX implements three cascade-mounted turbo-pumps maximizing pumping volume speed and compression ratio (including for light mass gases) which allows us to perform the experiments at extremely low pressures. For a total gas flow of 30sccm as presented in the previous section, we were able to reduce the growth pressure down to 0.02mbar. However, this pressure is still relatively higher than the pressure in the reported in-situ studies with current ETEM (10^{-3} – 10^{-2}mbar)[130]. Therefore, to be able to reproduce the conditions of the in-situ experiments in ETEM-

NanoMAX in the HFCVD-FENIX, we choose to explore a decrease in total gas flow which is expected to help to achieve successful growth at reduced pressure. To ensure sufficient carbon feed the ratio methane/hydrogen has also been modified toward enriched methane content.

5.2.1. Experimental conditions

To ensure uniformity of the experiment, we continued to use samples that have been deposited with 5nm Al_2O_3 and 1nm Fe layers. The gas flows were adjusted to 5sccmH_2 for the pretreatment step and 5sccmCH_4/2.5sccmH_2 for the SWCNTs synthesis. The choice of these values is also based on the conditions of the successfully in-situ experiments and the limitation of limit gas pressure inside l' ETEM-NanoMax. The other CVD parameters were unchanged: the filament power of 900W, the growth temperature of 800°C, the pretreatment time of 2 minutes, and the synthesis time of 30 minutes; the growth pressure was reduced by a step of half a decade until achieved the minimum possible with the current pumping set-up.

5.2.2. Morphological characterization of CNTs

Figure 5.5 shows the top view SEM images of CNTs grown from Fe catalyst at different growth pressures (a)0.005mbar, (b)0.01mbar, (c)0.05mbar, (d)0.1mbar, (e)0.5mbar, (f)1.0mbar, (g)5.0mbar, respectively. Although under these values for gas flow it was possible to reduce the pressure inside the HFCVD up to 10^{-4}mbar, we were not successful in growing CNTs when the pressure is below 0.005mbar (or $5x10^{-3}$mbar). A considerable growth pressure-dependent morphological change and variation of both the density and the length of CNTs are observed throughout the series of SEM images. When the growth pressure is in the range of 0.005mbar to 0.05mbar, the synthesized CNTs exhibit a sparse density, and their apparent (in-plane) lengths vary from 50 to 200nm. The CNTs tend to curl up and to grow in a random position on the substrate. For the synthesis performed at 0.1mbar, we notice, on the whole substrate surface, an increase in length and quantity of CNTs. Moreover, the CNTs appear straighter and easier to image with the SEM. The catalytic particles are also visible. The observed

elongation process continues until apparently achieving a saturation from onset pressure of 0.5mbar, which marks a remarkable increase in density. The increase of the CNT density with the increase of growth pressure has already been observed by several authors[154], [284], [343], [344]. Furthermore, above the onset of growth pressures of 0.5mbar, cross-sectional images acquired from the SEM demonstrate that tubes start to grow mainly as vertically aligned forest with the height of aligned CNTs as a dense nanotube forest varying from 100 nm at 0.5mbar and 200nm at 1mbar to 400nm at 5mbar (Figure 5.6), which is indicative of the high and homogeneous activation of the large majority of catalyst nanoparticles. Most nano-catalyst seeds appear to start the tube germination at the same time and to be able to sustain growth at a significantly similar growth rate. The alignment of nanotubes has been the subject of several studies including that of Xu et al in 2012 [345]. They quantified the alignment of nanotubes by a Herman's orientation factor (HOF) and found an almost linear relationship between the alignment and the density of nanotubes in the forest: the more aligned the tube is, the better the density of the nanotubes forest. Indeed, the less dense the forest is, the more available space there is for the CNTs to undulate. Contrary to the dense forest, the constraints between the neighboring nanotubes force the CNTs to push in the same direction and align themselves, giving a straighter aspect to the whole forest, which may be used to explain the observation of VACNTs from 0.5mbar of growth pressure. At the top of the VACNT forest on the samples grown at 0.5mbar, 1.0mbar and 5.0mbar, the CNTs are very entangled because of the nucleation and the high density of CNTs at the beginning of the growth. It is possible that during the growth time, some of the catalyst may get deactivated creating a local decrease in the density of CNTs compared to the rest of the forest. We could also note that the CNTs appear not individualized with several observed large diameters of bundles.

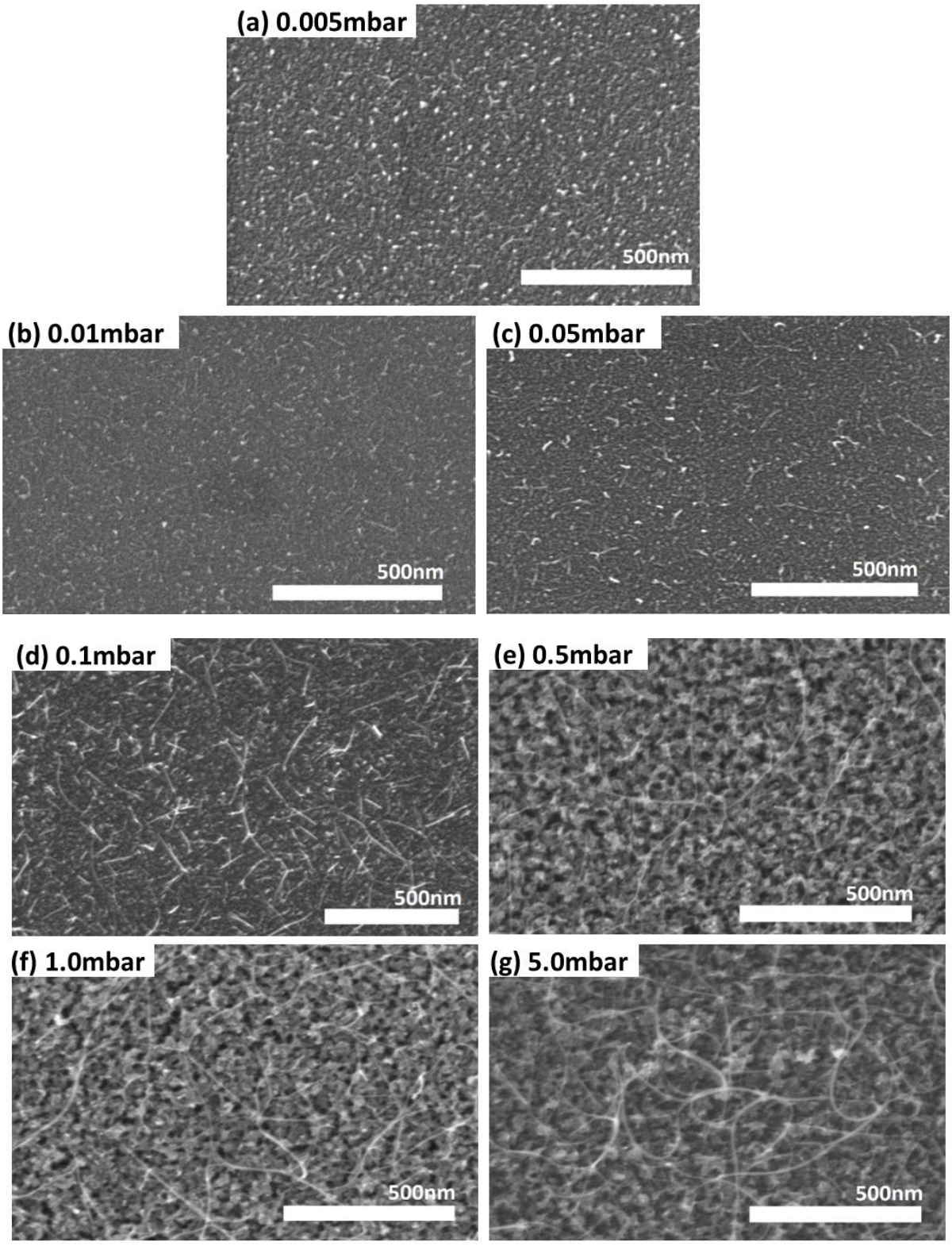

Figure 5.5 Top-view SEM of CNTs grown at various pressures: (a)5×10-3mbar, (b)1×10-2mbar, (c)5×10-2mbar, (d)1×10-1mbar, (e)5×10-1mbar, (f)1mbar and (g)5mbar

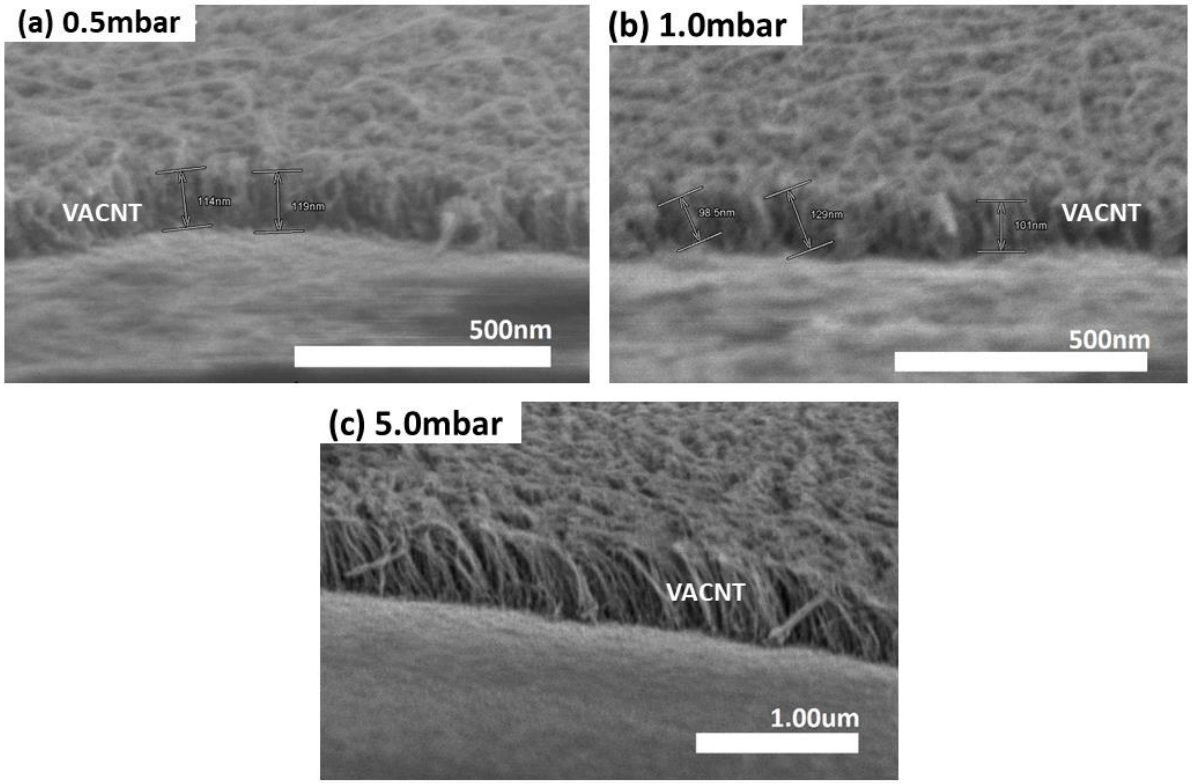

Figure 5.6 Cross-sectional view of SEM image with the formation of CNTs forest through the HFCVD at various growth pressure (a) 5×10-1mbar, (b) 1mbar, and (c) 5mbar. The height of VACNTs is 110, 100, and 400nm, respectively.

5.2.3. Analysis of Raman spectra

To assess the structure and quality of SWCNTs, Raman spectroscopy is one of the most powerful tools [231]. For an overview of nanotube characteristics, numerous mappings were recorded on a 50µmx50µm surface with a step of 5µm for each sample, for a total of 100 collecting points. Through their resonance with each wavelength, two separate excitation wavelengths (532nm and 633nm) are employed to detect the presence of SWCNTs. For each mapping, we simulated an average spectrum from 100 collecting points via the Origin software. All samples displayed two distinct peak groups in the high-frequency domain (D and G band) and respectively the low-frequency domain (radial breathing mode – RBM), which are specific to SWCNTs.

5.2.3.1. Quality of SWCNTs

The region of the two characteristic peaks of graphitic materials, the D and G bands, was monitored in all samples. The D band at 1340cm^{-1} originates from the scattering of local defects or disorders in sp^2-hybridized carbon. Meanwhile, the position and shape of the G band, which correspond to the planar oscillation of carbon atoms (E_{2g} mode) in the graphitic bond, varies depending on the growth pressure.

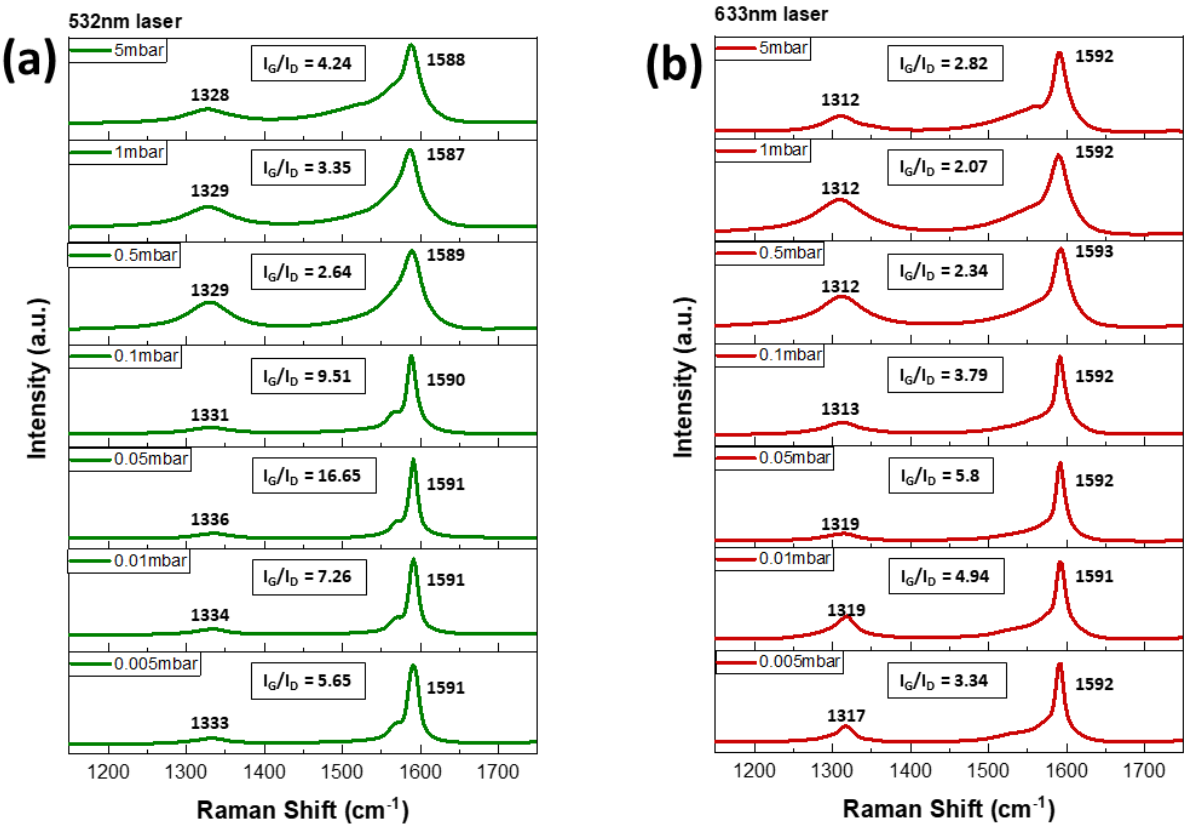

Figure 5.7 The high-frequency region of average spectra from 100 collecting points for the SWCNTs synthesized with Fe catalyst: The excitation wavelengths were (a) 532nm and (b) 633nm.

Under the radiation of 532nm laser, the G peak positioned at the approximate 1590cm^{-1} (Figure 5.7a) appears to broaden when the growth pressure is in the range between 0.5mbar to 5mbar. Toward the lower pressures, the G peak becomes narrower and exhibits increasingly splitting into two major components: G$^-$ with lower intensity at 1568cm^{-1} and G$^+$ at 1590cm^{-1} [231], [346], [347]. Similar observations are obtained when using 633nm excitation laser and have been cross-checked using the values of

full-width half maximum (FWHM) of G peak (Figure 5.8). Indeed, the G peak having the value of FWHM of approximately 11cm^{-1} (533nm laser) or 10cm^{-1} (633nm) is obtained for the samples synthesized in the growth pressure ranging from 0.005mbar to 0.1mbar, which is consistent with the shape of G peak as seen in Figure 5.7. Low values of full width half maximum (FWHM) in the G band are associated with the SWCNTs growth with the improvement of structural quality[348]. When the pressure increases up to 0.5mbar and 1mbar, the G peak appears broadened, consistent with the remarkable increase in FWHM value. At the growth pressure of 5mbar, the FWHM value slightly decreases with the appearance of a G$^-$ peak as a shoulder of G$^+$.

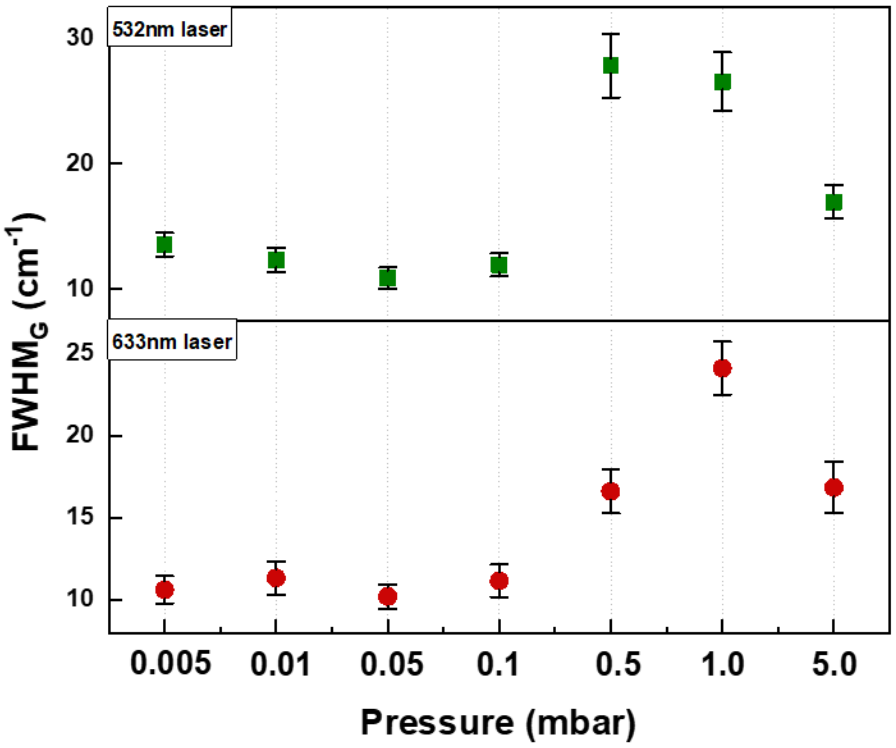

Figure 5.8 The plot of FWHM value of G peak against the growth pressure (mbar). The green- square and red circle are represented to the FWHM value estimated from the 532nm and 633nm excitation laser Raman spectra, respectively, through the curve fitting by Origin software.

The intensity ratio between G and D bands (I_G/I_D) can also be employed to infer on the structural quality of CNTs. The sample grown at a pressure of 0.05mbar exhibit the greatest ratio (I_G/I_D=16.65 with the green laser and I_G/I_D=5.8 with the red laser) (Figure 5.7). The I_G/I_D ratio decreases both above and below 0.05mbar, suggesting the SWCNTs crystalline quality degradation and introduction of a

significant number of defects in the tube's structure. By comparing the Raman spectra and the SEM images, the I_G/I_D ratio of vertically aligned carbon nanotubes appears much lower than that of the spaghetti-like CNTs. When the growth pressure is lower than 0.5mbar, the decrease in I_G/I_D ratio could be caused both by the reduction of the amount of carbon due to a reduction in the number of dissociated carbon feedstock molecules on the catalyst particles, which could result in premature termination of the elongation of CNTs and some supplementary etching by hydrogen gas (that can increase the density of CNTs' wall defects). In contrast, the rapid fall in the I_G/I_D ratio when the pressure exceeds 0.5mbar, may be attributed to: i) formation of some double or MWCNTs that typically exhibits lower I_G/I_D ratio and/or (ii) an excess of carbon supply, which might lead to inactivation of the catalysts, resulting in a reduced quantity of SWCNTs and an increase in the amount of amorphous carbon formed. The results demonstrate the influence of growth pressure on the crystalline quality of the resulting SWCNTs.

5.2.3.2. Diameter distribution

In the low-frequency Raman spectra, numerous peaks can be seen in the range 100 – 300cm^{-1} (Figure B.1, Figure B.2, Figure B.3, Figure B.4, Figure B.5, Figure B.6, Figure B.7 in Appendices & supplemental material). As seen in Table 5.2, the total number of detected peaks in the RBM region varied with the growth pressure (for the same number of mapping points per sample).

Table 5.2 The number of detected SWCNTs by Raman spectroscopy with two different wavelengths

Growth pressure (mbar)	0.005	0.01	0.05	0.01	0.5	1	5
N° of detected peaks in RBM region	398	507	846	1148	1183	1169	1095

In addition to differentiate SWCNTs and MWCNTs, RBM peaks are used also to estimate the diameter of SWCNTs using the relationship formula between frequency

and diameter of CNTs ($d = 248/\omega$ where ω is Raman shift, d is the diameter of tubes)[341] as well as the corresponding chirality of SWCNTs through the famous Kataura's plot[250]. The related statistical study of the diameter of the CNTs is summarized in Figure 5.9, from which one can observe that the increase of the growth pressure shifts the distribution of the SWCNTs diameter. At the growth pressure of 0.005mbar and 0.01mbar, the SWCNTs diameter ranges from 0.8nm to 2.4nm, with the main occurrences in 1.2 – 1.8nm region. When the pressure increases to 0.05mbar, there is a small increase in the population of small diameter (≤1nm) nanotubes with overall evenly distributed diameters from 1.0 to 2.4nm. The number of small diameter nanotubes continues to increase with the increase of growth pressure with a marked trend to become the most populated distribution. A comparison of the RBM peaks and Kataura's plot was also performed for all samples in order to study the influence of growth pressure on the distribution of the electronic properties of SWCNTs. Figure 5.10 summarize the determined percentages of the semiconductor and metallic characteristics within the samples. Based on the Kataura diagram fitted for these samples, we found that for excitation at 633 nm, SWNTs less than ~1 nm in diameter, thus with an RBM of more than ~240 cm^{-1}, are semiconducting and those possessing a diameter larger than 1 nm are predominantly metallic. According to the combined results from both excitation lasers, the number of semiconducting CNTs occurrences seems to be the majority, with the exception of the sample synthesized at 1mbar, where the number of metallic SWCNTs occurrences increases significantly and tends to be the observed majority.

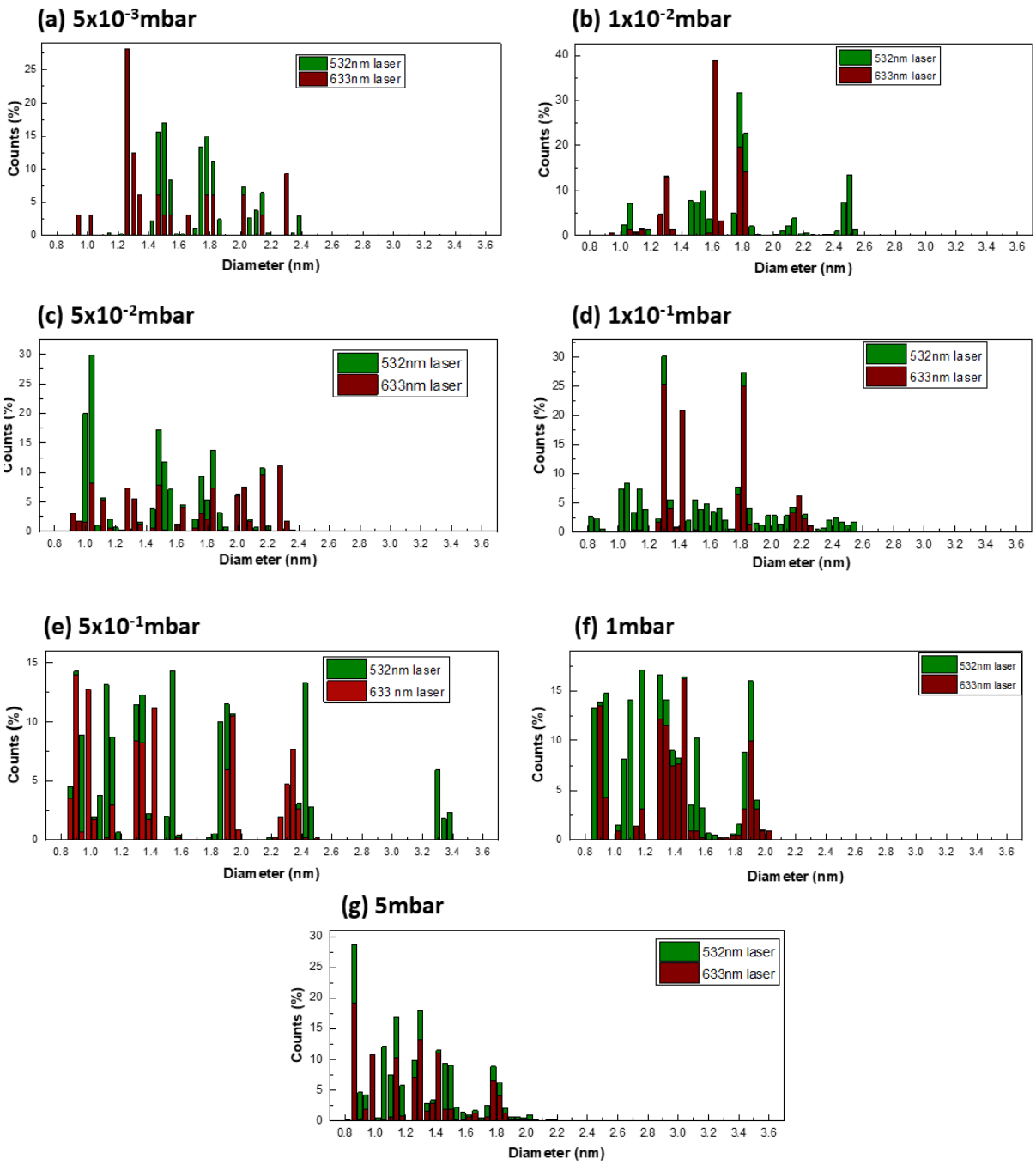

Figure 5.9 (a) – (g) Diameter distribution of SWCNTs from Raman spectra at 532nm and 633 wavelength excitations and (h) the total number of detected SWCNTs according to various growth pressures

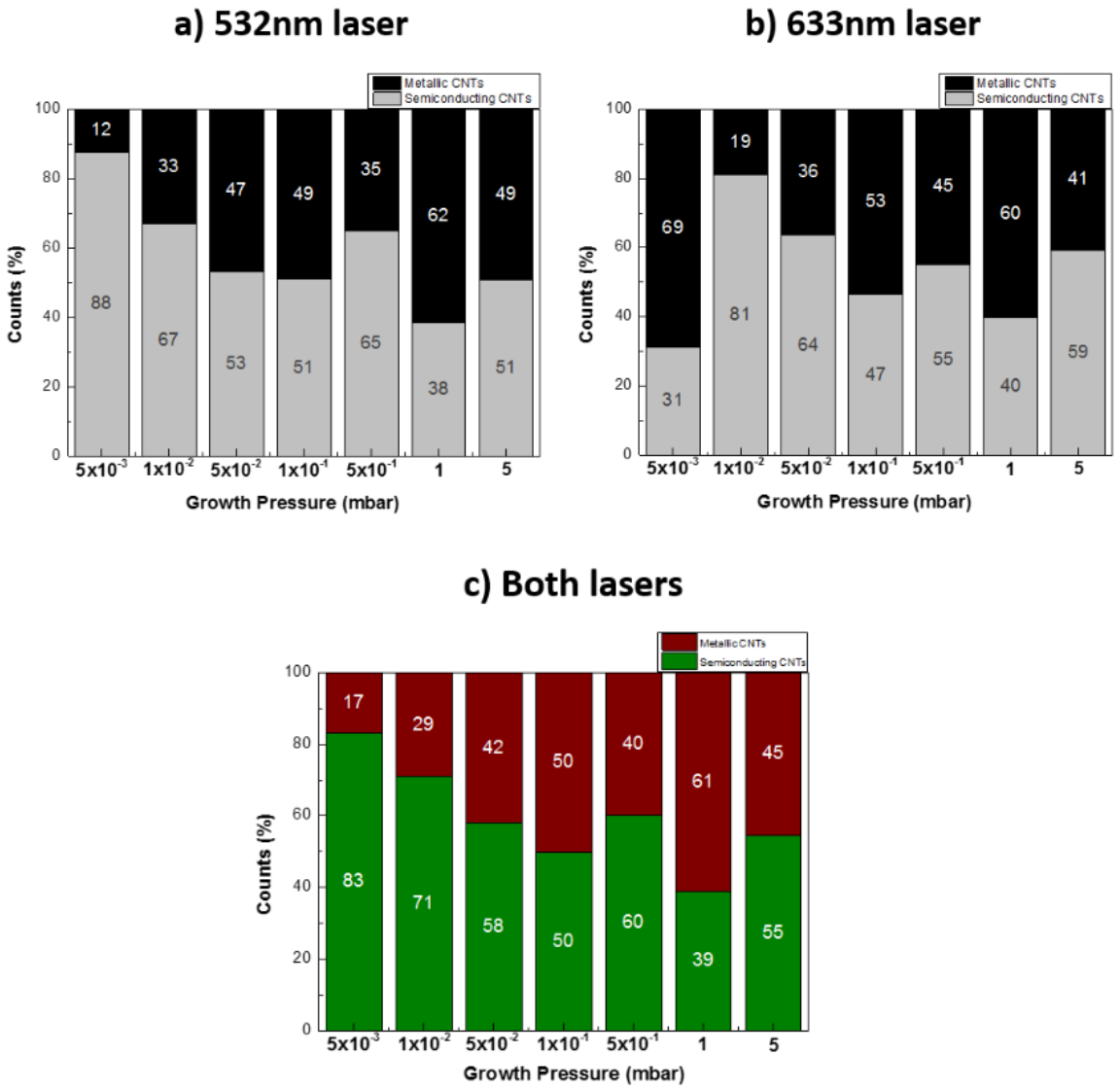

Figure 5.10 Determination metallic and semiconducting SWCNTs ratio by using Kataura plot: (a) green excitation laser, (b) red excitation laser, (c) combination results of two lasers

5.3. Discussion and Conclusion

We have observed that from a certain pressure point, the SWCNTs start to form in the vertical alignment. However, in this growth pressure range this is also accompanied by some degradation of the structural quality of SWCNTs which has been observed through the change in I_G/I_D ratio and G band shape in the RAMAN analysis. We presented here the work carried out at the beginning of this thesis and that has allowed us to parametrize a low-pressure hot filament-assisted CVD synthesis system and to determine the impact of growth pressure on growth of SWCNTs. The

samples were prepared using a molecular beam evaporated 1nm iron catalyst layer on top of 5nm Alumina buffer layer. The parametric studies carried out on our HFCVD system and presented in this chapter have allowed us to highlight the presence of at least one optimal SWCNTs growth regimes. When a total gas flow is 30sccm with CH_4:H_2 ratio of 1:2, our HFCVD allowed us to successfully synthesize the SWCNTs at the temperature of 800°C and the growth pressures from mbar range to as low as 0.02 mbar. We have also demonstrated that it is possible to reduce the growth pressure to 10^{-3}mbar by modifying the gas flow (5sccmCH_4 and 2.5sccm H_2). This limitation in growth pressure depending on the gas flow could be considered as a threshold below which the SWCNTs growth is completely inhibited. The morphology, quantity, and quality of SWCNTs could be modified by adjusting the growth pressure. At high gas flow regime, the presence of larger diameter SWCNTs due to the increase of growth pressure could be due to the increase of the average size of catalytic nanoparticles by coalescence and/or Ostwald ripening but at the same time the desorption of co-products of catalytic decomposition of methane would be cross-linked in the gas phase and deposited in the form of an amorphous carbon layer. When using the low gas flow regime, the decrease in the growth pressure does not appear to promote the growth of increased number of nanotubes in a significant way. The lower proportion of small diameter nanotubes in the low-pressure range is probably not related to the non-activation of small NPs. It seems that small catalyst nanoparticles are more sensitive to the nucleation limitation at 800°C where nucleation occurs at a higher pressure in the case of small diameter. These results thus support the hypothesis of competition between Ostwald ripening and nanotube growth [349].

6. Study of key parameter – growth temperature on the SWCNTs growth

There have been various efforts in the literature to investigate the influence of the growth temperature on the characteristics of CNTs, such as diameter, chirality, areal density, etc, which are the premise for the selective and controlled synthesis of CNTs. There are currently several conflicting research reports on the effect of temperature on the properties of CNTs when using CH_4 in CVD, particularly depending on the nature of the catalyst being used. Y.Zhang and co-workers [350] reported that when temperature increases, the diameter of CNTs increases, and observed a structural transition from SWCNTs to MWCNTs when using nickel as a catalyst. The dependence of the final product structure on the growth temperature was also observed in the publications of Song et al [153], in which the MWCNTs were favored to grow at low pressure on the Fe-Mo/Al_2O_3 catalyst, and Simon et al [351] who reported that with catalyst Pd on porous ceramic Al_2O_3 substrate, at high temperature, the formation of carbon nanofibers is eventually replaced by carbon nanotubes. The high temperature regime has been reported to induce not only removal of the impurities of CNTs during the annealing process [352] but also to help to increase the crystallinity of CNTs [353]. However, the literature reports several opposing observations about the impact of temperature. In term of diameter, Makris et al were successful in the synthesis of thinner and longer SWCNTs at high temperatures (800°C) with the use of Ni catalyst [88]. The high temperature also could lead to the encapsulation of catalyst nanoparticles [354], [355] caused by the formation of amorphous carbon [354]–[356]. Bouanis et al also mentioned the influence of growth temperature on the diameter distribution of as-grown SWCNTs when using Ru as catalyst precursors coupled with atomic hydrogen treatment [361]. They obtained the narrow distribution of SWCNTs diameter at 850°C with 90% of semiconducting-SWCNTs. The distribution of diameter became broader, the diameter of as-grown SWCNTs increased and the percentage of semiconducting-SWCNTs decreased when

they continued to increase the growth temperature up to 900°C and 950°C. There is the same trend of the influence of growth temperature in the publication of Salome et al in 2019 when they studied the properties of SWCNTs synthesized from three bimetallic catalyst systems (FeRu, CoRu and NiRu) [198]. At the low temperature (700°C for FeRu and CoRu, 800°C for NiRu), more than 65% of counted as-grown SWCNTs have diameter below 1.3nm. When the temperature increased up to 1000°C, the percentage of small diameters below 1.3nm decreased down to 23%, while the diameter above 1.6nm presented more than 40%.

6.1. Influence of growth temperature at standard pressure

6.1.1. Condition of the experiment

Although the temperature is known as the key parameter for the synthesis of SWCNTs, this parameter has not been previously optimized for the SWCNTs growth in our homemade CVD reactor (FENIX) particularly in the low pressure range. Most recent studies have demonstrated the successful SWCNTs growth with standard growth pressure ranging from a few mbar to hundreds of mbar [341], [358]–[360]. We have initiated the study of the effect of substrate temperature at standard growth pressure to ensure the synthesis of SWCNTs. Thus, the growths were performed at the following temperature: 500, 600, 700, 800, and 900°C; other growth conditions were given in Table 6-1. The support (Al_2O_3) and catalyst (Fe) film thicknesses were chosen 5nm and 1nm, respectively. All samples were kept under vacuum conditions until their use, in order to protect the surface from contamination and deep oxidation. Prior to starting the CNT growth experiments, the CVD system was pumped down to 10^{-8}mbar vacuum range. After reaching a sufficiently low vacuum, the sample and filament heating were turned on. Once the desired temperature was achieved, H_2 gas was fed into the reactor at 30sccm flow rate for 2 minutes to perform the pretreatment process, which included the annealing and dewetting of the catalytic film to form the nanoparticles. Then the growth mixture of gas (20sccmCH_4/10sccmH_2) was injected into the reactor to perform the growth of CNTs for 30 minutes at constant growth

pressure. The gaseous flow was turned off and the samples were allowed to cool down to room temperature after the termination of the growth by the abrupt pressure drop to ultra-high vacuum. To ensure the reproducibility value of the study, the synthesis of SWCNTs was systematically carried out simultaneously on four individual samples for each of the synthesis temperatures, and this process was repeated a minimum of three times.

Table 6.1 Growth conditions of CNTs grown on Fe catalyst

Sample name	T (°C)	CH_4 : H_2 (sccm)	P (mbar)	Times (mins)	Catalyst film thickness (nm)
Fe0.1	900	20:10	5	30	1
Fe0.2	800	20:10	5	30	1
Fe0.3	700	20:10	5	30	1
Fe0.4	600	20:10	5	30	1
Fe0.5	500	20:10	5	30	1
Fe1.1	900	20:10	2	30	1
Fe1.2	800	20:10	2	30	1
Fe1.3	700	20:10	2	30	1
Fe1.4	600	20:10	2	30	1
Fe1.5	500	20:10	2	30	1

6.1.2. Morphological structure

Figure 6.1 shows a series of top-view SEM images of the growth of CNTs recorded for each temperature at fixed growth pressure of 5mbar. It is expected that the temperature impacts the reactivity of the catalyst in the nanoparticle formation, which in turn influences the SWCNTs growth. We can observe that at a pressure of 5mbar, the formation of nanoparticles is visible, but the growth does not occur as shown in Figure 6.1a where the synthesis was performed at 500°C. Starting from 600°C, the temperature is sufficient to allow the absorption and diffusion of carbon atoms on the surface of the catalyst particle and to trigger the growth of CNTs (Figure 6.1b).

From the top-view SEM images, we can notice a disordered growth of CNT, without particular growth orientation, the nanotubes are entangled. When the temperature continues to increase up to 900°C, there is a significant increase in density of the as-grown CNTs.

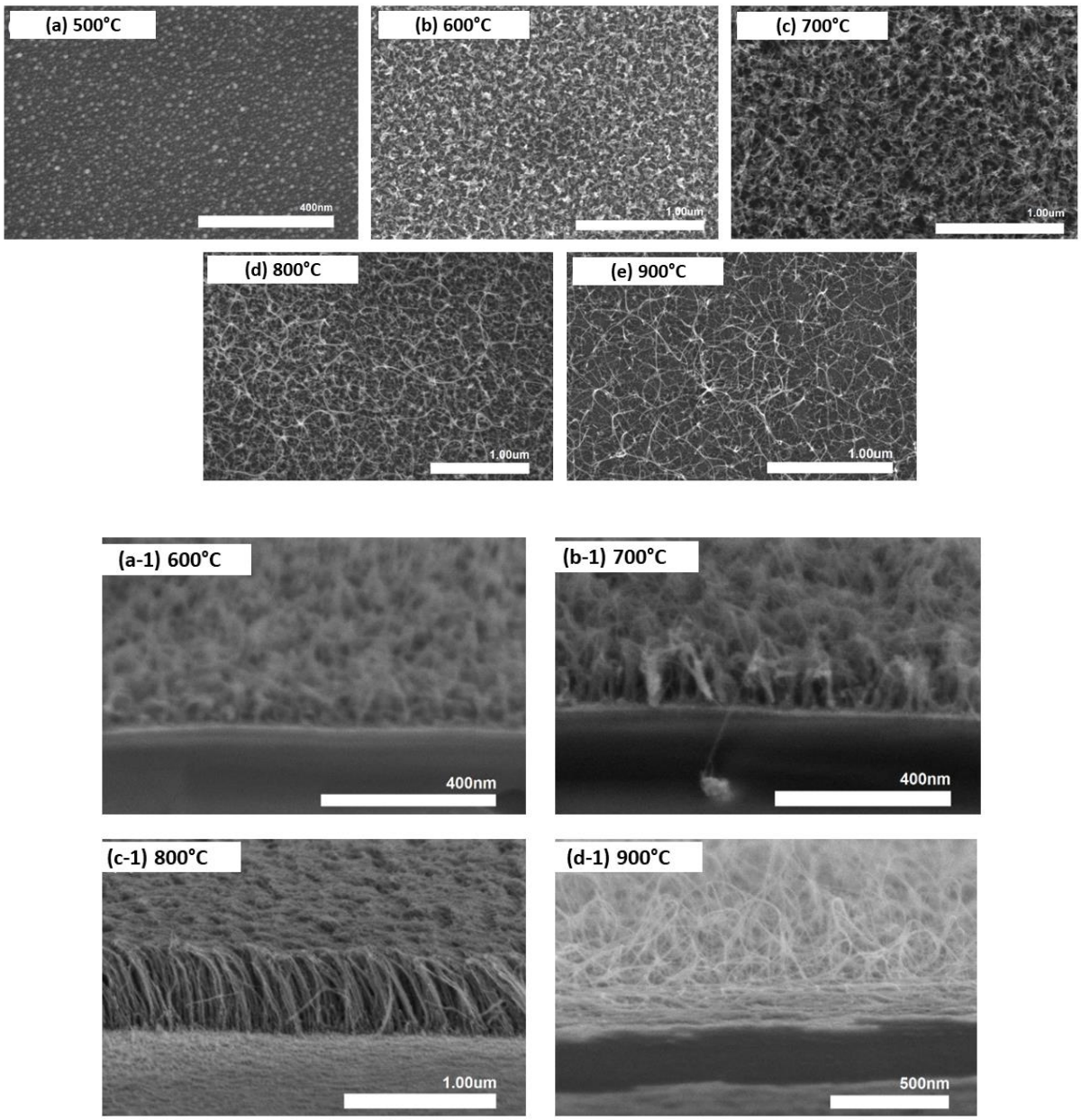

Figure 6.1 The top view SEM image of CNTs grown at 5mbar with different conditions: (a) 500°C, (b) 600°C, (c) 700°C, (d) 800°C and (e) 900°C, respectively. The cross-sectional SEM images were recorded to determine the orientation of as-grown CNTs at the temperature of: (a-1) 600°C, (b-1) 700°C, (c-1) 800°C, and (d-1) 900°C.

As we found on the previous study of growth pressure on the SWCNTs synthesis, 2mbar of growth pressure is expected to obtain the high productivity of high-quality

SWCNTs. Therefore, we also performed a series of experiment with 2mbar of growth pressure. When the synthesis pressure was reduced to 2mbar, we were able to successfully synthesize CNTs starting with a lower temperature onset i.e. at 500°C (Figure 6.2a), there is no CNTs below 500°C. We can hypothesize at this point that when pressure is reduced, the carbon supply rate becomes low enough, so that the slow carbon diffusion at 500°C does not lead to poisoning of the catalyst surface which would impede carbon nanotube formation. We precise that for experiments performed at a temperature below 500°C, we did not obtain any formation of CNTs. For the growth temperature range of 600°C to 900°C, the morphological change in as-grown CNTs appear similar to the series of observations from CNTs synthesized at 5mbar.

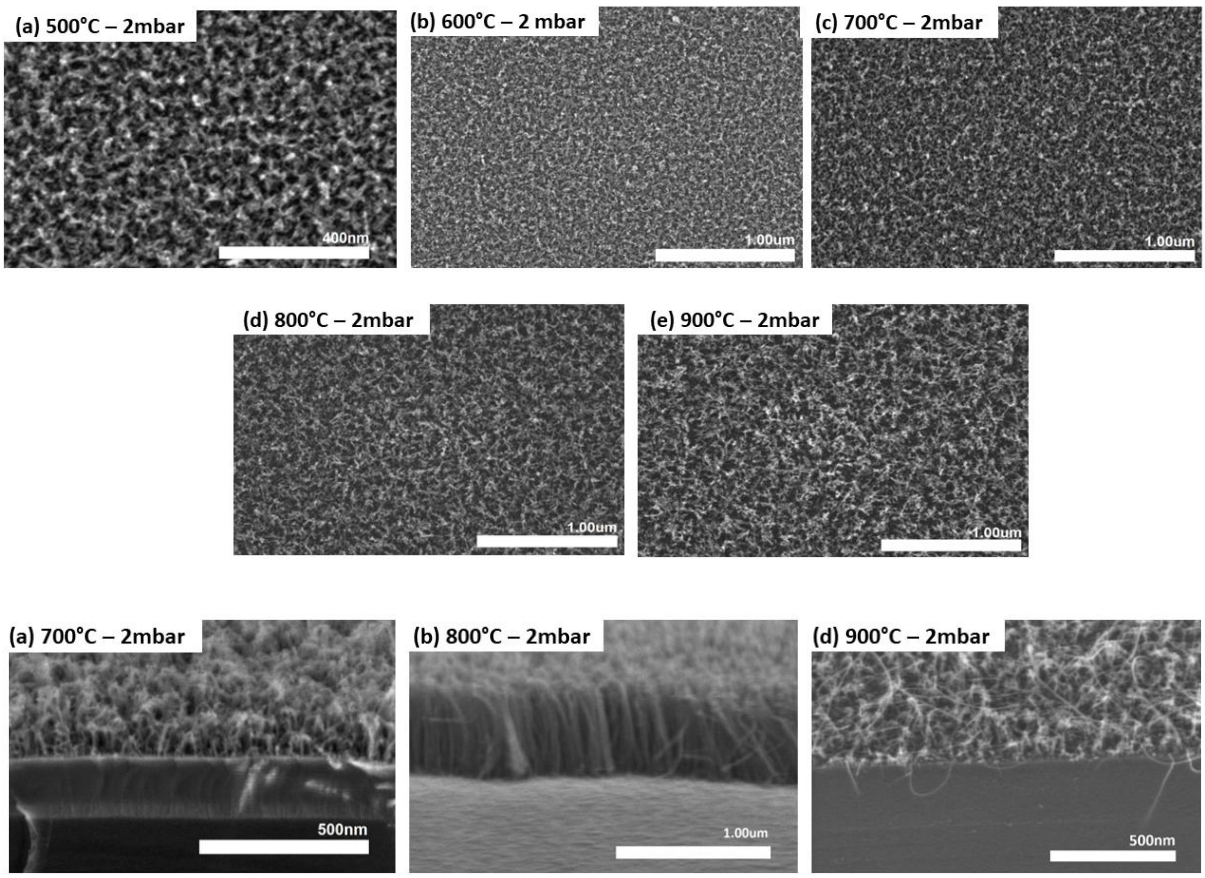

Figure 6.2 The top view SEM image of CNTs grown at 2 mbar with different conditions: (a) 500°C, (b) 600°C, (c) 700°C, (d) 800°C and (e) 900°C, respectively. The cross-sectional SEM images were recorded to determine the orientation of as-grown CNTs at the temperature of: (a-1) 700°C, (b-1) 800°C, and (c-1) 900°C.

For both 2 and 5 mbar growth pressures, an intriguing phenomenon is observed at 700°C and 800°C. At 700°C, CNTs growth begins to be influenced by the on-growing

neighboring CNTs, thereby tending to grow perpendicular to the substrate surface (Figure 6.1(b-1) and Figure 6.2(a-1)). Around 800°C, the CNTs clearly grow vertically and perpendicularly to the substrate (Figure 6.1(c-1) and Figure 6.2(b-1)) to form forest of aligned CNTs. This growth dynamics can be attributed to the homogeneous nucleation on the majority of the catalyst nanoparticles in precisely the same time during the initial stage and followed by significantly same homogenous CNTs growth rate. We can also note that some long non-aligned filamentous structure appears sparsely on top of CNTs. Their formation could be related with several hypothesis: (i) there are some nanoparticles that are able to nucleate easier/faster and probably have higher subsequent CNTs' growth rate, (ii) they lead to fast and longer growing CNTs that are not aligned, and (iii) these CNTs surpass the height of surrounding CNTs forest that have grown at a steadier rate. When the synthesis temperature was raised to 900°C, the quality of as-grown CNTs on the substrate appears to undergo some degradation when compared to those grown at 800°C (Figure 6.1e and Figure 6.2(c-1)): the vertically aligned growth mode no longer occurs, and rather long entangled CNTs were synthesized randomly on the substrate. Several factors may explain these observations. Indeed, if we refer to the conventional thermal CVD, the higher the growth temperature also the dissociation rate of the injected gas gets higher. In our case, the precursor gases are pre-dissociated via hot-filaments and thus one expects drastically reduction of the influence of furnace temperature (typically more than two times lower that the hot filaments temperature) on the gas dissociation rate. On the other hand, when the synthesis temperature exceeds 800°C, although the availability of reactive carbon in the reactor is little changed, the absorption and the carbon diffusion on the catalyst nanoparticles could be enhanced whilst the size of catalyst particles can also undergo significant change. If under this condition too much carbon is available during the growth it can either poison the catalyst particles, limiting or even preventing the growth of CNTs, or in certain conditions can lead to the formation of thick MWCNTs or even carbon nanofibers. This result has also been reported in a number of works, including that of Li et al.[361], who reported that in their CVD

synthesis, the yield of CNTs obtained was continuously reduced from > 800°C until reaching 1050 °C, the maximum temperature tested. Furthermore, an increase in the metal surface diffusion with the increase of temperature could enhance Ostwald ripening, leading to the formation of larger nanoparticles, more inhomogeneous diameter distribution, and consequently inhomogeneous CNTs growth conditions [286]–[288], [290].

6.1.3. Raman spectroscopy

Furthermore, Raman analysis (see also Chapter 2) was performed on the samples synthesized at the growth pressure of 5mbar and temperature of 500°C, 600°C,700°C, 800°C, and 900°C to analyze the quality of as-grown SWCNTs. Overall, all spectra show the two expected Raman regions at high-frequency region (~1335cm^{-1} – D band and ~1580cm^{-1} – G band) and respectively at low frequency (100-300cm^{-1} – RBM) characteristic for SWCNTs.

- High-frequency region

An example of D band and G band detected with 532nm excitation wavelength laser is presented in Figure 6.3a. 100 values of I_G/I_D ratio from mapping was calculated, and then simulated the average and plotted as a function of growth temperature (Figure 6.3b). When using 532nm excitation laser, the ratio was achieved at 1.46 for the sample grown at 600°C, and then with the increase in growth temperature, this ratio increased to 7.46 at 700°C, 7.45 at 800°C, and 21.41 at 900°C. The value of full width at half maximum (FWHM) of an average D band calculated from 100 points mapping Raman, as determined by Gaussian fits, is dependent on the growth temperature as shown in Figure 6.3c. The FWHM of the D band at the growth temperature of 600°C is 59.5. When the growth temperature increases the D band becomes narrower with the decrease in the value of FWHM, 36.9 at 700°C, 30.8 at 800°C and 24.5 at 900°C. We also observed the same trend when examining samples with a red laser excitation (633 nm wavelength). The FWHM of the D band is a measure of the spread of frequencies in the Raman signal, and a narrower FWHM

generally implies a more well-defined and less disordered carbon structure. In contrast, a broader FWHM is typically indicative of a higher degree of disorder or a more diverse range of defects. These observations suggest that when the temperature increases, the number of incorporated defect types decreases. This is consistent with the observation of Vinten et al [248] and Kwok et al [362].

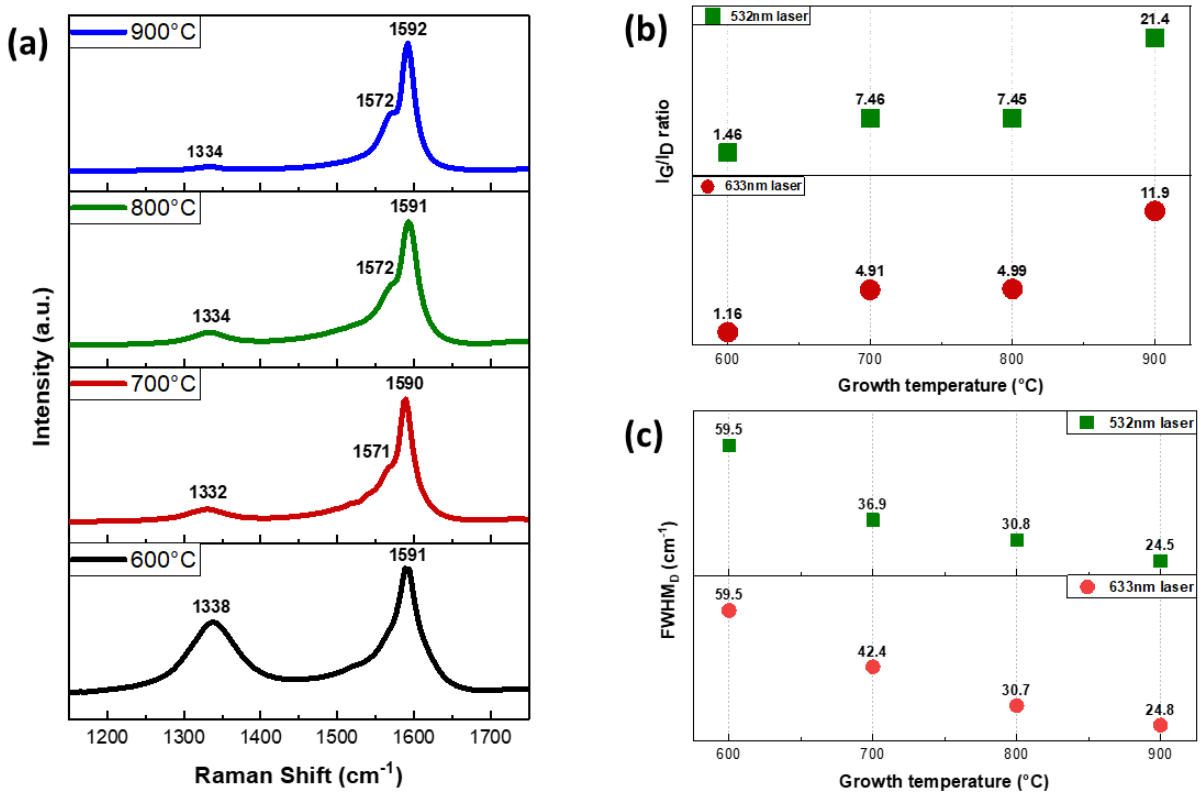

Figure 6.3 Raman spectra of the CNTs samples: (a) the average spectra of 100 points mapping - D band and G band of CNTs synthesized in the range of growth temperature from 600°C to 900°C in step of 100°C. The laser was excited at 532nm of wavelength. The plot of (b) I_G/I_D ratio and (c) FHWM of D band against temperature. The data was recorded under the excitation of 532 and 633nm wavelengths lasers.

The evolution of SWCNTs diameter

Confirming the presence of SWCNTs for all four growth temperatures, the peaks observed in RBM range from 100 to 300cm^{-1} in Figure 6.4 shows the evolution of RBM peaks as a function of the synthesis temperature for a constant growth pressure of 5mbar. The RBM peaks are distributed between 126 cm^{-1} and 284 cm^{-1}, indicating that the diameter of SWCNTs is distributed between 0.87 and 1.96nm. We can notice a general trend of a downshift of RBM peaks with the increasing temperature, which

indicates the formation of a larger diameter of SWCNTs. Indeed, it can be seen that at 600°C, the proportion of medium diameter SWCNTs (zone 2 in Figure 6.4) are in the vast majority. Between 700°C and 800°C, the diameter distribution seems similar, which the majority is small diameter SWCNTs (zone 2 and zone 3 in Figure 6.4). When the temperature continues to increase from 800°C to 900°C, the number of large diameters becomes more important and as the temperature increases, the proportion of small and medium diameters decreases. At 900°C, no peak is recorded in zones 3 suggesting that large diameter nanotubes are in majority.

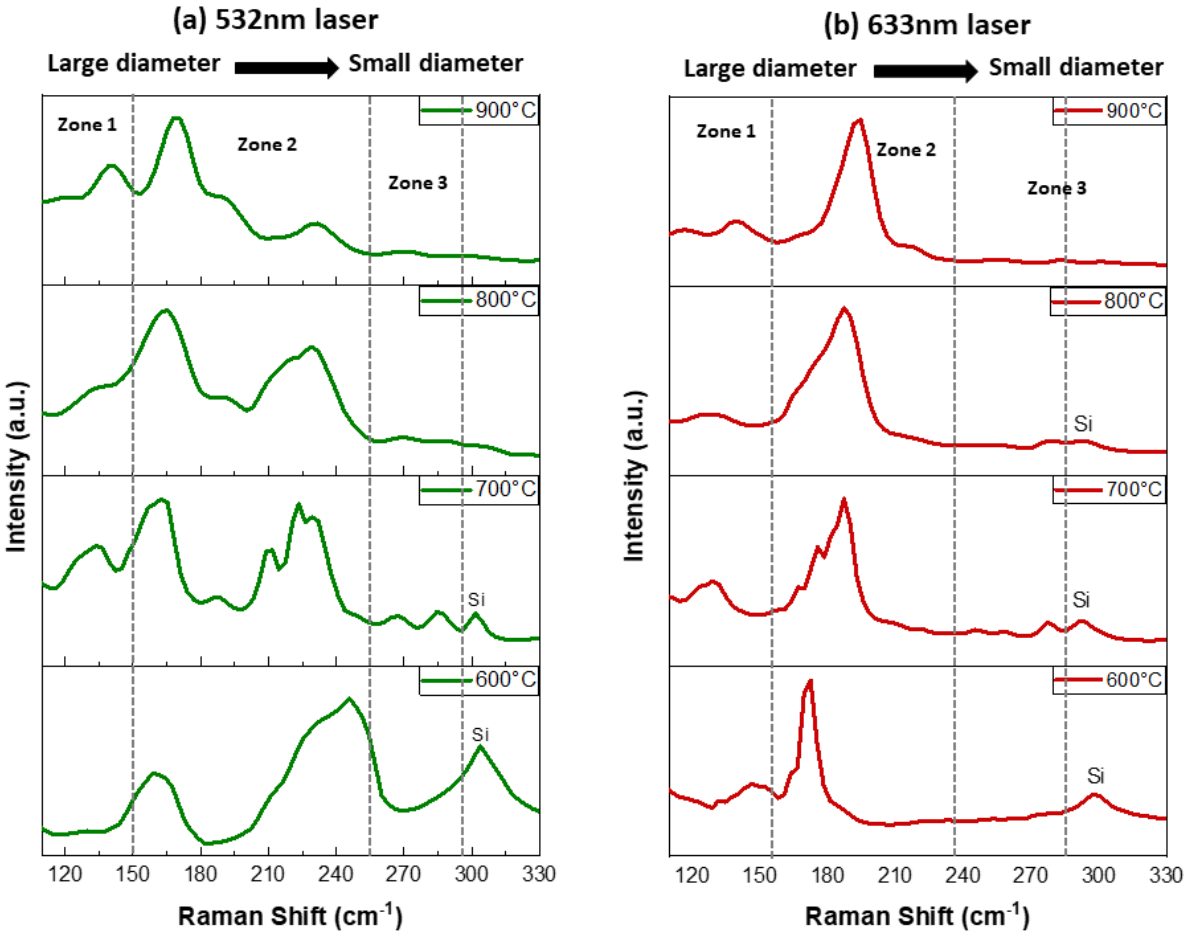

Figure 6.4 An average RBM - Raman spectra of 100point mapping for the samples synthesized at different temperature and at 5mbar. The excitation wavelength laser is: (a) 532nm and (b) 633nm

Three regimes are thus highlighted here: i) at low temperature (T = 600°C), we notice an increases of the proportion of small diameters. ii) at medium temperature (700°C ≤ T ≤ 800°C), the diameter distribution is stable and wide (from 0.87nm to

1.8nm); iii) at high temperature (T = 900°C), the thermal energy input leads to a net decrease in the proportion of small diameter nanotubes. This result is in agreement with the observation from SEM and TEM (see next paragraph). The higher growth temperature could induce pronounced agglomeration of catalyst particles and leads to an increase their size, resulting in large diameter SWCNTs. While the crystalline quality of CNTs appears maximized at 900°C, the alignment of the CNT starts to be lost. This indicates that, at this growth temperature, the formation of nanoparticles was not homogenous in regard of their resulting size, and at the same time, the high hydrocarbon precursor concentration favored encapsulation of a fraction of iron nanoparticles, thus incapacitating their catalyst properties. There is therefore a trade-off between structural quality and the alignment of CNTs by choosing a growth temperature between 700 and 800°C for our CVD system when synthesized at medium-high pressure.

6.1.4. Characterization of as-synthesized SWCNTs by ex-situ TEM

As mentioned in chapter 4 (section 4.2.5), the transferring of as-grown CNTs from Si/SiO_2 substrate to TEM grid carries a lot of risk in destroying some of the structural properties of CNTs. Based on that, to further clarify the tube structure, we decided to perform parallel experiments with the gold TEM support grids (300 mesh) used as the substrate. In order to have comparable results, the evaporation of the Al_2O_3/catalyst layers and the subsequent CNTs growth were performed in the same time as the conventional samples of Si/SiO_2 substrate, so we can reasonably expect that the nucleation and the growth conditions will be significantly the same for the both cases. The structure of the as-grown SWCNTs were analyzed by HR-TEM.

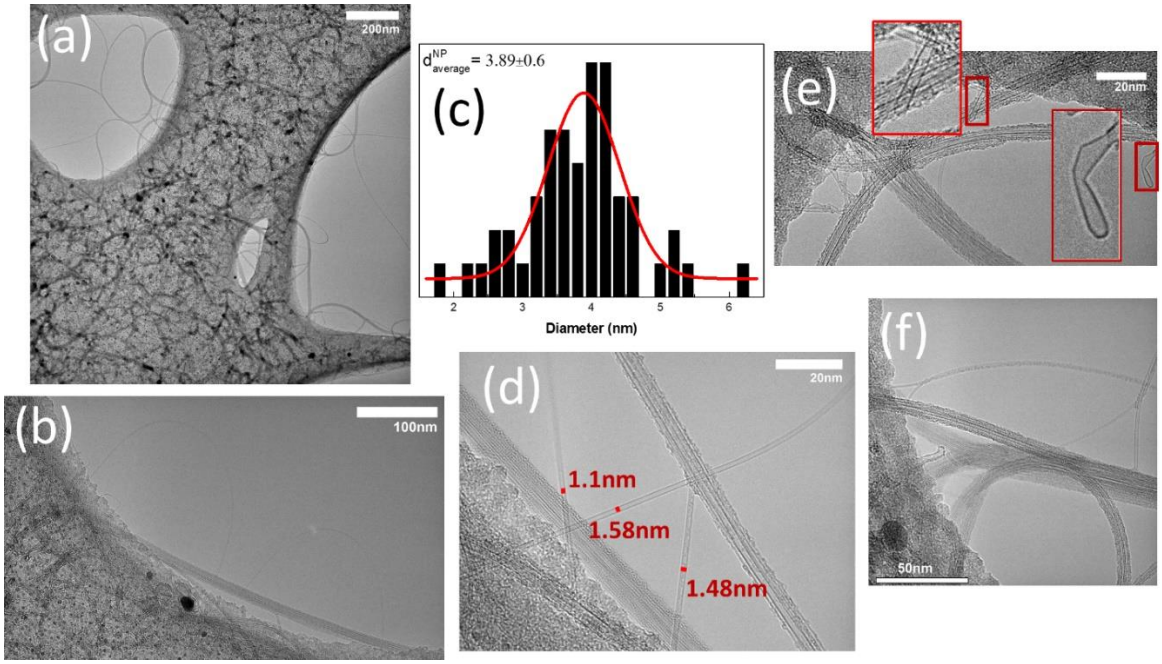

Figure 6.5 TEM micrographs of SWCNT growth using a 1nmFe/5nmAl_2O_3/carbon support sample that underwent pretreatment under radical hydrogen (30sccm) for 5mins. The growth parameters are CH_4:H_2 = 20:10, 5mbar, for a 30 min of growth time.

Figure 6.5 shows the several TEM-images of CNTs obtained for sample Fe0.2 in Table 6-1 at growth pressure of 5mbar at 800°C. Long-dense CNTs were observed in the low magnification images in Figure 6.5a and Figure 6.5b. A detailed analysis of the recorded images evidences a mixture of tubes that can be isolated or bundled, curved or straight, and can grow in any direction. The organization of SWCNTs into bundles of up to several tens of nanotubes is due to the Van der Waals forces between the nanotubes and/or the same growing speed of SWCNTs from the Fe nanoparticles which are very close. As expected from the results obtained on the SiO_2/Si sample, the density of the CNTs situated on a membrane support is very high, which makes difficult their analyses in terms of diameter and number of walls. Some individual SWCNTs, could be observed outside the membrane, for which their diameters seem to vary from 1nm to 2.5nm. Concerning the catalyst particles which are visible on the membrane their analysis is difficult to performed in order to determine their exact position relative to the SWCNTs. It appears that not all the particles have resulted in the formation of carbon nanotubes. The average size of the catalytic nanoparticles observed is of the order of 3.9nm (Figure 6.5c), which is much larger than the diameter

of the formed tubes. Some of the nanotubes' tips, free of catalyst nanoparticles, could be observed outside the membrane, suggesting a base-growth model of SWCNTs (Figure 6.5e). We could also observe a significant amount of amorphous carbons attached to the wall of SWCNTs, which could be caused by the sample preparations, the contamination during the synthesis, or the degradation of SWCNTs by the slow absorption of molecules present in the air [363].

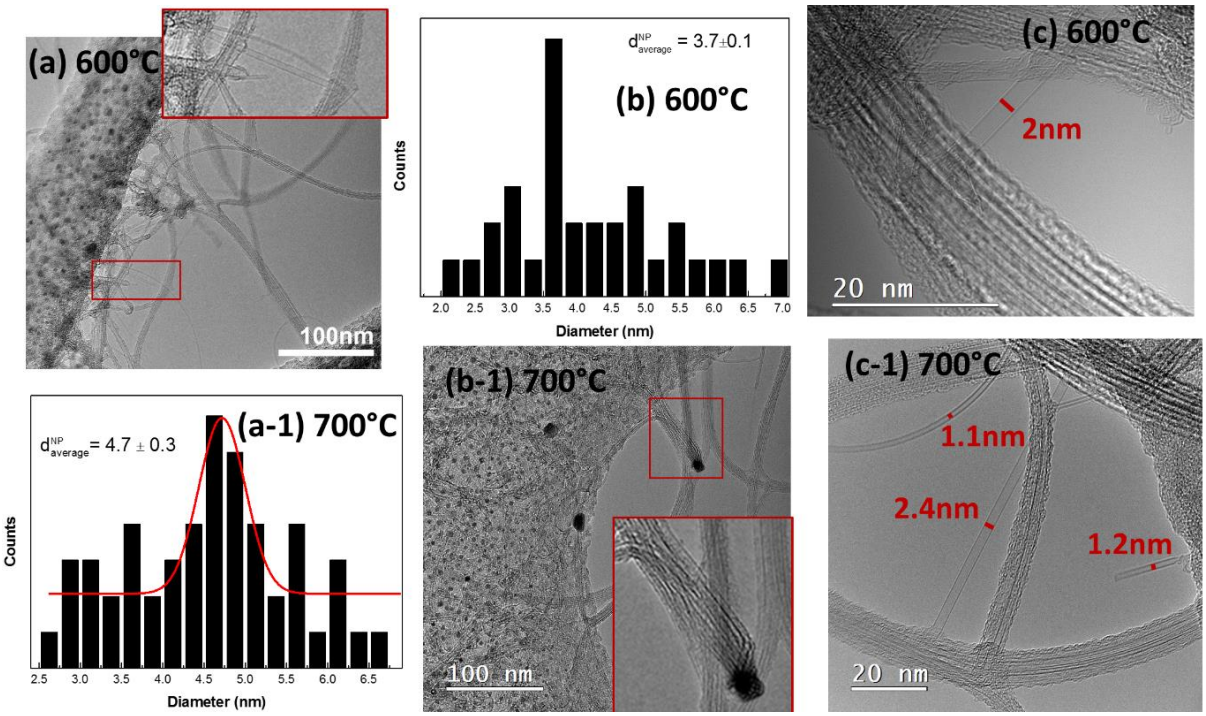

Figure 6.6 TEM images of SWCNTs synthesized at 600°C and 700°C of growth temperature: (a) SWCNTs formation at 600°C, (b) distribution of 100 nanoparticles after the synthesis at 600°C, (c) example of estimated diameter of SWCNTs at 600°C, (a-1) distribution of 100 nanoparticles once the synthesis was completed at 700°C, (b-1) formation of bundle of SWCNTs at 700°C and (c-1) estimation of diameters of different SWCNTs at 700°C, respectively.

The nanotubes synthesized at 600°C and 700°C (Figure 6.6) which correspond to the samples Fe0.4 and Fe0.3 in Table 6-1 present similar features to those obtained at 800°C. From Figures 6.6(a),(c) (b-1) and (c-1), these tubes are often grouped in clusters of few tubes feature significantly more structural defects in their tubular wall, as well as the presence of poorly graphitized or amorphous carbon. We also captured the presence of some isolated and high crystalline SWCNTs at high magnification. We can also remark that the diameters of the analyzed SWCNTs are relatively small, ranging

from 1 - 2.4 nm. After the growth, the average observed particles' size was 3.7 nm at 600°C and 4.7 nm at 700°C, which is larger than the average observed diameter of the SWCNTs. In addition, we also evidence a few tubes ends that were also devoid of catalytic nanoparticles, once again suggesting the formation of CNTs in the base-growth mode.

6.2. Influence of temperature at low growth pressure

In the previous chapter, the SWCNTs were successfully grown in the range of temperatures between 600 and 900°C at 5mbar and 2mbar of growth pressure. The unique design of our HFCVD allows us to perform the SWCNTs synthesis with the pressure as close as the in-situ experiment in ETEM, this statement was again verified through the first observation of the influence of growth pressure. Therefore, we further examined the effect of growth temperature coupled with low-pressure, particularly in the 0.5mbar range with a slow and continuous gas flow of 5sccm CH_4 and 2.5sccm H_2. We anticipate that a slow gas flow favors both the homogeneity of the gas mixture and a greater control of its diffusion on the surface of catalyst.

6.2.1. Experimental conditions

The sample preparation and CNTs synthesis methodology consisted of the following steps: (i) deposition of 5nm of Al_2O_3 and 1nm of Fe on the Si/SiO_2 substrate by molecular beam evaporation, (ii) sample transfer to the HFCVD reactor, (iii) once ultra-high vacuum was reached (10^{-7}-10^{-8}mbar) in the reactor , the substrate and the filaments were heated, (iv) subsequent step of the pretreatment of nanoparticles in 2 minutes under 5sccm of H_2 gas to prevent the coarsening, (v) when the pretreatment achieved, introduction of 5sccm of CH_4 and 2.5sccmH_2 in order to initiate and continue the growth of CNT for 30 minutes, (vi) rapid reactor pump-down out to achieve vacuum thus stopping the synthesis and subsequently sample was cooled to room temperature. We also note that the synthesis temperature was varied from 400°C to 900°C in step of 100°C.

6.2.2. Topological analysis of as-grown CNTs yields

The scanning electron microscopy (SEM) micrographs performed on samples obtained at different temperature and same pressure of 0.5mbar are summarized in Figure 6.7. At this pressure, it can be observed that the surface of the silicon wafer exhibits changes which are due to the formation of seeds that starts at temperatures as low as 400°C. Concerning the growth of CNTs we notice that it does not take place (Figure 6.7a) at such low temperature. The seeds appear to be only nanoparticles, carbon amalgams, or other by-products of the CNTs synthesis because we also did not obtain any CNTs characteristic peak when analyzing with Raman spectroscopy. It is well known that the CNTs need a catalyst particle of adequate size in order to grow; therefore, the increase of the as-grown SWCNT diameters at higher temperature is due to an increase in the mean catalyst size induced by a coarsening mechanism [198]. We hypothesize that at very low temperature as 400°C, the particle size is too small, and the carbon that condenses on its surface cannot take on the shape of the tube to initiate growth. From a growth temperature of 500°C, a coating with a fluffy-like appearance is formed on the sample. The fluffy-like structure could be attributed to the deposition of other graphitic structures (i.e amorphous carbon) on the wall of as-grown CNTs which will be confirmed by the Raman spectra (section 6.2.3). At higher temperatures of 600°C and 700°C the presence of some relatively short CNTs was observed. When the growth temperature increases up to 800°C, a significant increase in the density of grown CNTs was noticed from SEM analyses. We observed that the tubes also grow in an entangled manner, which makes difficult the estimation of the nanotubes area density. However, if the temperature continues to rise to 900°C, one can observe an apparent increased presence of CNTs at the support surface.

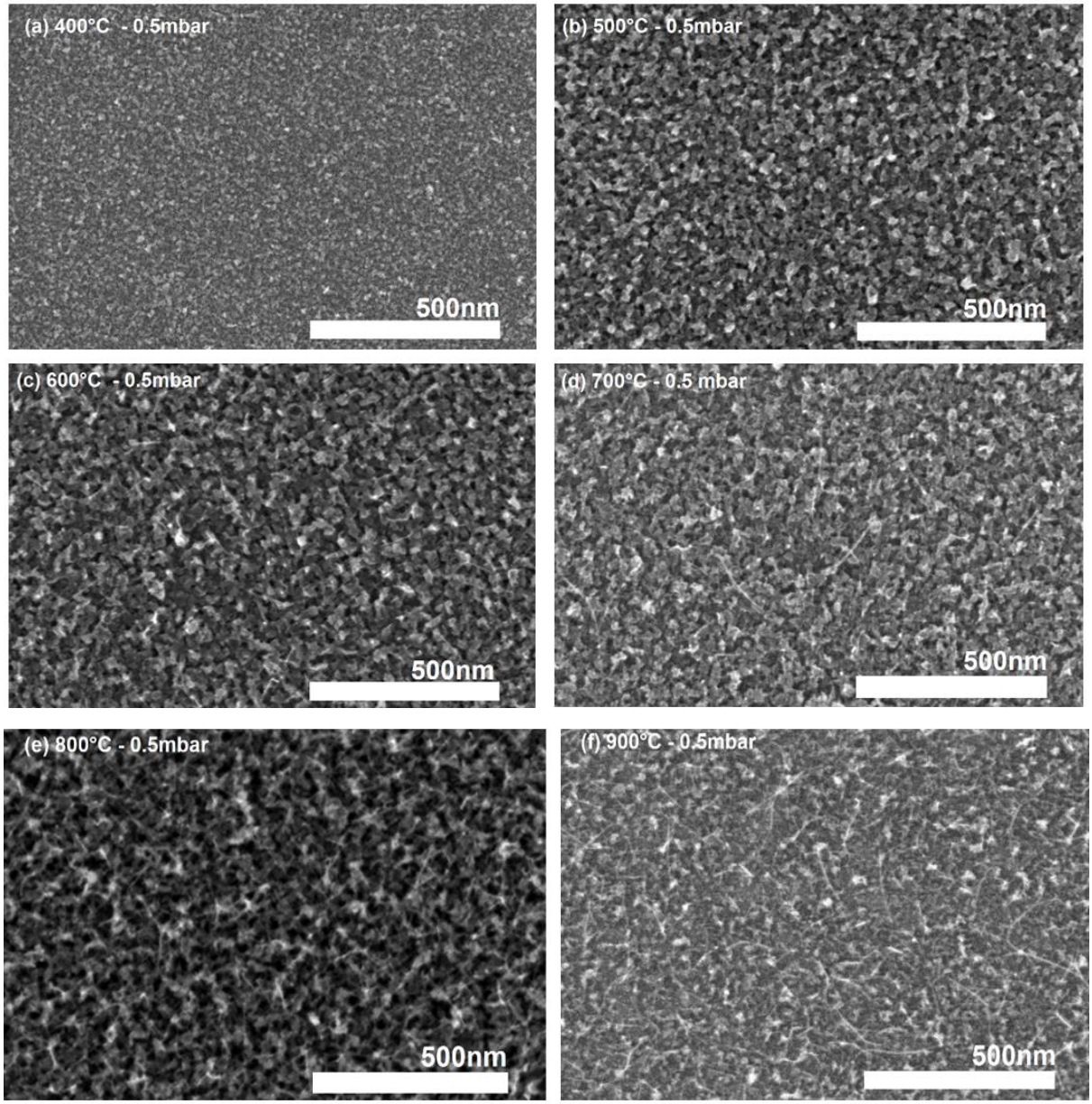

Figure 6.7 Top-view SEM images indicating the presence of CNTs after their growth at different temperatures and 0.5mbar of growth pressure

6.2.3. Raman spectroscopy

In order to verify the presence of SWCNTs for the presented samples, Raman analyses were performed using two different excitation wavelengths (532nm and 633nm). Figure 6.8a and Figure 6.8b illustrate representative examples of Raman spectra obtained with the 532nm laser excitation in the low and respectively the high-frequency regions, which are characteristic of the SWCNTs. At the low-frequency region, we observed the appearance of RBM peaks located in the range from 100cm^{-1}

to 300cm^{-1}. By comparing the peak positions, we also observe the tendency of a downward shift of the RBM peaks with the increasing temperature. The diameter of SWCNTs is estimated from the wavenumber by $d_t = {}^{248}/_{\omega_{RBM}}$ [231], and the distribution diameter of most SWCNTs is observed to range between 1 to 2nm. In detail, at the growth temperature of 500°C, we observed a main RBM peak at 231cm^{-1}, corresponding to the d = 1.1nm; nevertheless, the number of RBM peaks recorded in the 50µmx50µm area was about only 20 peaks. Accounting for an I_G/I_D ratio exceeding low (1.3 with the green laser and 1.1 with the red laser) we can infer that, although SWCNT may be synthesized at 500°C, the amount and quality of SWCNTs are quite poor, which is consistent with the SEM observation mentioned above. When the temperature was increased to 600°C, the number of observed RBM peaks increased significantly, we observed peaks located at 131cm^{-1}, 163cm^{-1}, 189cm^{-1}, 212cm^{-1}, 223cm^{-1}, 267cm^{-1}, and 285cm^{-1}, which correspond to SWCNT diameters ranging from 0.87 to 1.8 nm. Furthermore, the SWCNT diameters are estimated to be between 0.87 and 1.87 nm for 700°C, 0.87 - 1.9 nm for 800°C, and 0.85 - 2 nm for 900°C. The trend of increasing SWCNTs diameter with the increasing temperature matches the results obtained from the standard pressure synthesis (see previous section). We also plotted the intensity ratio of G band to respect the intensity of the D band (I_G/I_D) as a function of the growth temperature (Figure 6.8c). This ratio is proportional to the degree of graphitization and inversely proportional to the degree of contamination by defects in the analyzed CNTs (see chapter I). For the two excitation wavelengths, the observed evolution of the I_G/I_D ratio presents an increasing pattern. We observe that the degree of graphitization reaches a maximum between 700 – 800°C and thereafter marginally degrades outside this region. The deterioration is visibly marked when the temperature is raised up to 900°C or lowered down to 500°C. Although according to simulation reports [364], the defects are possible to be annealed at high temperature (900°C), the presence of additional compounds (i.e. additives, contaminants, or by-products) could be the reason for the observed formation of defects in our experiment. In contrast, at

low temperature (i.e. <600°C), the creation of defects was probably promoted by the low-activation-energy path dominant [365].

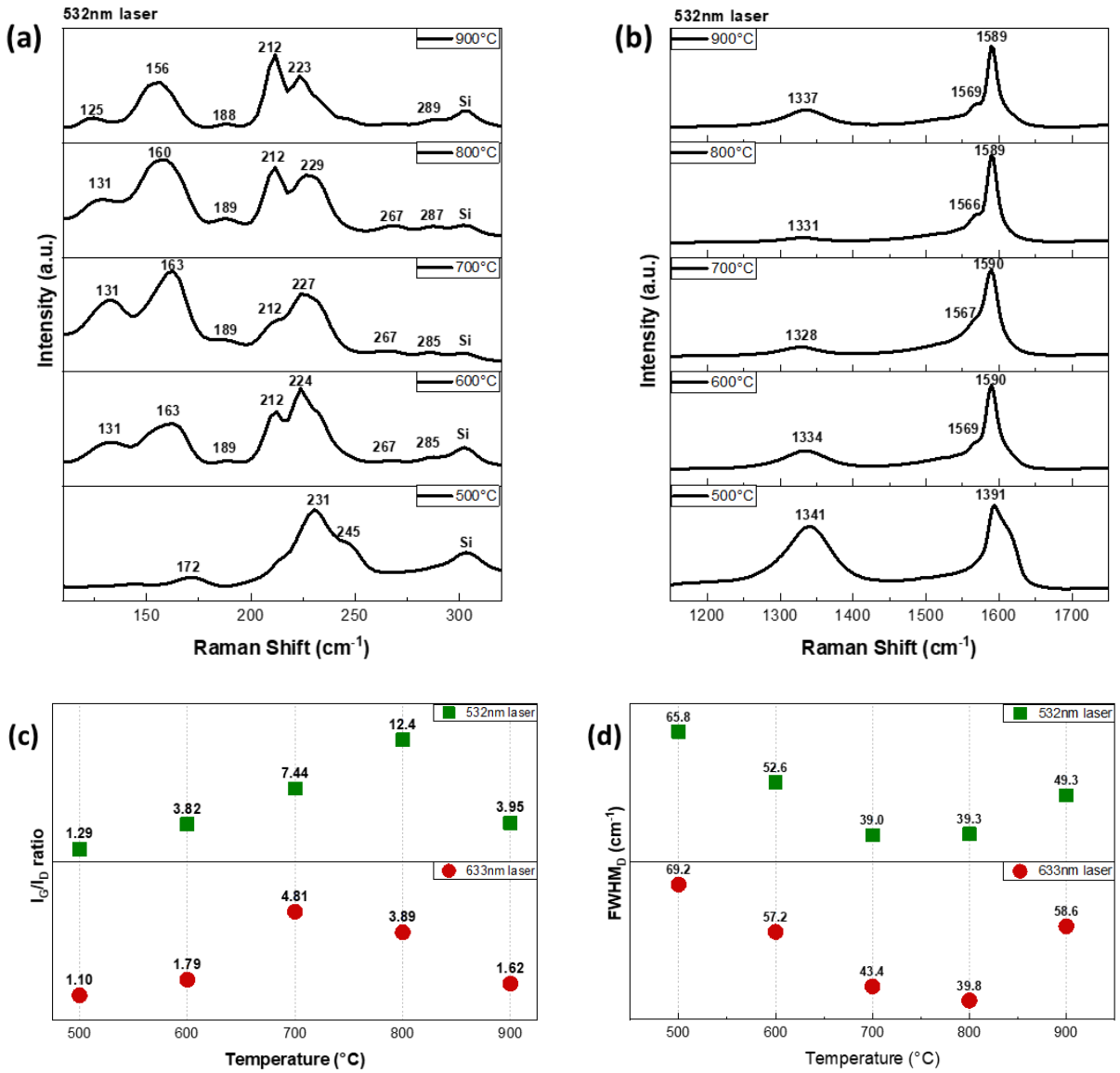

Figure 6.8 The average Raman spectra of 100-point mapping for the SWCNTs synthesized at 0.5mbar of pressure and at different temperatures: (a) low energy range, (b) D and G band. The wavelength of the excitation laser is 532nm. The dependence of (c) I_G/I_D ratio and $FWHM_D$ value in the function of growth temperature. The data was recorded under the excitation of two wavelengths at 633nm and 532nm lasers

6.2.4. In-situ XPS analysis on the catalytic chemical state of the sample synthetized at 800°C

To further investigate the composition and the nature of the surface of the observed CNTs, we undertook an in-situ XPS analysis on the sample synthetized at 800°C and 0.5mbar. The sample was prepared with the following procedure: (i) the deposition of 5nmAl_2O_3 and 1nmFe by MBE on 2cmx2cm Si/SiO_2 substrate, (ii) loading the sample in HFCVD reactor, (iii) the pretreatment of Fe nanoparticles under the 5sccmH_2 for 2 minutes at 800°C and 0.5mbar on the HFCVD reactor, (iv) the growth of CVD during 30minutes under 5sccmCH_4 and 2.5sccmH_2 at 800°C and 0.5mbar. Before starting each step, we transfer to the analysis platform to perform the in-situ XPS to analyze the state of catalyst. The X-ray from Al K alpha target was incident at 45° to the sample surface, on a large area of the sample surface. The electron energy analyser was operated with a pass energy of 12 eV for high resolution spectra. with a step scan size of 0.5eV. The details of curve fitting procedure are outlined as follows: (i) select the binding energy range for the background subtraction, (ii) select the linear method for the background subtraction, (iii) select the Gaussian-Lorentzian (GL) ratio to determine peak shape, (iv) select asymmetry factor (initial number is 1.0), (v) select full width at half maximum (FWHM) for the specific peaks, (vi) select the best fitted curve for experimentally obtained, which gives the minimum chi square. These steps were repeated until the best chi squared was given. The curve fitting parameters, i.e. FWHM, asymmetry factor, GL ratio, were manually input independent of the fitting software.

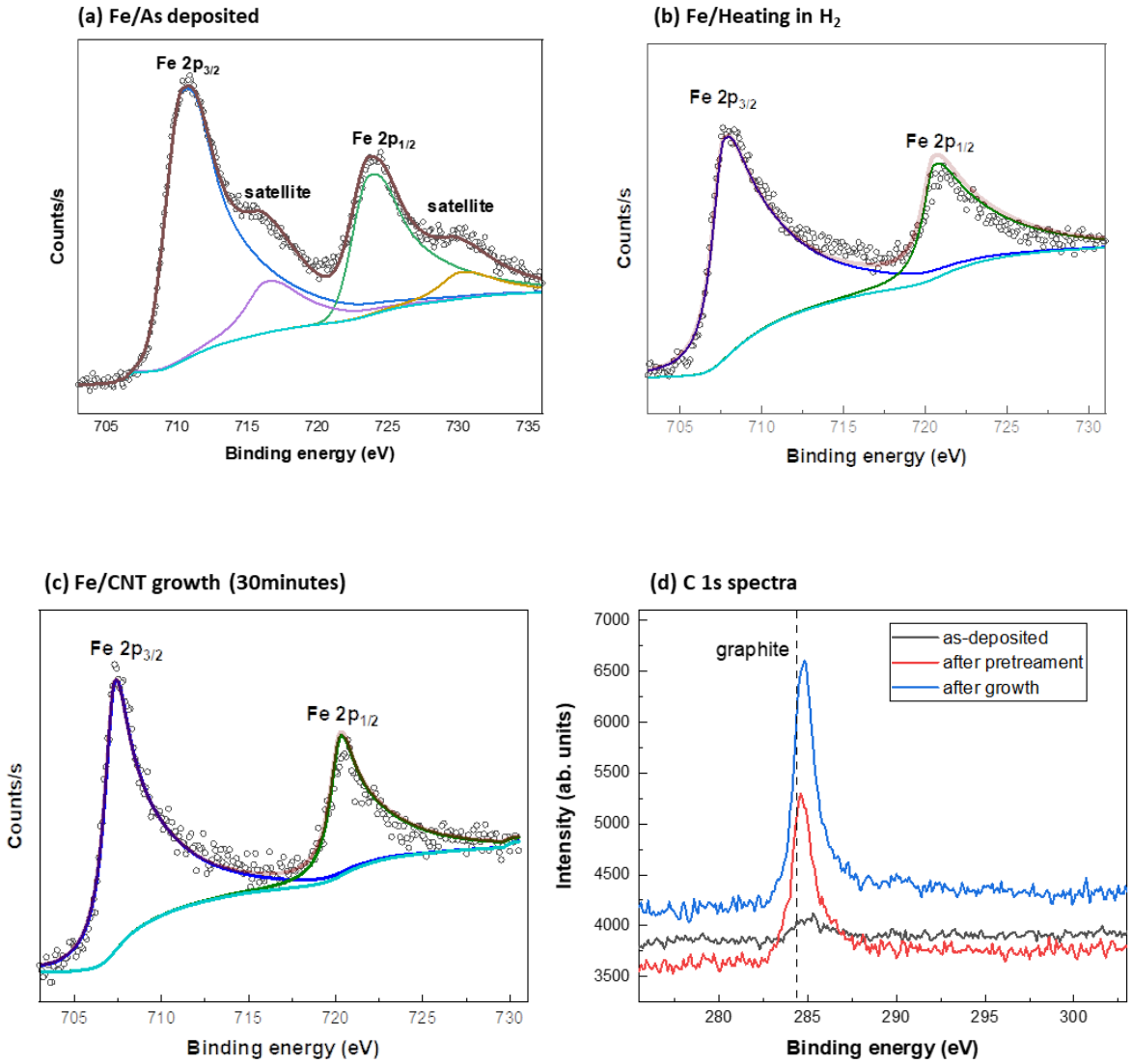

Figure 6.9 XPS spectra of Fe at different steps: (a) as deposited, (b) after the pretreatment under radical - H_2 environment and (c) after the SWCNTs synthesis for 30minutes under the mixture of CH_4/H_2 environment. (d) the C 1s spectra

The chemical state of Iron (Fe) catalyst during the SWCNTs growth was revealed through the XPS analysis. Figure 6.9 shows the XPS spectra of Fe-2p core-level for the sample at three different steps: (i) as deposited, (iii) after the pretreatment under H_{ra} environment, and (iii) after 30 minutes growth under CH_4/H_2 environment. Before the heating under the H_{ra} environment, the XPS spectrum of Fe-2p shows two distinct peaks around 710.47eV and 723.77eV, which correspond to the Fe-$2p^{3/2}$ and Fe-$2p^{1/2}$. They also contain two different satellite lines at 716.81eV and 730.61eV and there is no appearance for Fe^0 in the XPS spectrum. This spectrum is consistent with

the characteristics of Fe^{3+} in α-Fe_2O_3 [366]–[369] indicating that Fe catalyst surface was partially oxidized in the air [370] during the sample transfer between MBE and FENIX platform or suggesting a strong interaction between Fe and the surface oxygen atoms of alumina support, consistent with the reports of Mattevi et al [227], which is believed that this interaction restricts Fe surface mobility [227], resulting in the nucleation of vertically aligned CNT forest [227]. After the heating under H_{ra} environment for 2 minutes, the satellite lines disappeared, and the peaks of Fe-$2p^{3/2}$ and Fe-$2p^{1/2}$ are located at 707.67eV and 720.53eV with the value of full width at half maximum (FWHM) of 1.72eV and 1.72eV, respectively. This indicates the reduction from oxidized Fe to metallic Fe [263] and/or reacted with C to form Fe_3C[371]. We also observed an increase in intensity of C 1s peak (same peak position as C1s of graphite [263]) in Figure. 6.9d which suggests that the formation of carbon nanotube started. When the SWCNTs synthesis was terminated after 30 minutes, the position of Fe-$2p^{3/2}$ and Fe-$2p^{1/2}$ were located at 707.30eV and 720.28eV without satellite, which suggests the Fe nanoparticles were kept metallic during the synthesis. However, the FWHM of Fe-$2p^{3/2}$ and Fe-$2p^{1/2}$ are 1.45eV and 1.45eV. After the growth, the C 1s peak increases strongly, indicating the formation of carbon nanotube (Figure. 6.9d), while the Fe remained in its fully metallic state.

Transmission electron microscopy (TEM) analysis provided additional confirmation of the single-walled structures of the nanotubes. The growth process was directly performed on TEM grids under the same conditions as on Si/SiO_2 substrate via HFCVD at 800°C. As shown in Figure 6.10, there is several obtained isolated - SWCNTs, the growth is observed as relatively clean with some negligible deposition of amorphous carbon on their side wall, which is consistent with the maximum in I_G/I_D obtained through the Raman spectroscopy. However, the SWCNTs are extremely short, some of them can reach 30nm in length. This phenomenon could be due to the growth initiated already during the pretreatment which is consistent with the XPS results of C 1s peak and not successfully restarted after. We were able to determine the diameter of some SWCNTs through a detailed analysis of several TEM images in Figure 6.10a,

Figure 6.10c and Figure 6.10d. The Gaussian fitting result concludes that the mean diameter of SWCNTs is around 1.14nm, and more than 60% of SWCNT is located in the diameter ranging from 1.0nm to 1.4nm (Figure 6.10b).

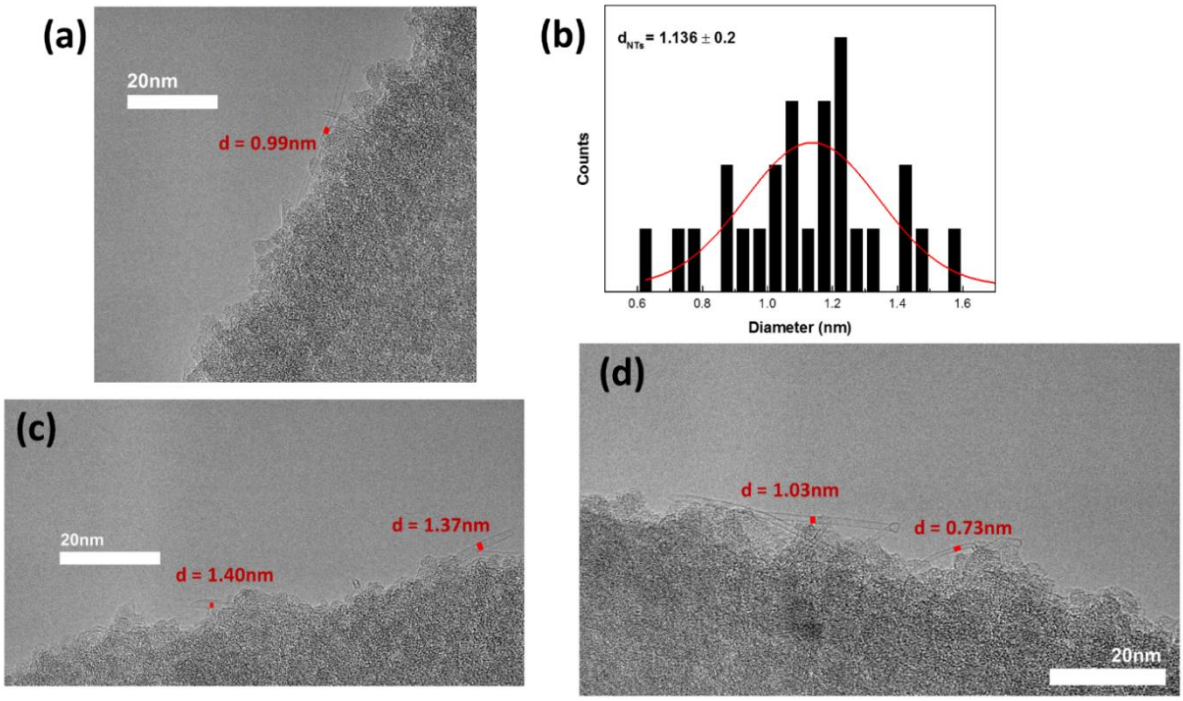

Figure 6.10 SWCNT sample grown with Fe catalyst at 0.5mbar and 800°C: (a – c – d): HRTEM micrographs, (b) Histogram distribution of individual SWCNT diameters. The numbers in (b) are mean diameter ± standard deviation

6.3 Discussion and Conclusion

It is widely assumed that the formation of CNTs consists of several processes including carbon atom dissolving, diffusing, and precipitating via the catalytic nanoparticles in the CVD process, which are directly affected by both the carbon atom concentration and the temperature [372]–[374]. At the growth pressure of 5mbar and 2mbar, the high carbon concentration caused by the long residence time of gas inside the reactor (constant total gas flow) could result in an increase in the amount of activated carbon precursor prior to reaching the catalyst. At this growth conditions, the growth temperature is significantly important in controlling the properties of SWCNTs: vertical alignment, diameter, chirality, and density[329], [361], [375]. We observed that the diameter of SWCNTs increases with the increase of temperature and

when the temperature is beyond a threshold, some small nanoparticles are either not activated or activated slowly owing to their higher supersaturation limit [349], [376], [377]. When the nanoparticles are small, the carbon concentration within the catalyst exceeds the threshold carbon concentration for the encapsulation of nanoparticles, resulting in the nucleation of carbon cages around the catalyst particles and the termination of SWCNTs growth [166], [229], [378]. This hypothesis can be used to explain why we could not observe the growth of small diameter SWCNTs at 900°C in our HFCVD set-up. Furthermore, the absence of larger nanoparticle activation at low temperatures (<600°C), which is sometimes attributed to poisoning due to the overloaded carbon content [379], [380], could lead to the formation of small diameter SWCNTs in this range temperature. The low carbon solubility of bigger nanoparticles caused by the low temperature in the reactor results in the lack of subsurface atoms, which facilitates stronger adhesion of sp^2 layer on the catalyst surface to encapsulate the nanoparticles, thereby inactivating the nanoparticles[126]. When reducing the growth pressure, we observed that the influence of the growth temperature becomes stronger on the synthesis of SWCNTs. The lower the pressure, the shorter the residence time of the gases in the reactor (at constant total gas flow input), which limits not only the quality of activated carbon precursor reaching the catalyst but also the amount of H_2 during the pretreatment. When using 0.5mbar of growth pressure, the trend of as-grown SWCNTs is identical to the hypothesis we used to explain the growth behavior on sample synthetized at the growth pressure of 5mbar and 2mbar. The optimal growth temperature remains between 700°C and 800°C, which is compatible with the modelled melting temperature of catalyst nanoparticles of 1-2nm [381] based on the Gibbs-Thomson effect [382]. These observations suggest that the decomposition of carbon source at the catalyst level is dependent not only on the growth pressure but also the temperature, which directly affects the nucleation and the growth of CNTs. This paves a way for better tuning of the SWCNTs growth process based on the purpose of each application.

7. In-situ single-wall carbon nanotubes growth experiments using RaCVD@ETEM combined approach

HR-TEM microscopy has become the reference tool for nanotube characterization. It allows obtaining crucial information on the shape, chemical and crystallographic state of the catalyst as well as on the chirality and the mono/multi walled character of the nanotubes. One of the most beautiful applications of this aproach is to couple the microscope with the possibility to allow the circulation of different gases, which is known as environmental HRTEM. It becomes then possible to synthesize carbon nanotubes *in situ* and thus to access the key information on the nucleation mechanisms and growth kinetics of nanotubes. By developing an environmental HRTEM microscope, Helveg et al [131] visualized the in situ atomic scale growth of MWCNTs by CH_4 decomposition on catalytic Ni nanoparticles at a temperature of 540°C. By observing the growth of nanotubes with the tip-growth mode, they studied the elongation/contraction process of catalyst during the gradual formation of the nanotubes structure and evidenced that the Ni catalyst retained a crystalline character (often oriented [111]) during the growth. Other studies have been carried out to determine the effect of temperature and pressure on the selective growth of nanotube by decomposition of acetylene (C_2H_2) on Ni nanoparticles. Sharma et al [344], [383]observed in an environmental HRTEM the preferential growth of SWNTs at high temperatures (T>650 °C) and pressures P<1 mTorr while for temperatures of 450 °C and pressures of 20 mTorr, the growth of MWNTs was favored. In each case, several models have been proposed to explain the correlation between the state, the shape of the catalyst and the structure of nanotubes. Lin et al [145] observed that Ni catalytic particles with diameter d<6 nm favored SWNT formation while those with diameters d> 6nm favored nanocage formation. By studying the evolution of the length of the nanotubes as a function of time, they detected 3 regimes: a first regime corresponding to an incubation period of the nanotube with the formation of the cap of the nanotube, a second regime corresponding to the important increase of the length of the nanotube and finally a third regime where the rate of growth becomes much

lower. They explain this third regime by the fact that the C atoms passivate the active sites and reduce the activity of the catalyst. It should be noted that we have also observed the formation of carbonaceous nanocages and visualized 3 identical growth regimes during in-situ synthesis of individual nanotubes under field emission. Moreover, by decomposing ethylene (C_2H_4) on catalytic Co nanoparticles deposited on SiO_2 nanoballs localized on a TEM grid, Zhu et al [384] showed that the size of the catalyst influenced not only the diameter but also the shape of the nanotubes in particular at their end. A catalyst with a small radius of curvature ($r<2$ nm) favors the nucleation mechanism of the nanotube by generating a hemispherical cap at its tip. On the contrary, a catalyst with higher radius of curvature ($r>2$ nm) is responsible for the formation of larger diameter SCWNTs with a conical shape at their tip. The small radius of curvature at this tapered end is explained by the formation of several carbon pentagons during the very early stages of SWNT nucleation. The authors suggest that the incorporation of pentagons during this nucleation step is energetically more favorable than reducing the likely existing dangling bonds and that it facilitates the curvature of the SCWNT structure while enhancing adhesion with the catalyst. Other in-situ synthesis studies under TEM show that the shape of the catalytic particle constantly changes while retaining metallic and crystalline properties during the growth of "Bamboo-like" MWCNTs [132]. During the in-situ atomic scale observation of the growth of nanotubes on Fe nanoparticles under C_2H_2 flow, Yoshida et al [130] revealed the change of chemical state of the catalyst which becomes Fe_3C during the growth phase. By performing Fourier transforms on the HRTEM images of the catalyst obtained during the nucleation and the growth of the nanotube, the authors thus highlight a mechanism of volume diffusion of the carbon atoms through the catalyst. Moreover, interesting results have been obtained during the in-situ observation of the catalytic dynamics during the nucleation mechanism of carbon nanotubes [122]. By coupling the results of nanotube growths obtained under environmental HR-TEM microscopy with XPS (X-ray Photoelectrons Spectroscopy) and EELS (Electron Energy Loss Spectroscopy) analyses, Hofmann et al. were able

to follow the chemical evolution of the catalyst. They showed that the catalytic iron and nickel nanoparticles remained in a metallic and active state during the growth phase of the nanotubes. The HR-TEM images underline that during the growth, the catalyst changes from its initial shape to an elongated shape with a very high deformability. Finally, Mattevi et al [227] showed that in order to control the size of the particles it is necessary to know their interactions with the support and the surrounding gases. The processes involved are extremely complex because, for the particle, its shape, its nature, its size but also the nature of the support and its microstructure, and for the gases, their reactivities which is a close function of the preceding parameters, are involved. Overall, we still have a lot of aspects that can be exploited from the in-situ experiment in the synthesis of SWCNTs. The studies all contribute to the improvement of the understanding of SWCNTs, from which it is possible to develop methods of synthesizing SWCNTs according to the purpose of each application.

This chapter focuses on the presentation of the experimental results obtained inside the environmental transmission electron microscope available in our lab. The main goals were to see if we can reproduce inside the NanoMAX-ETEM the same experimental process parameters performed in the HFCVD-FENIX presented in the previous chapters, as *in situ* synthesis of carbon nanotubes while continuously observing during the growth phase of nanotubes (RaCVD ETEM described in Chapter 3 – NanoMax). More specifically, we focused on the investigation of the nucleation and elongation mechanism of the nanotubes on the catalytic nanoparticle in the conditions explored by HFCVD in FENIX at low growth pressure. The goal was to synthesize the carbon nanotubes directly on the specific substrate (Environmental chip from Protochips) previously coated with catalysts. With this substrate, we can obtain information on the crystallographic state of the sample, visualize the *in-situ* formation of nanoparticles, and observe the growth of carbon nanotubes. Our in-situ real time TEM experiments were carried out using the experimental setup described in the previous chapter (section 3.3). The modified environmental transmission

electron microscope (Titan ETEM 60-300ST) was operated at 80keV. The microscope is equipped with a Cs image corrector, an UltraScan 2kx2k CCD camera and a direct electron K2 camera. All in-situ observations were done using the Protochips Fusion sample holder that has been slightly modified in order to be compatible with the CVD cells collimators. For all the experiments we used SiC (silicon carbide) heating membranes with different coatings provided with the sample holder. The temperature is controlled by the sample holder and all the indicated temperatures are based on the company provided calibrations. A schematic representation of the modified sample holder and the configuration of the E-chips (heating membranes) are shown and described in Figure 7.1.

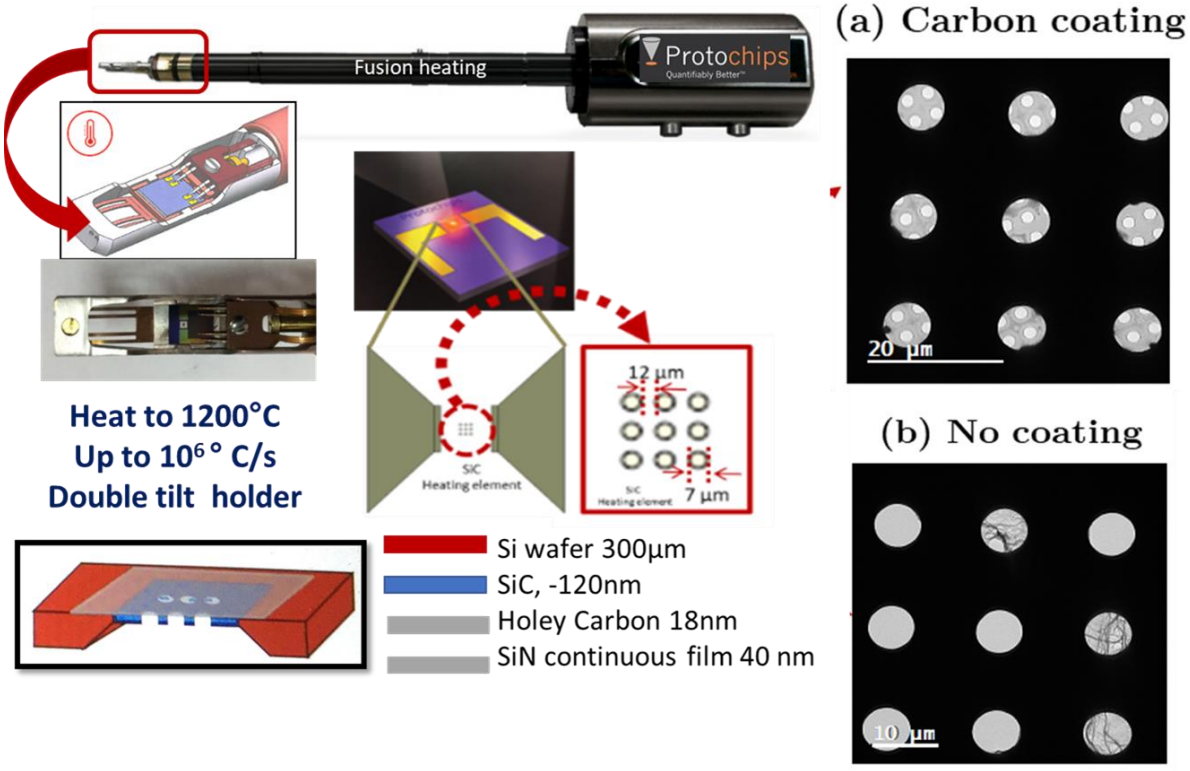

Figure 7.1 Protochips [267] holder and E-chip heating membrane configuration with in (a) carbon coating and (b) no coating with deposited carbon nanotubes

We have explored the different experimental protocols set up presented before. The initial results were obtained using Fe-monometallic catalyst. Other experiments are presented in the second and third parts which lead to the growth of carbon nanotube on different types of heating membranes using Mo/Fe binary metallic

catalyst. For all the in-situ experiments, we used Alumina as a support layer of catalyst. Depending on the nature of the hole membrane, the thickness of Al_2O_3 layer varied between 5 to 7nm with subsequent catalyst layer evaporation. This step was performed with the MBE mentioned in section 3.1. The experiments accounted for the two steps: the pretreatment and he growth of SWCNTs, which as summarized in Figure 7.2. During the first step, H_2 was introduced to perform pyrolysis – annealing the catalyst layer to form the nanoparticles and activate them. The second step was continued with the formation and elongation of SWCNTs from the catalytic nanoparticles under the H_2 / CH_4(or C_2H_2) environment.

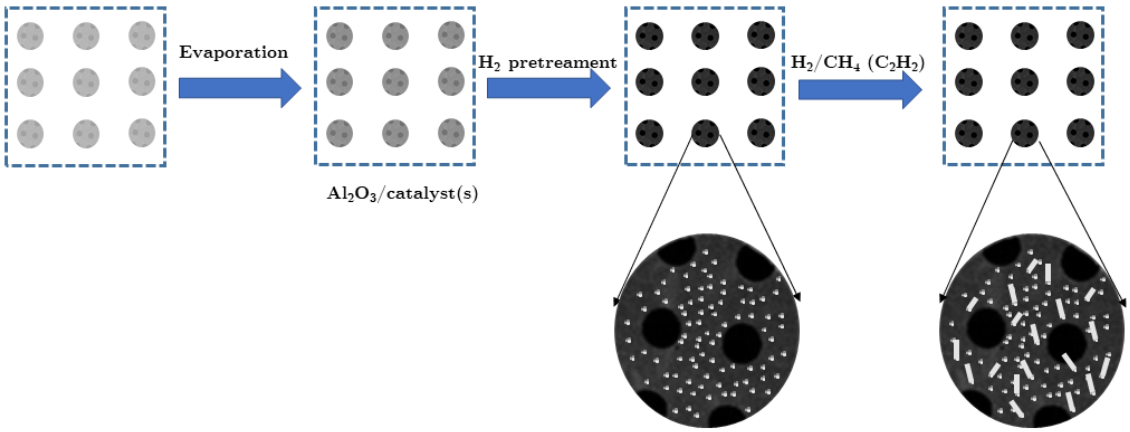

Figure 7.2 Illustration of the main steps to follow in the growth of CNTs by the in-situ TEM approach. a) illustration of the central area of the heating membrane, with the 9 regular holes containing the carbon membrane which present irregular holes; b) central area of the heating membrane after the deposition of two layers of Al_2O_3 and Fe; c) illustration of the catalyst pretreatment step which is done inside the microscope with a zoom on one of the 9 holes of the membrane; d) schematic illustration of the growth of the CNTs The presence of the carbon precursor is illustrated by the black circles in the source and that of hydrogen by the blue circles

7.1. Mono-metallic catalyst – Iron (Fe)

The goal was to grow single-wall carbon nanotubes (SWCNTs) with catalyst Fe, which is known as one of the most popular transition metal catalysts due to its highest solubility of carbon atoms (around 2% at 800°C in the bulk state) [130], [142], [143]. Firstly, ethanol-MWCNTs suspensions were dispersed onto the uncoated heating membrane compatible with the PO Fusion from Protochips (Figure 7.1b). The choice of using MWCNTs as underlying growth support for our experiments was

to be able to observe the nucleation step under the vacuum conditions. Once the MWCNTs deposit on the heating membrane we carried out the deposition of the Al_2O_3 barrier layer and Fe catalyst layers via the ultra-high MBE system allowing the reproducible deposition of layers as thin as 0.1nm. Both layers, the alumina support, and the Fe metal catalyst, were deposited at room temperature directly on the carbon coating heating membranes that serve as TEM observation window. The role of the alumina during the growth process is to prevent the carbon atoms diffusion from the support and to favor a base growth mode. The thickness of Al2O3 and Fe layer were fixed at 5 and 0.5 nm, respectively. The rough layer all along the tubes observed in TEM (Figure 7.3a) confirms their deposition. The EDX analysis performed confirms the existence of both Fe and Al_2O_3 composing elements, the resultant signals are shown in Figure 7.3c. The relatively large magnitude Al and O peaks are caused by the layer of Al_2O_3 that we deposited. A signal from Fe, which is attributed to the presence of a catalytic layer in the samples, was also observed. These various peaks are consistent with the deposited layers in the sample.

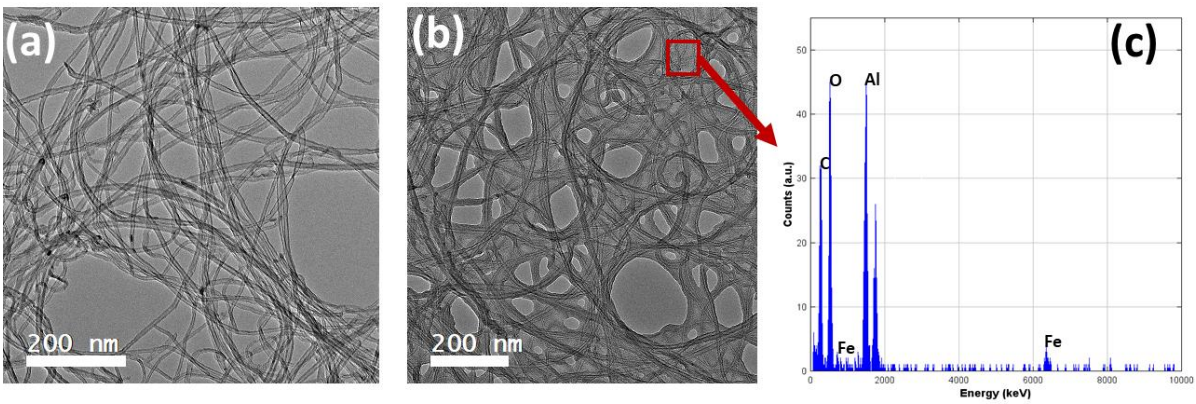

Figure 7.3 (a) TEM image of MWCNTs deposited on the heating membrane before and, (b) after the Fe@Al_2O_3 layers deposition, (c) TEM-EDX spectra illustrating the presence of the Fe, Al and O elements

Secondly, we heated gradually the sample by Joule effect for the pretreatment step of 500°C with a step of 10°C/s. The reaction kinetic of the Fe film reduction under H_2 flow is affected by both the external parameter (gas pressure, purity, and heating program) and the intrinsic properties of the film (thickness, surface chemistry,

and structure)[385], [386]. The first observation relates the dewetting of Fe film under an H_2 atmosphere into the Fe – catalytic nanoparticles even at relatively low temperatures (i.e. 400°C), supposedly due to the surface energy difference of the substrate and Fe. Figure 7.3b shows the Fe thin film layer prior to the introduction of H_2 gas; the image was captured at room temperature and ultra-high vacuum pressure with the MWCNTs as support. The system was exposed to the molecular H_2 and the temperature was gradually raised up to 500°C at a rate of 10°C/s. The H_2 pressure at the sample was about $8.75x10^{-3}$mbar with a gas flow rate of around 22.5sscm. No significant changes were recorded before 400°C under H_2 environment (Figure 7.4a). At 425°C, the Fe thin layer starts to dewet, resulting in the formation of small nanoparticles with a round shape. These nanoparticles become increasingly apparent at 500°C (Figure 7.4b) with an estimated size between 1-3nm and distributed homogeneously on the substrate. This observation is consistent with the theoretical model reported by Zhong et al [387], in which there is a relationship between the diameter (d) of nanoparticles and the thickness (h) of the initial film is proposed as $d = 6h$, assuming no loss of energy. The nanoparticles are then heated up to 550°C to remove any contamination on their surface.

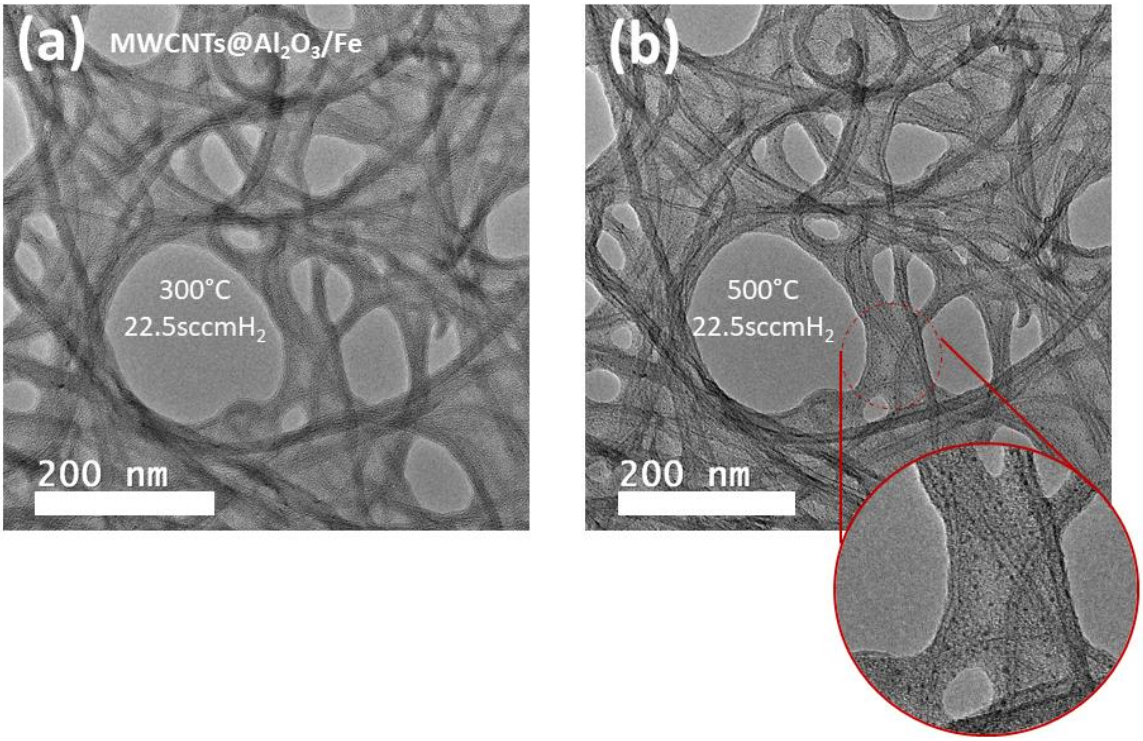

Figure 7.4 (a) Before pre-treament and (b) After pretreatment under the radical H_2 environment of the chip MWCNTs@Al_2O_3/Fe

Once the pre-treatment was achieved, the nanosized Fe catalysts are exposed to a flow of 2.5sccm acetylene (C_2H_2), which is one of the most reactive carbonaceous gases, and 6sccmH_2 inside the TEM chamber to initiate the CNTs growth while continuously heating the substrate up to 600°C. The iron–acetylene combination is known as one of the most efficient couples for easy synthesis of CNTs. Several low magnification TEM images illustrated in (Figure 7.5) evidence many SWCNTs synthetized using the chosen growth conditions. The image in (Figure 7.5 a) illustrate the successful synthesis of SWCNTs observed in the surrounding area. The bundles of SWCNTs are often observed (Figure 7.5b). SWCNTs grew from the catalyst nanoparticles with diameters varying between 0.95 to 2.5nm and the lengths ranges from few nanometers to micrometers (Figure 7.5 c-d). The SWCNTs exhibit a very good crystalline structure and their surface appears free of any amorphous carbon Figure 7.5(c-d). Furthermore, there was no observation of catalyst at the apex or inside the tubes, which suggests that SWCNTs grow from catalyst in the base-growth mode. However, in our images, the root of SWCNTs is embedded deeply in the support

layer and it is difficult to conclusively indentify the catalytic nanoparticle which acts as the nucleation of a given individual SWCNT. The image (Figure 7.5e) shows also the encapsulation of some Fe nanoparticles by several carbon layers as nanocages. Here, the elongation of carbon nanotube did not start probably because of an excessive carbon feeding and/or insufficient surface mobility of nanoparticles [145], thus the carbonaceous layer had the effect of encompassing the catalytic nanoparticles and poisoning them. By comparing the nanoparticle size and the observed diameter of the SWCNTs, we could conclude that larger catalytic nanoparticles prefer to form the nanocage, whereas the smaller Fe catalyst particles encourage the formation of SWCNTs under our experimental conditions. It could be a suggestion of the catalytic size selection in the determination of the final products. Furthermore, during the growth, at 600°C, under the presence of both H_2 and carbon species, the oxidized Fe films on Al_2O_3 support, which does not fully reduce during the pretreatment, will turn to form the nanoparticles rapidly and the average particle size still increases, likely due to unhindered Ostwald ripening, which lead to the increase in the density of nanoparticles observed after the synthesis.

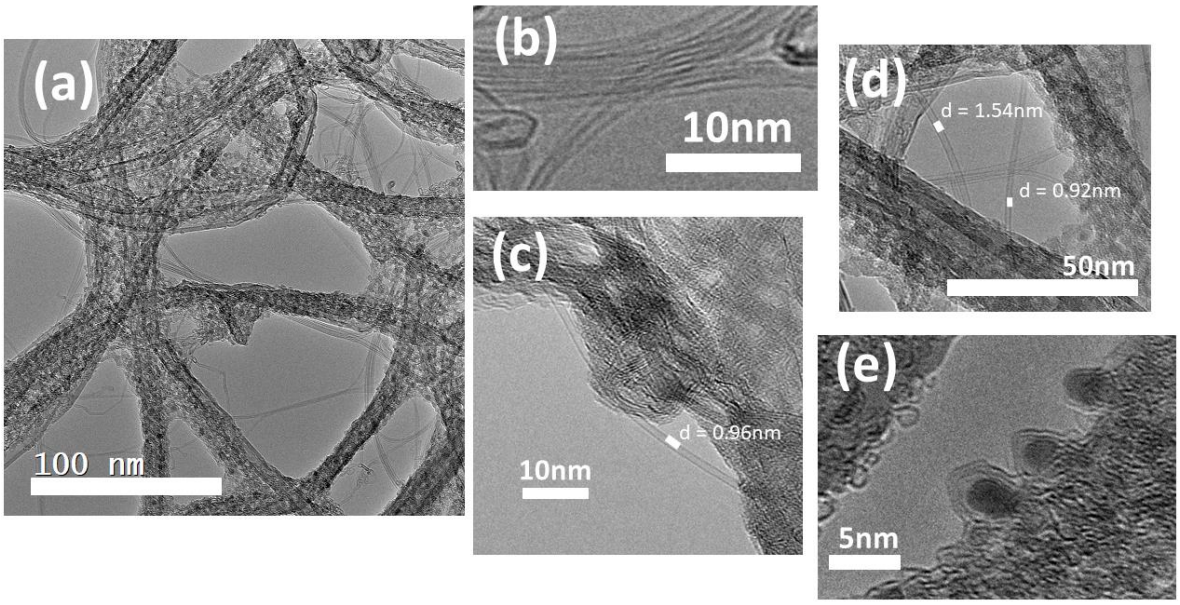

Figure 7.5 Transmission electron microscopy images of the surface of a sample showing the SWCNTs after their synthesis inside the TEM chamber: (a) low-magnification images confirm the growth of long SWCNTs, (b) formation of bundle SWCNTs, (c) – (d) Images showing estimated diameters of SWCNTs and (e) appearance of "nano-onions" of Fe covered with amorphous carbon on the surface of the catalyst

7.2. Binary-metallic catalyst Molybdenum and Iron (Mo/Fe)

The following paragraphs present the studies carried out on several specific samples and related analysis and observations through *in situ* experiments. In the previous chapter, we successfully obtained the synthesis of SWCNTs via the HFCVD in Fenix by the addition of molybdenum as a promoter for the iron catalyst on the Si/SiO_2 substrate. We hypothesized that the use of Mo could be a factor to control the properties of the as-grown SWCNTs. However, the great difficulty encountered is that we could only study the SWCNTs after the growth without the observation during the nucleation and growth phase of SWCNTs. This motivated us to reproduce the experiments with the binary metallic catalyst Mo/Fe, *in-situ,* in NanoMax. We will discuss the experimental details that we have implemented to synthesize SWCNTs, also mention the numerous difficulties we encountered, and finally present the characteristics of the obtained SWCNTs.

7.2.1. Uncoated E-chip as a substrate

The preparation of the sample on an uncoated E-chip followed the steps mentioned in the previous section: (i) deposition and cleaning of MWCNTs support layer, (ii) evaporation of 5nm of Al_2O_3/0.5nm of Mo/0.5nm of Fe by MBE (chapter 2), (iii) synthesis of SWCNTs in the NanoMAX microscope. Once the sample was placed inside the microscope chamber, we introduced 2sccm of radicals activated H_2 by heating the corresponding gas cell. The exposed sample was then heated at a rate of 10°C/s up to 550°C. As soon as the temperature reached 450°C, nanoparticles begin to form, highlighted by the gradual appearance of small black marks in the membrane (Figure 7.6b) at about 90s. These particles continued to increase in size and became more visible as the temperature reached 500°C and the pretreatment time was 120s. As soon as the size of the estimated nanoparticles is between 1nm and 3nm, they were exposed to a mixed environment composed of 2.5sccm C_2H_2 as the carbon precursor and 2sccm of molecular H_2. We remember that the role of molecular H_2 during the synthesis is to maintain a clean catalyst surface during the synthesis. Corresponding cell heating is not used for C_2H_2 due to fear of filament contamination and because

C_2H_2 readily decomposes at the growth temperature (as compared to CH_4) . Such carbon film not only neutralizes the filament surface thus reducing the temperature of filament and production of elemental hydrogen, but also decreases the efficiency of filament when it becomes thicker because of delay in the increase the capacity of the filament[341], [388]–[392].

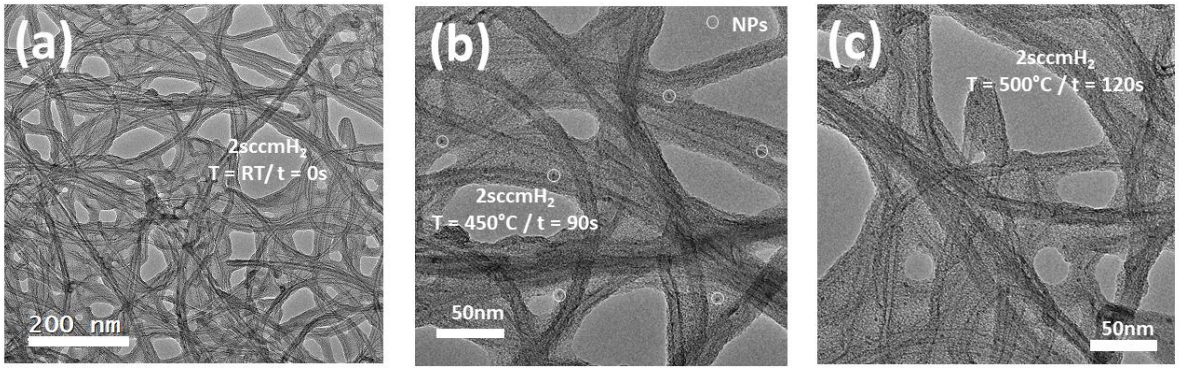

Figure 7.6 TEM images of the sample at different steps of the pretreatment: (a) before the pretreatment, (b) the formation of the initial nanoparticles at 450°C, (c) the formation of nanoparticles at 500°C

Figure 7.8 shows a series of TEM images, which represents the observed high-density SWCNTs growth. The lengths of SWCNTs were observed from several to hundreds of nanometers (Figure 1.7a). By analyzing several TEM images (Figure 7.7 b – f) we found a narrow distribution of the diameter of SWCNTs the high defect density in the tube wall, which is caused by many possible reasons such as: the front segment of SWCNT bent during the growth, the behavior of catalyst nanoparticle during the growth, the insufficient amount of carbon precursor, or maybe the irradiation impact of electron beam[393]. Normally, it is recommended that when using HRTEM, the accelerating voltage of the electron should be reduced to 80kV. Because at this voltage, the electrons, which are scattered by the nucleus of the atom, will not have enough energy to cause collision damage in carbon nanomaterials. However, Warner et al reported that their synthesized SWCNTs are unstable at voltages of 80kV, which directly affects their diameters. They increase not only in strain in carbon bond but also in the curvature. This group also found that with

smaller diameter SWCNTs, the curvature and distortion were more affected by the electron beam irradiation [394].

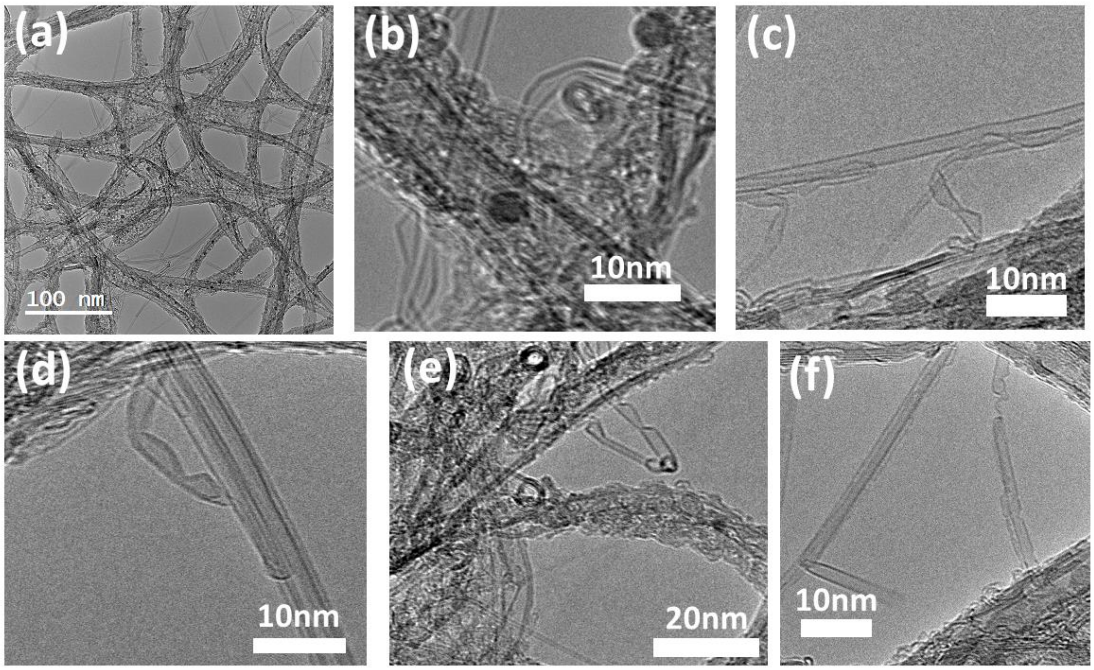

Figure 7.7 The defects on the tube wall of the as-grown SWCNTs which were recorded after the synthesis

When the growth of SWCNT was ended, we estimated the diameter of 100 individual SWCNTs to obtain their distribution (Figure 7.8a) from 0.5 to 2.5nm. This distribution is broader than that of the sample grown from only Fe due to the formation of smaller diameter SWCNTs. The dark point in Figure 7.8b represents the remaining nanoparticles from which the growth was not initiated. It appears that the nanoparticles become larger after the synthesis and their average size shifted to 2.86nm (Figure 7.8c) during the heating process. Compared to the sample grown from only Fe (previous section), not only the average SWCNTs diameter but also the mean size of the nanoparticles is smaller, which suggests that the aggregation of Fe catalyst was reduced by using Mo as a co-catalyst. Also, when the nanoparticles were enlarged to a larger diameter, the growth of MWCNTs was favored and often the fasts poisoning (Figure 7.8 d-e). These results are consistent with the results of the previous sample synthesized by HFCVD in FENIX (Chapter 4).

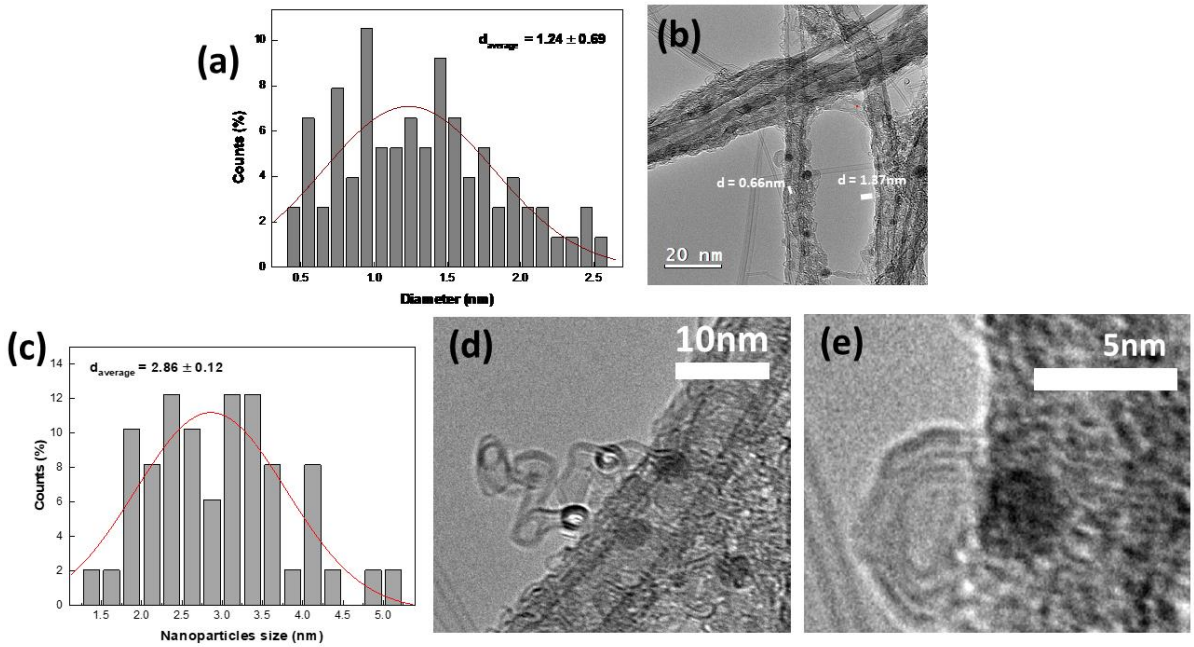

Figure 7.8 (a) Diameter distribution of SWCNTs from TEM images, (b) TEM image of SWCNTs and nanoparticles after growth at 600°C, (c) Nanoparticle size distribution determined from TEM images, (d) – (e) other carbon nanomaterials formation

7.2.2. Carbon coating E-chip as a substrate

In this experiment, we focused on reproducing the growth experiments on another type of substrate heating membranes: E-chip coated with Carbon as underlying support for synthesizing SWCNTs with a Mo/Fe catalyst. In order to avoid the contribution of the carbon coating, we needed to adjust the Al_2O_3 layer thickness to 7nm to increase the function of this barrier layer. Subsequently, we deposited 0.5nm of Mo and 0.5nm of Fe by molecular beam evaporation (MBE – Chapter 2). Figure 7.9a illustrates the rough surface of the sample after the evaporation which was recorded at low magnification inside the ETEM– NanoMax equipment before gas exposure and heating process. The gas introduction and heating are carried out sequentially as in the *in-situ* experiments performed in the previous section. Firstly, 22.5sccm H_2 was injected into the TEM column and the sample was heated at a rate of 10°C/s up to 500°C to create an environment of dewetting and annealing of catalytic film. Comparing to the previous in situ observations, the formation of nanoparticles is difficult to follow on this type of substrate since its

thickness is too important for allowing the observation of the formation of small NPs. After 2 minutes of pretreatment, we observed some small dark points on the support which can be linked with the formation of nanoparticles (Figure 7.9b). Then, the mixture of gas (2.5sccm C_2H_2 and 6sccmH_2) was continuously introduced to initiate the growth of SWCNTs. Like for others experiments the H_2 flow has been maintained during the growth in order to maintain the catalytic activity of the nanoparticles and the cleanness of the surface. Figures 7.9 c-d show a time-sequence of TEM images extracted from the video, which illustrate the growth and termination of SWCNTs.

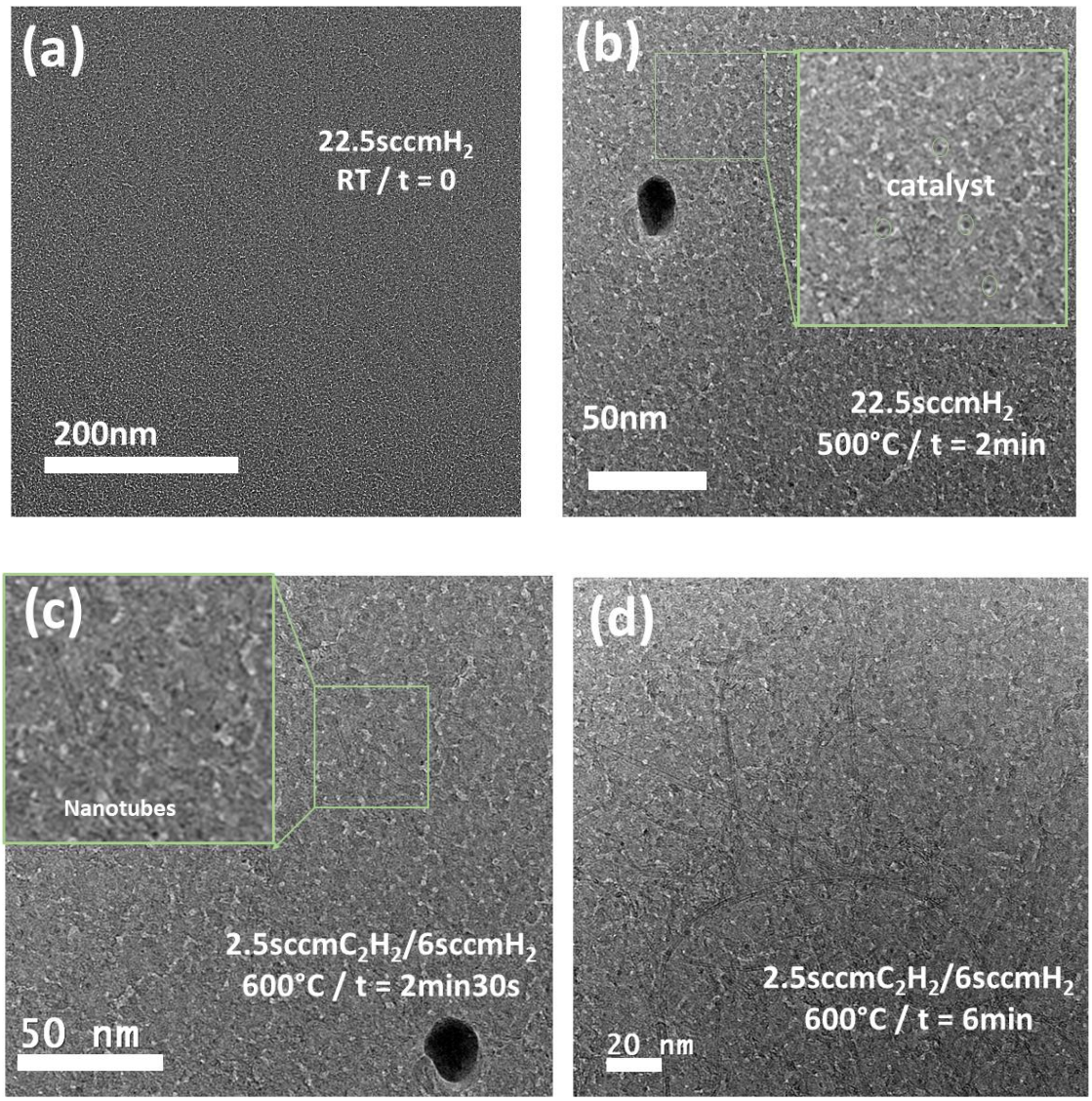

Figure 7.9 Time-sequence of TEM images extracted from video: (a) CNTs before the annealing and growth, (b) pretreatment of the catalytic thin film at 500°C after 2mins, (c) the growth of SWCNTs at 600°C, and (d) the termination of SWCNTs growth after 6mins

The growth of SWCNTs using the considered parameters was relatively very fast, resulting in difficulty of its capture. The mixture of straight long tubes, straight short tubes, and bundles of tubes are observed to overlap in the C membrane, which makes them impossible to accurately assess the diameter of individual SWCNT. Several long clean SWCNTs (1nm in diameter) were recorded at the membrane edges as in Figures 7.10 c-d. We also had a lot of difficulty in observing the catalytic nanoparticles, which indicates that the nanoparticles do not enlarge as much as in the previous studies during the heating process.

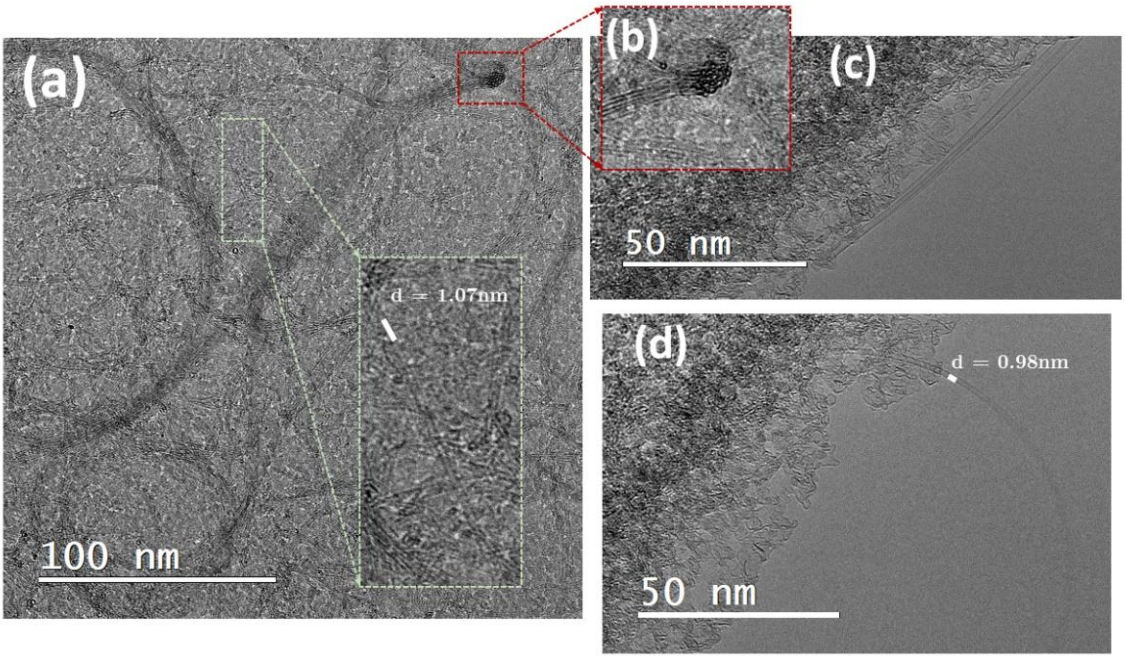

Figure 7.10 TEM images extracted from the growth of CNTs under a mixture of 2.5sccm of C_2H_2 and 6sccm of molecular H_2 at 600 °C: (a) SWCNTs in the membrane, (b) bundle of SWCNTs and (c)-(d) SWCNTs at the membrane edges (FEI -Titan NanoMAX)

To determine the diameter of SWCNTs synthesized on the C membrane, the ex-situ Raman spectroscopy measurement [20] was performed in an area of 7x7μm. Figures 7.11a-b show the RBM peaks recorded from 100 to 300cm^{-1} of wavenumber

under the excitation of 532nm and 633nm lasers. The position of peaks in this region indicates that the current sample contains small diameter tubes, in accordance with the RBM (ω_{RBM}) – SWCNT diameter (d_t) relationship: $\omega_{RBM} = 248/d_t$ [20]. The diameters are distributed heterogeneously from 0.8nm to 1.9nm as shown in Figure 7.11c. However, this does not reveal the full genuine diameter distribution in the sample because of the well-known pronunciation of Raman on resonant and small diameter SWCNTs. The average I_G/I_D ratio can reach approximately 6, which indicates the high purity of as-grown SWCNTs.

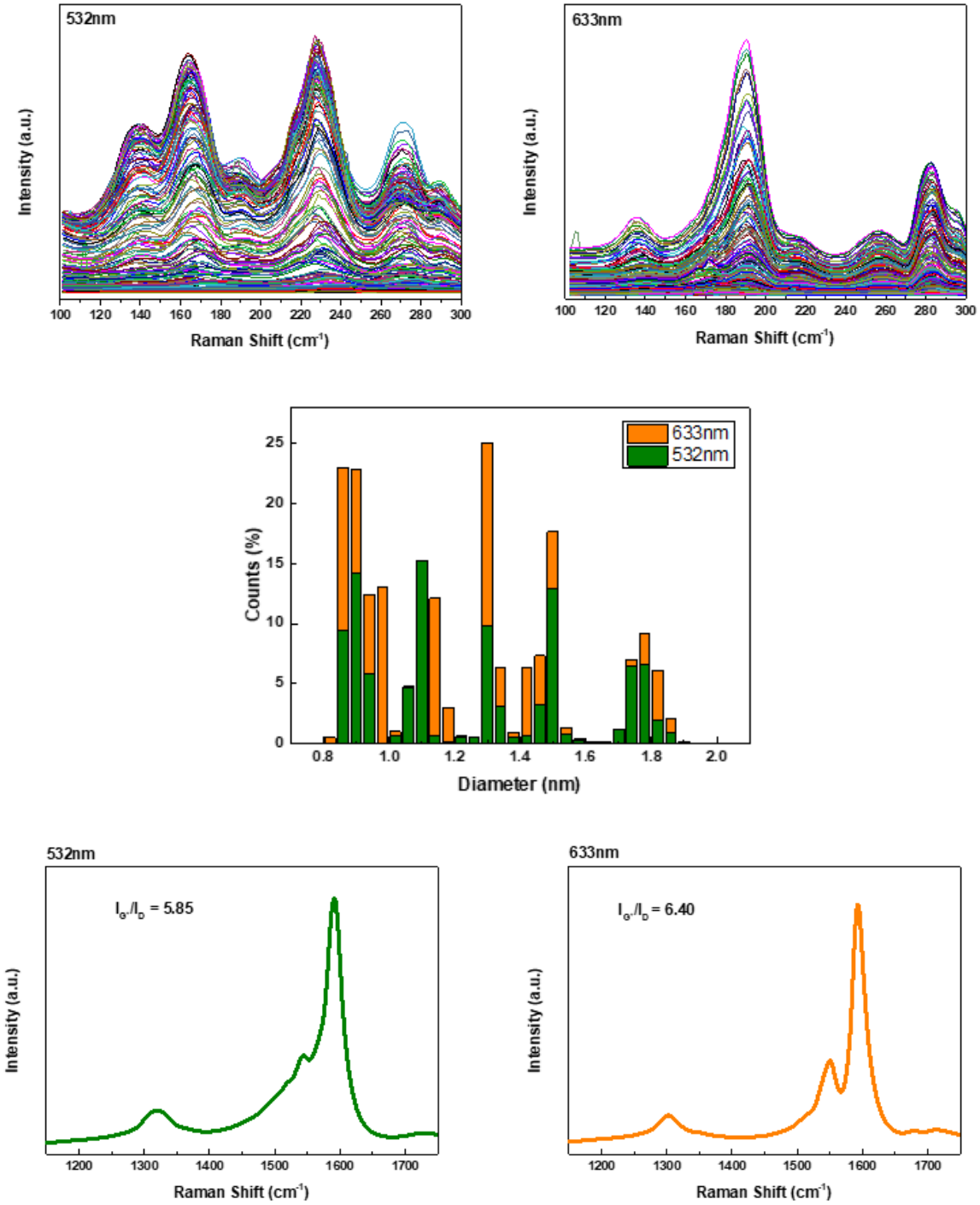

Figure 7.11 Ex-situ Raman studies: (a-b) Mapping in the RBM region with, (c) The diameter distribution of recorded SWCNTs, (d-e) the average spectra of D and G band from 100 points mapping with the value of I_D/I_G ratio

8. General Conclusion and Perspective

During this thesis, we explored the feasibility of implementing LPCVD in the synthesis of single walled carbon nanotubes (SWCNTs). We studied the influence of different growth parameters, such as temperature, pressure, gas flow, nature of catalyst to get a better understanding of the phenomena. Finally, we investigated how the promising LPCVD experiments could be reproduced in the in-situ CVD@ETEM. The central objective of the thesis was to develop and parametrize a macroscopic CVD synthesis path compatible with the potential coupling with the in-situ and real-time experiments in ETEM-NanoMax.

In chapter 1 and chapter 2, a series of bibliographical studies allowed us to review the various results from the literature, concerning the influence of certain operating parameters on the mechanisms of formation of the SWCNTs. We could see that the LP-HFCVD process seems to be one of the potential ways to produce SWCNTs at the conditions close to in-situ experiment in CVD@ETEM. We also found that for the synthesis of SWCNTs by CVD from methane, an increase in growth pressure or temperature allowed to obtain higher CNTs density.

In the following chapter, the growth of SWCNTs by HFCVD was first studied with different combination of the catalyst and the support layer. We observed a positive impact of the support layer Al_2O_3 on the efficiency and quality of the SWCNTs synthesis. This is the main reason why we used the Al_2O_3 layer for all the prepared sample in the following experiments. In order to improve the catalytic system, we considered preparing the bimetallic Fe-Mo catalysts with the objective of increasing the efficiency of the reaction or decreasing the defects in the as-grown SWCNTs. We have changed the thickness of the Mo layer in order to understand how this system works. We noticed that a sufficient amount Mo could enhance the stability of the catalyst which allow to increase the amount of SWCNTs obtained. On the other hand, we noted that molybdenum facilitated the decomposition of methane and consequently increased the activity of the system to produce carbon nanotubes. Based on this finding,

we came up with the idea of reproduction this experiment with the bimetallic Fe-Mo system to re-confirm our investigation

The second part of our work concerned the study of the influence of the CVD operating pressure on the density and diameter of SWCNTs. The catalyst pre-treated under the radicals activated H_2 environment led to the formation of nanoparticles, which is known as a nucleus for the SWCNTs growth. An increase of the growth pressure at different gas flow was tested. The lowest growth pressure achieved in our HFCVD to successfully grow the SWCNTs is 10^{-4}mbar, when introducing 5sccmCH_4 and 2.5sccmH_2. Regarding the reproducibility, several experiments were performed at several month intervals with similar operating conditions. We obtained the dependence of the density of CNTs and diameters of SWCNTs on the growth pressure. The series of successful experiments at the growth pressure of 10^{-3} and 10^{-2} mbar could be considered as a promising result to be reproduced in the in-situ experiment of ETEM. We have seen that several activation and deactivation processes are involved in the selectivity: i) The threshold pressure for nucleation at low pressure is all the higher as the diameter of the nanotube formed is small. ii) Encapsulation by an excess of carbon occurs at low temperatures and preferentially targets small nanoparticles.

The activation of carbon nanotube growth requires the reduction of the catalyst, but this alone does not determine the limits of the growth domain. At very low temperatures, only disordered structures are formed. Instead, thermal activation of a process is necessary for the structuring of carbon atoms on the catalyst surface, which can occur through either the diffusion of carbon adatoms on the metal surface or the healing of defects at the tube edge. An experimental study on the influence of temperature on SWCNT growth has shown that growth is limited by thermally activated surface processes at sufficiently high temperatures. The rate-limiting step is attributed to the dissociative adsorption of the precursor on the nanoparticle surface. This is supported by several factors, such as higher activation energies compared to carbon diffusion on metal, dependence on precursor and catalyst properties, and a shift

towards lower temperatures for the transition between growth regimes with increasing precursor reactivity.

Another area of focus, which has not been discussed thus far, is the synthesis of single-walled carbon nanotubes at both macroscopic and microscopic scales. In order to confirm the reproducibility of our experiments, which were conducted using the LP-HFCVD with the in-situ ETEM NanoMax system, we identified promising results from LP-HFCVD FENIX and reproduced them using the same synthesis conditions in the in-situ CVD@ETEM. Through this method, we were able to observe similar results while in-situ synthesizing SWCNTs using both Fe catalyst and Fe-Mo bimetallic catalyst systems. This approach allows us to perform the initial testing steps of SWCNT synthesis on the LP-HFCVD FENIX platform and then choose the appropriate experiments for each research purpose to reproduce using the CVD@ETEM in NanoMax system. By adopting this approach, we not only save time, money, and effort, but also improve the quality of efficient in-situ experiment.

Appendices & supplemental material

A. Appendix A: Different pressure at 800°C with high gas flow

Sample	5nmAl_2O_3/1nmFe on the SiO_2/Si substrate
Gas flow	2minutes pretreatment with 30sccmH_2 and 30minutes CNTs growth with 20sccmH_2/10sccmCH_4
Growth temperature	800°C

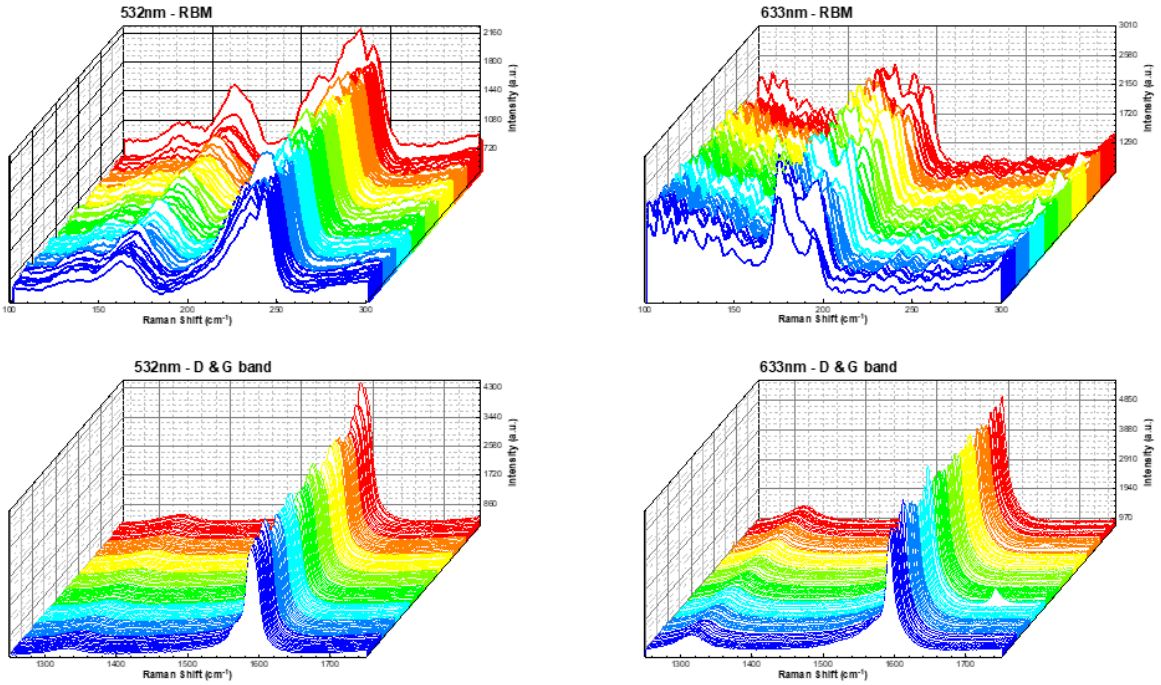

Figure A.1 The 100 points Raman mapping of sample synthesized at 800°C and 0.02mbar. The excitation wavelengths are 532nm and 633nm. The RBM region was recorded from 100cm^{-1} to 300cm^{-1}. The D band and G band were observed in high frequency region.

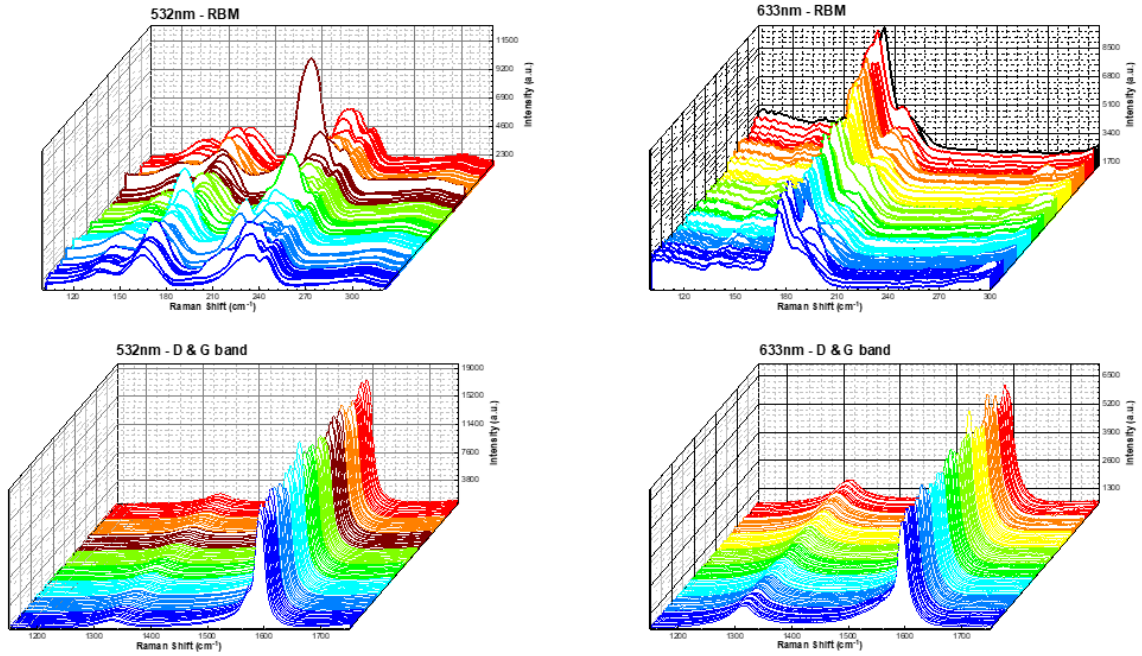

Figure A.2 The 100 points Raman mapping of sample synthesized at 800°C and 0.05mbar. The excitation wavelengths are 532nm and 633nm. The RBM region was recorded from 100cm^{-1} to 300cm^{-1}. The D band and G band were observed in high frequency region.

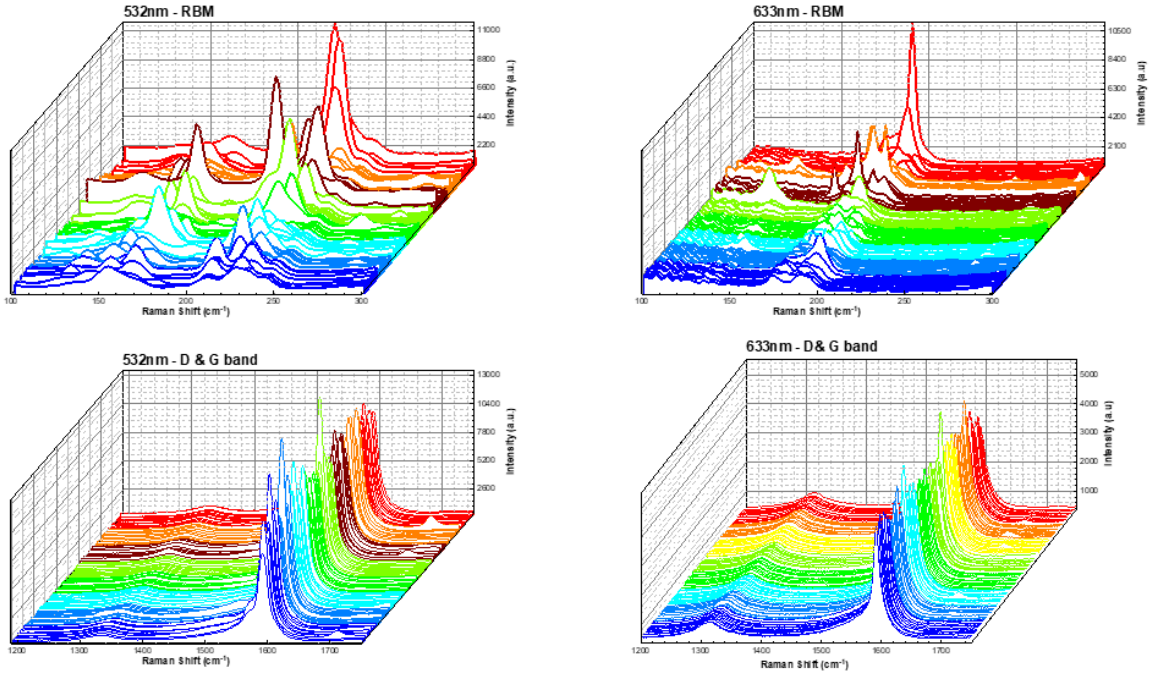

Figure A.3. The 100 points Raman mapping of sample synthesized at 800°C and 0.2mbar. The excitation wavelengths are 532nm and 633nm. The RBM region was recorded from 100cm^{-1} to 300cm^{-1}. The D band and G band were observed in high frequency region.

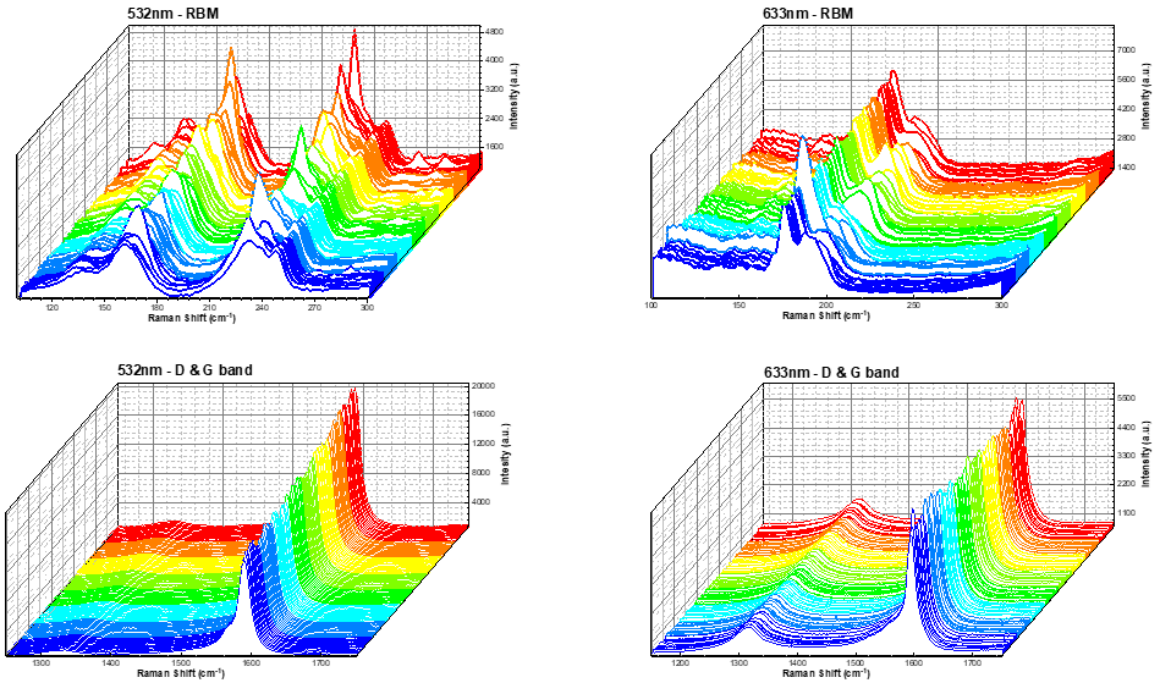

Figure A.4 The 100 points Raman mapping of sample synthesized at 800°C and 0.5mbar. The excitation wavelengths are 532nm and 633nm. The RBM region was recorded from 100cm^{-1} to 300cm^{-1}. The D band and G band were observed in high-frequency region.

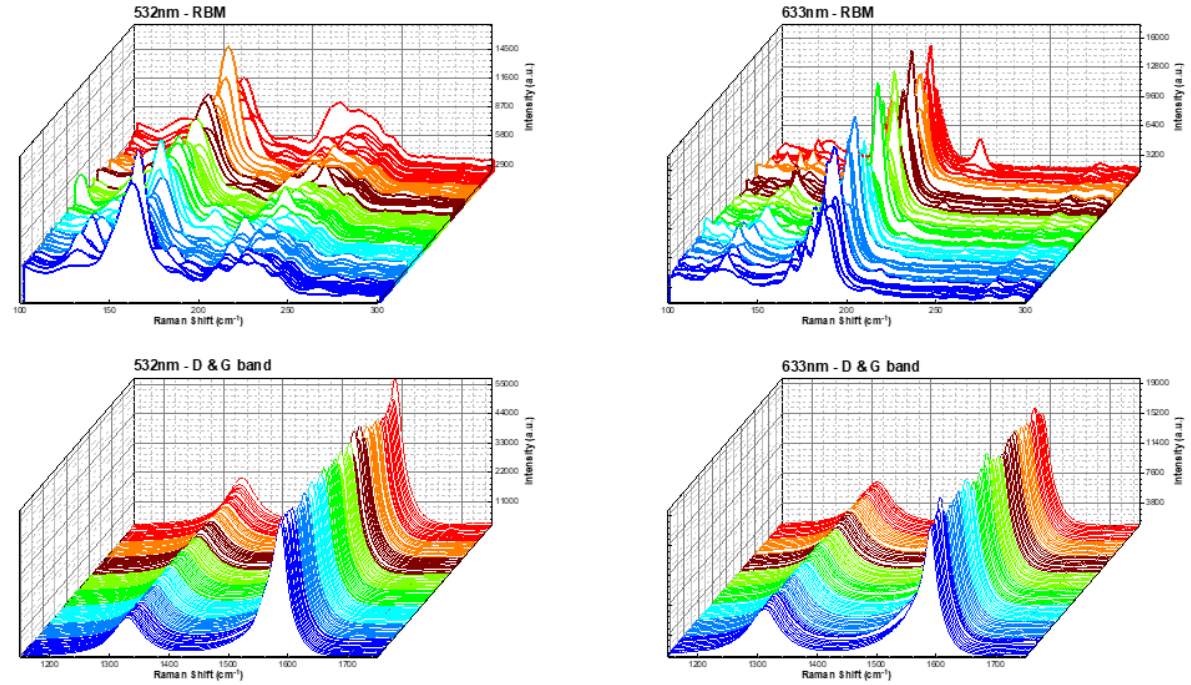

Figure A.5 The 100 points Raman mapping of sample synthesized at 800°C and 1.0mbar. The excitation wavelengths are 532nm and 633nm. The RBM region was recorded from 100cm^{-1} to 300cm^{-1}. The D band and G band were observed in high-frequency region.

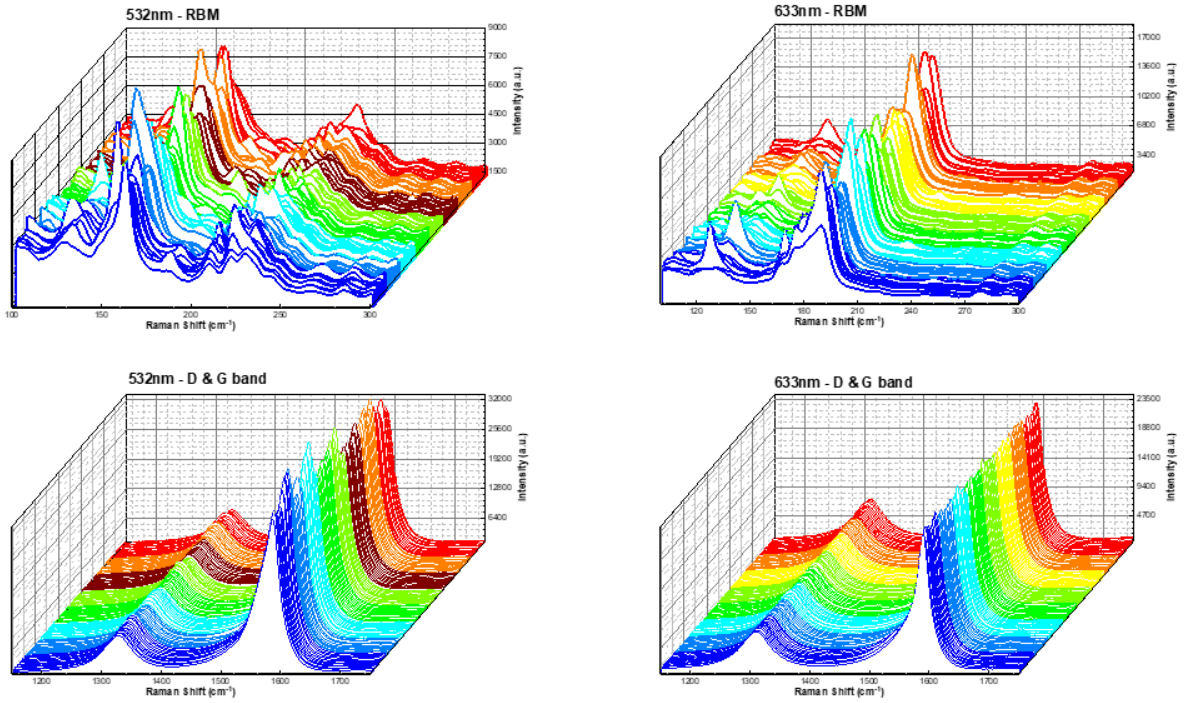

Figure A.6 The 100 points Raman mapping of sample synthesized at 800°C and 2.0mbar. The excitation wavelengths are 532nm and 633nm. The RBM region was recorded from 100cm^{-1} to 300cm^{-1}. The D band and G band were observed in high-frequency region.

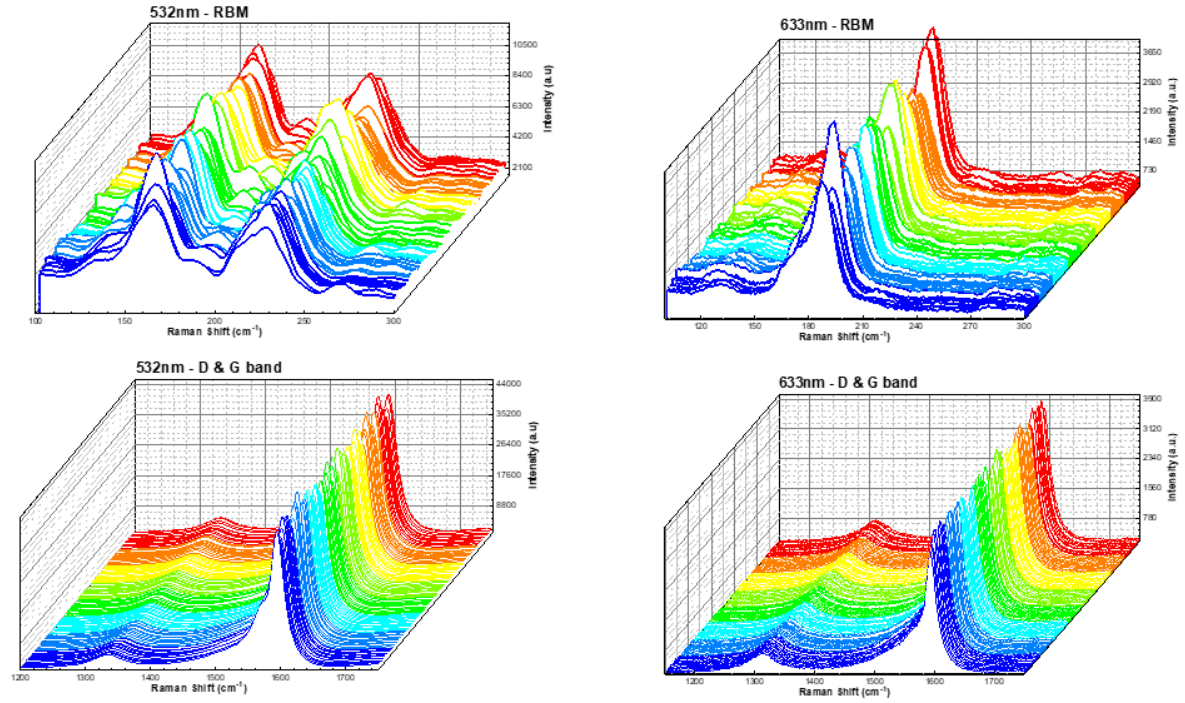

Figure A.7 The 100 points Raman mapping of sample synthesized at 800°C and 5.0mbar. The excitation wavelengths are 532nm and 633nm. The RBM region was recorded from 100cm^{-1} to 300cm^{-1}. The D band and G band were observed in high-frequency region.

B. Appendix B: Different pressure at 800°C with low gas flow

Sample	5nmAl_2O_3/1nmFe on the SiO_2/Si substrate
Gas flow	2minutes pretreatment with 5sccmH_2 and 30minutes CNTs growth with 2.5sccmH_2/5sccmCH_4
Growth temperature	800°C

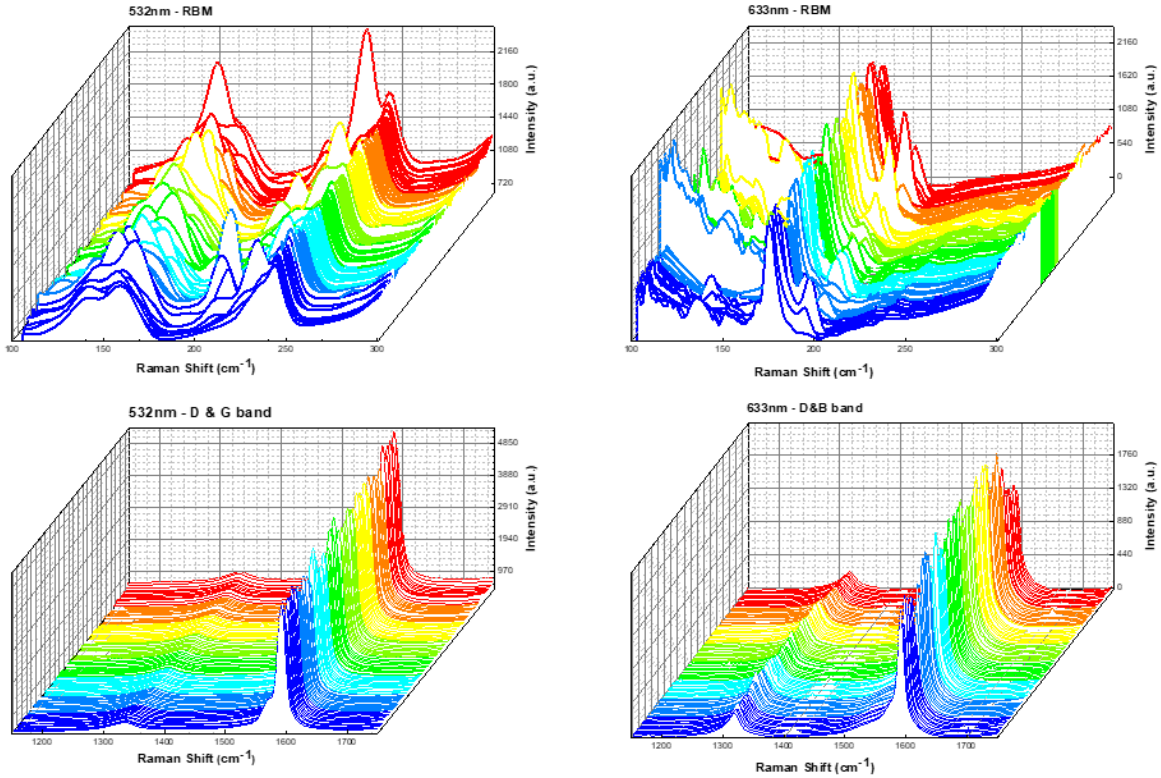

Figure B.1 The 100 points Raman mapping of sample synthesized at 800°C and 0.005mbar. The excitation wavelengths are 532nm and 633nm. The RBM region was recorded from 100cm^{-1} to 300cm^{-1}. The D band and G band were observed in high-frequency region.

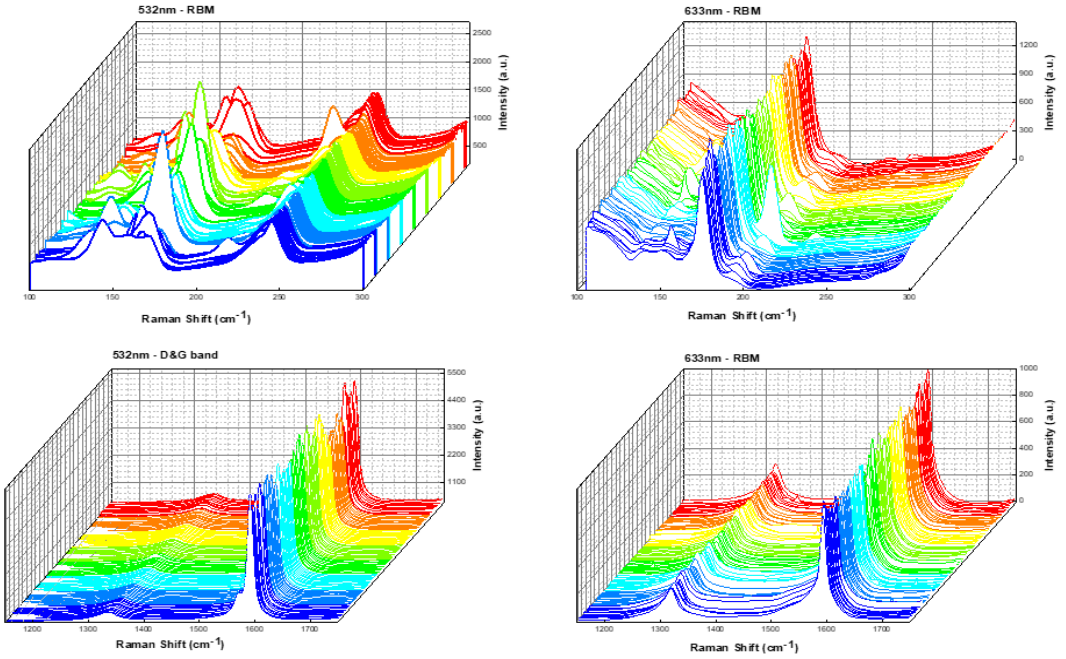

Figure B.2 The 100 points Raman mapping of sample synthesized at 800°C and 0.01mbar. The excitation wavelengths are 532nm and 633nm. The RBM region was recorded from 100cm^{-1} to 300cm^{-1}. The D band and G band were observed in high-frequency region.

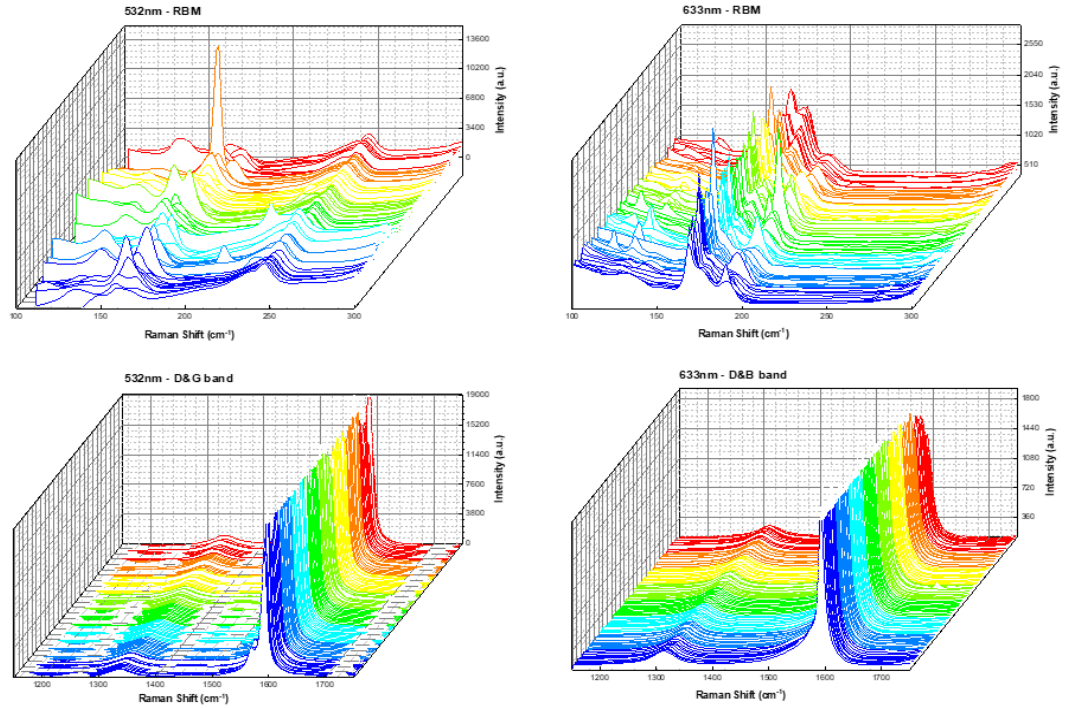

Figure B.3 The 100 points Raman mapping of sample synthesized at 800°C and 0.05mbar. The excitation wavelengths are 532nm and 633nm. The RBM region was recorded from 100cm^{-1} to 300cm^{-1}. The D band and G band were observed in high-frequency region.

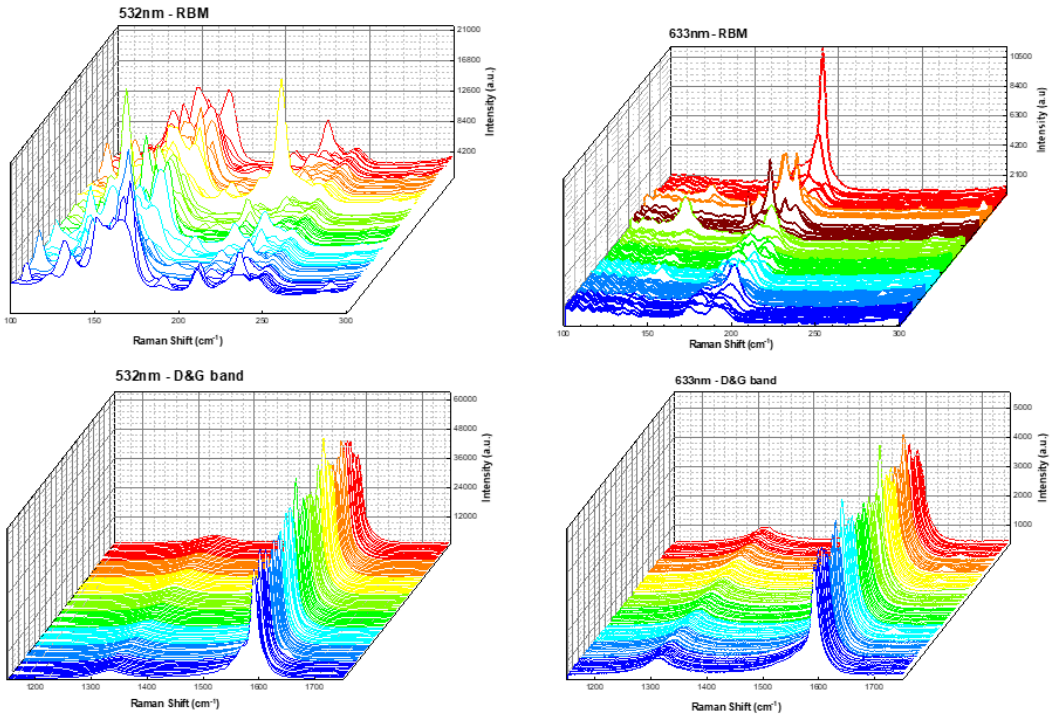

Figure B.4 The 100 points Raman mapping of sample synthesized at 800°C and 0.1mbar. The excitation wavelengths are 532nm and 633nm. The RBM region was recorded from 100cm^{-1} to 300cm^{-1}. The D band and G band were observed in high-frequency region.

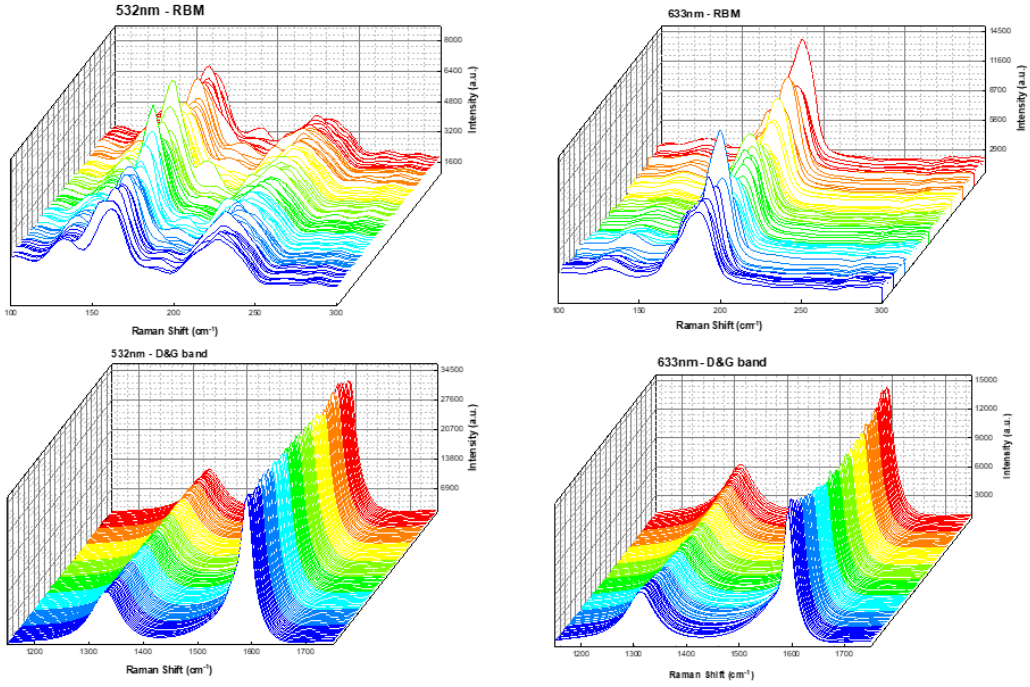

Figure B.5 The 100 points Raman mapping of sample synthesized at 800°C and 0.5mbar. The excitation wavelengths are 532nm and 633nm. The RBM region was recorded from 100cm^{-1} to 300cm^{-1}. The D band and G band were observed in high-frequency region.

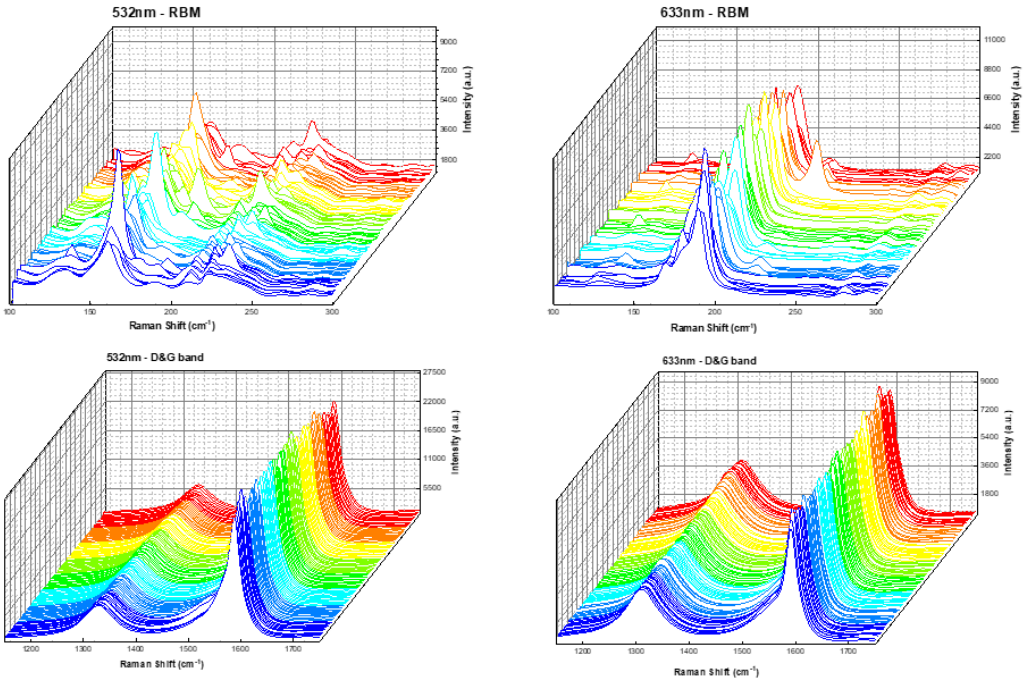

Figure B.6 The 100 points Raman mapping of sample synthesized at 800°C and 1.0mbar. The excitation wavelengths are 532nm and 633nm. The RBM region was recorded from 100cm^{-1} to 300cm^{-1}. The D band and G band were observed in high-frequency region.

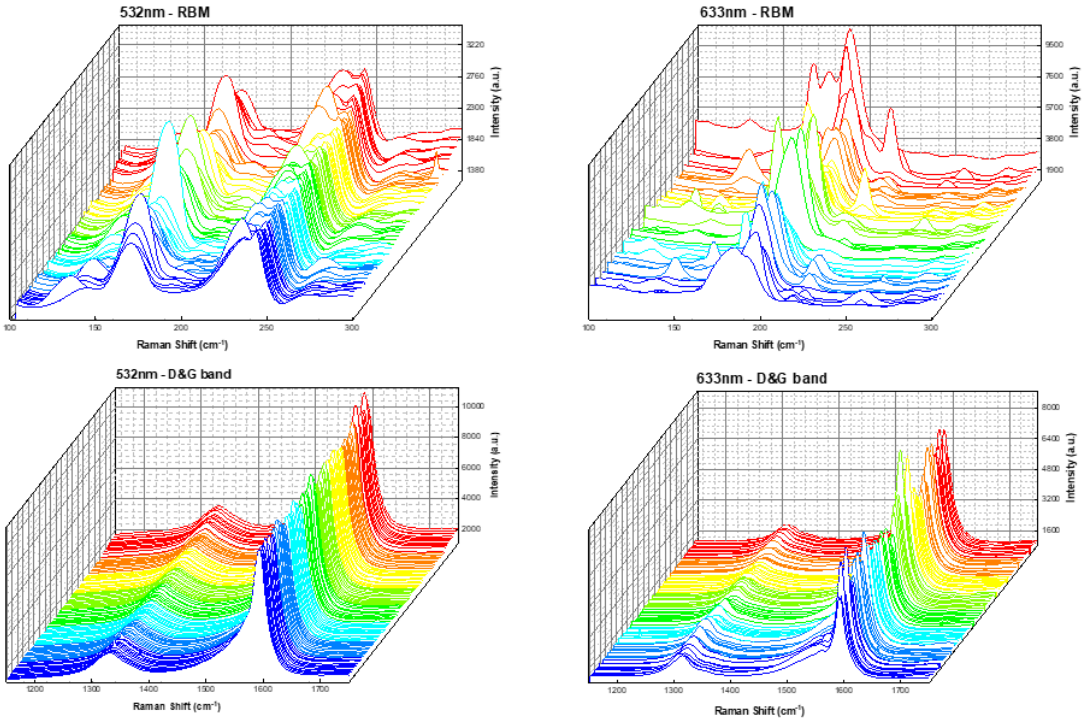

Figure B.7 The 100 points Raman mapping of sample synthesized at 800°C and 5.0mbar. The excitation wavelengths are 532nm and 633nm. The RBM region was recorded from 100cm^{-1} to 300cm^{-1}. The D band and G band were observed in high-frequency region.

C. Appendix C: Influence of temperature at standard pressures

Sample	5nmAl_2O_3/1nmFe on the SiO_2/Si substrate
Gas flow	2minutes pretreatment with 30sccmH_2 and 30minutes CNTs growth with 20sccmH_2/10sccmCH_4
Growth pressure	5mbar

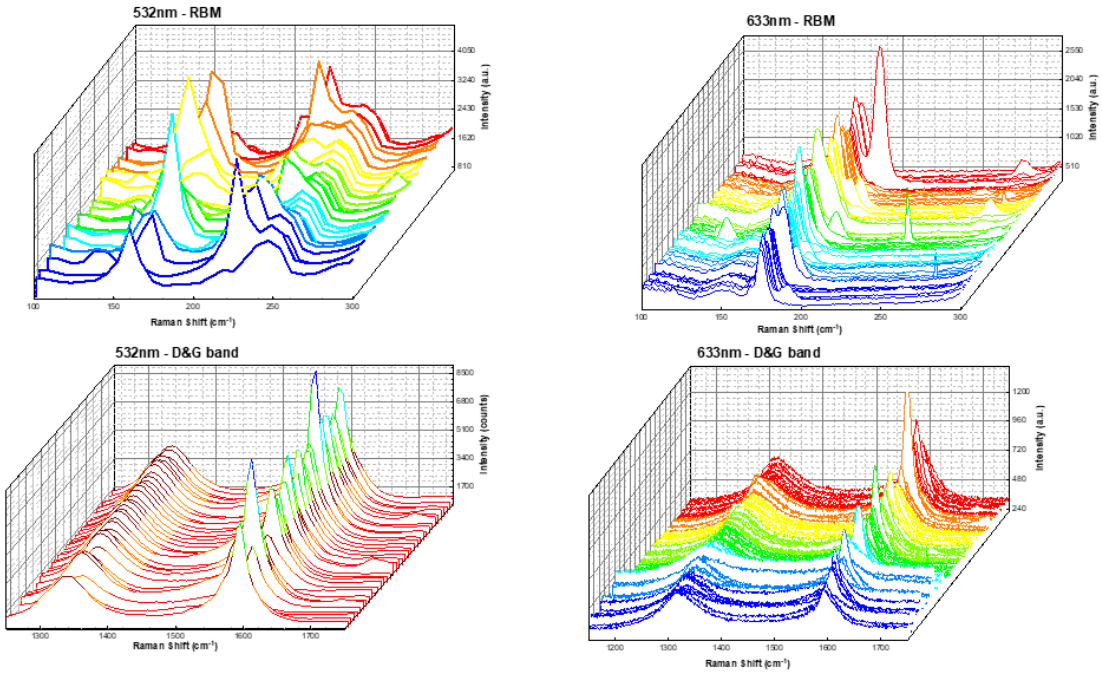

Figure C.1 The 100 points Raman mapping of sample synthesized at 600°C and 5.0mbar. The excitation wavelengths are 532nm and 633nm. The RBM region was recorded from 100cm^{-1} to 300cm^{-1}. The D band and G band were observed in high-frequency region.

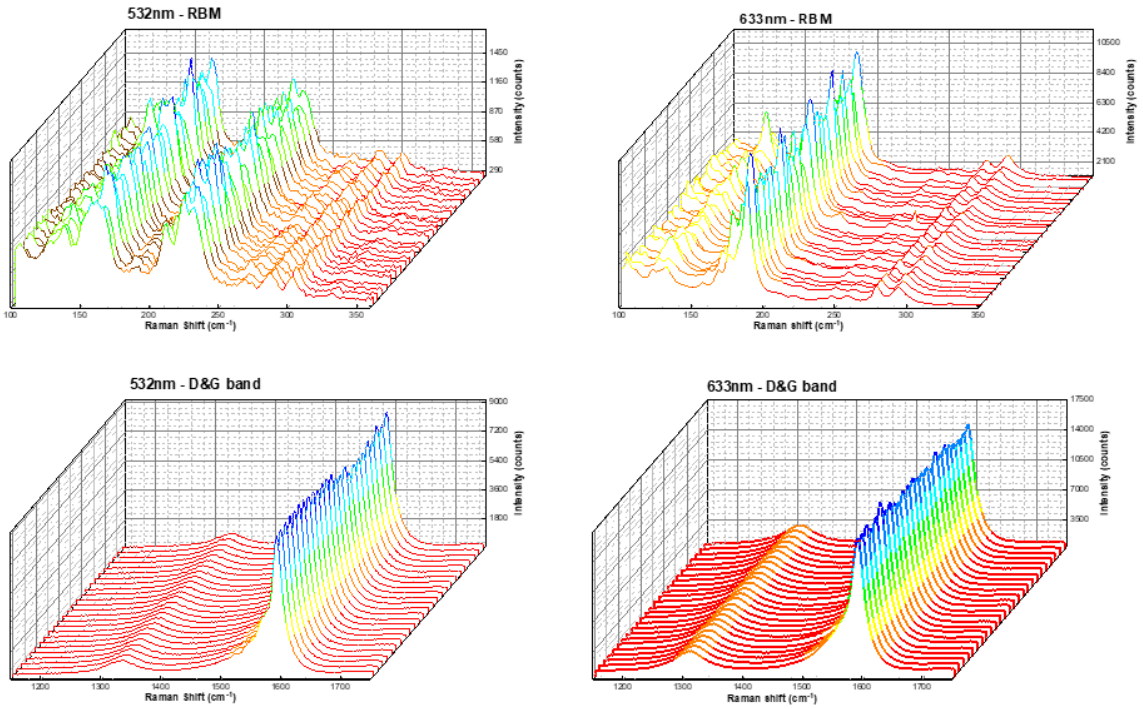

Figure C.2 The 100 points Raman mapping of sample synthesized at 700°C and 5.0mbar. The excitation wavelengths are 532nm and 633nm. The RBM region was recorded from 100cm^{-1} to 300cm^{-1}. The D band and G band were observed in high-frequency region.

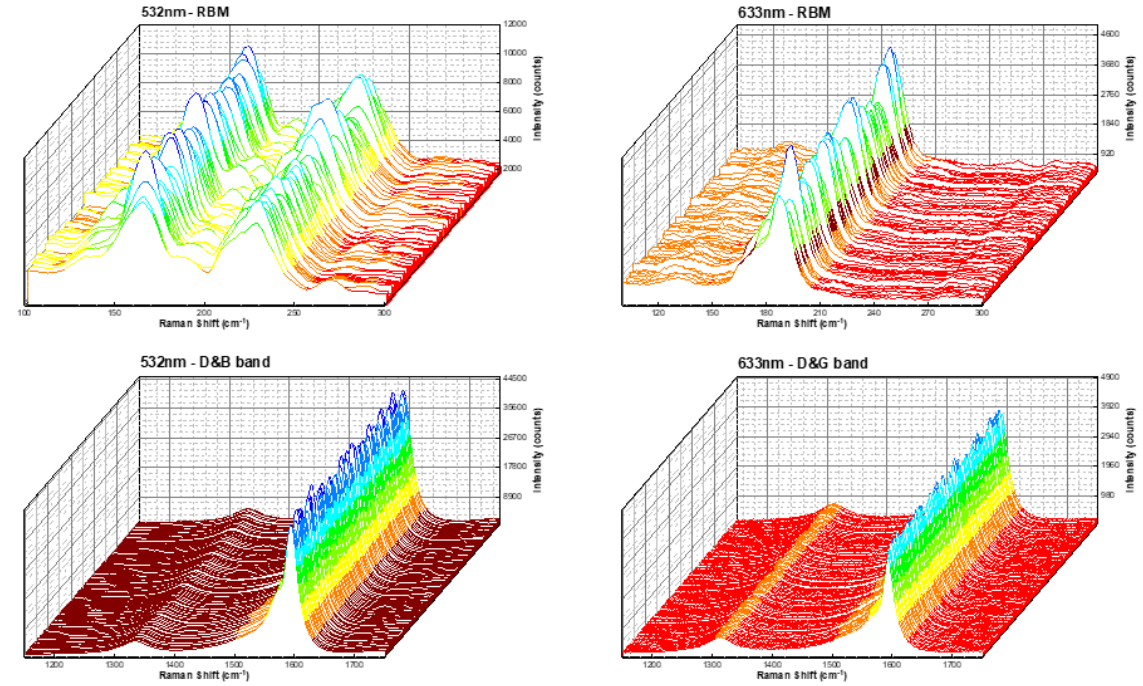

Figure C.3 The 100 points Raman mapping of sample synthesized at 800°C and 5.0mbar. The excitation wavelengths are 532nm and 633nm. The RBM region was recorded from 100cm^{-1} to 300cm^{-1}. The D band and G band were observed in high-frequency region.

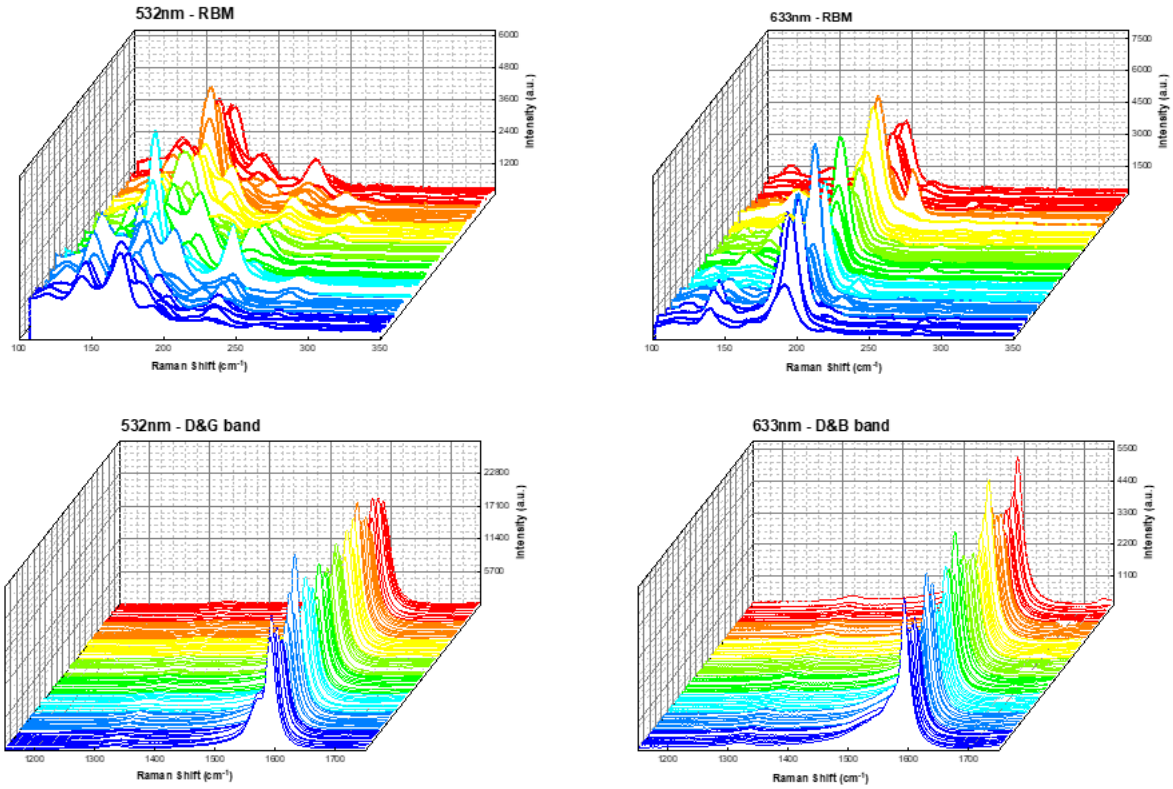

Figure C.4 The 100 points Raman mapping of sample synthesized at 900°C and 5.0mbar. The excitation wavelengths are 532nm and 633nm. The RBM region was recorded from 100cm^{-1} to 300cm^{-1}. The D band and G band were observed in high-frequency region.

D. Appendix D: Influence of temperature at low pressures

Sample	5nmAl_2O_3/1nmFe on the SiO_2/Si substrate
Gas flow	2minutes pretreatment with 5sccmH_2 and 30minutes CNTs growth with 2.5sccmH_2/5sccmCH_4
Growth pressure	0.5mbar

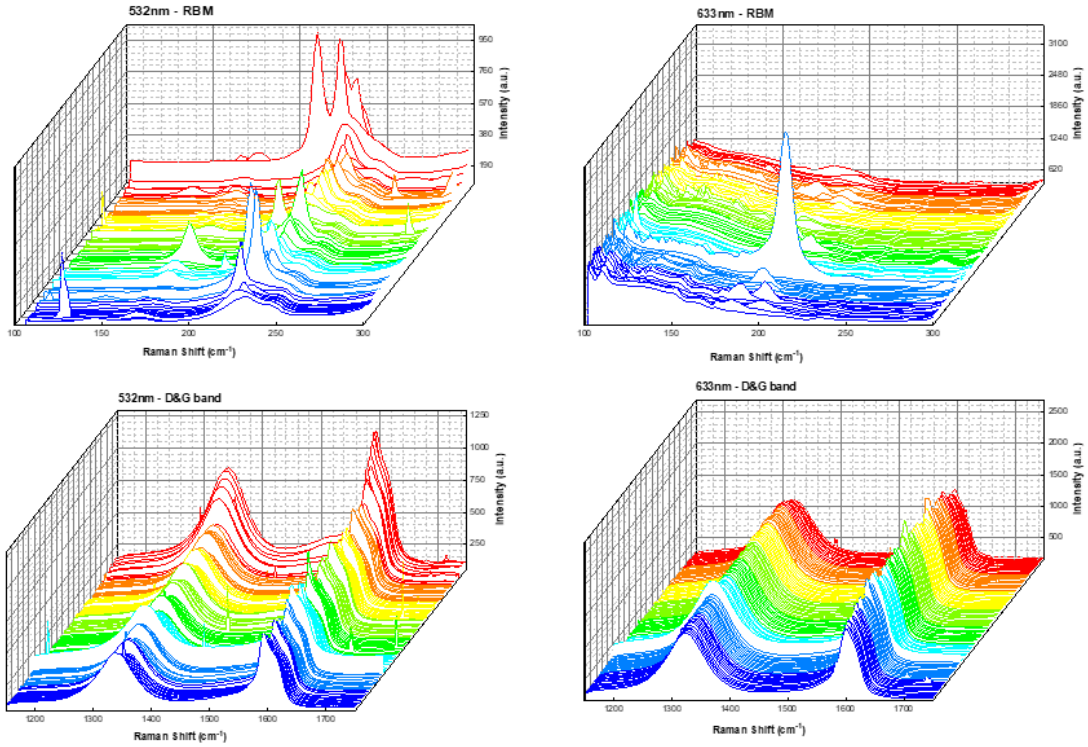

Figure D.1 The 100 points Raman mapping of sample synthesized at 500°C and 0.5mbar. The excitation wavelengths are 532nm and 633nm. The RBM region was recorded from 100cm^{-1} to 300cm^{-1}. The D band and G band were observed in high-frequency region.

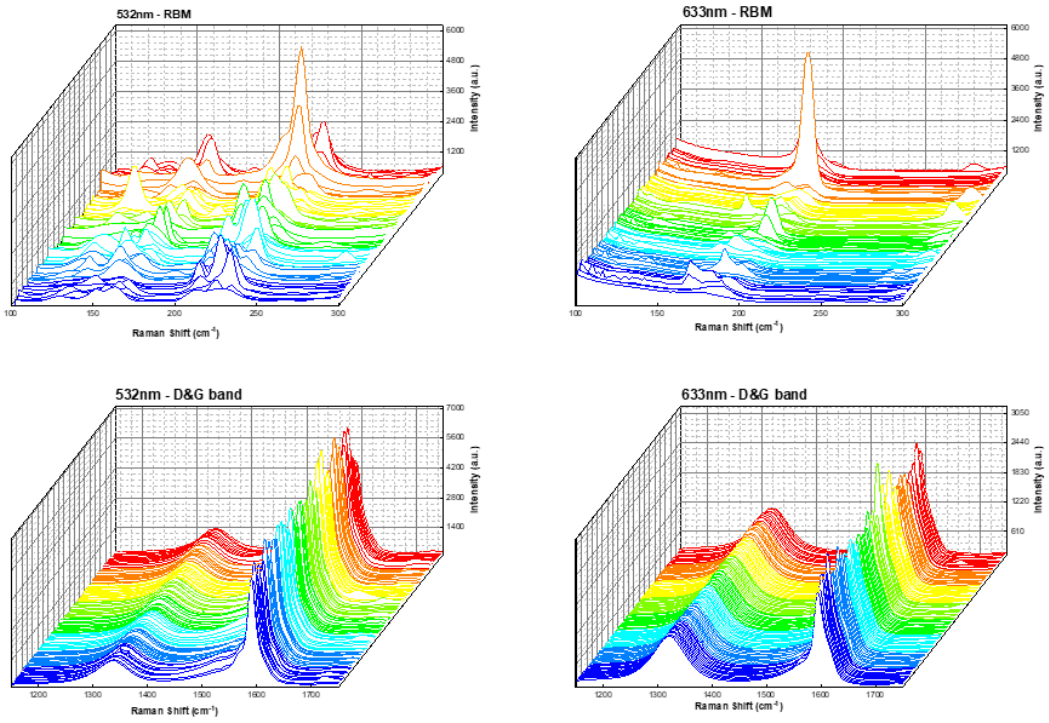

Figure D.2 The 100 points Raman mapping of sample synthesized at 600°C and 0.5mbar. The excitation wavelengths are 532nm and 633nm. The RBM region was recorded from 100cm^{-1} to 300cm^{-1}. The D band and G band were observed in high-frequency region.

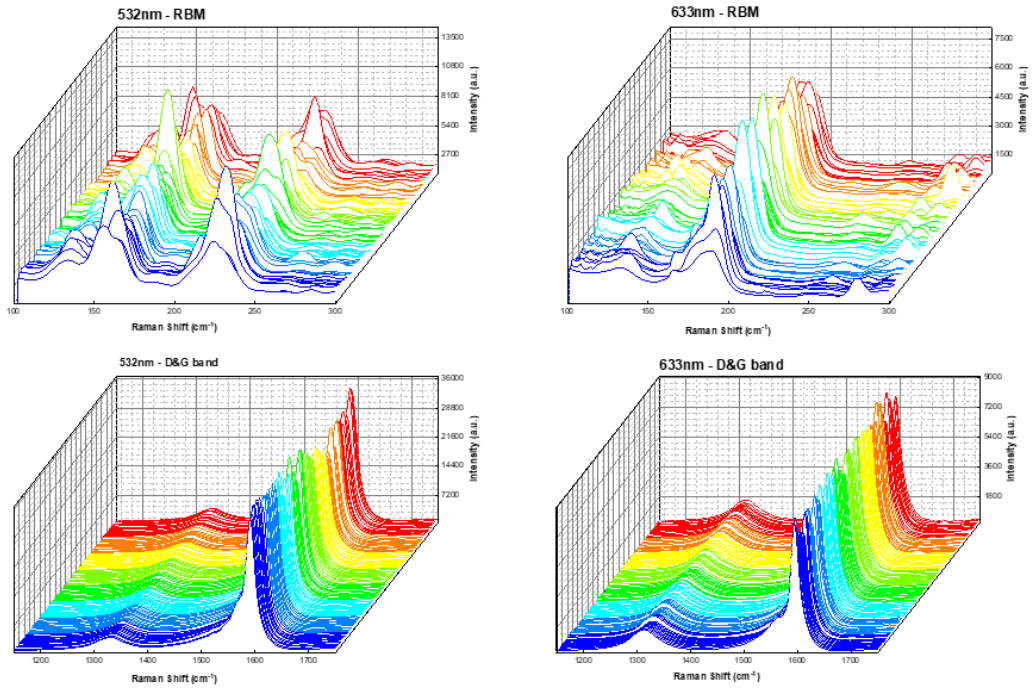

Figure D.3 The 100 points Raman mapping of sample synthesized at 700°C and 0.5mbar. The excitation wavelengths are 532nm and 633nm. The RBM region was recorded from 100cm^{-1} to 300cm^{-1}. The D band and G band were observed in high-frequency region.

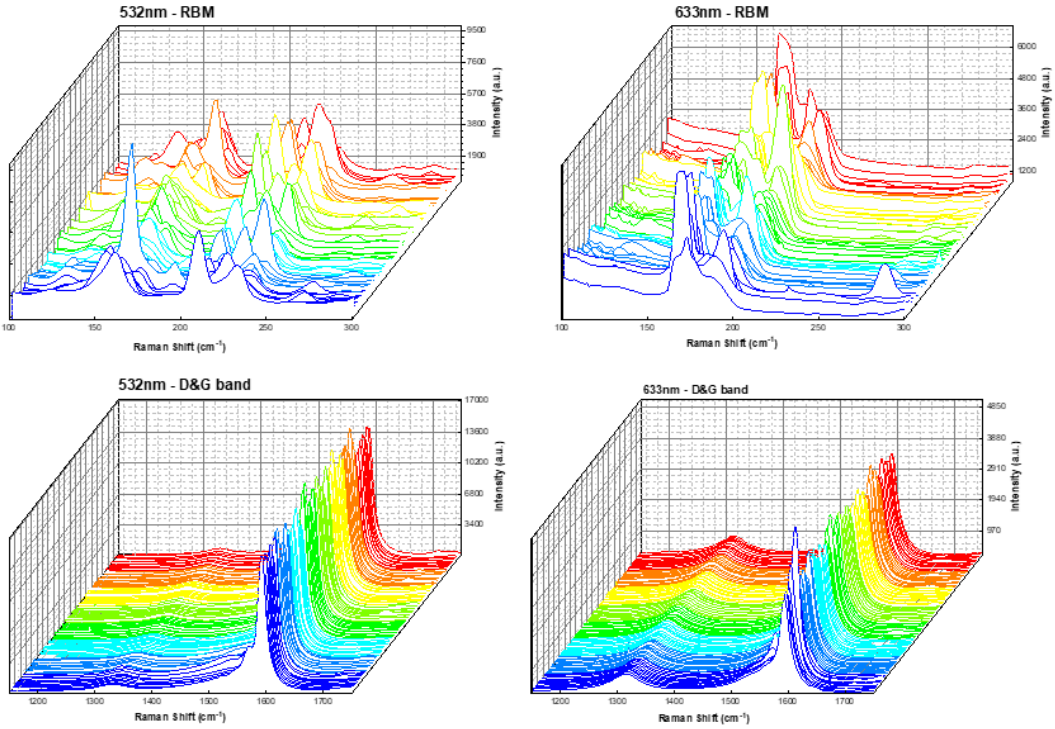

Figure D.4 The 100 points Raman mapping of sample synthesized at 800°C and 0.5mbar. The excitation wavelengths are 532nm and 633nm. The RBM region was recorded from 100cm^{-1} to 300cm^{-1}. The D band and G band were observed in high-frequency region.

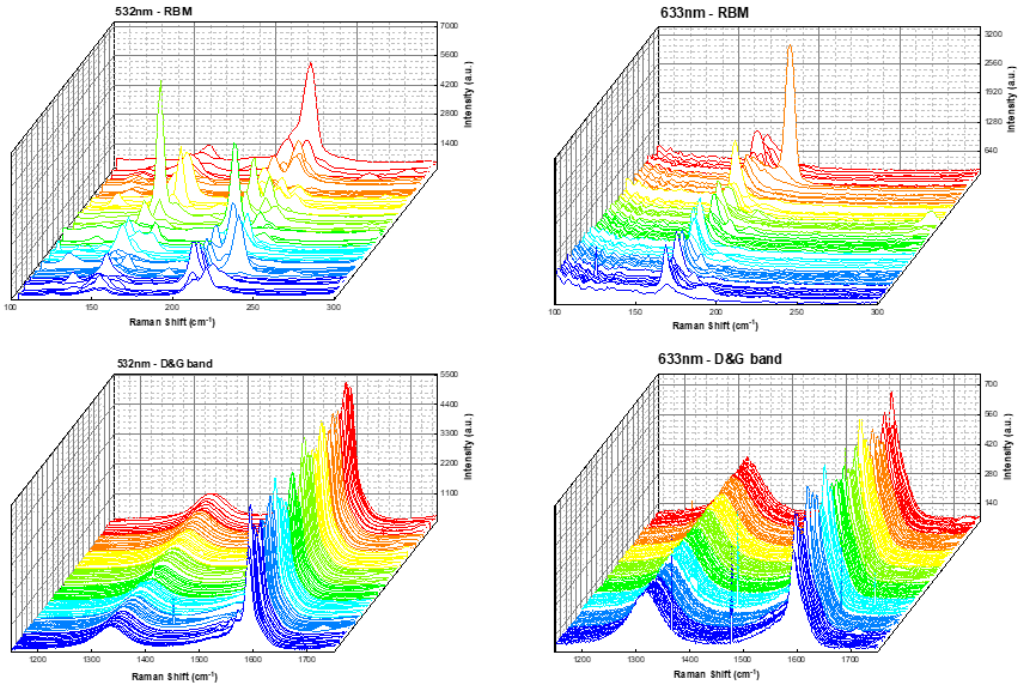

Figure D.5 The 100 points Raman mapping of sample synthesized at 900°C and 0.5mbar. The excitation wavelengths are 532nm and 633nm. The RBM region was recorded from 100cm^{-1} to 300cm^{-1}. The D band and G band were observed in high-frequency region.

The influence of temperature at 0.1mbar

Moreover, some additional experiments were conducted in order to observe the impact of growth temperature at lower pressure – 0.1mbar as summarized in Figure A.6. The catalytic film dewet to form the Fe nanoparticles when the temperature reaches 600°C (Figure D.6a). However, they appear to coalesce to form larger Fe aggregates. No nucleation of CNT was observed for this sample. When the temperature achieved 700°C, the Fe aggregates becomes larger, and we can notice the presence of a few short CNTs (Figure D.6b). The number and length of CNTs increase dramatically at 800°C (Figure D.6c), which is consistent with the observation in previous chapter. The growth is much poorer and tube density is very low when the temperature increases up to 900°C (Figure D.6d).

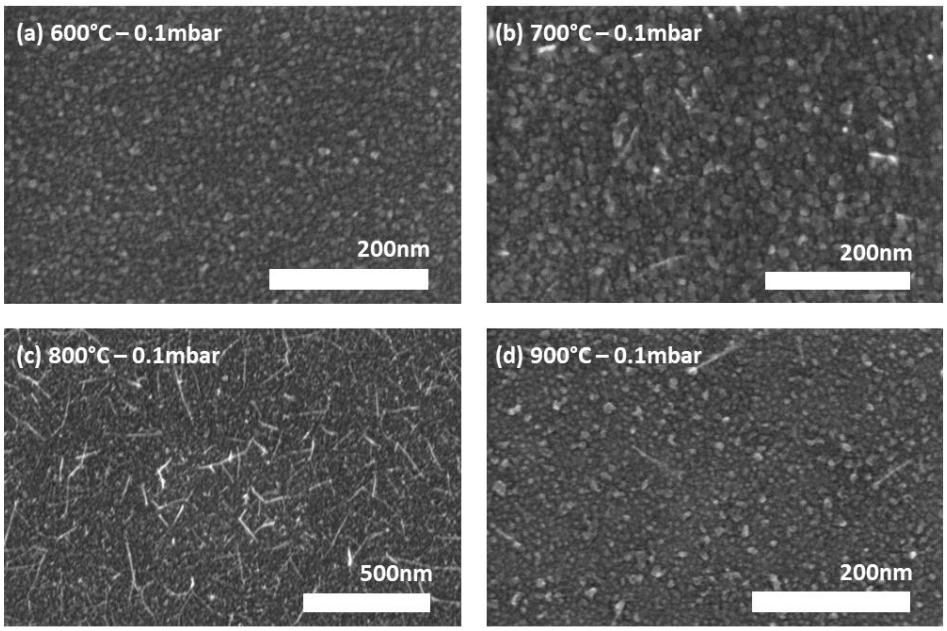

Figure D.6 The series of SEM images of samples synthesized at 0.1mbar and: (a)600°C, (b)700°C, (c)800°C, and (d)900°C

Bibliography

[1] R. P. Feynman, "There's Plenty of Room at the Bottom," *Eng. Sci.*, vol. 23, no. 5, Art. no. 5, Feb. 1960.

[2] H. W. Kroto, J. R. Heath, S. C. O'Brien, R. F. Curl, and R. E. Smalley, "C 60 : Buckminsterfullerene," *Nature*, vol. 318, no. 6042, pp. 162–163, Nov. 1985, doi: 10.1038/318162a0.

[3] S. Iijima, "Helical microtubules of graphitic carbon," *Nature*, vol. 354, no. 6348, pp. 56–58, Nov. 1991, doi: 10.1038/354056a0.

[4] K. S. Novoselov *et al.*, "Electric Field Effect in Atomically Thin Carbon Films," *Science*, vol. 306, no. 5696, pp. 666–669, Oct. 2004, doi: 10.1126/science.1102896.

[5] "The Nobel Prize in Physics 2010," NobelPrize.org. Accessed: Oct. 07, 2020. [Online]. Available: https://www.nobelprize.org/prizes/physics/2010/summary/

[6] P. Tian, L. Tang, K. S. Teng, and S. P. Lau, "Graphene quantum dots from chemistry to applications," *Mater. Today Chem.*, vol. 10, pp. 221–258, Dec. 2018, doi: 10.1016/j.mtchem.2018.09.007.

[7] M. Noked, A. Soffer, and D. Aurbach, "The electrochemistry of activated carbonaceous materials: past, present, and future," *J. Solid State Electrochem.*, vol. 15, no. 7, p. 1563, May 2011, doi: 10.1007/s10008-011-1411-y.

[8] Y.-P. Sun, K. Fu, Y. Lin, and W. Huang, "Functionalized Carbon Nanotubes: Properties and Applications," *Acc. Chem. Res.*, vol. 35, no. 12, pp. 1096–1104, Dec. 2002, doi: 10.1021/ar010160v.

[9] V. N. Popov, "Carbon nanotubes: properties and application," *Mater. Sci. Eng. R Rep.*, vol. 43, no. 3, pp. 61–102, Jan. 2004, doi: 10.1016/j.mser.2003.10.001.

[10] R. Saito, G. Dresselhaus, and M. S. Dresselhaus, *Physical Properties of Carbon Nanotubes*. PUBLISHED BY IMPERIAL COLLEGE PRESS AND DISTRIBUTED BY WORLD SCIENTIFIC PUBLISHING CO., 1998. doi: 10.1142/p080.

[11] P. Avouris, J. Appenzeller, R. Martel, and S. J. Wind, "Carbon nanotube electronics," *Proc. IEEE*, vol. 91, no. 11, pp. 1772–1784, Nov. 2003, doi: 10.1109/JPROC.2003.818338.

[12] D. Janas and K. K. Koziol, "Carbon nanotube fibers and films: synthesis, applications and perspectives of the direct-spinning method," *Nanoscale*, vol. 8, no. 47, pp. 19475–19490, Dec. 2016, doi: 10.1039/C6NR07549E.

[13] W. Zhang, Z. Zhang, and Y. Zhang, "The application of carbon nanotubes in target drug delivery systems for cancer therapies," *Nanoscale Res. Lett.*, vol. 6, no. 1, p. 555, Oct. 2011, doi: 10.1186/1556-276X-6-555.

[14] M. Kumar and Y. Ando, "Chemical vapor deposition of carbon nanotubes: a review on growth mechanism and mass production.," *J. Nanosci. Nanotechnol.*, vol. 10, no. 6, pp. 3739–3758, 2010, doi: 10.1166/jnn.2010.2939.

[15] J. Prasek *et al.*, "Methods for carbon nanotubes synthesis—review," *J. Mater. Chem.*, vol. 21, no. 40, pp. 15872–15884, Oct. 2011, doi: 10.1039/C1JM12254A.
[16] D. S. Bethune *et al.*, "Cobalt-catalysed growth of carbon nanotubes with single-atomic-layer walls," *Nature*, vol. 363, no. 6430, pp. 605–607, Jun. 1993, doi: 10.1038/363605a0.
[17] S. Iijima and T. Ichihashi, "Single-shell carbon nanotubes of 1-nm diameter," *Nature*, vol. 363, no. 6430, pp. 603–605, Jun. 1993, doi: 10.1038/363603a0.
[18] M. Picher, P. A. Lin, J. L. Gomez-Ballesteros, P. B. Balbuena, and R. Sharma, "Nucleation of Graphene and Its Conversion to Single-Walled Carbon Nanotubes," *Nano Lett.*, vol. 14, no. 11, pp. 6104–6108, Nov. 2014, doi: 10.1021/nl501977b.
[19] N. Hamada, S. Sawada, and A. Oshiyama, "New one-dimensional conductors: Graphitic microtubules," *Phys. Rev. Lett.*, vol. 68, no. 10, pp. 1579–1581, Mar. 1992, doi: 10.1103/PhysRevLett.68.1579.
[20] M. S. Dresselhaus, G. Dresselhaus, R. Saito, and A. Jorio, "Raman spectroscopy of carbon nanotubes," *Phys. Rep.*, vol. 409, no. 2, pp. 47–99, Mar. 2005, doi: 10.1016/j.physrep.2004.10.006.
[21] J. W. Mintmire, B. I. Dunlap, and C. T. White, "Are fullerene tubules metallic?," *Phys. Rev. Lett.*, vol. 68, no. 5, pp. 631–634, Feb. 1992, doi: 10.1103/PhysRevLett.68.631.
[22] T. Ando, "The electronic properties of graphene and carbon nanotubes," *NPG Asia Mater.*, vol. 1, no. 1, Art. no. 1, Oct. 2009, doi: 10.1038/asiamat.2009.1.
[23] A. H. Castro Neto, F. Guinea, N. M. R. Peres, K. S. Novoselov, and A. K. Geim, "The electronic properties of graphene," *Rev. Mod. Phys.*, vol. 81, no. 1, pp. 109–162, Jan. 2009, doi: 10.1103/RevModPhys.81.109.
[24] "Carbon Nanotubes: Basic Concepts and Physical Properties | Wiley," Wiley.com. Accessed: Jun. 21, 2022. [Online]. Available: https://www.wiley.com/en-us/Carbon+Nanotubes%3A+Basic+Concepts+and+Physical+Properties-p-9783527403868
[25] N. M. R. Peres, "The transport properties of graphene," *J. Phys. Condens. Matter*, vol. 21, no. 32, p. 323201, Jul. 2009, doi: 10.1088/0953-8984/21/32/323201.
[26] J. W. Mintmire and C. T. White, "Universal Density of States for Carbon Nanotubes," *Phys. Rev. Lett.*, vol. 81, no. 12, pp. 2506–2509, Sep. 1998, doi: 10.1103/PhysRevLett.81.2506.
[27] A. Kleiner and S. Eggert, "Band gaps of primary metallic carbon nanotubes," *Phys. Rev. B*, vol. 63, no. 7, p. 073408, Jan. 2001, doi: 10.1103/PhysRevB.63.073408.
[28] R. Saito, M. Fujita, G. Dresselhaus, and M. S. Dresselhaus, "Electronic Structure of Carbon Fibers based on C60," *MRS Online Proc. Libr.*, vol. 247, no. 1, pp. 333–338, Dec. 1992, doi: 10.1557/PROC-247-333.

[29] R. Saito, M. Fujita, G. Dresselhaus, and M. S. Dresselhaus, "Electronic structure of graphene tubules based on C60," *Phys. Rev. B*, vol. 46, no. 3, pp. 1804–1811, Jul. 1992, doi: 10.1103/PhysRevB.46.1804.

[30] P. Delaney, H. J. Choi, J. Ihm, S. G. Louie, and M. L. Cohen, "Broken symmetry and pseudogaps in ropes of carbon nanotubes," *Nature*, vol. 391, no. 6666, pp. 466–468, Jan. 1998, doi: 10.1038/35099.

[31] Y.-K. Kwon, S. Saito, and D. Tománek, "Effect of intertube coupling on the electronic structure of carbon nanotube ropes," *Phys. Rev. B*, vol. 58, no. 20, pp. R13314–R13317, Nov. 1998, doi: 10.1103/PhysRevB.58.R13314.

[32] H. Kataura *et al.*, "Optical properties of single-wall carbon nanotubes," *Synth. Met.*, vol. 103, no. 1, pp. 2555–2558, Jun. 1999, doi: 10.1016/S0379-6779(98)00278-1.

[33] R. Saito, G. Dresselhaus, and M. S. Dresselhaus, "Trigonal warping effect of carbon nanotubes," *Phys. Rev. B*, vol. 61, no. 4, pp. 2981–2990, Jan. 2000, doi: 10.1103/PhysRevB.61.2981.

[34] "1D eletronic DOS full table." Accessed: Jun. 22, 2021. [Online]. Available: http://www.photon.t.u-tokyo.ac.jp/~maruyama/kataura/1D_DOS.html

[35] T. S. Li and M. F. Lin, "Electron-electron scattering rates in moderate-gap toroidal carbon nanotubes," *Phys. Rev. B*, vol. 76, no. 7, p. 073409, Aug. 2007, doi: 10.1103/PhysRevB.76.073409.

[36] C. T. White and J. W. Mintmire, "Density of states reflects diameter in nanotubes," *Nature*, vol. 394, no. 6688, pp. 29–30, Jul. 1998, doi: 10.1038/27801.

[37] G. Overney, W. Zhong, and D. Tománek, "Structural rigidity and low frequency vibrational modes of long carbon tubules," *Z. Für Phys. At. Mol. Clust.*, vol. 27, no. 1, pp. 93–96, Mar. 1993, doi: 10.1007/BF01436769.

[38] B. I. Yakobson, C. J. Brabec, and J. Bernholc, "Nanomechanics of Carbon Tubes: Instabilities beyond Linear Response," *Phys. Rev. Lett.*, vol. 76, no. 14, pp. 2511–2514, Apr. 1996, doi: 10.1103/PhysRevLett.76.2511.

[39] J.-P. Salvetat *et al.*, "Mechanical properties of carbon nanotubes," *Appl. Phys. A*, vol. 69, no. 3, pp. 255–260, Sep. 1999, doi: 10.1007/s003390050999.

[40] J. Y. Huang *et al.*, "Superplastic carbon nanotubes," *Nature*, vol. 439, no. 7074, Art. no. 7074, Jan. 2006, doi: 10.1038/439281a.

[41] M. R. Predtechenskiy *et al.*, "New Perspectives in SWCNT Applications: Tuball SWCNTs. Part 2. New Composite Materials through Augmentation with Tuball.," *Carbon Trends*, vol. 8, p. 100176, Jul. 2022, doi: 10.1016/j.cartre.2022.100176.

[42] B. G. Demczyk *et al.*, "Direct mechanical measurement of the tensile strength and elastic modulus of multiwalled carbon nanotubes," *Mater. Sci. Eng. A*, vol. 334, no. 1, pp. 173–178, Sep. 2002, doi: 10.1016/S0921-5093(01)01807-X.

[43] M. R. Loos and K. Schulte, "Is It Worth the Effort to Reinforce Polymers With Carbon Nanotubes?," *Macromol. Theory Simul.*, vol. 20, no. 5, pp. 350–362, 2011, doi: 10.1002/mats.201100007.

[44] J. Hone, M. Whitney, and A. Zettl, "Thermal conductivity of single-walled carbon nanotubes," *Synth. Met.*, vol. 103, no. 1, pp. 2498–2499, Jun. 1999, doi: 10.1016/S0379-6779(98)01070-4.

[45] J. Hone, M. Whitney, C. Piskoti, and A. Zettl, "Thermal conductivity of single-walled carbon nanotubes," *Phys. Rev. B*, vol. 59, no. 4, pp. R2514–R2516, Jan. 1999, doi: 10.1103/PhysRevB.59.R2514.

[46] S. Berber, Y.-K. Kwon, and D. Tománek, "Unusually High Thermal Conductivity of Carbon Nanotubes," *Phys. Rev. Lett.*, vol. 84, no. 20, pp. 4613–4616, May 2000, doi: 10.1103/PhysRevLett.84.4613.

[47] J. Che, T. Çagin, and W. A. Goddard, "Thermal conductivity of carbon nanotubes," *Nanotechnology*, vol. 11, no. 2, pp. 65–69, Jun. 2000, doi: 10.1088/0957-4484/11/2/305.

[48] E. Pop, D. Mann, Q. Wang, K. Goodson, and H. Dai, "Thermal Conductance of an Individual Single-Wall Carbon Nanotube above Room Temperature," *Nano Lett.*, vol. 6, no. 1, pp. 96–100, Jan. 2006, doi: 10.1021/nl052145f.

[49] J. E. Graebner, "Thermal Conductivity of Diamond," in *Diamond: Electronic Properties and Applications*, L. S. Pan and D. R. Kania, Eds., in The Kluwer International Series in Engineering and Computer Science. , Boston, MA: Springer US, 1995, pp. 285–318. doi: 10.1007/978-1-4615-2257-7_7.

[50] L. M. Ericson *et al.*, "Macroscopic, Neat, Single-Walled Carbon Nanotube Fibers," *Science*, vol. 305, no. 5689, pp. 1447–1450, Sep. 2004, doi: 10.1126/science.1101398.

[51] S. C. Tsang, P. J. F. Harris, and M. L. H. Green, "Thinning and opening of carbon nanotubes by oxidation using carbon dioxide," *Nature*, vol. 362, no. 6420, Art. no. 6420, Apr. 1993, doi: 10.1038/362520a0.

[52] J. Chen *et al.*, "Solution Properties of Single-Walled Carbon Nanotubes," *Science*, vol. 282, no. 5386, pp. 95–98, Oct. 1998, doi: 10.1126/science.282.5386.95.

[53] B. Yu, F. Zhou, G. Liu, Y. Liang, W. T. S. Huck, and W. Liu, "The electrolyte switchable solubility of multi-walled carbon nanotube/ionic liquid (MWCNT/IL) hybrids," *Chem. Commun.*, no. 22, pp. 2356–2358, May 2006, doi: 10.1039/B603878F.

[54] D. M. Guldi, G. M. A. Rahman, F. Zerbetto, and M. Prato, "Carbon Nanotubes in Electron Donor−Acceptor Nanocomposites," *Acc. Chem. Res.*, vol. 38, no. 11, pp. 871–878, Nov. 2005, doi: 10.1021/ar040238i.

[55] R. J. Chen, Y. Zhang, D. Wang, and H. Dai, "Noncovalent Sidewall Functionalization of Single-Walled Carbon Nanotubes for Protein Immobilization," *J. Am. Chem. Soc.*, vol. 123, no. 16, pp. 3838–3839, Apr. 2001, doi: 10.1021/ja010172b.

[56] M. Burghard, "Asymmetric End-Functionalization of Carbon Nanotubes," *Small*, vol. 1, no. 12, pp. 1148–1150, 2005, doi: 10.1002/smll.200500257.

[57] C. Li *et al.*, "Complementary Detection of Prostate-Specific Antigen Using In2O3 Nanowires and Carbon Nanotubes," *J. Am. Chem. Soc.*, vol. 127, no. 36, pp. 12484–12485, Sep. 2005, doi: 10.1021/ja053761g.

[58] W. Krätschmer, L. D. Lamb, K. Fostiropoulos, and D. R. Huffman, "Solid C60: a new form of carbon," *Nature*, vol. 347, no. 6291, Art. no. 6291, Sep. 1990, doi: 10.1038/347354a0.

[59] C. Journet and P. Bernier, "Production of carbon nanotubes," *Appl. Phys. A*, vol. 67, no. 1, pp. 1–9, Jul. 1998, doi: 10.1007/s003390050731.

[60] X. Li, H. Zhu, B. Jiang, J. Ding, C. Xu, and D. Wu, "High-yield synthesis of multi-walled carbon nanotubes by water-protected arc discharge method," *Carbon*, vol. 41, no. 8, pp. 1664–1666, Jan. 2003, doi: 10.1016/S0008-6223(03)00128-3.

[61] N. Arora and N. N. Sharma, "Arc discharge synthesis of carbon nanotubes: Comprehensive review," *Diam. Relat. Mater.*, vol. 50, pp. 135–150, Nov. 2014, doi: 10.1016/j.diamond.2014.10.001.

[62] Y. Su, Z. Yang, H. Wei, E. S.-W. Kong, and Y. Zhang, "Synthesis of single-walled carbon nanotubes with selective diameter distributions using DC arc discharge under CO mixed atmosphere," *Appl. Surf. Sci.*, vol. 257, no. 7, pp. 3123–3127, Jan. 2011, doi: 10.1016/j.apsusc.2010.10.127.

[63] M. Jahanshahi and A. D. Kiadehi, "Fabrication, Purification and Characterization of Carbon Nanotubes: Arc-Discharge in Liquid Media (ADLM)," *Synth. Appl. Carbon Nanotub. Their Compos.*, May 2013, doi: 10.5772/51116.

[64] S. Jong Lee, H. Koo Baik, J. Yoo, and J. Hoon Han, "Large scale synthesis of carbon nanotubes by plasma rotating arc discharge technique," *Diam. Relat. Mater.*, vol. 11, no. 3, pp. 914–917, Mar. 2002, doi: 10.1016/S0925-9635(01)00639-2.

[65] V. K. Varadan, *Nanoscience and Nanotechnology in Engineering*. page 124: World Scientific, 2010.

[66] T. Guo, P. Nikolaev, A. Thess, D. T. Colbert, and R. E. Smalley, "Catalytic growth of single-walled manotubes by laser vaporization," *Chem. Phys. Lett.*, vol. 243, no. 1, pp. 49–54, Sep. 1995, doi: 10.1016/0009-2614(95)00825-O.

[67] N. Braidy, M. A. El Khakani, and G. A. Botton, "Single-wall carbon nanotubes synthesis by means of UV laser vaporization," *Chem. Phys. Lett.*, vol. 354, no. 1, pp. 88–92, Mar. 2002, doi: 10.1016/S0009-2614(02)00110-0.

[68] A. Thess *et al.*, "Crystalline Ropes of Metallic Carbon Nanotubes," *Science*, vol. 273, no. 5274, pp. 483–487, Jul. 1996, doi: 10.1126/science.273.5274.483.

[69] A. Oberlin, M. Endo, and T. Koyama, "Filamentous growth of carbon through benzene decomposition," *J. Cryst. Growth*, vol. 32, no. 3, pp. 335–349, Mar. 1976, doi: 10.1016/0022-0248(76)90115-9.

[70] J.-W. Snoeck, G. F. Froment, and M. Fowles, "Filamentous Carbon Formation and Gasification: Thermodynamics, Driving Force, Nucleation, and Steady-State Growth," *J. Catal.*, vol. 169, no. 1, pp. 240–249, Jul. 1997, doi: 10.1006/jcat.1997.1634.

[71] J. L. Figueiredo, C. A. Bernardo, J. J. Chludzinski, and R. T. K. Baker, "The reversibility of filamentous carbon growth and gasification," *J. Catal.*, vol. 110, no. 1, pp. 127–138, Mar. 1988, doi: 10.1016/0021-9517(88)90303-X.

[72] X.-D. Wang, K. Vinodgopal, and G.-P. Dai, *Synthesis of Carbon Nanotubes by Catalytic Chemical Vapor Deposition*. IntechOpen, 2019. doi: 10.5772/intechopen.86995.

[73] L. W. Liu *et al.*, "Chemical Vapor Deposition of Individual Single-Walled Carbon Nanotubes Using Nickel Sulfate as Catalyst Precursor," *J. Phys. Chem. B*, vol. 108, no. 48, pp. 18460–18462, Dec. 2004, doi: 10.1021/jp047721v.

[74] A. Kaneko, K. Yamada, R. Kumahara, H. Kato, and Y. Homma, "Comparative Study of Catalytic Activity of Iron and Cobalt for Growing Carbon Nanotubes on Alumina and Silicon Oxide," *J. Phys. Chem. C*, vol. 116, no. 49, pp. 26060–26065, Dec. 2012, doi: 10.1021/jp309232w.

[75] B. Wang, L. Wei, L. Yao, L.-J. Li, Y. Yang, and Y. Chen, "Pressure-Induced Single-Walled Carbon Nanotube (n,m) Selectivity on Co–Mo Catalysts," *J. Phys. Chem. C*, vol. 111, no. 40, pp. 14612–14616, Oct. 2007, doi: 10.1021/jp0762525.

[76] D. Selbmann, B. Bendjemil, A. Leonhardt, T. Pichler, C. Täschner, and M. Ritschel, "A parametric study of the synthesis and purification of single-walled carbon nanotubes using the high-pressure carbon monoxide process," *Appl. Phys. A*, vol. 90, no. 4, pp. 637–643, Mar. 2008, doi: 10.1007/s00339-007-4365-2.

[77] G. Zhong, T. Iwasaki, K. Honda, Y. Furukawa, I. Ohdomari, and H. Kawarada, "Low Temperature Synthesis of Extremely Dense and Vertically Aligned Single-Walled Carbon Nanotubes," *Jpn. J. Appl. Phys.*, vol. 44, no. 4R, p. 1558, Apr. 2005, doi: 10.1143/JJAP.44.1558.

[78] F. Z. Bouanis, L. Baraton, V. Huc, D. Pribat, and C. S. Cojocaru, "High-quality single-walled carbon nanotubes synthesis by hot filament CVD on Ru nanoparticle catalyst," *Thin Solid Films*, vol. 519, no. 14, pp. 4594–4597, May 2011, doi: 10.1016/j.tsf.2011.01.326.

[79] Md. M. Rahman, H. Younes, G. Ni, T. Zhang, and A. Al Ghaferi, "Synthesis and optical characterization of carbon nanotube arrays," *Mater. Res. Bull.*, vol. 77, pp. 243–252, May 2016, doi: 10.1016/j.materresbull.2016.01.050.

[80] B. C. Liu *et al.*, "Single-walled carbon nanotubes produced by catalytic chemical vapor deposition of acetylene over Fe–Mo/MgO catalyst," *Chem. Phys. Lett.*, vol. 383, no. 1, pp. 104–108, Jan. 2004, doi: 10.1016/j.cplett.2003.10.134.

[81] F. Ramírez Rodríguez, B. L. López, and L. F. Giraldo, "Single Wall Carbon Nanotubes Synthesis through Methane Chemical Vapor Deposition over MCM-41–Co Catalysts: Variables Optimization," *C — J. Carbon Res.*, vol. 4, no. 2, p. 37, Jun. 2018, doi: 10.3390/c4020037.

[82] M. G. Donato, G. Messina, C. Milone, A. Pistone, and S. Santangelo, "Experiments on C nanotubes synthesis by Fe-assisted ethane decomposition," *Diam. Relat. Mater.*, vol. 17, no. 3, pp. 318–324, Mar. 2008, doi: 10.1016/j.diamond.2007.12.043.

[83] H. Ago *et al.*, "Gas analysis of the CVD process for high yield growth of carbon nanotubes over metal-supported catalysts," *Carbon*, vol. 44, no. 14, pp. 2912–2918, Nov. 2006, doi: 10.1016/j.carbon.2006.05.049.

[84] S. Ahmad *et al.*, "Systematic investigation of the catalyst composition effects on single-walled carbon nanotubes synthesis in floating-catalyst CVD," *Carbon*, vol. 149, pp. 318–327, Aug. 2019, doi: 10.1016/j.carbon.2019.04.026.

[85] M. J. Bronikowski, "CVD growth of carbon nanotube bundle arrays," *Carbon*, vol. 44, no. 13, pp. 2822–2832, Nov. 2006, doi: 10.1016/j.carbon.2006.03.022.

[86] A. M. Cassell, J. A. Raymakers, J. Kong, and H. Dai, "Large Scale CVD Synthesis of Single-Walled Carbon Nanotubes," *J. Phys. Chem. B*, vol. 103, no. 31, pp. 6484–6492, Aug. 1999, doi: 10.1021/jp990957s.

[87] L. Ci *et al.*, "Crystallization behavior of the amorphous carbon nanotubes prepared by the CVD method," *J. Cryst. Growth*, vol. 233, no. 4, pp. 823–828, Dec. 2001, doi: 10.1016/S0022-0248(01)01606-2.

[88] Th. Dikonimos Makris, L. Giorgi, R. Giorgi, N. Lisi, and E. Salernitano, "CNT growth on alumina supported nickel catalyst by thermal CVD," *Diam. Relat. Mater.*, vol. 14, no. 3, pp. 815–819, Mar. 2005, doi: 10.1016/j.diamond.2004.11.001.

[89] A. R. Harutyunyan, B. K. Pradhan, U. J. Kim, G. Chen, and P. C. Eklund, "CVD Synthesis of Single Wall Carbon Nanotubes under 'Soft' Conditions," *Nano Lett.*, vol. 2, no. 5, pp. 525–530, May 2002, doi: 10.1021/nl0255101.

[90] A. Hussain *et al.*, "Floating catalyst CVD synthesis of single walled carbon nanotubes from ethylene for high performance transparent electrodes," *Nanoscale*, vol. 10, no. 20, pp. 9752–9759, May 2018, doi: 10.1039/C8NR00716K.

[91] J. Lu, J. Miao, T. Xu, B. Yan, T. Yu, and Z. Shen, "Growth of horizontally aligned dense carbon nanotubes from trench sidewalls," *Nanotechnology*, vol. 22, no. 26, p. 265614, Jul. 2011, doi: 10.1088/0957-4484/22/26/265614.

[92] C.-C. Chiu, M. Yoshimura, and K. Ueda, "Patterned growth of carbon nanotubes through AFM nano-oxidation," *Diam. Relat. Mater.*, vol. 18, no. 2, pp. 355–359, Feb. 2009, doi: 10.1016/j.diamond.2008.09.010.

[93] J. An, Z. Zhan, S. V. Hari Krishna, and L. Zheng, "Growth condition mediated catalyst effects on the density and length of horizontally aligned single-walled carbon nanotube arrays," *Chem. Eng. J.*, vol. 237, pp. 16–22, Feb. 2014, doi: 10.1016/j.cej.2013.10.012.

[94] O. Zaytseva and G. Neumann, "Carbon nanomaterials: production, impact on plant development, agricultural and environmental applications," *Chem. Biol. Technol. Agric.*, vol. 3, no. 1, p. 17, Jul. 2016, doi: 10.1186/s40538-016-0070-8.

[95] R. Stöckel, K. Janischowsky, M. Stammler, L. Ley, M. Albrecht, and H. P. Strunk, "Carbon nanostructures — Diamond nucleation centers formed during the bias pretreatment," *Diam. Relat. Mater.*, vol. 7, no. 2, pp. 147–151, Feb. 1998, doi: 10.1016/S0925-9635(97)00207-X.

[96] A. M. Bonnot, M. Deldem, E. Beaugnon, T. Fournier, M. C. Schouler, and M. Mermoux, "Carbon nanostructures and diamond growth by HFCVD: role of the

substrate preparation and synthesis conditions," *Diam. Relat. Mater.*, vol. 8, no. 2, pp. 631–635, Mar. 1999, doi: 10.1016/S0925-9635(98)00333-1.

[97] C. Sorin Cojocaru, D. Kim, D. Pribat, and J.-E. Bourée, "Synthesis of multi-walled carbon nanotubes by combining hot-wire and dc plasma-enhanced chemical vapor deposition," *Thin Solid Films*, vol. 501, no. 1, pp. 227–232, Apr. 2006, doi: 10.1016/j.tsf.2005.07.162.

[98] N. Hong, K. Koh, and S. Lee, "Fast Growth of Millimeter-Long Vertically-Aligned Carbon Nanotubes via Hot Filament Chemical Vapor Deposition," *J. Korean Phys. Soc.*, vol. 53, no. 9, pp. 3603–3607, Dec. 2008, doi: 10.3938/jkps.53.3603.

[99] C. S. Cojocaru, M. Larijani, D. S. Misra, M. K. Singh, P. Veis, and F. Le Normand, "A new polarised hot filament chemical vapor deposition process for homogeneous diamond nucleation on Si(100)," *Diam. Relat. Mater.*, vol. 13, no. 2, pp. 270–276, Feb. 2004, doi: 10.1016/j.diamond.2003.10.076.

[100] R. Haubner, W. Schwinger, J. Haring, and R. Schöftner, "Sol–gel preparation of catalyst particles on substrates for hot-filament CVD nanotube deposition," *Diam. Relat. Mater.*, vol. 17, no. 7, pp. 1452–1457, Jul. 2008, doi: 10.1016/j.diamond.2008.01.039.

[101] K. M. McNamara and K. K. Gleason, "Comparison of Tantalum and Rhenium Filaments in Diamond CVD Using Selective Carbon-13 Labeling," *J. Electrochem. Soc.*, vol. 140, no. 2, p. L22, Feb. 1993, doi: 10.1149/1.2221094.

[102] M. Sommer and F. W. Smith, "Activity of tungsten and rhenium filaments in CH4/H2 and C2H2/H2 mixtures: Importance for diamond CVD," *J. Mater. Res.*, vol. 5, no. 11, pp. 2433–2440, Nov. 1990, doi: 10.1557/JMR.1990.2433.

[103] S. Choi, S. Lee, and K. H. Koh, "Hot filament effects on CVD of carbon nanotubes," *Phys. Status Solidi RRL – Rapid Res. Lett.*, vol. 1, no. 4, pp. 156–158, 2007, doi: 10.1002/pssr.200701089.

[104] N. T. Hong, K. H. Koh, N. T. T. Tam, P. N. Minh, P. H. Khoi, and S. Lee, "Combined model for growing mechanism of carbon nanotubes using HFCVD: effect of temperature and molecule gas diffusion," *Thin Solid Films*, vol. 517, no. 12, pp. 3562–3565, Apr. 2009, doi: 10.1016/j.tsf.2009.01.066.

[105] N. T. Hong, S. Y. Kim, K. H. Koh, and S. Lee, "Quantitative elucidation of the rapid growth and growth saturation of millimeter-scale vertically aligned carbon nanotubes by hot-filament chemical vapor deposition," *Thin Solid Films*, vol. 519, no. 14, pp. 4432–4436, May 2011, doi: 10.1016/j.tsf.2011.01.317.

[106] Y.-Q. Xu, E. Flor, H. Schmidt, R. E. Smalley, and R. H. Hauge, "Effects of atomic hydrogen and active carbon species in 1mm vertically aligned single-walled carbon nanotube growth," *Appl. Phys. Lett.*, vol. 89, no. 12, p. 123116, Sep. 2006, doi: 10.1063/1.2349280.

[107] K.-H. Kim, A. Gohier, J. E. Bourée, M. Châtelet, and C.-S. Cojocaru, "The role of catalytic nanoparticle pretreatment on the growth of vertically aligned carbon nanotubes by hot-filament chemical vapor deposition," *Thin Solid Films*, vol. 575, pp. 84–91, Jan. 2015, doi: 10.1016/j.tsf.2014.10.013.

[108] D. Grunsky, M. Kupich, B. Hofferberth, and B. Schroeder, "Investigation of the tantalum catalyst during the hot wire chemical vapor deposition of thin silicon films," *Thin Solid Films*, vol. 501, no. 1, pp. 322–325, Apr. 2006, doi: 10.1016/j.tsf.2005.07.222.

[109] S. Okoli, R. Haubner, and B. Lux, "Carburization of tungsten and tantalum filaments during low-pressure diamond deposition," *Surf. Coat. Technol.*, vol. 47, no. 1, pp. 585–599, Aug. 1991, doi: 10.1016/0257-8972(91)90329-U.

[110] R. S. Wagner and W. C. Ellis, "Vapor-liquid-solid mechanism of single crystal growth," *Appl. Phys. Lett.*, vol. 4, no. 5, pp. 89–90, Mar. 1964, doi: 10.1063/1.1753975.

[111] R. T. K. Baker, P. S. Harris, R. B. Thomas, and R. J. Waite, "Formation of filamentous carbon from iron, cobalt and chromium catalyzed decomposition of acetylene," *J. Catal.*, vol. 30, no. 1, pp. 86–95, Jul. 1973, doi: 10.1016/0021-9517(73)90055-9.

[112] R. T. K. Baker, M. A. Barber, P. S. Harris, F. S. Feates, and R. J. Waite, "Nucleation and growth of carbon deposits from the nickel catalyzed decomposition of acetylene," *J. Catal.*, vol. 26, no. 1, pp. 51–62, Jul. 1972, doi: 10.1016/0021-9517(72)90032-2.

[113] R. T. K. Baker, "Catalytic growth of carbon filaments," *Carbon*, vol. 27, no. 3, pp. 315–323, Jan. 1989, doi: 10.1016/0008-6223(89)90062-6.

[114] M. Kumar, *Carbon Nanotube Synthesis and Growth Mechanism*. IntechOpen, 2011. doi: 10.5772/19331.

[115] F. Ding, A. Rosén, and K. Bolton, "The role of the catalytic particle temperature gradient for SWNT growth from small particles," *Chem. Phys. Lett.*, vol. 393, no. 4, pp. 309–313, Aug. 2004, doi: 10.1016/j.cplett.2004.06.056.

[116] C. Ducati, I. Alexandrou, M. Chhowalla, J. Robertson, and G. a. J. Amaratunga, "The role of the catalytic particle in the growth of carbon nanotubes by plasma enhanced chemical vapor deposition," *J. Appl. Phys.*, vol. 95, no. 11, pp. 6387–6391, Jun. 2004, doi: 10.1063/1.1728293.

[117] C. Klinke, J. Bonard, K. Kern, and K. Kern, "Thermodynamic calculations on the catalytic growth of multiwall carbon nanotubes," 2005, doi: 10.1103/PHYSREVB.71.035403.

[118] F. Ding, K. Bolton, and A. Rosén, "Molecular dynamics study of SWNT growth on catalyst particles without temperature gradients," *Comput. Mater. Sci.*, vol. 35, no. 3, pp. 243–246, Mar. 2006, doi: 10.1016/j.commatsci.2004.08.010.

[119] J. Rostrup-Nielsen and D. L. Trimm, "Mechanisms of carbon formation on nickel-containing catalysts," *J. Catal.*, vol. 48, no. 1, pp. 155–165, Jun. 1977, doi: 10.1016/0021-9517(77)90087-2.

[120] E. L. Evans, J. M. Thomas, P. A. Thrower, and P. L. Walker, "Growth of filamentary carbon on metallic surfaces during the pyrolysis of methane and acetone," *Carbon*, vol. 11, no. 5, pp. 441–445, Oct. 1973, doi: 10.1016/0008-6223(73)90302-3.

[121] R. T. Yang and J. P. Chen, "Mechanism of carbon filament growth on metal catalysts," *J. Catal.*, vol. 115, no. 1, pp. 52–64, Jan. 1989, doi: 10.1016/0021-9517(89)90006-7.
[122] S. Hofmann *et al.*, "In situ Observations of Catalyst Dynamics during Surface-Bound Carbon Nanotube Nucleation," *Nano Lett.*, vol. 7, no. 3, pp. 602–608, Mar. 2007, doi: 10.1021/nl0624824.
[123] Y. Chen and J. Zhang, "Diameter controlled growth of single-walled carbon nanotubes from SiO2 nanoparticles," *Carbon*, vol. 49, no. 10, pp. 3316–3324, Aug. 2011, doi: 10.1016/j.carbon.2011.04.016.
[124] A. Rinaldi *et al.*, "Dissolved Carbon Controls the Initial Stages of Nanocarbon Growth," *Angew. Chem. Int. Ed.*, vol. 50, no. 14, pp. 3313–3317, 2011, doi: 10.1002/anie.201006639.
[125] L. Ma *et al.*, "Fabrication and Water Treatment Application of Carbon Nanotubes (CNTs)-Based Composite Membranes: A Review," *Membranes*, vol. 7, no. 1, p. 16, Mar. 2017, doi: 10.3390/membranes7010016.
[126] V. Jourdain and C. Bichara, "Current understanding of the growth of carbon nanotubes in catalytic chemical vapour deposition," *Carbon*, vol. 58, pp. 2–39, Jul. 2013, doi: 10.1016/j.carbon.2013.02.046.
[127] S. Hofmann *et al.*, "State of Transition Metal Catalysts During Carbon Nanotube Growth," *J. Phys. Chem. C*, vol. 113, no. 5, pp. 1648–1656, Feb. 2009, doi: 10.1021/jp808560p.
[128] F. Ding, K. Bolton, and A. Rosén, "Iron-carbide cluster thermal dynamics for catalyzed carbon nanotube growth," *J. Vac. Sci. Technol. A*, vol. 22, no. 4, pp. 1471–1476, Jul. 2004, doi: 10.1116/1.1752895.
[129] A. Moisala, A. G. Nasibulin, and E. I. Kauppinen, "The role of metal nanoparticles in the catalytic production of single-walled carbon nanotubes—a review," *J. Phys. Condens. Matter*, vol. 15, no. 42, pp. S3011–S3035, Oct. 2003, doi: 10.1088/0953-8984/15/42/003.
[130] H. Yoshida, S. Takeda, T. Uchiyama, H. Kohno, and Y. Homma, "Atomic-Scale In-situ Observation of Carbon Nanotube Growth from Solid State Iron Carbide Nanoparticles," *Nano Lett.*, vol. 8, no. 7, pp. 2082–2086, Jul. 2008, doi: 10.1021/nl080452q.
[131] S. Helveg *et al.*, "Atomic-scale imaging of carbon nanofibre growth," *Nature*, vol. 427, no. 6973, pp. 426–429, Jan. 2004, doi: 10.1038/nature02278.
[132] M. Lin, J. P. Y. Tan, C. Boothroyd, K. P. Loh, E. S. Tok, and Y.-L. Foo, "Dynamical Observation of Bamboo-like Carbon Nanotube Growth," *Nano Lett.*, vol. 7, no. 8, pp. 2234–2238, Aug. 2007, doi: 10.1021/nl070681x.
[133] W. Cho, M. Schulz, and V. Shanov, "Growth termination mechanism of vertically aligned centimeter long carbon nanotube arrays," *Carbon*, vol. 69, pp. 609–620, Apr. 2014, doi: 10.1016/j.carbon.2013.12.088.
[134] S. Esconjauregui, C. M. Whelan, and K. Maex, "The reasons why metals catalyze the nucleation and growth of carbon nanotubes and other carbon nanomorphologies," *Carbon*, vol. 47, no. 3, pp. 659–669, Mar. 2009, doi: 10.1016/j.carbon.2008.10.047.

[135] L. Ni, K. Kuroda, L.-P. Zhou, K. Ohta, K. Matsuishi, and J. Nakamura, "Decomposition of metal carbides as an elementary step of carbon nanotube synthesis," *Carbon*, vol. 47, no. 13, pp. 3054–3062, Nov. 2009, doi: 10.1016/j.carbon.2009.07.009.

[136] N. Latorre *et al.*, "Carbon Nanotube Growth by Catalytic Chemical Vapor Deposition: A Phenomenological Kinetic Model," *J. Phys. Chem. C*, vol. 114, no. 11, pp. 4773–4782, Mar. 2010, doi: 10.1021/jp906893m.

[137] T. de los Arcos, M. G. Garnier, J. W. Seo, P. Oelhafen, V. Thommen, and D. Mathys, "The Influence of Catalyst Chemical State and Morphology on Carbon Nanotube Growth," *J. Phys. Chem. B*, vol. 108, no. 23, pp. 7728–7734, Jun. 2004, doi: 10.1021/jp049495v.

[138] A. K. Schaper, H. Hou, A. Greiner, and F. Phillipp, "The role of iron carbide in multiwalled carbon nanotube growth," *J. Catal.*, vol. 222, no. 1, pp. 250–254, Feb. 2004, doi: 10.1016/j.jcat.2003.11.011.

[139] P. Landois *et al.*, "Growth of aligned multi-walled carbon nanotubes: First in situ and time-resolved X-ray diffraction analysis," *Phys. Status Solidi B*, vol. 248, no. 11, pp. 2449–2453, 2011, doi: 10.1002/pssb.201100201.

[140] C. T. Wirth *et al.*, "The Phase of Iron Catalyst Nanoparticles during Carbon Nanotube Growth," *Chem. Mater.*, vol. 24, no. 24, pp. 4633–4640, Dec. 2012, doi: 10.1021/cm301402g.

[141] P. M. F. J. Costa and P. J. Ferreira, "In Situ TEM of Carbon Nanotubes," in *Advanced Transmission Electron Microscopy: Applications to Nanomaterials*, F. L. Deepak, A. Mayoral, and R. Arenal, Eds., Cham: Springer International Publishing, 2015, pp. 207–247. doi: 10.1007/978-3-319-15177-9_7.

[142] X. Feng *et al.*, "In Situ TEM observation of the gasification and growth of carbon nanotubes using iron catalysts," *Nano Res.*, vol. 4, no. 8, p. 767, Apr. 2011, doi: 10.1007/s12274-011-0133-x.

[143] C. Chen *et al.*, "Catalyst-Free In Situ Carbon Nanotube Growth in Confined Space via High Temperature Gradient," Research. Accessed: Sep. 23, 2019. [Online]. Available: https://spj.sciencemag.org/research/2018/1793784/

[144] J. Gavillet, A. Loiseau, C. Journet, F. Willaime, F. Ducastelle, and J.-C. Charlier, "Root-Growth Mechanism for Single-Wall Carbon Nanotubes," *Phys. Rev. Lett.*, vol. 87, no. 27, p. 275504, Dec. 2001, doi: 10.1103/PhysRevLett.87.275504.

[145] M. Lin, J. P. Ying Tan, C. Boothroyd, K. P. Loh, E. S. Tok, and Y.-L. Foo, "Direct Observation of Single-Walled Carbon Nanotube Growth at the Atomistic Scale," *Nano Lett.*, vol. 6, no. 3, pp. 449–452, Mar. 2006, doi: 10.1021/nl052356k.

[146] Y. Li, W. Kim, Y. Zhang, M. Rolandi, D. Wang, and H. Dai, "Growth of Single-Walled Carbon Nanotubes from Discrete Catalytic Nanoparticles of Various Sizes," *J. Phys. Chem. B*, vol. 105, no. 46, pp. 11424–11431, Nov. 2001, doi: 10.1021/jp012085b.

[147] M. He *et al.*, "Growth kinetics of single-walled carbon nanotubes with a (2n, n) chirality selection," *Sci. Adv.*, vol. 5, no. 12, p. eaav9668, Dec. 2019, doi: 10.1126/sciadv.aav9668.

[148] Zhong, T. Iwasaki, J. Robertson, and H. Kawarada, "Growth Kinetics of 0.5 cm Vertically Aligned Single-Walled Carbon Nanotubes," *J. Phys. Chem. B*, vol. 111, no. 8, pp. 1907–1910, Mar. 2007, doi: 10.1021/jp067776s.

[149] M.-F. C. Fiawoo, A.-M. Bonnot, H. Amara, C. Bichara, J. Thibault-Pénisson, and A. Loiseau, "Evidence of Correlation between Catalyst Particles and the Single-Wall Carbon Nanotube Diameter: A First Step towards Chirality Control," *Phys. Rev. Lett.*, vol. 108, no. 19, p. 195503, May 2012, doi: 10.1103/PhysRevLett.108.195503.

[150] F. Zhang *et al.*, "Growth of semiconducting single-wall carbon nanotubes with a narrow band-gap distribution," *Nat. Commun.*, vol. 7, no. 1, p. 11160, Mar. 2016, doi: 10.1038/ncomms11160.

[151] M. V. Kharlamova, "Investigation of growth dynamics of carbon nanotubes," *Beilstein J. Nanotechnol.*, vol. 8, no. 1, pp. 826–856, Apr. 2017, doi: 10.3762/bjnano.8.85.

[152] G. Zhong *et al.*, "Acetylene: A Key Growth Precursor for Single-Walled Carbon Nanotube Forests," *J. Phys. Chem. C*, vol. 113, no. 40, pp. 17321–17325, Oct. 2009, doi: 10.1021/jp905134b.

[153] J. Song, L. Wang, S. Feng, J. Zhao, and Z. Zhu, "Growth of carbon nanotubes by the catalytic decomposition of methane over Fe-Mo/Al2O3 catalyst: effect of temperature on tube structure," *New Carbon Mater.*, vol. 24, no. 4, pp. 307–313, Dec. 2009, doi: 10.1016/S1872-5805(08)60054-2.

[154] H. Kondo, N. Fukuoka, and T. Maruyama, "Low Temperature Growth of Single-Walled Carbon Nanotubes from Pt Catalysts under Low Ethanol Pressure by Alcohol Gas Source Method," *J. Nanotechnol.*, vol. 2012, p. e690304, Oct. 2012, doi: 10.1155/2012/690304.

[155] X. Zhao, X. Zhang, Q. Liu, Z. Zhang, and Y. Li, "Growth of Single-walled Carbon Nanotubes on Substrates Using Carbon Monoxide as Carbon Source," *Chem. Res. Chin. Univ.*, vol. 37, no. 5, pp. 1125–1129, Oct. 2021, doi: 10.1007/s40242-021-1277-1.

[156] B. Wang, C. H. P. Poa, L. Wei, L.-J. Li, Y. Yang, and Y. Chen, "(n,m) Selectivity of Single-Walled Carbon Nanotubes by Different Carbon Precursors on Co−Mo Catalysts," *J. Am. Chem. Soc.*, vol. 129, no. 29, pp. 9014–9019, Jul. 2007, doi: 10.1021/ja070808k.

[157] G. Keskar, R. Rao, J. Luo, J. Hudson, and A. M. Rao, "Growth, Nitrogen Doping and Characterization of Isolated Single-Wall Carbon Nanotubes using Liquid Precursors," *MRS Online Proc. Libr.*, vol. 858, no. 1, pp. 146–151, Dec. 2004, doi: 10.1557/PROC-858-HH2.2.

[158] J. S. Barnard, C. Paukner, and K. K. Koziol, "The role of carbon precursor on carbon nanotube chirality in floating catalyst chemical vapour deposition," *Nanoscale*, vol. 8, no. 39, pp. 17262–17270, Oct. 2016, doi: 10.1039/C6NR03895F.

[159] W.-W. Liu, A. Aziz, S.-P. Chai, A. R. Mohamed, and C.-T. Tye, "The effect of carbon precursors (methane, benzene and camphor) on the quality of carbon nanotubes synthesised by the chemical vapour decomposition," *Phys. E Low-Dimens. Syst. Nanostructures*, vol. 43, no. 8, pp. 1535–1542, Jun. 2011, doi: 10.1016/j.physe.2011.05.012.

[160] T. T. Cao, T. T. T. Ngo, V. C. Nguyen, X. T. Than, B. T. Nguyen, and N. M. Phan, "Single-walled carbon nanotubes synthesized by chemical vapor deposition of C2H2 over an Al2O3 supported mixture of Fe, Mo, Co catalysts," *Adv. Nat. Sci. Nanosci. Nanotechnol.*, vol. 2, no. 3, p. 035007, Jul. 2011, doi: 10.1088/2043-6262/2/3/035007.

[161] W. M. Haynes, Ed., *CRC Handbook of Chemistry and Physics*, 95th ed. Boca Raton: CRC Press, 2014. doi: 10.1201/b17118.

[162] A. R. Biris *et al.*, "Effect of hydrogen on the growth and morphology of single wall carbon nanotubes synthesized on a FeMo/MgO catalytic system," *Phys. Lett. A*, vol. 372, no. 17, pp. 3051–3057, Apr. 2008, doi: 10.1016/j.physleta.2008.01.023.

[163] M. Dors, H. Nowakowska, M. Jasiński, and J. Mizeraczyk, "Chemical Kinetics of Methane Pyrolysis in Microwave Plasma at Atmospheric Pressure," *Plasma Chem. Plasma Process.*, vol. 34, no. 2, pp. 313–326, Mar. 2014, doi: 10.1007/s11090-013-9510-4.

[164] K. B. K. Teo *et al.*, "Uniform patterned growth of carbon nanotubes without surface carbon," *Appl. Phys. Lett.*, vol. 79, no. 10, pp. 1534–1536, Sep. 2001, doi: 10.1063/1.1400085.

[165] A. Kaniyoor *et al.*, "High throughput production of single-wall carbon nanotube fibres independent of sulfur-source," *Nanoscale*, vol. 11, no. 39, pp. 18483–18495, Oct. 2019, doi: 10.1039/C9NR06623C.

[166] K. Hata, D. N. Futaba, K. Mizuno, T. Namai, M. Yumura, and S. Iijima, "Water-assisted highly efficient synthesis of impurity-free single-walled carbon nanotubes," *Science*, vol. 306, no. 5700, pp. 1362–1364, Nov. 2004, doi: 10.1126/science.1104962.

[167] H. Nishino *et al.*, "Water-Assisted Highly Efficient Synthesis of Single-Walled Carbon Nanotubes Forests from Colloidal Nanoparticle Catalysts," *J. Phys. Chem. C*, vol. 111, no. 48, pp. 17961–17965, Dec. 2007, doi: 10.1021/jp0723719.

[168] Z. Zhu, H. Jiang, T. Susi, A. G. Nasibulin, and E. I. Kauppinen, "The Use of NH3 to Promote the Production of Large-Diameter Single-Walled Carbon Nanotubes with a Narrow (n,m) Distribution," *J. Am. Chem. Soc.*, vol. 133, no. 5, pp. 1224–1227, Feb. 2011, doi: 10.1021/ja1087634.

[169] A. Aghaei, M. Shaterian, H. Hosseini Monfared, and A. Farokhi, "Designing a strategy for fabrication of single-walled carbon nanotube via CH4/N2 gas by the chemical vapor deposition method," *Adv. Powder Technol.*, vol. 33, no. 3, p. 103500, Mar. 2022, doi: 10.1016/j.apt.2022.103500.

[170] M. Li, K. Yasui, H. Sugime, and S. Noda, "Enhanced CO2-assisted growth of single-wall carbon nanotube arrays using Fe/AlOx catalyst annealed without

CO2," *Carbon*, vol. 185, pp. 264–271, Nov. 2021, doi: 10.1016/j.carbon.2021.09.031.
[171] T. Sato, H. Sugime, and S. Noda, "CO2-assisted growth of millimeter-tall single-wall carbon nanotube arrays and its advantage against H2O for large-scale and uniform synthesis," *Carbon*, vol. 136, pp. 143–149, Sep. 2018, doi: 10.1016/j.carbon.2018.04.060.
[172] P. B. Amama *et al.*, "Role of Water in Super Growth of Single-Walled Carbon Nanotube Carpets," *Nano Lett.*, vol. 9, no. 1, pp. 44–49, Jan. 2009, doi: 10.1021/nl801876h.
[173] D. N. Futaba, J. Goto, S. Yasuda, T. Yamada, M. Yumura, and K. Hata, "General Rules Governing the Highly Efficient Growth of Carbon Nanotubes," *Adv. Mater.*, vol. 21, no. 47, pp. 4811–4815, 2009, doi: 10.1002/adma.200901257.
[174] Z. Chen, D. Y. Kim, K. Hasegawa, and S. Noda, "Methane-Assisted Chemical Vapor Deposition Yielding Millimeter-Tall Single-Wall Carbon Nanotubes of Smaller Diameter," *ACS Nano*, vol. 7, no. 8, pp. 6719–6728, Aug. 2013, doi: 10.1021/nn401556t.
[175] G. A. Somorjai and Y. Li, *Introduction to Surface Chemistry and Catalysis, 2nd Edition | Wiley*. 2010. [Online]. Available: https://www.wiley.com/en-us/Introduction+to+Surface+Chemistry+and+Catalysis%2C+2nd+Edition-p-9780470508237
[176] H. Wang, L. Yang, X. Sui, H. E. Karahan, X. Wang, and Y. Chen, "Selective synthesis of single walled carbon nanotubes on metal (iron, nickel or cobalt) sulfate-based catalysts," *Carbon*, vol. 129, pp. 128–136, Apr. 2018, doi: 10.1016/j.carbon.2017.12.002.
[177] Z. P. Huang, D. Z. Wang, J. G. Wen, M. Sennett, H. Gibson, and Z. F. Ren, "Effect of nickel, iron and cobalt on growth of aligned carbon nanotubes," *Appl. Phys. A*, vol. 74, no. 3, pp. 387–391, Mar. 2002, doi: 10.1007/s003390101186.
[178] S. M. Jafarpour, M. Kini, S. E. Schulz, and S. Hermann, "Effects of catalyst configurations and process conditions on the formation of catalyst nanoparticles and growth of single-walled carbon nanotubes," *Microelectron. Eng.*, vol. 167, pp. 95–104, Jan. 2017, doi: 10.1016/j.mee.2016.11.007.
[179] C. P. Deck and K. Vecchio, "Prediction of carbon nanotube growth success by the analysis of carbon–catalyst binary phase diagrams," *Carbon*, vol. 44, no. 2, pp. 267–275, Feb. 2006, doi: 10.1016/j.carbon.2005.07.023.
[180] H. Navas *et al.*, "Interplay of interfacial compounds, catalyst thickness and carbon precursor supply in the selectivity of single-walled carbon nanotube growth," *Carbon*, vol. 80, pp. 599–609, Dec. 2014, doi: 10.1016/j.carbon.2014.09.003.
[181] R. T. K. Baker, J. J. Chludzinski, N. S. Dudash, and A. J. Simoens, "The formation of filamentous carbon from decomposition of acetylene over vanadium and molybdenum," *Carbon*, vol. 21, no. 5, pp. 463–468, Jan. 1983, doi: 10.1016/0008-6223(83)90138-0.

[182] H. Hongo, F. Nihey, T. Ichihashi, Y. Ochiai, M. Yudasaka, and S. Iijima, "Support materials based on converted aluminum films for chemical vapor deposition growth of single-wall carbon nanotubes," *Chem. Phys. Lett.*, vol. 380, no. 1, pp. 158–164, Oct. 2003, doi: 10.1016/j.cplett.2003.08.103.

[183] S. Lee *et al.*, "Selective growth of carbon nanotube for via interconnects by oxidation and selective reduction of catalyst," *Appl. Phys. Lett.*, vol. 93, no. 18, p. 182106, Nov. 2008, doi: 10.1063/1.3021363.

[184] D. Takagi, Y. Kobayashi, H. Hibino, S. Suzuki, and Y. Homma, "Mechanism of Gold-Catalyzed Carbon Material Growth," *Nano Lett.*, vol. 8, no. 3, pp. 832–835, Mar. 2008, doi: 10.1021/nl0728930.

[185] W. Zhou *et al.*, "Copper Catalyzing Growth of Single-Walled Carbon Nanotubes on Substrates," *Nano Lett.*, vol. 6, no. 12, pp. 2987–2990, Dec. 2006, doi: 10.1021/nl061871v.

[186] D. Takagi, Y. Homma, H. Hibino, S. Suzuki, and Y. Kobayashi, "Single-Walled Carbon Nanotube Growth from Highly Activated Metal Nanoparticles," *Nano Lett.*, vol. 6, no. 12, pp. 2642–2645, Dec. 2006, doi: 10.1021/nl061797g.

[187] D. Yuan, L. Ding, H. Chu, Y. Feng, T. P. McNicholas, and J. Liu, "Horizontally Aligned Single-Walled Carbon Nanotube on Quartz from a Large Variety of Metal Catalysts," *Nano Lett.*, vol. 8, no. 8, pp. 2576–2579, Aug. 2008, doi: 10.1021/nl801007r.

[188] J. E. Herrera and D. E. Resasco, "Loss of single-walled carbon nanotubes selectivity by disruption of the Co–Mo interaction in the catalyst," *J. Catal.*, vol. 221, no. 2, pp. 354–364, Jan. 2004, doi: 10.1016/j.jcat.2003.08.005.

[189] M. Li *et al.*, "Diameter-specific growth of single-walled carbon nanotubes using tungsten supported nickel catalysts," *Carbon*, vol. 118, pp. 485–492, Jul. 2017, doi: 10.1016/j.carbon.2017.03.083.

[190] K. Hernadi, A. Fonseca, J. B. Nagy, Á. Fudala, D. Bernaerts, and I. Kiricsi, "Catalytic production of carbon nanofibers over iron carbide doped with Sn2+," *Appl. Catal. Gen.*, vol. 228, no. 1, pp. 103–113, Mar. 2002, doi: 10.1016/S0926-860X(01)00972-3.

[191] T. Maruyama, T. Saida, S. Naritsuka, and S. Iijima, "Single-Walled Carbon Nanotube Synthesis by Chemical Vapor Deposition Using Platinum-Group Metal Catalysts," *Int. J. Mater. Metall. Eng.*, vol. 12, no. 3, pp. 129–133, Feb. 2018.

[192] D. E. Resasco *et al.*, "A Scalable Process for Production of Single-walled Carbon Nanotubes (SWNTs) by Catalytic Disproportionation of CO on a Solid Catalyst," *J. Nanoparticle Res.*, vol. 4, no. 1, pp. 131–136, Apr. 2002, doi: 10.1023/A:1020174126542.

[193] D. E. Resasco, W. E. Alvarez, J. E. Herrera, and L. Balzano, "Method for producing single walled carbon nanotubes," US7357907B2, Apr. 15, 2008 Accessed: Jul. 19, 2022. [Online]. Available: https://patents.google.com/patent/US7357907B2/en

[194] G. D. Nessim *et al.*, "Tuning of Vertically-Aligned Carbon Nanotube Diameter and Areal Density through Catalyst Pre-Treatment," *Nano Lett.*, vol. 8, no. 11, pp. 3587–3593, Nov. 2008, doi: 10.1021/nl801437c.

[195] M. Cantoro *et al.*, "Catalytic Chemical Vapor Deposition of Single-Wall Carbon Nanotubes at Low Temperatures," *Nano Lett.*, vol. 6, no. 6, pp. 1107–1112, Jun. 2006, doi: 10.1021/nl060068y.

[196] M. Picher, E. Anglaret, and V. Jourdain, "High temperature activation and deactivation of single-walled carbon nanotube growth investigated by in situ Raman measurements," *Diam. Relat. Mater.*, vol. 19, no. 5, pp. 581–585, May 2010, doi: 10.1016/j.diamond.2009.12.003.

[197] H. Zhang, G. Cao, Z. Wang, Y. Yang, Z. Shi, and Z. Gu, "Influence of Hydrogen Pretreatment Condition on the Morphology of Fe/Al2O3 Catalyst Film and Growth of Millimeter-Long Carbon Nanotube Array," *J. Phys. Chem. C*, vol. 112, no. 12, pp. 4524–4530, Mar. 2008, doi: 10.1021/jp710338d.

[198] S. Forel *et al.*, "Tuning bimetallic catalysts for a selective growth of SWCNTs," *Nanoscale*, vol. 11, no. 9, pp. 4091–4100, Feb. 2019, doi: 10.1039/C8NR09589B.

[199] W.-P. Wang *et al.*, "The effects of hydrogen plasma pretreatment on the formation of vertically aligned carbon nanotubes," *Appl. Surf. Sci.*, vol. 253, no. 23, pp. 9248–9253, Sep. 2007, doi: 10.1016/j.apsusc.2007.05.060.

[200] S. Esconjauregui *et al.*, "Growth of high-density vertically aligned arrays of carbon nanotubes by plasma-assisted catalyst pretreatment," *Appl. Phys. Lett.*, vol. 95, no. 17, p. 173115, Oct. 2009, doi: 10.1063/1.3256012.

[201] J. B. In, C. P. Grigoropoulos, A. A. Chernov, and A. Noy, "Growth Kinetics of Vertically Aligned Carbon Nanotube Arrays in Clean Oxygen-free Conditions," *ACS Nano*, vol. 5, no. 12, pp. 9602–9610, Dec. 2011, doi: 10.1021/nn2028715.

[202] Y. Li, K. Ji, Y. Duan, G. Meng, and Z. Dai, "Effect of Hydrogen Concentration on the Growth of Carbon Nanotube Arrays for Gecko-Inspired Adhesive Applications," *Coatings*, vol. 7, no. 12, Art. no. 12, Dec. 2017, doi: 10.3390/coatings7120221.

[203] D. Venegoni, P. Serp, R. Feurer, Y. Kihn, C. Vahlas, and P. Kalck, "Parametric study for the growth of carbon nanotubes by catalytic chemical vapor deposition in a fluidized bed reactor," *Carbon*, vol. 40, no. 10, pp. 1799–1807, Aug. 2002, doi: 10.1016/S0008-6223(02)00057-X.

[204] J.-F. Colomer *et al.*, "Synthesis of single-wall carbon nanotubesby catalytic decomposition of hydrocarbons," *Chem. Commun.*, no. 14, pp. 1343–1344, Jan. 1999, doi: 10.1039/A903142A.

[205] P. B. Amama *et al.*, "Influence of Alumina Type on the Evolution and Activity of Alumina-Supported Fe Catalysts in Single-Walled Carbon Nanotube Carpet Growth," *ACS Nano*, vol. 4, no. 2, pp. 895–904, Feb. 2010, doi: 10.1021/nn901700u.

[206] Ph. Mauron, Ch. Emmenegger, P. Sudan, P. Wenger, S. Rentsch, and A. Züttel, "Fluidised-bed CVD synthesis of carbon nanotubes on Fe2O3/MgO," *Diam. Relat. Mater.*, vol. 12, no. 3, pp. 780–785, Mar. 2003, doi: 10.1016/S0925-9635(02)00337-0.

[207] T. Moteki, Y. Murakami, S. Noda, S. Maruyama, and T. Okubo, "Zeolite Surface As a Catalyst Support Material for Synthesis of Single-Walled Carbon Nanotubes," *J. Phys. Chem. C*, vol. 115, no. 49, pp. 24231–24237, Dec. 2011, doi: 10.1021/jp207930m.

[208] A. K. Sinha, D. W. Hwang, and L.-P. Hwang, "A novel approach to bulk synthesis of carbon nanotubes filled with metal by a catalytic chemical vapor deposition method," *Chem. Phys. Lett.*, vol. 332, no. 5, pp. 455–460, Dec. 2000, doi: 10.1016/S0009-2614(00)01315-4.

[209] M. A. Ermakova, D. Y. Ermakov, A. L. Chuvilin, and G. G. Kuvshinov, "Decomposition of Methane over Iron Catalysts at the Range of Moderate Temperatures: The Influence of Structure of the Catalytic Systems and the Reaction Conditions on the Yield of Carbon and Morphology of Carbon Filaments," *J. Catal.*, vol. 201, no. 2, pp. 183–197, Jul. 2001, doi: 10.1006/jcat.2001.3243.

[210] R. L. Vander Wal, T. M. Ticich, and V. E. Curtis, "Substrate–support interactions in metal-catalyzed carbon nanofiber growth," *Carbon*, vol. 39, no. 15, pp. 2277–2289, Dec. 2001, doi: 10.1016/S0008-6223(01)00047-1.

[211] Z. Li *et al.*, "Carbon Nanotube Growth on Calcium Carbonate Supported Molybdenum-Transition Bimetal Catalysts," *Catal. Lett.*, vol. 131, no. 3, pp. 356–363, Sep. 2009, doi: 10.1007/s10562-009-0061-5.

[212] T. V. Reshetenko, L. B. Avdeeva, Z. R. Ismagilov, and A. L. Chuvilin, "Catalytic filamentous carbon as supports for nickel catalysts," *Carbon*, vol. 42, no. 1, pp. 143–148, Jan. 2004, doi: 10.1016/j.carbon.2003.10.015.

[213] P. E. Anderson and N. M. Rodríguez, "Influence of the Support on the Structural Characteristics of Carbon Nanofibers Produced from the Metal-Catalyzed Decomposition of Ethylene," *Chem. Mater.*, vol. 12, no. 3, pp. 823–830, Mar. 2000, doi: 10.1021/cm990582n.

[214] Q. Liang, Q. Li, L. Gao, and Z. Yu, "Carbon nanotubes prepared from CO on pre-reduced La2NiO4 perovskite precursor," *Mater. Res. Bull.*, vol. 36, no. 3, pp. 471–477, Feb. 2001, doi: 10.1016/S0025-5408(00)00480-3.

[215] K. Hernadi, A. Fonseca, J. B. Nagy, D. Bernaerts, and A. A. Lucas, "Fe-catalyzed carbon nanotube formation," *Carbon*, vol. 34, no. 10, pp. 1249–1257, Jan. 1996, doi: 10.1016/0008-6223(96)00074-7.

[216] Á. Kukovecz *et al.*, "Catalytic synthesis of carbon nanotubes over Co, Fe and Ni containing conventional and sol–gel silica–aluminas," *Phys. Chem. Chem. Phys.*, vol. 2, no. 13, pp. 3071–3076, Jan. 2000, doi: 10.1039/B002331K.

[217] DerSilberspiegel, *English: The Ellingham diagram is giving the free energy of formation of metal oxides and the corresponding oxygen partial pressure at equilibrium. Labels in English.* 2016. Accessed: Oct. 20, 2022. [Online]. Available: https://commons.wikimedia.org/wiki/File:Ellingham_Richardson-diagram_english.svg

[218] H. An *et al.*, "Chirality specific and spatially uniform synthesis of single-walled carbon nanotubes from a sputtered Co–W bimetallic catalyst," *Nanoscale*, vol. 8, no. 30, pp. 14523–14529, Jul. 2016, doi: 10.1039/C6NR02749K.

[219] M. Liu *et al.*, "Efficient growth of vertically-aligned single-walled carbon nanotubes combining two unfavorable synthesis conditions," *Carbon*, vol. 146, pp. 413–419, May 2019, doi: 10.1016/j.carbon.2019.01.109.
[220] A. A. Puretzky *et al.*, "Incremental growth of short SWNT arrays by pulsed chemical vapor deposition," *Small Weinh. Bergstr. Ger.*, vol. 8, no. 10, pp. 1534–1542, May 2012, doi: 10.1002/smll.201102173.
[221] A. J. Hart, A. H. Slocum, and L. Royer, "Growth of conformal single-walled carbon nanotube films from Mo/Fe/Al2O3 deposited by electron beam evaporation," *Carbon*, vol. 44, no. 2, pp. 348–359, Feb. 2006, doi: 10.1016/j.carbon.2005.07.008.
[222] V. M. Irurzun, Y. Tan, and D. E. Resasco, "Sol−Gel Synthesis and Characterization of Co−Mo/Silica Catalysts for Single-Walled Carbon Nanotube Production," *Chem. Mater.*, vol. 21, no. 11, pp. 2238–2246, Jun. 2009, doi: 10.1021/cm900250k.
[223] T. da Cunha *et al.*, "Design of Silica Nanoparticles-Supported Metal Catalyst by Wet Impregnation with Catalytic Performance for Tuning Carbon Nanotubes Growth," *Catalysts*, vol. 11, no. 8, Art. no. 8, Aug. 2021, doi: 10.3390/catal11080986.
[224] Y. Guo *et al.*, "Effect of different catalyst preparation methods on the synthesis of carbon nanotubes with the flame pyrolysis method," *AIP Adv.*, vol. 8, no. 3, p. 035111, Mar. 2018, doi: 10.1063/1.5020936.
[225] A. Bashir, T. I. Awan, A. Tehseen, M. B. Tahir, and M. Ijaz, "Chapter 3 - Interfaces and surfaces," in *Chemistry of Nanomaterials*, T. I. Awan, A. Bashir, and A. Tehseen, Eds., Elsevier, 2020, pp. 51–87. doi: 10.1016/B978-0-12-818908-5.00003-2.
[226] S. Noda *et al.*, "Millimeter-Thick Single-Walled Carbon Nanotube Forests: Hidden Role of Catalyst Support," *Jpn. J. Appl. Phys.*, vol. 46, no. 5L, p. L399, Apr. 2007, doi: 10.1143/JJAP.46.L399.
[227] C. Mattevi *et al.*, "In-situ X-ray Photoelectron Spectroscopy Study of Catalyst−Support Interactions and Growth of Carbon Nanotube Forests," *J. Phys. Chem. C*, vol. 112, no. 32, pp. 12207–12213, Aug. 2008, doi: 10.1021/jp802474g.
[228] E. polytechnique, *Laboratoire de Physique des Interfaces et des Couches Minces / Fenix*. 2016. Accessed: Oct. 26, 2022. [Photo]. Available: https://www.flickr.com/photos/117994717@N06/25763457773/
[229] G. Zhang *et al.*, "Ultra-high-yield growth of vertical single-walled carbon nanotubes: Hidden roles of hydrogen and oxygen," *Proc. Natl. Acad. Sci.*, vol. 102, no. 45, pp. 16141–16145, Nov. 2005, doi: 10.1073/pnas.0507064102.
[230] M. S. Dresselhaus, G. Dresselhaus, and P. Avouris, Eds., *Carbon Nanotubes: Synthesis, Structure, Properties, and Applications*. in Topics in Applied Physics. Berlin Heidelberg: Springer-Verlag, 2001. doi: 10.1007/3-540-39947-X.
[231] M. S. Dresselhaus, G. Dresselhaus, A. Jorio, A. G. Souza Filho, and R. Saito, "Raman spectroscopy on isolated single wall carbon nanotubes," *Carbon*, vol. 40, no. 12, pp. 2043–2061, Jan. 2002, doi: 10.1016/S0008-6223(02)00066-0.

[232] H. M. Heise, R. Kuckuk, A. K. Ojha, A. Srivastava, V. Srivastava, and B. P. Asthana, "Characterisation of carbonaceous materials using Raman spectroscopy: a comparison of carbon nanotube filters, single- and multi-walled nanotubes, graphitised porous carbon and graphite," *J. Raman Spectrosc.*, vol. 40, no. 3, pp. 344–353, 2009, doi: 10.1002/jrs.2120.

[233] D. Zhang *et al.*, "(n,m) Assignments and quantification for single-walled carbon nanotubes on SiO2/Si substrates by resonant Raman spectroscopy," *Nanoscale*, vol. 7, no. 24, pp. 10719–10727, Jun. 2015, doi: 10.1039/C5NR01076D.

[234] A. Jorio *et al.*, "Structural (n, m) determination of isolated single-wall carbon nanotubes by resonant Raman scattering.," *Phys. Rev. Lett.*, vol. 86, no. 6, pp. 1118–1121, 2001, doi: 10.1103/PhysRevLett.86.1118.

[235] M. Milnera, J. Kürti, M. Hulman, and H. Kuzmany, "Periodic Resonance Excitation and Intertube Interaction from Quasicontinuous Distributed Helicities in Single-Wall Carbon Nanotubes," *Phys. Rev. Lett.*, vol. 84, no. 6, pp. 1324–1327, Feb. 2000, doi: 10.1103/PhysRevLett.84.1324.

[236] S. M. Bachilo, M. S. Strano, C. Kittrell, R. H. Hauge, R. E. Smalley, and R. B. Weisman, "Structure-Assigned Optical Spectra of Single-Walled Carbon Nanotubes," *Science*, vol. 298, no. 5602, pp. 2361–2366, Dec. 2002, doi: 10.1126/science.1078727.

[237] A. M. Rao *et al.*, "Diameter-Selective Raman Scattering from Vibrational Modes in Carbon Nanotubes," *Science*, vol. 275, no. 5297, pp. 187–191, Jan. 1997, doi: 10.1126/science.275.5297.187.

[238] S. D. M. Brown *et al.*, "Origin of the Breit-Wigner-Fano lineshape of the tangential G-band feature of metallic carbon nanotubes," *Phys. Rev. B*, vol. 63, no. 15, p. 155414, Mar. 2001, doi: 10.1103/PhysRevB.63.155414.

[239] H. Telg *et al.*, "Chiral Index Dependence of the G+ and G– Raman Modes in Semiconducting Carbon Nanotubes," *ACS Nano*, vol. 6, no. 1, pp. 904–911, Jan. 2012, doi: 10.1021/nn2044356.

[240] M. A. Pimenta *et al.*, "The anomalous dispersion of the disorder-induced and the second-order Raman Bands in Carbon Nanotubes," *Braz. J. Phys.*, vol. 30, pp. 423–427, Jun. 2000, doi: 10.1590/S0103-97332000000200026.

[241] R. Saito, T. Takeya, T. Kimura, G. Dresselhaus, and M. S. Dresselhaus, "Raman intensity of single-wall carbon nanotubes," *Phys. Rev. B*, vol. 57, no. 7, pp. 4145–4153, Feb. 1998, doi: 10.1103/PhysRevB.57.4145.

[242] G. S. Duesberg, I. Loa, M. Burghard, K. Syassen, and S. Roth, "Polarized Raman Spectroscopy on Isolated Single-Wall Carbon Nanotubes," *Phys. Rev. Lett.*, vol. 85, no. 25, pp. 5436–5439, Dec. 2000, doi: 10.1103/PhysRevLett.85.5436.

[243] S. D. M. Brown, A. Jorio, M. S. Dresselhaus, and G. Dresselhaus, "Observations of the D-band feature in the Raman spectra of carbon nanotubes," *Phys. Rev. B*, vol. 64, no. 7, p. 073403, Jul. 2001, doi: 10.1103/PhysRevB.64.073403.

[244] A. C. Ferrari and J. Robertson, "Interpretation of Raman spectra of disordered and amorphous carbon," *Phys. Rev. B*, vol. 61, no. 20, pp. 14095–14107, May 2000, doi: 10.1103/PhysRevB.61.14095.
[245] I. Shlimak and M. Kaveh, "Raman Spectra in Irradiated Graphene: Line Broadening, Effects of Aging and Annealing," *Graphene*, vol. 9, no. 2, Art. no. 2, Apr. 2020, doi: 10.4236/graphene.2020.92002.
[246] A. C. Dillon, P. A. Parilla, J. L. Alleman, T. Gennett, K. M. Jones, and M. J. Heben, "Systematic inclusion of defects in pure carbon single-wall nanotubes and their effect on the Raman D-band," *Chem. Phys. Lett.*, vol. 401, no. 4, pp. 522–528, Jan. 2005, doi: 10.1016/j.cplett.2004.11.104.
[247] P. Puech *et al.*, "Analyzing the Raman Spectra of Graphenic Carbon Materials from Kerogens to Nanotubes: What Type of Information Can Be Extracted from Defect Bands?," *C*, vol. 5, no. 4, Art. no. 4, Dec. 2019, doi: 10.3390/c5040069.
[248] P. Vinten, J. Lefebvre, and P. Finnie, "Kinetic critical temperature and optimized chemical vapor deposition growth of carbon nanotubes," *Chem. Phys. Lett.*, vol. 469, no. 4, pp. 293–297, Feb. 2009, doi: 10.1016/j.cplett.2008.12.095.
[249] Y. Yabe, Y. Ohtake, T. Ishitobi, Y. Show, T. Izumi, and H. Yamauchi, "Synthesis of well-aligned carbon nanotubes by radio frequency plasma enhanced CVD method," *Diam. Relat. Mater.*, vol. 13, no. 4, pp. 1292–1295, Apr. 2004, doi: 10.1016/j.diamond.2003.11.067.
[250] "Kataura plot by S. Maruyama." Accessed: Jul. 12, 2021. [Online]. Available: http://www.photon.t.u-tokyo.ac.jp/~maruyama/kataura/kataura.html
[251] S. Nanot *et al.*, "Single-Walled Carbon Nanotubes," in *Springer Handbook of Nanomaterials*, R. Vajtai, Ed., in Springer Handbooks. , Berlin, Heidelberg: Springer, 2013, pp. 105–146. doi: 10.1007/978-3-642-20595-8_4.
[252] R. Rao, J. Carpena-Núñez, P. Nikolaev, M. A. Susner, K. G. Reyes, and B. Maruyama, "Advanced machine learning decision policies for diameter control of carbon nanotubes," *Npj Comput. Mater.*, vol. 7, no. 1, Art. no. 1, Oct. 2021, doi: 10.1038/s41524-021-00629-y.
[253] K. C. A. Smith and C. W. Oatley, "The scanning electron microscope and its fields of application," *Br. J. Appl. Phys.*, vol. 6, no. 11, pp. 391–399, Nov. 1955, doi: 10.1088/0508-3443/6/11/304.
[254] J. I. Goldstein, D. E. Newbury, J. R. Michael, N. W. M. Ritchie, J. H. J. Scott, and D. C. Joy, "Secondary Electrons," in *Scanning Electron Microscopy and X-Ray Microanalysis*, J. I. Goldstein, D. E. Newbury, J. R. Michael, N. W. M. Ritchie, J. H. J. Scott, and D. C. Joy, Eds., New York, NY: Springer, 2018, pp. 29–37. doi: 10.1007/978-1-4939-6676-9_3.
[255] J. I. Goldstein, D. E. Newbury, J. R. Michael, N. W. M. Ritchie, J. H. J. Scott, and D. C. Joy, "Image Formation," in *Scanning Electron Microscopy and X-Ray Microanalysis*, J. I. Goldstein, D. E. Newbury, J. R. Michael, N. W. M. Ritchie, J. H. J. Scott, and D. C. Joy, Eds., New York, NY: Springer, 2018, pp. 93–110. doi: 10.1007/978-1-4939-6676-9_6.

[256] J. I. Goldstein, D. E. Newbury, J. R. Michael, N. W. M. Ritchie, J. H. J. Scott, and D. C. Joy, "Backscattered Electrons," in *Scanning Electron Microscopy and X-Ray Microanalysis*, J. I. Goldstein, D. E. Newbury, J. R. Michael, N. W. M. Ritchie, J. H. J. Scott, and D. C. Joy, Eds., New York, NY: Springer, 2018, pp. 15–28. doi: 10.1007/978-1-4939-6676-9_2.

[257] Claudionico~commonswiki, *English: Illustration of the phenomena that occur from the interaction of highly energetic electrons with matter, also depicting the pear shape interaction volume which is typically observed in this type of interactions.* 2013. Accessed: Jun. 07, 2022. [Online]. Available: https://commons.wikimedia.org/wiki/File:Electron_Interaction_with_Matter.svg

[258] H. Hertz, "Ueber einen Einfluss des ultravioletten Lichtes auf die electrische Entladung," *Ann. Phys.*, vol. 267, no. 8, pp. 983–1000, 1887, doi: 10.1002/andp.18872670827.

[259] A. Einstein, "Über einen die Erzeugung und Verwandlung des Lichtes betreffenden heuristischen Gesichtspunkt," *Ann. Phys.*, vol. 322, no. 6, pp. 132–148, 1905, doi: 10.1002/andp.19053220607.

[260] K. Siegbahn and Kungl. Vetenskaps-societeten i Uppsala, *ESCA; atomic, molecular and solid state structure studied by means of electron spectroscopy,.* Uppsala: Almqvist & Wiksells, 1967.

[261] "The Nobel Prize in Physics 1981," NobelPrize.org. Accessed: Jun. 09, 2022. [Online]. Available: https://www.nobelprize.org/prizes/physics/1981/summary/

[262] S. O. Kasap, *Principles of Electronic Materials and Devices*. McGraw-Hill, 2006.

[263] J. F. Moulder, *Handbook of X-ray Photoelectron Spectroscopy: A Reference Book of Standard Spectra for Identification and Interpretation of XPS Data.* Physical Electronics Division, Perkin-Elmer Corporation, 1992.

[264] D. Briggs and M. P. Seah, *Practical Surface Analysis, Auger and X-ray Photoelectron Spectroscopy*. Wiley, 1990.

[265] R. Gurwitz, R. Cohen, and I. Shalish, "Interaction of light with the ZnO surface: Photon induced oxygen 'breathing,' oxygen vacancies, persistent photoconductivity, and persistent photovoltage," *J. Appl. Phys.*, vol. 115, no. 3, p. 033701, Jan. 2014, doi: 10.1063/1.4861413.

[266] "Avantage Data System." Accessed: Jun. 09, 2022. [Online]. Available: https://www.thermofisher.com/order/catalog/product/IQLAADGACKFAKRMAVI

[267] "Fusion Select Components," Protochips. Accessed: May 18, 2022. [Online]. Available: https://www.protochips.com/products/fusion/fusion-select-components/

[268] H. Ohno, D. Takagi, K. Yamada, S. Chiashi, A. Tokura, and Y. Homma, "Growth of Vertically Aligned Single-Walled Carbon Nanotubes on Alumina and Sapphire Substrates," *Jpn. J. Appl. Phys.*, vol. 47, no. 4R, p. 1956, Apr. 2008, doi: 10.1143/JJAP.47.1956.

[269] F. Muñoz-Muñoz *et al.*, "The control of thickness on aluminum oxide nanotubes by Atomic Layer Deposition using carbon nanotubes as removable templates," *Powder Technol.*, vol. 286, pp. 602–609, Dec. 2015, doi: 10.1016/j.powtec.2015.09.015.

[270] E. Jiran and C. V. Thompson, "Capillary instabilities in thin films," *J. Electron. Mater.*, vol. 19, no. 11, pp. 1153–1160, Nov. 1990, doi: 10.1007/BF02673327.

[271] L. Lari, S. Steinhauer, and V. K. Lazarov, "In situ TEM oxidation study of Fe thin-film transformation to single-crystal magnetite nanoparticles," *J. Mater. Sci.*, vol. 55, no. 27, pp. 12897–12905, Sep. 2020, doi: 10.1007/s10853-020-04917-8.

[272] H. Li, "Influence of Fe Films in the Growth of Carbon Nanotubes by Chemical Vapor Deposition," *J. Phys. Conf. Ser.*, vol. 1838, no. 1, p. 012032, Mar. 2021, doi: 10.1088/1742-6596/1838/1/012032.

[273] M. Volmer and A. Weber, "Keimbildung in übersättigten Gebilden," *Z. Für Phys. Chem.*, vol. 119U, no. 1, pp. 277–301, Jan. 1926, doi: 10.1515/zpch-1926-11927.

[274] M. Cantoro *et al.*, "Effects of pre-treatment and plasma enhancement on chemical vapor deposition of carbon nanotubes from ultra-thin catalyst films," *Diam. Relat. Mater.*, vol. 15, no. 4, pp. 1029–1035, Apr. 2006, doi: 10.1016/j.diamond.2006.01.007.

[275] S.-H. Lee and G.-H. Jeong, "Effect of catalytic metals on diameter-controlled growth of single-walled carbon nanotubes: Comparison between Fe and Au," *Electron. Mater. Lett.*, vol. 8, no. 1, pp. 5–9, Feb. 2012, doi: 10.1007/s13391-011-0930-0.

[276] Y. Wang *et al.*, "Comparison study of catalyst nanoparticle formation and carbon nanotube growth: Support effect," *J. Appl. Phys.*, vol. 101, no. 12, p. 124310, Jun. 2007, doi: 10.1063/1.2749412.

[277] Y. Li *et al.*, "How Catalysts Affect the Growth of Single-Walled Carbon Nanotubes on Substrates," *Adv. Mater.*, vol. 22, no. 13, pp. 1508–1515, 2010, doi: 10.1002/adma.200904366.

[278] A. Okita *et al.*, "Effects of hydrogen on carbon nanotube formation in CH4/H2 plasmas," *Carbon*, vol. 45, no. 7, pp. 1518–1526, Jun. 2007, doi: 10.1016/j.carbon.2007.03.022.

[279] A. Talla, N. J. Suliali, W. E. Goosen, Z. N. Urgessa, S. V. Motloung, and J. R. Botha, "Effect of annealing temperature and atmosphere on the structural, morphological and luminescent properties of TiO2 nanotubes," *Phys. B Condens. Matter*, vol. 640, p. 414026, Sep. 2022, doi: 10.1016/j.physb.2022.414026.

[280] A. I. Yardimci, S. Yılmaz, and Y. Selamet, "The effects of catalyst pretreatment, growth atmosphere and temperature on carbon nanotube synthesis using Co–Mo/MgO catalyst," *Diam. Relat. Mater.*, vol. 60, pp. 81–86, Nov. 2015, doi: 10.1016/j.diamond.2015.10.025.

[281] Y. Y. Wei, G. Eres, V. I. Merkulov, and D. H. Lowndes, "Effect of catalyst film thickness on carbon nanotube growth by selective area chemical vapor deposition," *Appl. Phys. Lett.*, vol. 78, no. 10, pp. 1394–1396, Mar. 2001, doi: 10.1063/1.1354658.

[282] R. Rao *et al.*, "Maximization of carbon nanotube yield by solid carbon-assisted dewetting of iron catalyst films," *Carbon*, vol. 165, pp. 251–258, Sep. 2020, doi: 10.1016/j.carbon.2020.04.064.

[283] C.-W. Tsai and E. H. G. Langner, "The effect of synthesis temperature on the particle size of nano-ZIF-8," *Microporous Mesoporous Mater.*, vol. 221, pp. 8–13, Feb. 2016, doi: 10.1016/j.micromeso.2015.08.041.

[284] C. L. Pint *et al.*, "Temperature and Gas Pressure Effects in Vertically Aligned Carbon Nanotube Growth from Fe–Mo Catalyst," *J. Phys. Chem. C*, vol. 112, no. 36, pp. 14041–14051, Sep. 2008, doi: 10.1021/jp8025539.

[285] C. J. Gommes, "Ostwald ripening of confined nanoparticles: chemomechanical coupling in nanopores," *Nanoscale*, vol. 11, no. 15, pp. 7386–7393, Apr. 2019, doi: 10.1039/C9NR01349K.

[286] A. Börjesson and K. Bolton, "First Principles Studies of the Effect of Ostwald Ripening on Carbon Nanotube Chirality Distributions," *ACS Nano*, vol. 5, no. 2, pp. 771–779, Feb. 2011, doi: 10.1021/nn101214v.

[287] H. Ham, N.-H. Park, S. S. Kim, and H. W. Kim, "Evidence of Ostwald ripening during evolution of micro-scale solid carbon spheres," *Sci. Rep.*, vol. 4, no. 1, Art. no. 1, Jan. 2014, doi: 10.1038/srep03579.

[288] G. Madras and B. J. McCoy, "Temperature effects during Ostwald ripening," *J. Chem. Phys.*, vol. 119, no. 3, pp. 1683–1693, Jul. 2003, doi: 10.1063/1.1578617.

[289] D. K. Pattadar and F. P. Zamborini, "Effect of Size, Coverage, and Dispersity on the Potential-Controlled Ostwald Ripening of Metal Nanoparticles," *Langmuir*, vol. 35, no. 50, pp. 16416–16426, Dec. 2019, doi: 10.1021/acs.langmuir.9b02421.

[290] S. Sakurai *et al.*, "Role of Subsurface Diffusion and Ostwald Ripening in Catalyst Formation for Single-Walled Carbon Nanotube Forest Growth," *J. Am. Chem. Soc.*, vol. 134, no. 4, pp. 2148–2153, Feb. 2012, doi: 10.1021/ja208706c.

[291] F. A. Halden and W. D. Kingery, "Surface Tension at Elevated Temperatures. II. Effect of C, N, O and S on Liquid Iron Surface Tension and Interfacial Energy with Al2O3," *J. Phys. Chem.*, vol. 59, no. 6, pp. 557–559, Jun. 1955, doi: 10.1021/j150528a018.

[292] B. Wang, Y. Yang, L.-J. Li, and Y. Chen, "Effect of different catalyst supports on the (n,m) selective growth of single-walled carbon nanotube from Co–Mo catalyst," *J. Mater. Sci.*, vol. 44, no. 12, pp. 3285–3295, Jun. 2009, doi: 10.1007/s10853-009-3444-5.

[293] E. Van Hooijdonk, C. Bittencourt, R. Snyders, and J.-F. Colomer, "Functionalization of vertically aligned carbon nanotubes," *Beilstein J. Nanotechnol.*, vol. 4, pp. 129–152, Feb. 2013, doi: 10.3762/bjnano.4.14.

[294] I. Levchenko, Z.-J. Han, S. Kumar, S. Yick, J. Fang, and K. Ostrikov, *Large Arrays and Networks of Carbon Nanotubes: Morphology Control by Process Parameters*. IntechOpen, 2013. doi: 10.5772/52674.

[295] Y. Zhang, G. Sun, Z. Zhan, and L. Zheng, "Influence of Al2O3 buffer layer on catalyst morphology and spinnability of carbon nanotube arrays," *J. Mater. Sci.*, vol. 52, no. 11, pp. 6196–6204, Jun. 2017, doi: 10.1007/s10853-017-0828-9.

[296] H. Yoshida, T. Shimizu, T. Uchiyama, H. Kohno, Y. Homma, and S. Takeda, "Atomic-scale analysis on the role of molybdenum in iron-catalyzed carbon nanotube growth," *Nano Lett.*, vol. 9, no. 11, pp. 3810–3815, 2009, doi: 10.1021/nl9019903.

[297] A. Yahyazadeh and B. Khoshandam, "Carbon nanotube synthesis via the catalytic chemical vapor deposition of methane in the presence of iron, molybdenum, and iron–molybdenum alloy thin layer catalysts," *Results Phys.*, vol. 7, pp. 3826–3837, Jan. 2017, doi: 10.1016/j.rinp.2017.10.001.

[298] E. Lamouroux, P. Serp, Y. Kihn, and P. Kalck, "Identification of key parameters for the selective growth of single or double wall carbon nanotubes on FeMo/Al2O3 CVD catalysts," *Appl. Catal. Gen.*, vol. 323, pp. 162–173, Apr. 2007, doi: 10.1016/j.apcata.2007.02.019.

[299] T. Koilraj and K. Kalaichelvan, "Synthesis of carbon nanotubes using Fe-Mo/Al2O3 bimetallic catalyst by CVD method," *IEEE-Int. Conf. Adv. Eng. Sci. Manag. ICAESM-2012*, Jan. 2012.

[300] S. C. Lyu *et al.*, "Synthesis of high-quality single-walled carbon nanotubes by catalytic decomposition of C2H2," *Chem. Commun.*, no. 6, pp. 734–735, Jan. 2003, doi: 10.1039/B300109A.

[301] Y. Li *et al.*, "Mass production of high-quality multi-walled carbon nanotube bundles on a Ni/Mo/MgO catalyst," *Carbon*, vol. 2, no. 43, pp. 295–301, 2005, doi: 10.1016/j.carbon.2004.09.014.

[302] X. Li, M. Baker-Fales, H. Almkhelfe, N. R. Gaede, T. S. Harris, and P. B. Amama, "Rational Modification of a Metallic Substrate for CVD Growth of Carbon Nanotubes," *Sci. Rep.*, vol. 8, no. 1, Art. no. 1, Mar. 2018, doi: 10.1038/s41598-018-22467-7.

[303] "ImageJ." Accessed: Jul. 07, 2022. [Online]. Available: https://imagej.nih.gov/ij/

[304] A. C. Ferrari, J. Robertson, C. Thomsen, S. Reich, and J. Maultzsch, "Resonant Raman spectroscopy of nanotubes," *Philos. Trans. R. Soc. Lond. Ser. Math. Phys. Eng. Sci.*, vol. 362, no. 1824, pp. 2337–2359, Nov. 2004, doi: 10.1098/rsta.2004.1444.

[305] C. Powell, "X-ray Photoelectron Spectroscopy Database XPS,Version 4.1, NIST Standard Reference Database 20." National Institute of Standards and Technology, 1989. doi: 10.18434/T4T88K.

[306] B. Kobe, M. Badley, J. D. Henderson, S. Anderson, M. C. Biesinger, and D. Shoesmith, "Application of quantitative X-ray photoelectron spectroscopy (XPS) imaging: investigation of Ni-Cr-Mo alloys exposed to crevice corrosion

solution," *Surf. Interface Anal.*, vol. 49, no. 13, pp. 1345–1350, 2017, doi: 10.1002/sia.6325.

[307] William. Swartz and D. M. Hercules, "X-ray photoelectron spectroscopy of molybdenum compounds. Use of electron spectroscopy for chemical analysis (ESCA) in quantitative analysis," *Anal. Chem.*, vol. 43, no. 13, pp. 1774–1779, Nov. 1971, doi: 10.1021/ac60307a020.

[308] W. A. Brainard and D. R. Wheeler, "An XPS study of the adherence of refractory carbide silicide and boride rf-sputtered wear-resistant coatings," *J. Vac. Sci. Technol.*, vol. 15, no. 6, pp. 1800–1805, Nov. 1978, doi: 10.1116/1.569845.

[309] L. Leclercq, M. Provost, H. Pastor, and G. Leclercq, "Catalytic properties of transition metal carbides: II. Activity of bulk mixed carbides of molybdenum and tungsten in hydrocarbon conversion," *J. Catal.*, vol. 117, no. 2, pp. 384–395, Jun. 1989, doi: 10.1016/0021-9517(89)90349-7.

[310] M. Descostes, F. Mercier, N. Thromat, C. Beaucaire, and M. Gautier-Soyer, "Use of XPS in the determination of chemical environment and oxidation state of iron and sulfur samples: constitution of a data basis in binding energies for Fe and S reference compounds and applications to the evidence of surface species of an oxidized pyrite in a carbonate medium," *Appl. Surf. Sci.*, vol. 165, no. 4, pp. 288–302, Oct. 2000, doi: 10.1016/S0169-4332(00)00443-8.

[311] S. J. Roosendaal, B. van Asselen, J. W. Elsenaar, A. M. Vredenberg, and F. H. P. M. Habraken, "The oxidation state of Fe(100) after initial oxidation in O2," *Surf. Sci.*, vol. 442, no. 3, pp. 329–337, Dec. 1999, doi: 10.1016/S0039-6028(99)01006-7.

[312] P. Mills and J. L. Sullivan, "A study of the core level electrons in iron and its three oxides by means of X-ray photoelectron spectroscopy," *J. Phys. Appl. Phys.*, vol. 16, no. 5, pp. 723–732, May 1983, doi: 10.1088/0022-3727/16/5/005.

[313] I. N. Shabanova and V. A. Trapeznikov, "A study of the electronic structure of Fe3C, Fe3Al and Fe3Si by x-ray photoelectron spectroscopy," *J. Electron Spectrosc. Relat. Phenom.*, vol. 6, no. 4, pp. 297–307, Jan. 1975, doi: 10.1016/0368-2048(75)80039-9.

[314] C. Verissimo, A. L. Gobbi, and S. A. Moshkalev, "Synthesis of carbon nanotubes directly over TEM grids aiming the study of nucleation and growth mechanisms," *Appl. Surf. Sci.*, vol. 254, no. 13, pp. 3890–3895, Apr. 2008, doi: 10.1016/j.apsusc.2007.12.009.

[315] J. W. M. Jacobs and J. F. C. M. Verhoeven, "Specimen preparation technique for high resolution transmission electron microscopy studies on model supported metal catalysts," *J. Microsc.*, vol. 143, no. 1, pp. 103–116, 1986, doi: 10.1111/j.1365-2818.1986.tb02768.x.

[316] F. Enquist and A. Spetz, "The fabrication of amorphous SiO2 substrates suitable for transmission electron microscopy studies of ultrathin polycrystalline films," *Thin Solid Films*, vol. 145, no. 1, pp. 99–104, Dec. 1986, doi: 10.1016/0040-6090(86)90256-7.

[317] G. Gu, G. Philipp, X. Wu, M. Burghard, A. M. Bittner, and S. Roth, "Growth of Single-Walled Carbon Nanotubes from Microcontact-Printed Catalyst Patterns on Thin Si3N4 Membranes," *Adv. Funct. Mater.*, vol. 11, no. 4, pp. 295–298, 2001, doi: 10.1002/1616-3028(200108)11:4<295::AID-ADFM295>3.0.CO;2-2.

[318] O. A. Nerushev, S. Dittmar, R.-E. Morjan, F. Rohmund, and E. E. B. Campbell, "Particle size dependence and model for iron-catalyzed growth of carbon nanotubes by thermal chemical vapor deposition," *J. Appl. Phys.*, vol. 93, no. 7, pp. 4185–4190, Apr. 2003, doi: 10.1063/1.1559433.

[319] R. Sharma, E. Moore, P. Rez, and M. M. J. Treacy, "Site-Specific Fabrication of Fe Particles for Carbon Nanotube Growth," *Nano Lett.*, vol. 9, no. 2, pp. 689–694, Feb. 2009, doi: 10.1021/nl803180e.

[320] S. K. Youn and H. G. Park, "Morphological Evolution of Fe–Mo Bimetallic Catalysts for Diameter and Density Modulation of Vertically Aligned Carbon Nanotubes," *J. Phys. Chem. C*, vol. 117, no. 36, pp. 18657–18665, Sep. 2013, doi: 10.1021/jp402941u.

[321] M. Pérez-Mendoza, C. Vallés, W. K. Maser, M. T. Martínez, and A. M. Benito, "Influence of molybdenum on the chemical vapour deposition production of carbon nanotubes," *Nanotechnology*, vol. 16, no. 5, pp. S224–S229, Mar. 2005, doi: 10.1088/0957-4484/16/5/016.

[322] M. Hu, Y. Murakami, M. Ogura, S. Maruyama, and T. Okubo, "Morphology and chemical state of Co-Mo catalysts for growth of single-walled carbon nanotubes vertically aligned on quartz substrates," *J. Catal.*, vol. 225, no. 1, pp. 230–239, 2004, doi: 10.1016/j.jcat.2004.04.013.

[323] H. Sugime, S. Noda, S. Maruyama, and Y. Yamaguchi, "Multiple 'optimum' conditions for Co-Mo catalyzed growth of vertically aligned single-walled carbon nanotube forests," *Carbon*, vol. 47, no. 1, pp. 234–241, 2009, doi: 10.1016/j.carbon.2008.10.001.

[324] S. M. Bachilo, L. Balzano, J. E. Herrera, F. Pompeo, D. E. Resasco, and R. B. Weisman, "Narrow (n,m)-Distribution of Single-Walled Carbon Nanotubes Grown Using a Solid Supported Catalyst," *J. Am. Chem. Soc.*, vol. 125, no. 37, pp. 11186–11187, Sep. 2003, doi: 10.1021/ja036622c.

[325] O. Gohardani, M. C. Elola, and C. Elizetxea, "Potential and prospective implementation of carbon nanotubes on next generation aircraft and space vehicles: A review of current and expected applications in aerospace sciences," *Prog. Aerosp. Sci.*, vol. 70, pp. 42–68, Oct. 2014, doi: 10.1016/j.paerosci.2014.05.002.

[326] C. Cantalini, L. Valentini, I. Armentano, J. M. Kenny, L. Lozzi, and S. Santucci, "Carbon nanotubes as new materials for gas sensing applications," *J. Eur. Ceram. Soc.*, vol. 24, no. 6, pp. 1405–1408, Jan. 2004, doi: 10.1016/S0955-2219(03)00441-2.

[327] S. Z. Mortazavi, A. Reyhani, and A. Iraji zad, "The effect of Pd addition to Fe as catalysts on growth of carbon nanotubes by TCVD method," *Appl. Surf.*

Sci., vol. 254, no. 20, pp. 6416–6421, Aug. 2008, doi: 10.1016/j.apsusc.2008.04.019.

[328] T. Maruyama, Y. Mizutani, S. Naritsuka, and S. Iijima, "Single-Walled Carbon Nanotube Growth in High Vacuum Using Pt Catalyst in Alcohol Gas Source Method," *Mater. Express*, vol. 1, no. 4, pp. 267–272, Dec. 2011, doi: 10.1166/mex.2011.1046.

[329] S. Bandow *et al.*, "Effect of the Growth Temperature on the Diameter Distribution and Chirality of Single-Wall Carbon Nanotubes," *Phys. Rev. Lett.*, vol. 80, no. 17, pp. 3779–3782, Apr. 1998, doi: 10.1103/PhysRevLett.80.3779.

[330] H. Dai, A. G. Rinzler, P. Nikolaev, A. Thess, D. T. Colbert, and R. E. Smalley, "Single-wall nanotubes produced by metal-catalyzed disproportionation of carbon monoxide," *Chem. Phys. Lett.*, vol. 260, no. 3, pp. 471–475, Sep. 1996, doi: 10.1016/0009-2614(96)00862-7.

[331] L. C. QIN, "CVD synthesis of carbon nanotubes," *J. Mater. Sci. Lett.*, vol. 16, no. 6, pp. 457–459, Mar. 1997, doi: 10.1023/A:1018504108114.

[332] N. H. Lee and S.-H. Nahm, "Critical conditions at low pressure to improve the quality of directly spinnable CNTs," *Fuller. Nanotub. Carbon Nanostructures*, vol. 27, no. 10, pp. 779–787, Oct. 2019, doi: 10.1080/1536383X.2019.1640213.

[333] X. Zhang *et al.*, "Spinning and Processing Continuous Yarns from 4-Inch Wafer Scale Super-Aligned Carbon Nanotube Arrays," *Adv. Mater.*, vol. 18, no. 12, pp. 1505–1510, 2006, doi: 10.1002/adma.200502528.

[334] Y. A. Kasumov *et al.*, "CVD growth of carbon nanotubes at very low pressure of acetylene," *Appl. Phys. A*, vol. 88, no. 4, pp. 687–691, Sep. 2007, doi: 10.1007/s00339-007-4028-3.

[335] A. Kozawa, T. Saida, S. Naritsuka, and T. Maruyama, "Synthesis of single-walled carbon nanotubes from Pd catalysts by gas source method using ethanol in high vacuum," *Jpn. J. Appl. Phys.*, vol. 55, no. 1S, p. 01AE02, Oct. 2015, doi: 10.7567/JJAP.55.01AE02.

[336] T. Shiokawa, B. P. Zhang, M. Suzuki, T. Kobayashi, and K. Ishibashi, "Low pressure CVD growth of single-wall carbon nanotubes," in *Digest of Papers Microprocesses and Nanotechnology 2005*, Oct. 2005, pp. 92–93. doi: 10.1109/IMNC.2005.203753.

[337] P. Delhaes, "Chemical vapor deposition and infiltration processes of carbon materials," *Carbon*, vol. 40, no. 5, pp. 641–657, Apr. 2002, doi: 10.1016/S0008-6223(01)00195-6.

[338] J. Antes, Z. Hu, W. Zhang, and K. J. Hüttinger, "Chemistry and kinetics of chemical vapour deposition of pyrocarbon: VII. Confirmation of the influence of the substrate surface area/reactor volume ratio," *Carbon*, vol. 37, no. 12, pp. 2031–2039, Jan. 1999, doi: 10.1016/S0008-6223(99)00070-6.

[339] H. J. Jeong, H. D. Park, J. D. Lee, and J. O. Park, "Densification of carbon/carbon composites by pulse chemical vapor infiltration," *Carbon*, vol. 34, no. 3, pp. 417–421, Jan. 1996, doi: 10.1016/0008-6223(95)00208-1.

[340] J. Maultzsch, H. Telg, S. Reich, and C. Thomsen, "Radial breathing mode of single-walled carbon nanotubes: Optical transition energies and chiral-index

assignment," *Phys. Rev. B*, vol. 72, no. 20, p. 205438, Nov. 2005, doi: 10.1103/PhysRevB.72.205438.

[341] S. Chaisitsak, A. Yamada, and M. Konagai, "Hot filament enhanced CVD synthesis of carbon nanotubes by using a carbon filament," *Diam. Relat. Mater.*, vol. 13, no. 3, pp. 438–444, Mar. 2004, doi: 10.1016/S0925-9635(03)00572-7.

[342] W. Z. Li, J. G. Wen, Y. Tu, and Z. F. Ren, "Effect of gas pressure on the growth and structure of carbon nanotubes by chemical vapor deposition," *Appl. Phys. A*, vol. 73, no. 2, pp. 259–264, Aug. 2001, doi: 10.1007/s003390100916.

[343] B. Ganjipour, S. Mohajerzadeh, H. Hesamzadeh, and A. Khodadadi, "Effect of Pressure on Morphology of the Grown Layers of Carbon Nanotubes by Modified Plasma-Enhanced Chemical Vapor Deposition," *Fuller. Nanotub. Carbon Nanostructures*, vol. 13, no. sup1, pp. 365–373, Apr. 2005, doi: 10.1081/FST-200039354.

[344] R. Sharma, P. Rez, M. Brown, G. Du, and M. M. J. Treacy, "Dynamic observations of the effect of pressure and temperature conditions on the selective synthesis of carbon nanotubes," *Nanotechnology*, vol. 18, no. 12, p. 125602, Feb. 2007, doi: 10.1088/0957-4484/18/12/125602.

[345] M. Xu, D. N. Futaba, M. Yumura, and K. Hata, "Alignment Control of Carbon Nanotube Forest from Random to Nearly Perfectly Aligned by Utilizing the Crowding Effect," *ACS Nano*, vol. 6, no. 7, pp. 5837–5844, Jul. 2012, doi: 10.1021/nn300142j.

[346] B. T. Madhava and W. Shiren, "Separation of Metallic and Semiconducting Carbon Nanotubes," *Recent Pat. Nanotechnol.*, vol. 4, no. 1, pp. 1–9, Dec. 2009.

[347] L. Shi *et al.*, "Templated direct growth of ultra-thin double-walled carbon nanotubes," *Nanoscale*, vol. 10, no. 45, pp. 21254–21261, Nov. 2018, doi: 10.1039/C8NR06925E.

[348] M. S. Roslan *et al.*, "Growth of Wall-controlled MWCNTs by Magnetic Field Assisted Arc Discharge Plasma," *J. Saudi Chem. Soc.*, vol. 23, no. 2, pp. 171–181, Feb. 2019, doi: 10.1016/j.jscs.2018.06.003.

[349] H. Navas *et al.*, "Unveiling the Evolutions of Nanotube Diameter Distribution during the Growth of Single-Walled Carbon Nanotubes," *ACS Nano*, vol. 11, no. 3, pp. 3081–3088, Mar. 2017, doi: 10.1021/acsnano.7b00077.

[350] H. Ming, D. Peiling, Z. Yunlong, G. Jing, and R. Xiaoxue, "Effect of Reaction Temperature on Carbon Yield and Morphology of CNTs on Copper Loaded Nickel Nanoparticles," *J. Nanomater.*, vol. 2016, p. e8106845, Mar. 2016, doi: 10.1155/2016/8106845.

[351] A. Simon *et al.*, "Carbon nanotubes and carbon nanofibers fabricated on tubular porous Al2O3 substrates," *Carbon*, vol. 90, pp. 25–33, Aug. 2015, doi: 10.1016/j.carbon.2015.03.048.

[352] Q.-M. Gong, Z. Li, Y. Wang, B. Wu, Z. Zhang, and J. Liang, "The effect of high-temperature annealing on the structure and electrical properties of well-

aligned carbon nanotubes," *Mater. Res. Bull.*, vol. 42, no. 3, pp. 474–481, Mar. 2007, doi: 10.1016/j.materresbull.2006.06.023.

[353] M. Pudukudy, Z. Yaakob, and M. S. Takriff, "Methane decomposition over unsupported mesoporous nickel ferrites: effect of reaction temperature on the catalytic activity and properties of the produced nanocarbon," *RSC Adv.*, vol. 6, no. 72, pp. 68081–68091, Jul. 2016, doi: 10.1039/C6RA14660K.

[354] C. O. Calgaro and O. W. Perez-Lopez, "Decomposition of methane over Co3−xAlxO4 (x=0–2) coprecipitated catalysts: The role of Co phases in the activity and stability," *Int. J. Hydrog. Energy*, vol. 42, no. 50, pp. 29756–29772, Dec. 2017, doi: 10.1016/j.ijhydene.2017.10.082.

[355] N. A. Hermes, M. A. Lansarin, and O. W. Perez-Lopez, "Catalytic Decomposition of Methane Over M–Co–Al Catalysts (M = Mg, Ni, Zn, Cu)," *Catal. Lett.*, vol. 141, no. 7, pp. 1018–1025, Jul. 2011, doi: 10.1007/s10562-011-0611-5.

[356] H. Y. Wang and A. C. Lua, "Methane decomposition using Ni–Cu alloy nanoparticle catalysts and catalyst deactivation studies," *Chem. Eng. J.*, vol. 262, pp. 1077–1089, Feb. 2015, doi: 10.1016/j.cej.2014.10.063.

[357] F. Z. Bouanis *et al.*, "Diameter controlled growth of SWCNTs using Ru as catalyst precursors coupled with atomic hydrogen treatment," *Chem. Eng. J.*, vol. 332, pp. 92–101, Jan. 2018, doi: 10.1016/j.cej.2017.09.073.

[358] A. R. Biris *et al.*, "Analytic studies of high quality singlewall carbon nanotubes synthesized on a novel Fe:Mo:MgO catalyst," *Phys. E Low-Dimens. Syst. Nanostructures*, vol. 43, no. 1, pp. 552–558, Nov. 2010, doi: 10.1016/j.physe.2010.09.014.

[359] L. Ding *et al.*, "Selective Growth of Well-Aligned Semiconducting Single-Walled Carbon Nanotubes," *Nano Lett.*, vol. 9, no. 2, pp. 800–805, Feb. 2009, doi: 10.1021/nl803496s.

[360] J.-F. Colomer *et al.*, "Large-scale synthesis of single-wall carbon nanotubes by catalytic chemical vapor deposition (CCVD) method," *Chem. Phys. Lett.*, vol. 317, no. 1, pp. 83–89, Jan. 2000, doi: 10.1016/S0009-2614(99)01338-X.

[361] W. Z. Li, J. G. Wen, and Z. F. Ren, "Effect of temperature on growth and structure of carbon nanotubes by chemical vapor deposition," *Appl. Phys. A*, vol. 74, no. 3, pp. 397–402, Mar. 2002, doi: 10.1007/s003390201284.

[362] C. T. M. Kwok *et al.*, "Temperature and time dependence study of single-walled carbon nanotube growth by catalytic chemical vapor deposition," *Carbon*, vol. 48, no. 4, pp. 1279–1288, Apr. 2010, doi: 10.1016/j.carbon.2009.11.053.

[363] M. L. Geier *et al.*, "Solution-processed carbon nanotube thin-film complementary static random access memory," *Nat. Nanotechnol.*, vol. 10, no. 11, Art. no. 11, Nov. 2015, doi: 10.1038/nnano.2015.197.

[364] S. Karoui, H. Amara, C. Bichara, and F. Ducastelle, "Nickel-Assisted Healing of Defective Graphene," *ACS Nano*, vol. 4, no. 10, pp. 6114–6120, Oct. 2010, doi: 10.1021/nn101822s.

[365] M. Picher, H. Navas, R. Arenal, E. Quesnel, E. Anglaret, and V. Jourdain, "Influence of the growth conditions on the defect density of single-walled carbon nanotubes," *Carbon*, vol. 50, no. 7, pp. 2407–2416, Jun. 2012, doi: 10.1016/j.carbon.2012.01.055.

[366] J. Luo *et al.*, "Rationally Designed Hierarchical TiO2@Fe2O3 Hollow Nanostructures for Improved Lithium Ion Storage," *Adv. Energy Mater.*, vol. 3, no. 6, pp. 737–743, 2013, doi: 10.1002/aenm.201200953.

[367] P. S. Bagus, C. J. Nelin, C. R. Brundle, N. Lahiri, E. S. Ilton, and K. M. Rosso, "Analysis of the Fe 2p XPS for hematite ∝ Fe2O3: Consequences of covalent bonding and orbital splittings on multiplet splittings," *J. Chem. Phys.*, vol. 152, no. 1, p. 014704, Jan. 2020, doi: 10.1063/1.5135595.

[368] M. R. Shenoy *et al.*, "Visible light sensitive hexagonal boron nitride (hBN) decorated Fe2O3 photocatalyst for the degradation of methylene blue," *J. Mater. Sci. Mater. Electron.*, vol. 32, no. 4, pp. 4766–4783, Feb. 2021, doi: 10.1007/s10854-020-05215-4.

[369] Y. Huang *et al.*, "Facile synthesis of ∝-Fe2O3 nanodisk with superior photocatalytic performance and mechanism insight," *Sci. Technol. Adv. Mater.*, vol. 16, no. 1, p. 014801, Feb. 2015, doi: 10.1088/1468-6996/16/1/014801.

[370] K. Wandelt, "Photoemission studies of adsorbed oxygen and oxide layers," *Surf. Sci. Rep.*, vol. 2, no. 1, pp. 1–121, Sep. 1982, doi: 10.1016/0167-5729(82)90003-6.

[371] C. S. Kuivila, J. B. Butt, and P. C. Stair, "Characterization of surface species on iron synthesis catalysts by X-ray photoelectron spectroscopy," *Appl. Surf. Sci.*, vol. 32, no. 1, pp. 99–121, Jun. 1988, doi: 10.1016/0169-4332(88)90076-1.

[372] H. Amara and C. Bichara, "Modeling the Growth of Single-Wall Carbon Nanotubes," *Top. Curr. Chem.*, vol. 375, no. 3, p. 55, May 2017, doi: 10.1007/s41061-017-0141-8.

[373] Y. Shibuta and S. Maruyama, "Molecular dynamics simulation of formation process of single-walled carbon nanotubes by CCVD method," *Chem. Phys. Lett.*, vol. 382, no. 3, pp. 381–386, Dec. 2003, doi: 10.1016/j.cplett.2003.10.080.

[374] J. Zhao, A. Martinez-Limia, and P. B. Balbuena, "Understanding catalysed growth of single-wall carbon nanotubes," *Nanotechnology*, vol. 16, no. 7, pp. S575–S581, Jun. 2005, doi: 10.1088/0957-4484/16/7/035.

[375] M. He *et al.*, "High temperature growth of single-walled carbon nanotubes with a narrow chirality distribution by tip-growth mode," *Chem. Eng. J.*, vol. 341, pp. 344–350, Jun. 2018, doi: 10.1016/j.cej.2018.02.051.

[376] M. Picher, E. Anglaret, R. Arenal, and V. Jourdain, "Self-Deactivation of Single-Walled Carbon Nanotube Growth Studied by in Situ Raman Measurements," *Nano Lett.*, vol. 9, no. 2, pp. 542–547, Feb. 2009, doi: 10.1021/nl802661z.

[377] M. Picher, E. Anglaret, R. Arenal, and V. Jourdain, "Processes Controlling the Diameter Distribution of Single-Walled Carbon Nanotubes during Catalytic Chemical Vapor Deposition," *ACS Nano*, vol. 5, no. 3, pp. 2118–2125, Mar. 2011, doi: 10.1021/nn1033086.

[378] L. Zhang *et al.*, "Growth Termination and Multiple Nucleation of Single-Wall Carbon Nanotubes Evidenced by in Situ Transmission Electron Microscopy," *ACS Nano*, vol. 11, no. 5, pp. 4483–4493, May 2017, doi: 10.1021/acsnano.6b05941.

[379] B. Hou, C. Wu, T. Inoue, S. Chiashi, R. Xiang, and S. Maruyama, "Extended alcohol catalytic chemical vapor deposition for efficient growth of single-walled carbon nanotubes thinner than (6,5)," *Carbon*, vol. 119, pp. 502–510, Aug. 2017, doi: 10.1016/j.carbon.2017.04.045.

[380] C. Lu and J. Liu, "Controlling the Diameter of Carbon Nanotubes in Chemical Vapor Deposition Method by Carbon Feeding," *J. Phys. Chem. B*, vol. 110, no. 41, pp. 20254–20257, Oct. 2006, doi: 10.1021/jp0632283.

[381] A. R. Harutyunyan, T. Tokune, and E. Mora, "Liquid as a required catalyst phase for carbon single-walled nanotube growth," *Appl. Phys. Lett.*, vol. 87, no. 5, p. 051919, Aug. 2005, doi: 10.1063/1.2005395.

[382] Ph. Buffat and J.-P. Borel, "Size effect on the melting temperature of gold particles," *Phys. Rev. A*, vol. 13, no. 6, pp. 2287–2298, Jun. 1976, doi: 10.1103/PhysRevA.13.2287.

[383] R. Sharma and Z. Iqbal, "In situ observations of carbon nanotube formation using environmental transmission electron microscopy," *Appl. Phys. Lett.*, vol. 84, no. 6, pp. 990–992, Feb. 2004, doi: https://doi.org/10.1063/1.1646465.

[384] H. Zhu, K. Suenaga, A. Hashimoto, K. Urita, K. Hata, and S. Iijima, "Atomic-Resolution Imaging of the Nucleation Points of Single-Walled Carbon Nanotubes," *Small*, vol. 1, no. 12, pp. 1180–1183, 2005, doi: 10.1002/smll.200500200.

[385] V. Papaefthimiou *et al.*, "Effect of the Specific Surface Sites on the Reducibility of α-Fe2O3/Graphene Composites by Hydrogen," *J. Phys. Chem. C*, vol. 117, no. 39, pp. 20313–20319, Oct. 2013, doi: 10.1021/jp4067718.

[386] M.-F. Rau, D. Rieck, and J. W. Evans, "Investigation of iron oxide reduction by TEM," *Metall. Trans. B*, vol. 18, no. 1, pp. 257–278, Mar. 1987, doi: 10.1007/BF02658451.

[387] G. Zhong, J. H. Warner, M. Fouquet, A. W. Robertson, B. Chen, and J. Robertson, "Growth of Ultrahigh Density Single-Walled Carbon Nanotube Forests by Improved Catalyst Design," *ACS Nano*, vol. 6, no. 4, pp. 2893–2903, Apr. 2012, doi: 10.1021/nn203035x.

[388] C. F. Cullis, D. J. Hucknall, and J. V. Shepherd, "Studies of the Reactions of Ethynyl Radicals with Hydrocarbons," *Proc. R. Soc. Lond. Ser. Math. Phys. Sci.*, vol. 335, no. 1603, pp. 525–545, 1973.

[389] Y. Song, J.-H. Kim, K.-S. Kim, S. Kim, and P. K. Song, "Effect of C2H2/H2 Gas Mixture Ratio in Direct Low-Temperature Vacuum Carburization," *Metals*, vol. 8, no. 7, Art. no. 7, Jul. 2018, doi: 10.3390/met8070493.

[390] P. H. Dawson and A. J. B. Robertson, "Decomposition of acetylene on incandescent niobium," *Trans. Faraday Soc.*, vol. 60, no. 0, pp. 1122–1130, Jan. 1964, doi: 10.1039/TF9646001122.

[391] C. E. Johnson and W. A. Weimer, "Gas-Phase Precursors to Diamond and the sp2 Carbon Impurity," *J. Electrochem. Soc.*, vol. 141, no. 8, p. 2161, Aug. 1994, doi: 10.1149/1.2055079.

[392] J. A. Smith, E. Cameron, M. N. R. Ashfold, Y. A. Mankelevich, and N. V. Suetin, "On the mechanism of CH3 radical formation in hot filament activated CH4/H2 and C2H2/H2 gas mixtures," *Diam. Relat. Mater.*, vol. 10, no. 3, pp. 358–363, Mar. 2001, doi: 10.1016/S0925-9635(00)00443-X.

[393] B. W. Smith and D. E. Luzzi, "Electron irradiation effects in single wall carbon nanotubes," *J. Appl. Phys.*, vol. 90, no. 7, pp. 3509–3515, Oct. 2001, doi: 10.1063/1.1383020.

[394] J. H. Warner *et al.*, "Investigating the Diameter-Dependent Stability of Single-Walled Carbon Nanotubes," *ACS Nano*, vol. 3, no. 6, pp. 1557–1563, Jun. 2009, doi: 10.1021/nn900362a.

Abstract

The outstanding properties of single-walled carbon nanotubes (SWCNTs) depend strongly on their atomic structure, which can be determined through different synthesis methods. However, the synthesis of a well-defined structural single-walled carbon tubes (SWCNTs) which could be used for a certain application has been a major challenge for the scientific community. According to various published studies, we can see that the synthesis of SWCNTs can be preliminary controlled via the physical parameters of growth in the CVD system (such as temperature, pressure, carbonaceous precursors, catalyst, etc.). Although growth pressure has been theoretically proven to greatly influence the formation of catalytic nanoparticles, and subsequently SWCNTs, there are not too many studies to date addressing this parameter. This can be explained by the lack of CVD systems that allow the synthesis of SWCNTs over a large pressure range, especially at low pressure levels.

In this thesis, a modified HFCVD system is suitable for pressure changes over a large range, thereby enabling to perform the synthesis of SWCNTs not only at medium and high pressure, but also at as low pressure as 10^{-4}mbar. In our first experiments, we used Fe catalyst – a common catalyst in the synthesis of SWCNTs and a temperature of 800°C – a temperature at which we have recorded much success in synthesizing SWCNTs in another HFCVD system placed in LPICM. Each different growth pressure is carefully studied with at least three samples to guarantee that the experiments are reproducible. This study makes it possible to better understand the effects of pressure on the growth of SWCNTs. We were able to show the successful synthesis of SWCNTs at as low growth pressure as in in-situ SWCNTs synthesis through environmental transmission electron microscopy (ETEM).

Besides, the change in diameter of SWCNTs with temperature at different pressure is also observed in the case of using Fe catalyst, and the existence of specific optimal growth temperatures, which is proven through analytical methods such as Raman spectroscopy or SEM and TEM images. An explanation based on the evolution of

carbon solubility in the catalyst particle, depending on the size, temperature and pressure is proposed to explain the resulting phenomena. In the next step, we perform studies on the effects of the bimetallic FeMo system on the synthesis of SWCNTs. Preliminary studies by Raman spectroscopy and ex-situ TEM images showed a certain influence of the concentration ratio between Fe and Mo on the growth of SWCNTs, thereby confirming each interest of using bimetallic FeMo for the SWCNTs growth. Finally, an in-situ experiments with the CVD system implemented in the ETEM (NanoMax) were carried out to specifically document the synthesis of SWCNTs with the bimetallic FeMo. A comparison was done between Fe single-metal catalyst system and FeMo bimetallic system to reach reliable findings concerning the preference of FeMo system on the synthesis of SWCNTs, thereby paving the way for the further selective synthesis of SWCNTs.

Résumé de la these

Le présent manuscrit se concentre principalement sur l'investigation de la croissance des nanotubes de carbone à paroi unique (SWCNTs) par dépôt chimique en phase vapeur à basse pression (LPCVD) et diverses techniques de caractérisation, à la fois ex-situ et in-situ. La synthèse des SWCNTs avec une structure atomique bien définie, adaptée à une application spécifique, demeure un défi majeur pour la communauté scientifique. Les propriétés exceptionnelles des SWCNTs dépendent fortement de leur structure atomique, qui peut être déterminée par différentes méthodes de synthèse.

Selon diverses études publiées, la synthèse des SWCNTs peut être préliminairement contrôlée via les paramètres physiques de croissance dans le système de dépôt chimique en phase vapeur (CVD) tels que la température, la pression, les précurseurs carbonés, le catalyseur, etc. Bien que la pression de croissance ait été théoriquement prouvée pour influencer considérablement la formation de nanoparticules catalytiques et par conséquent des SWCNTs, il existe peu d'études à ce jour abordant ce paramètre. Cela s'explique par le manque de systèmes CVD permettant la synthèse des SWCNTs sur une large plage de pressions, en particulier à basse pression.

Dans cette thèse, un système HFCVD modifié est adapté aux variations de pression sur une grande plage, permettant ainsi la synthèse des SWCNTs non seulement à pression moyenne et élevée, mais aussi à une pression aussi basse que le 10^{-4} mbar. Nous avons utilisé le catalyseur Fe - un catalyseur courant dans la synthèse des SWCNTs - et une température de 800 °C, une température à laquelle nous avons enregistré beaucoup de succès dans la synthèse des SWCNTs dans un autre système HFCVD placé au LPICM. Chaque pression de croissance différente est soigneusement étudiée avec au moins trois échantillons pour garantir la reproductibilité des expériences. Cette étude permet de mieux comprendre les effets de la pression sur la croissance des SWCNTs, montrant la synthèse réussie de SWCNTs à une pression de

croissance aussi basse que dans la synthèse in-situ des SWCNTs par microscopie électronique en transmission environnementale (ETEM).

De plus, le changement de diamètre des SWCNTs avec la température à différentes pressions est également observé dans le cas de l'utilisation du catalyseur Fe, avec l'existence de températures de croissance optimales spécifiques, démontrées par des méthodes analytiques telles que la spectroscopie Raman ou les images SEM et TEM. Une explication basée sur l'évolution de la solubilité du carbone dans la particule catalytique, en fonction de la taille, de la température et de la pression, est proposée pour expliquer les phénomènes résultants.

Dans la phase suivante, des études sont menées sur les effets du système bimétallique FeMo sur la synthèse des SWCNTs. Des études préliminaires par spectroscopie Raman et des images TEM ex-situ ont montré une certaine influence du rapport de concentration entre Fe et Mo sur la croissance des SWCNTs, confirmant ainsi l'intérêt d'utiliser le bimétallique FeMo pour la croissance des SWCNTs. Enfin, des expériences in-situ avec le système CVD implémenté dans l'ETEM (NanoMax) ont été réalisées pour documenter spécifiquement la synthèse des SWCNTs avec le bimétallique FeMo. Une comparaison a été faite entre le système de catalyseur simple Fe et le système bimétallique FeMo pour atteindre des conclusions fiables concernant la préférence du système FeMo pour la synthèse des SWCNTs, ouvrant ainsi la voie à une synthèse sélective ultérieure des SWCNTs.

Le manuscrit se poursuit en abordant l'investigation de la croissance des SWCNTs par LPCVD à basse pression, mettant l'accent sur la paramétrisation d'un chemin de synthèse macroscopique compatible avec le couplage potentiel avec des expériences in-situ et en temps réel dans l'ETEM-NanoMax. Les chapitres suivants présentent une revue de la littérature sur les nanotubes de carbone, une exploration du processus de synthèse des SWCNTs par CVD, ainsi que la description des techniques de fabrication et de caractérisation des SWCNTs.

La thèse examine également l'influence de la pression et de la température sur la reproductibilité et l'uniformité de la croissance des SWCNTs, avec une analyse détaillée des résultats obtenus. La focus sur la cristallinité, la densité et le diamètre des SWCNTs avec le catalyseur bimétallique Mo-Fe est abordé, avec une comparaison quantitative avec le catalyseur Fe couramment utilisé. Les chapitres ultérieurs explorent les résultats des études sur la nucléation et la croissance des SWCNTs en utilisant l'ETEM-NanoMax, fournissant une compréhension approfondie de l'évolution en fonction des différents paramètres de croissance.

En conclusion, le manuscrit présente une synthèse approfondie de l'exploration de la mise en œuvre du LPCVD dans la synthèse des SWCNTs, mettant en évidence les paramètres de croissance influents et explorant la possibilité de reproduire les expériences LPCVD prometteuses dans le CVD@ETEM in-situ. L'objectif central de la thèse est de développer et de paramétrer un chemin de synthèse CVD macroscopique compatible avec le couplage potentiel avec des expériences in-situ et en temps réel dans l'ETEM-NanoMax.

Mots clés : Nanotubes de carbone à paroi unique (SWCNTs), Dépôt chimique en phase vapeur à basse pression (LPCVD), Microscopie électronique en transmission environnementale (ETEM)

ECOLE DOCTORALE

Titre: Synthèse de SWCNTs par dépôt chimique en phase vapeur (CVD) à basse pression, assisté par des radicaux, pour une mise en œuvre potentielle d'une technique d'analyse in-situ et en temps réel (ETEM - NanoMax)

Mots clés: dépôt chimique en phase vapeur à basse pression (LPCVD), nanomatériau, nanostructure, nanotubes de carbone à paroi simple (SWCNT)

Résumé: Dans ma thèse, le dépôt chimique en phase vapeur à filament chaud (HFCVD) a été utilisé pour synthétiser les nanotubes de carbone monoparois (SWCNTs). L'étape initiale était centrée sur la mise en place d'un système HFCVD dans le but d'identifier les conditions optimales de croissance pour produire des SWCNTs sur des substrats de silicium. Dans ce but, des études de l'influence de divers paramètres de croissance, dont la quantité de catalyseur employée, la température de synthèse, la pression de croissance dans le réacteur CVD, ont été réalisées. En particulier, la variation de la pression s'est avérée efficace pour contrôler la croissance des SWCNTs. Les SWCNTs obtenus ont été systématiquement caractérisés par microscopie électronique à balayage, microscopie électronique à transmission, et spectroscopie Raman.
Grâce à cette approche innovante, les conditions de croissance d'échantillons prometteurs ont été utilisées comme prototype pour l'investigation in-situ en microscopie électronique à transmission environnementale (ETEM) implémentée avec une source de gaz CVD (NanoMAX). Le NanoMAX est une technique puissante, qui nous permet d'étudier en temps réel et in-situ les changements dynamiques des catalyseurs pendant la nucléation et la formation des SWCNTs, puis d'optimiser et de contrôler la croissance des SWCNTs.

Title: Low – pressure, radical assisted chemical vapor deposition (CVD) synthesis of SWCNTs for potential implementation in-situ and real-time analysis technique (ETEM – NanoMax)

Keywords: low-pressure chemical vapor deposition (LPCVD), nanomaterial, nanostructure, single-walled carbon nanotubes (SWCNTs)

Abstract: In my thesis, the hot-filament chemical vapor deposition (HFCVD) was used to synthesize the single-walled carbon nanotubes (SWCNTs). The initial step was centered on setting up a HFCVD system with the purpose to identify the optimal growth conditions for producing SWCNTs on silicon substrates. To this goal, the studies of the influence of various growth parameters, including the quantity of catalyst employed, the synthesis temperature, growth pressure in the CVD reactor, were carried out. In particular, the variation of pressure was shown to be effective in controlling the growth of SWCNTs. The obtained SWCNTs were systematically characterized by scanning electron microscopy, transmission electron microscopy, and Raman spectroscopy.
Thanks to this innovative approach, the growth conditions of promising samples have been used as a prototype for the in-situ investigation in the environment transmission electron microscopy (ETEM) implemented with CVD gas source (NanoMAX). The NanoMAX is a powerful technique, which allows us to study real-time and in-situ the dynamic changes of catalysts during the nucleation and the formation of SWCNTs, followed by the optimization and controlling the growth of SWCNTs.